UNIVERSITY OF CALIFORNIA, SAN DIEGO

Development of Solid-state NMR Spectroscopy for Membrane Proteins: Application to the Mercury Transporter MerF

A dissertation submitted in partial satisfaction of the
requirements for the degree Doctor of Philosophy

in

Chemistry

by

Jiaozhi George Lu

Committee in Charge:

Professor Patricia A. Jennings
Professor Tadeusz F. Molinski
Professor Stanley J. Opella, Chair
Professor Brian Palenik
Professor Hector Viadiu

2014

The Dissertation of Jiaozhi George Lu is approved, and it is acceptable in quality and form for publication on microfilm and electronically

_____

_____

_____

_____

_____
Chair

University of California, San Diego

2014

DEDICATION

To my wife, Cathy, my daughter, Ellen,

and my parents, Ping Lu and Yaqun Hu,

who provided their endless support over the years

TABLE OF CONTENTS

LIST OF ABBREVIATIONS

^{1}H	Proton
^{2}H	Deuterium
^{13}C	Carbon-13
^{15}N	Nitrogen-15
^{31}P	Phosphorus-31
14-o-PC	1,2-di-O-tetradecyl-*sn*-glycero-3-phosphocholine
6-o-PC	1,2-di-O-hexyl-*sn*-glycero-3-phosphocholine
AMS	Ammonium sulfate
CNBr	Cyanogen bromide
CRDSD	Cross-relaxation driven spin diffusion
CSA	Chemical shift anisotropy
CW	Continuous wave
DARR	Dipolar assisted rotational resonance
DC	Dipolar coupling
DCCICS	Dipolar coupling correlated isotropic chemical shift
DHPC	1,2-dihexanoy-sn-glycero-3-phosphocholine
DMPC	1,2-dimyristoyl-sn-glycero-3-phosphocholine
DPC	Dodecylphosphocholine
DTT	Dithiothreitol
EDTA	Ethylenediamine tetracetic acid
FSLG	Frequency-switched Lee-Goldberg decoupling

HcCxCx	^{1}H-^{13}C dipolar coupling / ^{13}C chemical shift / ^{13}C chemical shift
HEPES	4-(2-hydroxyethyl)-1-piperazineethanesulfonic acid
HETCOR	Heteronuclear correlation
HFIP	1,1,1,3,3,3-Hexafluoro-2-propanol
Hg(II)	Hg^{2+} ion
HnNCa	^{1}H-^{15}N dipolar coupling / ^{15}N chemical shift / ^{13}Cα chemical shift
HnNCo	^{1}H-^{15}N dipolar coupling / ^{15}N chemical shift / ^{13}CO chemical shift
HSQC	Heteronuclear single quantum coherence
INEPT	Insensitive nuclei enhanced polarization transfer
IPTG	Isopropyl β-thiogalactoside
KSI	Ketosteroid isomerase
kD	Kilo-Dalton
LB	Luria-Bertani
MSHOT	Magic sandwich with high order truncation
MMHH	Mismatched Hartmann-Hahn condition
NMR	Nuclear magnetic resonance
NOE	Nuclear overhauser effect
PDB	Protein data bank
PDLF	Proton-detected local field
PDSD	Proton-driven spin diffusion
PELF	Proton-evolved local field
PISA	Polarity index slant angle

PISEMA	Polarization inversion with spin exchange at the magic angle
PRE	Paramagnetic Relaxation Enhancement
SDS	Sodium dodecyl sulfate
SDS-PAGE	Sodium dodecyl sulfate-polyacrylamide gel electrophoresis
SLF	Separated local field
RMSD	Root mean squared deviation
TFE	2,2,2-Trifluoroethanol
TM	Transmembrane
TSAR	Third spin assisted recoupling

LIST OF FIGURES

LIST OF TABLES

ACKNOWLEDGEMENTS

First and foremost, I would like to thank my thesis advisor, Professor Stanley Opella for giving me the opportunity to conduct cutting edge research in his laboratory. The graduate thesis work would not be possible without his guidance and encouragement, and the work has benefited from the laboratory research environment that is both intellectually challenging and uplifting. I would also like to thank other members in my thesis committee, Professor Patricia Jennings, Professor Hector Viadiu, Professor Tadeusz Molinski and Professor Brian Palenik, for their guidance, supportiveness and openness to the discussion with me of scientific questions.

I would like to give many thanks to the members of the Opella research group. Special acknowledgement must be given to Dr. Woo Sung Son for teaching me all the biochemical and spectroscopic techniques when I first joined the group and for his leading role in the Mer project research in the first few years before he left to start his own research laboratory. Other members of the Mer project group include Dr. Henry Nothnagel, who provided me with stimulating discussions and showed me various biochemical techniques, Nemil Vora, who spent several years as undergraduate research assistant working together on the MerF project, Dr. Aubrey Davis and Sam Rana. Dr. Gabriel Cook, Dr. Fabio Casagrande, Dr. Dongtao Cui, David Black, Leah Cho and Lindsay Dawson have shared the same office with me and provided endless guidance and discussions of both science and life. I would like to thank Dr. Ye Tian for assisting in the calculation of MerF structure and showing me many computational

techniques. Dr. Sang Ho Park, Dr. Anna De Angelis, Dr. Yan Wang, Dr. Fabian Filipp, Hua Zhang, Yanwen Mai, Mignon Chu, Lena Jairam, Sabrina Berkamp, Jasmina Radiocic, Vivian Wang and Mitchell Zhao have shared their wetlab experiences and biochemical knowledge with me in a daily base. Dr. Xuemei Huang and Dr. Anthony Mrse have provided important training about solution NMR spectroscopy and many stimulating discussions about science. I would like to thank Dr. Bibhuti Das for teaching me a tremendous amount of knowledge about NMR spectroscopy. Dr. Chin Wu, Dr. Chris Grant, Dr. Alexander Nevzorov, Dr. Yuan Yang, Dr. J. Michael Kaiser, Dr. Ilya Litvak, Wei Lin and Eugene Lin at the Center for NMR Spectroscopy and Imaging of Proteins, "The Bubble", have also taught me many solid-state NMR techniques and theories, shared and encouraged my study on spectroscopy, and provided important assistance in solving practical instrumentation problem whenever needed. Last but not the least, I would like to thank Elena Vitoshka-tarasov and Roxanne Connell for their wonderful jobs as the administrative assistants of the laboratory, assisting me from time to time on fulfilling various UCSD processes.

I would also like to thank Professor Francesca Marassi at Sanford-Burnham Medical Research Institute, Professor Alexander Nevzorov at North Carolina State University and Professor Wonpil Im at The University of Kansas for the collaborations on various projects. I would like to thank Professor Brian Sykes and Professor Michael James at University of Alberta who were my undergraduate research advisors and mentors. They opened the door of my career towards structural

biology and gave me the confidence to pursue a doctorate degree. I would like to thank Professor James Williamson, Professor Ardem Patapoutian and Professor Kurt Wüthrich at The Scripps Research Institute for accommodating me during Ph.D. rotation and opening my eyes to many fascinating researches in biophysics and neuroscience.

Chapter 2, in full, is a reprint of the material "A general assignment method for oriented sample (OS) solid-state NMR of proteins based on the correlation of resonances through heteronuclear dipolar couplings in samples aligned parallel and perpendicular to the magnetic field" as it appears in J. Magn. Reson. 209(2):195-206 by Lu GJ, Son WS, Opella SJ. The thesis author was the primary author of the paper.

Chapter 3, in full, is a reprint of the material "Improved ^{1}H amide resonance line narrowing in oriented sample solid-state NMR of membrane proteins in phospholipid bilayers" as it appears in J. Magn. Reson. 220:54-61 by Lu GJ, Park SH, Opella SJ. The thesis author was the primary author of the paper.

Chapter 4, in full, is a reprint of the material "Resonance assignments of a membrane protein in phospholipid bilayers by combining multiple strategies of oriented sample solid-state NMR" as it appears in J. Biomol. NMR 58(1): 69-81 by Lu GJ, Opella SJ. The thesis author was the primary author of the paper.

Chapter 5, in full, is a reprint of the material "Motion-adapted pulse sequences for oriented sample (OS) solid-state NMR of biopolymers" as it appears in J. Chem. Phys. 139(8):084203 by Lu GJ, Opella SJ. The thesis author was the primary author of the paper.

Chapter 6, in full, is a reprint of the material "Mechanism of dilute-spin-exchange in solid-state NMR" as it appears in J. Chem. Phys. 140(12):124201 by Lu GJ, Opella SJ. The thesis author was the primary author of the paper.

Chapter 7 is a reprint of the material "The structure of the mercury transporter MerF in phospholipid bilayers: a large conformational rearrangement results from N-terminal truncation" as it appears in J. Am. Chem. Soc. 135(25):9299-9302 by Lu GJ, Tian Y, Vora N, Marassi FM, Opella SJ. The thesis author was the primary author of the paper.

Chapter 8 is currently being prepared for submission for publication of the material.

VITA

2007 Bachelor of Science, University of Alberta, Canada

2014 Doctor of Philosophy, University of California, San Diego

PUBLICATIONS

Lu GJ, Opella SJ (2014) Mechanism of dilute-spin-exchange in solid-state NMR. *J. Chem. Phys.* 140(12):124201.

Lu GJ, Opella SJ (2014) Resonance assignments of a membrane protein in phospholipid bilayers by combining multiple strategies of oriented sample solid-state NMR. *J. Biomol. NMR* 58(1): 69-81.

Lu GJ, Opella SJ (2013) Motion-adapted pulse sequences for oriented sample (OS) solid-state NMR of biopolymers. *J. Chem. Phys.* 139(8):084203.

Lu GJ, Tian Y, Vora N, Marassi FM, Opella SJ (2013) The structure of the mercury transporter MerF in phospholipid bilayers: a large conformational rearrangement results from N-terminal truncation. *J. Am. Chem. Soc.* 135(25):9299-9302.

Son WS, Park SH, Nothnagel HJ, Lu GJ, Wang Y, Zhang H, Cook GA, Howell SC, Opella SJ (2012) 'q-Titration' of long-chain and short-chain lipids differentiates between structured and mobile residues of membrane proteins studied in bicelles by solution NMR spectroscopy. *J. Magn. Reson.* 214:111-118.

Das BB, Nothnagel HJ, Lu GJ, Son WS, Tian Y, Marassi FM, Opella SJ (2012) Structure determination of a membrane protein in proteoliposomes. *J. Am. Chem. Soc.* 134(4):2047-2056.

Lu GJ, Park SH, Opella SJ (2012) Improved ^{1}H amide resonance line narrowing in oriented sample solid-state NMR of membrane proteins in phospholipid bilayers. *J. Magn. Reson.* 220:54-61.

Marassi FM, Das BB, Lu GJ, Nothnagel HJ, Park SH, Son WS, Tian Y, Opella SJ (2011) Structure determination of membrane proteins in five easy pieces. *Methods* 55(4):363-369.

Lu GJ, Son WS, Opella SJ (2011) A general assignment method for oriented sample (OS) solid-state NMR of proteins based on the correlation of resonances through heteronuclear dipolar couplings in samples aligned parallel and perpendicular to the magnetic field. *J. Magn. Reson.* 209(2):195-206.

Knox RW, Lu GJ, Opella SJ, Nevzorov AA (2010) A resonance assignment method for oriented-sample solid-state NMR of proteins. *J. Am. Chem. Soc.* 132(24):8255-8257.

Cherney LT, Cherney MM, Garen CR, Lu GJ, James MNG (2008) Crystal structure of the arginine repressor protein in complex with the DNA operator from Mycobacterium tuberculosis. *J. Mol. Biol.* 384(5):1330-1340.

Cherney LT, Cherney MM, Garen CR, Lu GJ, James MNG (2008) Structure of the C-terminal domain of the arginine repressor protein from Mycobacterium tuberculosis. *Acta Crystallogr D Biol Crystallogr* 64(Pt 9):950-956.

Lu GJ, Garen CR, Cherney MM, Cherney LT, Lee C, James MNG (2007) Expression, purification and preliminary X-ray analysis of the C-terminal domain of an arginine repressor protein from Mycobacterium tuberculosis. *Acta Crystallogr Sect F Struct Biol Cryst Commun* 63(Pt 11):936-939.

ABSTRACT OF THE DISSERTATION

Development of Solid-state NMR Spectroscopy for Membrane Proteins and Application to the Mercury Transporter MerF

by

Jiaozhi George Lu

Doctor of Philosophy in Chemistry

University of California, San Diego, 2014

Professor Stanley J. Opella, Chair

Atomic-resolution membrane protein structures can be determined by solid-state Nuclear Magnetic Resonance (NMR) spectroscopy, and the unique advantage of the approach is that membrane proteins reside in near-native lipid bilayer environment at physiological pH and temperature, which minimizes the potential distortions of the protein structure caused by the environment. Here, the full-length mercury transporter protein, MerF, is the focus of the structural studies, and the protein is an essential part of the bacterial mercury detoxification system that has been exploited as a potential engineering target for mercury bioremediation strategies. The backbone structures of

the full-length MerF are determined in two environments, (i) magnetically aligned bicelles by oriented-sample (OS) solid-state NMR and (ii) proteoliposome by rotationally aligned (RA) solid-state NMR; and notably, both environments provide the planar lipid bilayer environment for the protein. The structural study of MerF in aligned bicelle has initially been challenging for the OS solid-state NMR, and consequently, methods have been developed to tackle the two major obstacles, the spectral resolution and resonance assignments. New pulse sequence, MSHOT-Pi4/Pi, has demonstrated a reduction of the ^{1}H resonance line width by more than a factor of two, a significant improvement in spectral resolution. New resonance assignment method, Dipolar Coupling Correlated Isotropic Chemical Shift (DCCICS) Analysis, has been developed that is able to transfer resonance assignment from isotropic NMR methods to OS solid-state NMR spectra. The combined usage of several resonance assignment strategies and special tactics, such as applying DCCICS to the new high-resolution proton-evolved local field experiments for terminal and loop residues, has resulted in the complete assignment of all backbone immobile residues of the full-length MerF protein in magnetically aligned bicelle. Meanwhile, RA solid-state NMR is developed in the lab as a new method that combines the strength of magic-angle-spinning (MAS) solid-state NMR in obtaining resonance assignment and the concept of molecular alignment from OS solid-state NMR in obtaining angular restraints. In applying to the structural study of MerF, the method is further incorporated with multi-contact cross polarization and sequential backbone “walk” with three three-dimensional experiments, and the first structure of full-length MerF is determined with

the method. In comparison to the previously determined structure of the truncated MerF (MerFt), the full-length structure reveals that the protein truncation has caused large conformational rearrangement at a place more than ten residues away from the truncation site, which serves as an example to demonstrate the importance of studying the full-length unmodified proteins by structural biologists. Additionally, the structure reveals that both mercury-binding sites are located at the intracellular side of the membrane, hinting at the observation of a conformation that allows intramolecular transfer of mercury ions. Subsequently after the complete assignment of MerF in OS solid-state NMR, the MerF structure determined by RA solid-state NMR is further improved by incorporating additional angular restraints from OS solid-state NMR and by the new treatment of dihedral restraints derived from the experimental study of C-terminal dynamics. Lastly, as a side project, the theoretical foundation of MSHOT-Pi4 pulse sequence is further explored. The observation that the pulse sequence selectively improves the resolution of membrane protein samples but not of standard single crystal sample has been analytically generalized as the principle of "motion-adapted" pulse sequence, where it is found that the interference between sample's spatial rotational motion and the radio-frequency pulse rotation in the quantum spin space is the cause of the selectivity. As a related endeavor, the mechanisms of dilute spin exchange and the magic-angle ^{1}H spin-lock pulses have been analyzed theoretically and demonstrated in standard and biological samples. Mixed-order proton-relay mechanism is proposed to be the main contributor to dilute spin exchange in stationary aligned sample, and once more, the difference of pulse performance between standard

and biological samples is observed that may be a consequence of several causes including sample motion. In conclusion, the development of various methods in OS and RA solid-state NMR are likely to find their usage in future structural studies of membrane proteins; the theoretical principle of motion-adapted property opens up new avenue to develop pulse sequences for membrane protein samples; and the atomic-resolution backbone structures of MerF contribute information for structural biologist and for the mechanistic study of mercury transportation.

Chapter 1 General Introduction

1.1 Introduction to Nuclear Magnetic Resonance (NMR) Spectroscopy

Structural biology aims to understand the mechanism and the chemistry occur in a biomolecule at the atomic resolution. In other words, structural biologists often focus on a specific biomolecule or set of biomolecules such as protein, protein complex and nucleic acids, and study their function and mechanism in depth by understanding individual atom's location and dynamics within the biomolecule. To achieve the aims of structural biology, physical methods are often used as the tools. For example, X-ray crystallography relies on the diffraction pattern of the X-ray beam passing through the protein crystal to obtain the high-resolution electron density map of the molecule. Nuclear Magnetic Resonance (NMR) spectroscopy, on the other hand, relies on the interaction of nuclear quantum spins to derive the coordinates and dynamics of individual atoms in the molecule.

NMR spectroscopy techniques can be broadly divided into solution NMR and solid-state NMR. Solution NMR has been established earlier but possessed certain limitations. The high resolution obtained in solution NMR spectra relies on the molecules under investigation to undergo fast isotropic rotational tumbling. When the size of the molecule increases, the tumbling rate decreases and the line width of the spectra becomes broadened. This inherent sample size limitation is a commonly known major limitation to the biological application of solution NMR, as many proteins above the size of 30 kD are difficult to be analyzed by routine solution NMR

method and instrumentation. Solid-state NMR, on the other hand, does not possess the same inherent limitation on molecular weight. To achieve high resolution in solid-state NMR, high-power pulses sequences are often designed specifically to remove the undesired spin interactions that cause line broadening. In addition, sample manipulations including fast spinning at the magic angle or macroscopic sample alignment often accompany the usage of corresponding pulse sequences. Nevertheless, it should be pointed out that the large size of the proteins also leads to the crowdedness of the spectra, simply because of the large number of unique sites. Thus the difficulty in resolving individual peaks due to spectral crowdedness is an obstacle common for both solution and solid-state NMR approaches.

Specifically for the application of NMR towards membrane proteins, the inherent size limitation of solution NMR becomes more severe, because membrane proteins require the membrane mimetic to support their solubility in aqueous buffers, which further increases the total molecular weight of the assembly. The desire to reduce the total molecular weight drives the usage of detergent micelle as the main membrane mimetic for studying membrane proteins by solution NMR; however, detergent micelles do not provide the same lipid bilayer environment as what the membrane proteins usually residue in at the cellular membrane. Several examples of membrane protein structures determined in detergent micelles have already been shown to contain distortions when they are compared with the structure of the same molecule determined in lipid bilayer (Zhou and Cross, 2013). Therefore, it is important to develop strategies to study membrane protein structures

To determine the high-resolution membrane protein structure in a native-like lipid bilayer environment is the main motivation of the research in the laboratory and that described in this thesis. The assembly of membrane proteins with lipid bilayer tends to be much larger than that with detergent micelles, and as a result, the membrane proteins do not undergo fast isotropic tumbling. Instead of using solution NMR, solid-state NMR methodologies are developed for the task.

Structural restraints are measured and used as the input for restraint-guided molecular dynamics calculation of the structure in the process of structure determination by NMR. The three major groups of structural restraints are (1) distance restraint, which determine the distance between two nuclei, (2) angular restraint, which reflects the angle between chemical bond and a common molecular or external axis, and (3) dihedral angle restraint, which is the relative angle between adjacent chemical bonds and is often derived from isotropic chemical shifts (Cornilescu et al., 1999). For solution NMR, the distance restraint is often in the form of Nuclear Overhauser Effect (NOE) and the angular restraint in the form of Residual Dipolar Coupling (RDC) (Tjandra et al., 1997; Tolman et al., 1995). Similarly, in solid-state NMR the distance restraint can often be derived from spin diffusion experiments. In favorable cases such as the Src-homology 3 domain structure (Castellani et al., 2002), sufficient amount of distance restraints could be obtained to define the high-resolution structure of the protein. However, for helical membrane proteins it is often difficult to collect enough distance restraints, especially the long-range ones between transmembrane helices. Instead, the high-resolution membrane protein structure

determination approach developed in the laboratory and described in this thesis utilizes primarily the angular restraints supplemented with a few long-range inter-helical distance restraints.

The interaction of nuclear quantum spins, including mainly ^{1}H, ^{2}H, ^{13}C and ^{15}N, forms the basis of the NMR spectroscopy, and for the application described in this thesis the interactions mainly include the chemical shifts and dipolar couplings. Each spin possesses its own chemical shift, which depends on both the chemical environment surrounding the nucleus and the orientation of the nucleus principle axis with respect to the external magnetic field. In the case of solution NMR where fast isotropic tumbling of the molecules occur, the orientation dependent part of the chemical shift is averaged. Consequently, the orientation information is lost and the remaining chemical shift components are commonly referred to as the isotropic chemical shift. Dipolar coupling values are determined by the distance between the two nuclei and the angle of the vector with respect to the magnetic field. Dipolar coupling are usually averaged to zero in solution NMR because of the isotropic motion. In solid-state NMR, long-range dipolar couplings between non-bonded atoms are the main contributor to the distance restraints, but a sufficient amount of them are difficult to observe. On the other hand, because the bond length between two directly bonded atoms are relatively stable, the short-range dipolar couplings between bonded atoms mainly provide angular restraints. These restraints can be used to determine membrane protein structures at high resolution.

1.2 Introduction to Mercury Detoxification System

Bacterial mercury detoxification system was found from microbes survived in heavily mercury polluted lakes and rivers (Hobman et al., 1994; Lund and Brown, 1987; Misra et al., 1984). The naturally evolved mercury detoxification system is able to catalyze the reduction reaction of Hg^{2+} ion or methyl mercury $[CH_3Hg]^+$ into elemental mercury Hg^0, which is comparatively less toxic and volatile. Elemental mercury can freely diffuse through cellular membranes and water, and eventually evaporate into the air to join the global recycling of mercury compounds. Notably, the influx and detoxifying strategy employed by the bacterial mercury detoxification systems is drastically different from most of the other cellular detoxification systems, which usually uses the energy from ATP or chemiosmotic to pump out and sequester the toxin compounds (Krämer et al., 2007). Therefore, the mercury detoxification system is in a certain sense a mercury purification system that provides a potential engineering target for the bioremediation of mercury pollution, and efforts have been seen towards engineering the system into bacteria and plants (Jan et al., 2009; Ruiz and Daniell, 2009).

The genes of mercury detoxification system are encoded as the *mer* operon on the transponsons or large plasmids that are capable of transmitting among microbes (Barrineau et al., 1985). The mercury detoxification system usually contains periplasmic chaperon protein MerP, mercury reductase enzyme MerA, organomercurial lyase MerB, various mercury transporter protein and metalloregulatory protein MerR and MerD. MerR is responsible for sensing the

presence of toxic mercury compounds and regulating the expression of the genes. The basal level expression of MerR is controlled by a promoter separated from the rest of the component of the system. MerR binds the DNA promoter region of the *mer* operon and recruits the RNA polymerase to form the pre-initiation complex. Then upon the binding of Hg^{2+} to MerR, the transcription would start. On the other hand, MerD serves as the antagonist of MerR and the down-regulator of the gene transcription and thus the system is activated in a well-controlled fashion (Nucifora et al., 1989). Hg^{2+} ions can diffuse into the periplasm of the bacterial cells, where they become tightly bound to MerP and their toxicity towards other protein are eliminated. Next, the mercury transporter proteins facilitate the passive diffusion of Hg^{2+} ions through the inner bacterial cell membrane by increasing the kinetic rate of transportation. It has been shown that the transportation is the rate-limiting step of the entire mercury detoxification process (Nakahara et al., 1979), which is one of the reasons for the structural studies on the transporter proteins. Hg^{2+} ions are then passed from the transporter to the enzyme, mercury reductase MerA. If $[CH_3Hg]^+$ is the toxic mercury compounds transported into the cell, it would be first passed to MerB, which catalyzes the protonolysis of the carbon-mecury bond and yields the Hg^{2+} (Di Lello et al., 2004), and then the Hg^{2+} ions are processed by MerA in the same fashion.

The mercury transporter proteins include MerT, MerF, MerE, MerC, MerH and MerTP. In each plasmid containing *mer* operon, a specific set but usually not all of the transporter genes are present, and it is believed that the specific combination of transporter proteins confers the different selectivity on toxic mercury compounds. The

mercury binding sites are composed of a pair of cysteine residues. The spacing between the two cysteines is different among the various mercury transporter proteins, and the spacing has been shown to influence the affinity of the site towards various heavy metal compounds (DeSilva et al., 2002). Therefore, one of the reasons proposed to explain the existence of multiple transporter proteins is the adaptation to different toxic mercury environment.

The structures of the water-soluble components of the mercury detoxification systems have already been available due to the technical feasibility of determining the structure of soluble proteins. The structure of the mercuric reductase MerA was determined using X-ray crystallography first in the 90s (Schiering et al., 1991) and later at higher resolution (PDB: 1ZX9 1.90Å, 1ZK7 1.60Å) (Ledwidge et al., 2005). The structures of the periplasmic chaperone MerP were solved using solution NMR (PDB: 1AFI, 1AFJ, 2HQI) in reduced (Steele and Opella, 1997) and oxidized condition (Qian et al., 1998) and using X-ray crystallography (PDB: 1OSD) (Serre et al., 2004). Similarly, the structures of the organomercurial lyase MerB were solved by solution NMR (PDB: 1S6L) (Di Lello et al., 2004) and by X-ray crystallography (PDB: 3F0O, 3F0P, 3F2F, 3F2G, 3F2H) (Lafrance-Vanasse et al., 2009).

On the contrary, structural studies on the transporter proteins have significantly lagged behind, which reflects the general technological difficulty in membrane protein structure determination. MerF and MerE were the first transporter proteins being studied structurally because they are the shortest ones having only two transmembrane helices. The structures of the truncated helical core construct of MerF, named MerFt,

were obtained in SDS detergent micelle by solution NMR (Howell et al., 2005), in DMPC/DHPC magnetically aligned bicelle by OS solid-state NMR (De Angelis et al., 2006b) and in DMPC proteoliposome by RA solid-state NMR (Das et al., 2012). MerFt structures in aligned bicelle and proteolipsome are well conserved, but the structure in SDS micelle has different dynamics (Lu et al., 2013a). A question raised from the structures of MerFt is on the location of the N-terminal mercury binding site. Previously, the binding site was predicted to locate in the middle of the first helix (Wilson et al., 2000); however, the MerFt structures all showed that this binding site locates at the interface between the membrane and cytosol. One of the possible causes of the controversy was suspected to be the truncation of the protein. In this thesis, the structure of the full-length MerF determined in proteoliposome will be described (Lu et al., 2013a), and the current preparation of the full-length protein in proteoliposome and aligned bicelle again shows that the binding site locates at the interface between membrane and cytosol. Nevertheless, it is shown that truncation made in MerFt causes a conformational rearrangement of the entire N-terminal region containing more than 10 residues after the truncation site.

Chapter 2. Resonance Assignment Method: Dipolar Coupling Correlated Isotropic Chemical Shift (DCCICS) Analysis

2.1 Abstract

A general method for assigning oriented sample (OS) solid-state NMR spectra of proteins is demonstrated. In principle, this method requires only a single sample of a uniformly ^{15}N-labeled membrane protein in magnetically aligned bilayers, and a previously assigned isotropic chemical shift spectrum obtained either from solution NMR on micelle or isotropic bicelle samples or from magic angle spinning (MAS) solid-state NMR on unoriented proteoliposomes. The sequential isotropic resonance assignments are transferred to the OS solid-state NMR spectra of aligned samples by correlating signals from the same residue observed in protein-containing bilayers aligned with their normals parallel and perpendicular to the magnetic field. The underlying principle is that the resonances from the same residue have heteronuclear dipolar couplings that differ by exactly a factor of two between parallel and perpendicular alignments. The method is demonstrated on the membrane-bound form of Pf1 coat protein in phospholipid bilayers, whose assignments have been previously made using an earlier generation of methods that relied on the preparation of many selectively labeled (by residue type) samples. The new method provides the correct resonance assignments using only a single uniformly ^{15}N-labeled sample, two solid-state NMR spectra, and a previously assigned isotropic spectrum. Significantly, this approach is equally applicable to residues in alpha helices, beta sheets, loops, and any

other elements of tertiary structure. Moreover, the strategy bridges between OS solid-state NMR of aligned samples and solution NMR or MAS solid-state NMR of unoriented samples. In combination with the development of complementary experimental methods, it provides a step towards unifying these apparently different NMR approaches.

2.2 Introduction

Oriented Sample (OS) solid-state NMR spectroscopy is well suited for studies of biological supramolecular structures, such as virus particles and membranes, that immobilize the constituent macromolecules and provide a mechanism through their diamagnetic anisotropy for them to be aligned in the magnetic field of an NMR spectrometer. The atomic-resolution structures of several coat proteins in virus particles and a number of helical membrane proteins in phospholipid bilayers (De Angelis et al., 2006b; Ketchem et al., 1993; Opella et al., 1999; Park et al., 2006a; Thiriot et al., 2004; Traaseth et al., 2009; Wang et al., 2001; Zeri et al., 2003a) have been determined in this way. In protein structure determination by OS solid-state NMR spectroscopy, the frequencies of the heteronuclear dipolar couplings and anisotropic chemical shifts associated with individual sites, typically the amide nitrogen and hydrogen of the peptide bonds, are measured from narrow single-line resonances that are resolved in multidimensional solid-state NMR spectra. The measured frequencies from these anisotropic spin interactions are orientationally

dependent and therefore can be converted in a straightforward manner into angular constraints for the calculation of the three-dimensional protein structures.

Despite the strength of the method in obtaining angular constraints for all sites relative to a single external axis (Park et al., 2010a), most examples have been relatively small proteins. The application of the OS solid-state NMR to larger membrane proteins has been hindered mainly by limitations of the resonance assignment procedures. Efficient resonance assignment schemes that "walk" down the polypeptide backbone generally rely on the use of 100% uniformly ^{13}C and ^{15}N labeled samples. In solution NMR and MAS solid-state NMR, the rapid reorientation or rotation of the proteins average out the homonuclear $^{13}C/^{13}C$ dipolar couplings; however, this is not the case in stationary sample, such as single crystals or magnetically aligned bilayers, where the dense network of homonuclear $^{13}C/^{13}C$ dipolar couplings interferes with most solid-state NMR experiments. Methods for applying solid-state NMR to stationary samples uniformly labeled with ^{13}C are in early stages of development. The current principal assignment method, the shotgun approach (Marassi and Opella, 2003), relies on the periodicity of the regular protein secondary structures, α-helix (Marassi and Opella, 2000; Wang et al., 2000) or β-sheet (Marassi, 2001), and the ability to readily label proteins by residue type when they are expressed in bacteria grown on minimal media containing only one type of amino acid that is isotopically labeled. This approach is limited by the need to prepare multiple samples, though the calculations for non-periodic tertiary structures are being improved. Spectroscopic methods based on dilute spin exchange (Marassi et al.,

1999a; Nevzorov, 2008; Nevzorov, 2009; Xu et al., 2008) can be used to assign resonances in uniformly labeled samples, but even in its recently improved forms, its application to membrane proteins is limited by its relatively low sensitivity (Knox et al., 2010). More powerful assignment methods are needed to extend OS solid-state NMR to larger, uniformly labeled proteins and to accelerate the rate of structure determination.

Robust sequential assignment methods have been established in solution NMR (Cavanagh J, 1996) and in MAS solid-state NMR (Castellani et al., 2002; McDermott, 2009; Takegoshi et al., 2001) largely through the use of 100% uniformly ^{13}C and ^{15}N labeled samples that are tractable because of the averaging of the $^{13}C/^{13}C$ homonuclear dipolar couplings by the natural or experimentally induced isotropic motions. Both types of experiments yield resonances characterized by one or more isotropic chemical shift frequencies. As a result, the isotropic chemical shift assignments for proteins are frequently available, and here we demonstrate that they can be integrated into OS solid-state NMR experiments as part of a general assignment strategy. Notably, the development of a method that integrates these different NMR methods can take advantage of their individual strengths, as the ease of resolving resonances and obtaining angular constraints in OS solid-state NMR is combined with the established assignment methods in solution NMR and MAS solid-state NMR. A limitation is that the protein resonances must have similar isotropic chemical shifts in the lipids that constitute the micelle or isotropic bicelles samples used in solution NMR, or unoriented and possibly frozen liposomes in MAS solid-state NMR, and the liquid

crystalline bilayers used in OS solid-state NMR. In favorable cases, the limitation can be partially alleviated by performing a q-titration experiment (Opella et al., 2008) to extrapolate from micelles or isotropic bicelles to the liquid crystalline bilayer environment used in OS solid-state NMR experiments.

Here we demonstrate that the isotropic chemical shifts can be "back calculated" from OS solid-state NMR spectra obtained from samples aligned with their bilayer normals parallel and perpendicular to the magnetic field (De Angelis et al., 2006c). Since the isotropic chemical shift frequencies vary from site-to-site in a protein they provide a unique "tag" for each residue. Consequently, they can serve as the carrier of assignment information between experimental OS solid-state NMR spectra and assigned solution NMR or MAS solid-state NMR spectra. The method for transferring the isotropic chemical shift assignments to stationary aligned samples relies on identifying those heteronuclear dipolar coupling frequencies in parallel alignment that are exactly twice as large as those in the perpendicular alignment. This is possible because the isotropic values for dipolar couplings are zero at all sites. The method utilizes only chemical shift and heteronuclear dipolar coupling data, which can be measured by two- or three- dimensional versions of heteronuclear correlation (HETCOR) and separated local field (SLF) experiments. The results obtained in this way can be readily augmented by assignment information from other experiments and spin interactions.

The membrane protein examples used to illustrate the assignment method are in magnetically aligned bilayers. While they naturally align with their normals

perpendicular to the field, they can be "flipped" to the parallel alignment through the addition of lanthanide ions (De Angelis et al., 2004) that bind weakly to the phospholipids changing their magnetic susceptibility. Alternatively, there are phospholipids that naturally align with their normals parallel to the field (Park et al., 2008). The experiments are equally applicable to membrane proteins in lipid bilayers that are mechanically aligned on glass plates, since they can be physically arranged in the sample coil so that the bilayer normals are either parallel or perpendicular to the direction of the magnetic field (De Angelis et al., 2005; Ketchem et al., 1997; Opella et al., 2001). In this article we demonstrate the principles of this new assignment method using simulated spectra, and its experimental application to two well-characterized examples of membrane proteins. This method has the potential to be applied to larger and more complex membrane proteins as the measurements of chemical shifts and heteronuclear dipolar couplings associated with ^{13}C nuclei and higher field magnets are employed, and automated computer programs substitute for the step-by-step procedures used in these initial examples.

2.3 Principles and Simulated Spectra

In both MAS solid-solid state NMR of powder samples and solution NMR of liquid samples, the angular dependencies of the anisotropic chemical shift and dipolar spin interactions are eliminated by motional averaging, which results in the isotropic values of the chemical shifts determining the observed frequencies of individual resonances in the NMR spectra. In contrast, the angular dependence of the chemical

shift interaction is retained in stationary samples, including the uniaxially aligned samples used for protein structure determination by OS solid-state NMR spectroscopy. The observed resonance frequencies are determined by the directions and magnitudes of the principal elements of the chemical shift tensor relative to the magnetic field; this is obvious in powder patterns, which result from the sum of the frequencies from all orientations, and in the rotation patterns of single crystals, which can be obtained around multiple axes and used to characterize the chemical shift tensors. A useful property is that the magnitudes of the principal values available from either powder patterns or rotation patterns of single crystals by themselves provide sufficient information to determine the isotropic chemical shift frequency for any site. OS solid-state NMR of aligned membrane proteins differs in that only two orthogonal orientations are available; current technology enables samples to be prepared with their bilayer normals parallel or perpendicular to the magnetic field. It is possible to work with the perpendicular orientation because the proteins typically undergo fast axial diffusion about the bilayer normal in liquid crystalline phospholipid bilayers; the resulting single-line resonances complement those observed with the parallel alignment where molecular motion is not required (Park et al., 2006b).

To calculate the isotropic value of the chemical shift from aligned samples, the resonance frequencies measured for both the parallel and perpendicular alignments are combined. The use of magnetically aligned bilayers provides two major advantages. First, the protein-containing bilayers can be “flipped” between alignments with the bilayer normals perpendicular or parallel to the field by the addition of lanthanide

ions, which enables the use of the same sample for the acquisition of both types of spectra. In general, the paramagnetic ions interact with the lipid head groups and do not perturb the proteins, although controls are always advisable. Second, the proteins undergo rapid uniaxial rotational diffusion about the normals of liquid crystalline bilayers at a frequency that is fast compared to the relevant NMR timescales determined by the frequency spans of the chemical shifts and heteronuclear dipolar couplings (approximately 100 kHz at a ^{1}H resonance frequency of 700 MHz), and this results in Equation 2.1, the so-called "bicelle equation" (De Angelis et al., 2006b; Nevzorov and Opella, 2003b; Spiess, 1974; Spiess et al., 1974), which greatly simplifies the calculations of the isotropic values compared with the situation in a rigid lattice:

$$\delta_{iso}^{i} = \frac{\delta_{\parallel}^{i} + 2\delta_{\perp}^{i} S_{rel}}{2S_{rel} + 1} \qquad \text{Eq 2.1}$$

In Equation 2.1, δ_{iso} is the isotropic chemical shift frequency and $\delta_{\parallel}$ and $\delta\perp$ are the anisotropic chemical shift frequencies observed in parallel and perpendicular bilayer samples, respectively. S_{rel} accounts for the small differences in order parameters (Sanders et al., 1994a) observed for the lipids and proteins in the two alignments; it is a global parameter, since the same value can be applied to all the residues in the same sample.

In principle, the isotropic chemical shift frequency of a resonance can be calculated from three measureable parameters, $\delta_{\parallel}$, $\delta\perp$, and S_{rel}. In practice, however, since $\delta_{\parallel}$ and $\delta\perp$ frequencies from many residues are observed in the same spectra of uniformly ^{15}N labeled samples, it is generally not possible to identify which pair of $\delta_{\parallel}$

and $\delta\perp$ frequencies belongs to the same residue by inspection. Here we demonstrate that the heteronuclear dipolar couplings measured for the resonances in the parallel and perpendicular samples can be used to identify those signals that come from the same site in the two spectra. To reiterate the principle of the method, this is feasible because the dipolar couplings always have an isotropic value of zero, and their magnitudes differ by exactly a factor of two between the parallel and perpendicular alignments. In practice, this means that the heteronuclear dipolar coupling frequencies observed in SLF spectra always "flip" around zero, and differ by a factor of $2S_{rel}$ between the parallel and perpendicular sample alignments, as is represented by the "bicelle equation" for dipolar couplings:

$$D_{\parallel}^{i} + 2D_{\perp}^{i}S_{rel} = 0 \qquad \text{Eq 2.2}$$

$D_{\parallel}$ and $D\perp$ are the dipolar coupling frequencies of a resonance from a single site in samples aligned with their bilayer normals parallel and perpendicular to the magnetic field, respectively. In practice, it is advisable to make a list of all signals observed in both parallel and perpendicular spectra ranked according to the magnitudes of their dipolar coupling frequencies. A signal of the same rank in the lists obtained with the two alignments corresponds to the resonance from the same site, which provides a practical method to unambiguously identify the pairs of $\delta_{\parallel}$ and $\delta\perp$ frequencies from each residue from experimental data. This ranking method is demonstrated in the second experimental example of a uniformly ^{15}N labeled sample. Note that since the small correction factor, S_{rel}, is a global parameter, adjusting its value does not affect the rank-ordered list.

The last parameter required for Equation 2.1 is S_{rel}. After ranking the frequencies by their magnitudes, the dipolar couplings of all pairs of correlated resonances can be averaged to obtain an accurate value of the S_{rel} using Equation 2.3:

$$S_{rel} = \frac{1}{N}\sum_{i=1}^{N}\left(-\frac{D_{\parallel}^{i}}{2D_{\perp}^{i}}\right) \qquad \text{Eq 2.3}$$

Alternatively, S_{rel} can be determined from a separate experiments that measure the order parameters of either the protein backbone or the phospholipids in the planar bilayers. We have found that a small error in S_{rel} value usually has negligible effect on the outcome of this assignment method, and therefore S_{rel} can also be assigned an empirical value of 0.9 without penalty to the assignment process. S_{rel} together with the pair of $\delta_{\parallel}$ and $\delta\perp$ frequencies measured for each residue gives the isotropic chemical shifts from Equation 2.1.

A favorable feature of the "bicelle equation" is that the calculation of isotropic chemical shifts is immune to referencing errors. For example, a referencing error of the ^{15}N chemical shifts in the solid-state NMR spectra on the parallel bicelle sample would result in the addition of a factor $\varepsilon_{\parallel}$ to the $\delta_{\parallel}$ values of all residues. According to Equation 2.1, a factor of $\frac{\varepsilon_{\parallel}}{2S_{rel}+1}$ would consequently be added to all of the δ_{iso} values. Since S_{rel} is determined by comparing dipolar coupling values, it is unaffected by the referencing error and remains the same for all residues. Therefore, the same factor $\frac{\varepsilon_{\parallel}}{2S_{rel}+1}$ is added to δ_{iso} for all residues, and this factor can be removed by applying a systematic shift to all δ_{iso} values using the following procedure. After δ_{iso}

values of all residues are obtained from solid-state NMR spectra, we calculate their average value. Similarly, we calculate the average of the isotropic chemical shifts observed in the corresponding solution NMR spectra or MAS solid-state NMR spectra. The difference between these two average values is applied as a universal correction factor to the calculated δ_{iso} of all residues. Note that systematic differences between isotropic chemical shift frequencies measured from solution NMR and solid-state NMR spectra have been observed previously (Kurita et al., 2003), and there are a number of plausible reasons for this variation, including differences in referencing standards and methods, magnetic susceptibility of the samples, sample temperature, etc. As a result, a universal correction factor is likely to be required even when careful referencing methods are used in all experiments. Similarly, the accuracy of the resonance correlations would not be affected by solution NMR referencing errors, which often occur when the ^{1}H chemical shift is compared to the frequency of a water resonance instead of from an internal standard such as DSS (4,4-dimethyl-4-silapentane-1-sulfonic acid). Thus, we have found it necessary in practical applications to proteins to take into account both referencing errors and any systematic differences in chemical shifts by applying a correction factor to all δ_{iso} values.

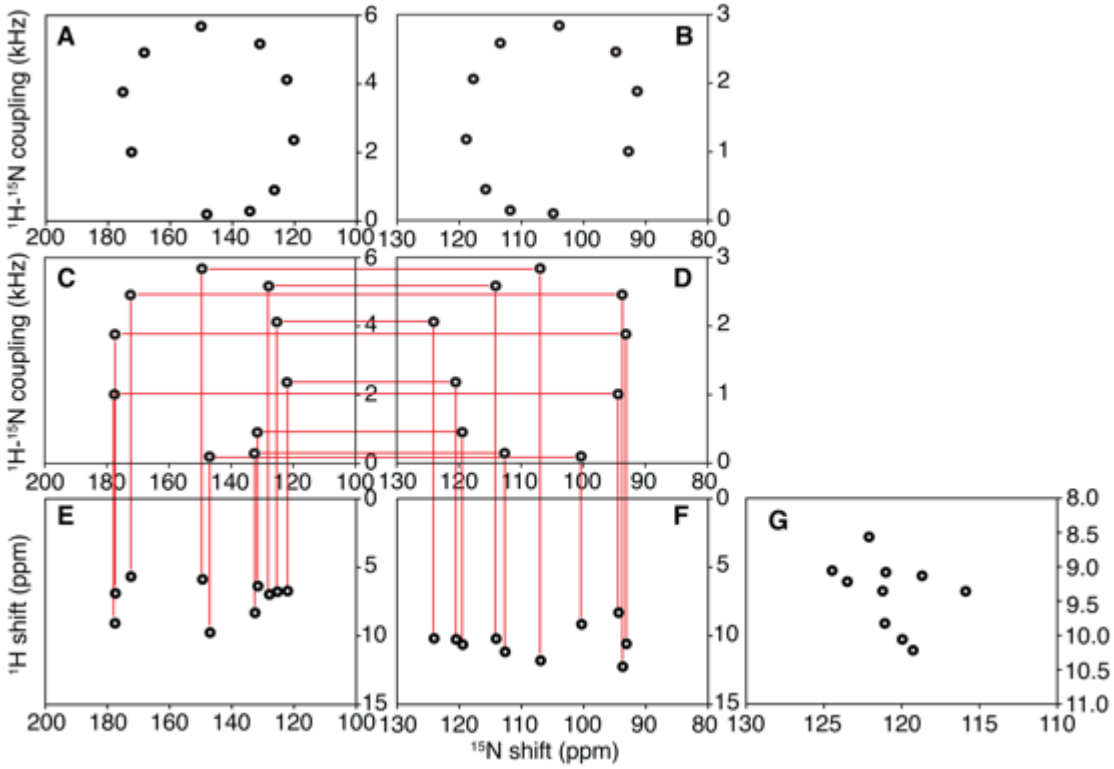

Figure 2.1. Spectral representations of numerical simulations that illustrate the method of dipolar coupling correlated isotropic chemical shift analysis. A., C., and E. are spectra from "flipped samples" with their bilayer normals parallel to the magnetic field. B., D., and F. are spectra from standard samples with their bilayer normals perpendicular to the magnetic field. A. and B. are SLF spectra simulated for an ideal 10-residue helix, where all amide sites have the same isotropic chemical shift. C. and D. are SLF spectra for the same helix with randomized chemical shift tensors as described in the text. The isotropic value of the heteronuclear dipolar coupling is zero. E. and F. are HETCOR spectra that can be correlated to the SLF spectra through the ^{15}N chemical shift frequencies. G. Is the spectral representation of the ^{15}N and ^{1}H isotropic chemical shift values calculated from the two HETCOR spectra.

This approach to assigning resonances in the OS solid-state NMR spectra of membrane proteins is illustrated schematically in Figure 2.1 using simulated two-dimensional ^{1}H/^{15}N SLF and HETCOR spectra from an ideal trans-membrane helix with a 40° tilt angle relative to the bilayer normal. By using only ten signals with their frequencies marked by "dots", the characteristic polarity index slant angle (PISA)

wheels (Marassi and Opella, 2000; Wang et al., 2000) can be readily recognized in the SLF spectra in Figure 2.1.A and 2.1.B. They appear as "ideal" helical wheels because they are simulated using the same isotropic chemical shift values (and the same consensus chemical shift tensors) for the ^{1}H and ^{15}N nuclei in all ten residues. A more realistic situation is simulated by the pair of spectra in Figure 2.1.C and 2.1.D where the isotropic chemical shifts vary significantly among the residues as well as from the "ideal" value calculated from the "consensus" chemical shift tensors. The site-to-site variations in the positions of resonances induced by differences in the chemical shift frequencies can significantly distort the PISA wheels observed in high field OS solid-state NMR spectra. Significantly, the heteronuclear dipolar couplings are invariant, and retain the feature that their frequencies differ by exactly a factor of two between these two spectra, which enables the correlation between pairs of resonances in the spectra of samples aligned with their bilayer normals parallel (Figure 2.1.C) and perpendicular (Figure 2.1.D) to the magnetic field. The scale for the dipolar coupling frequency is between 0 kHz and 6 kHz for the parallel spectrum shown in Figure 1A and 1C, which is exactly twice that of the 0 kHz to 3 kHz scale for the perpendicular spectrum in Figure 2.1.B and 2.1.D. As discussed above, even though the value of S_{rel} is reduced from 1.0 to experimentally determined values in the range of 0.8 to 0.9 in membrane protein samples, it is still feasible to establish correlations by drawing horizontal lines between pairs of resonances at the same position in Figure 2.1.C and 2.1.D, after applying the same scaling factor, S_{rel}, to the data obtained from samples in the parallel and perpendicular alignments. Additional chemical shift dimensions can

be added to the established dipolar correlation. For example, the amide ^{1}H frequencies observed in $^{1}H/^{15}N$ HETCOR spectra (Figure 2.1.E and 2.1.F) can be linked to the two SLF spectra through their associated ^{15}N chemical shifts. For simplicity, only two-dimensional HETCOR spectra (Nevzorov and Opella, 2007) are shown in Figure 2.1 to illustrate the method. However, HETCOR can be combined with SLF spectroscopy in a three-dimensional experiment (Nevzorov et al., 2007; Ramamoorthy et al., 1995), which was used in the second experimental example of a uniformly ^{15}N labeled protein. By utilizing the isotropic chemical shift frequencies of both ^{1}H and ^{15}N in an amide site, a two-dimensional $^{1}H/^{15}N$ chemical shift correlation spectrum can be generated, as shown in Figure 2.1.G, which has the same spectral frequencies as a heteronuclear correlation spectrum obtained on the same protein by solution NMR or MAS solid-state NMR. This is under the assumption that all of the amide sites have similar environmental and structural influences on their chemical shifts, which is frequently the case when similar lipids are used to prepare the samples. Bicelles are characterized by q, the molar ratio of the long chain (DMPC) to the short chain (DHPC) phospholipids. Low q (<1) DMPC:DHPC isotropic bicelles are used for solution NMR and high q (>2.5) magnetically-alignable DMPC:DHPC bilayers for OS solid-state NMR. A concern and potential limitation of the method is when isotropic chemical shift assignments obtained by solution NMR are used, since membrane proteins may adopt different conformations in different lipid environments. To recognize these differences and minimize the possibility of assignment errors, we routinely perform “q titration” solution NMR experiments as demonstrated in the

second experimental example of a uniformly ^{15}N labeled protein, where data from low q samples are used to extrapolate the chemical shifts to the high q samples used in OS solid-state NMR experiments. This problem is generally not present with assignments made by MAS solid-state NMR on proteoliposomes with only long-chain lipids.

2.4 Resonance Assignment of Selectively ^{15}N-Phe labeled MerE

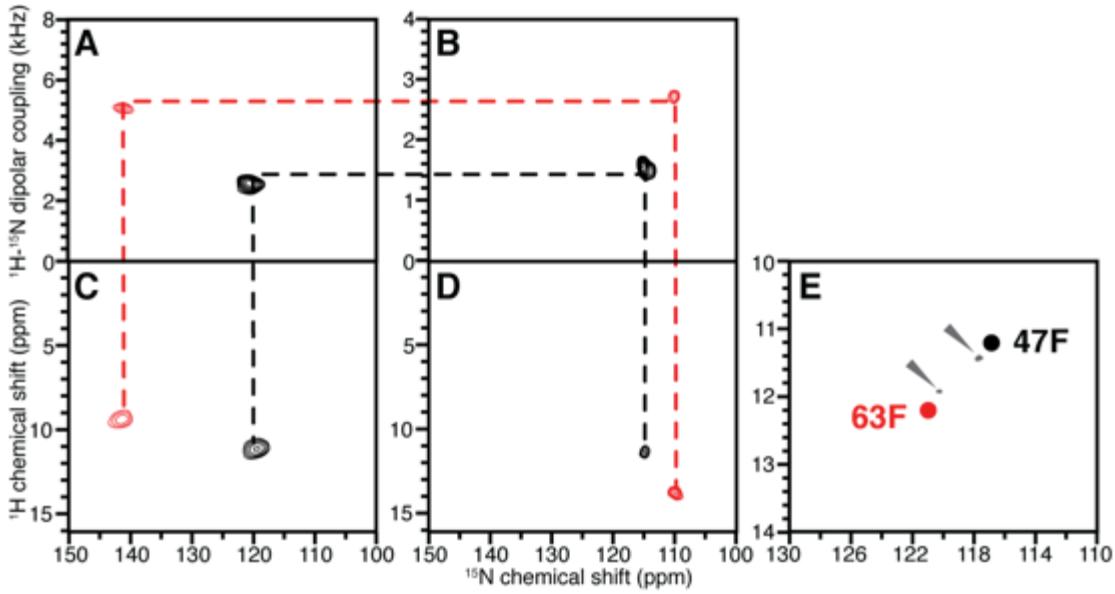

Figure 2.2. Example of resonance assignments using experimental data from ^{15}N-Phe-labeled MerE in magnetically aligned bilayers. A. and B. SLF spectra. C. and D. HETCOR spectra. A. and C. Sample with the bilayer normals parallel to the magnetic field. B. and D. Sample with the bilayer normals perpendicular to the magnetic field. The two resonances (red and black) observed in the experimental spectra are correlated by the dashed lines across the four spectra. E. The red and black dots represent the isotropic chemical shifts of the two residues calculated from the experimental solid-state NMR spectra in A. – D. The two gray "dots" represent the resonance frequencies observed in an experimental two-dimensional HSQC solution NMR spectrum.

MerE is a 78-residue mercury transport membrane protein with two trans-membrane helices. ^{15}N-Phe labeled MerE provides a simple example to demonstrate the assignment of resonances by combining heteronuclear dipolar coupling correlations with a previously assigned isotropic solution NMR spectrum. MerE has three phenylalanine residues: F 47, F 63 and F 74. Like most mobile residues located near the N- or C- termini of a membrane protein in phospholipid bilayers, the resonance from F 74 near the C-terminus is not observed in any of the one- or two-dimensional solid-state NMR spectra, presumably because the local backbone motions average out the dipolar interactions used for cross-polarization. Thus, ^{15}N-Phe labeled MerE provides two resonances; they are known to come from phenylalanine residues, but have not previously been assigned to specific residues. The experimental solid-state NMR spectra in Figure 2.2 were obtained from protein-containing bilayer samples aligned with their normals parallel (Figure 2.2.A and 2.2.C) and perpendicular (Figure 2.2.B and 2.2.D) to the magnetic field. Both the isotropic ^{1}H and ^{15}N chemical shift frequencies were determined from these experimental solid-state NMR spectra using the procedures described above, and were compared with the resonance frequencies and assignments observed in the solution NMR spectrum. The positions of the two gray "dots" in Figure 2.2.E represent the solution NMR chemical shifts, and the assignments to Phe 47 and Phe 63 made using standard solution NMR triple-resonance methods are noted. The red and black "dots" correspond to the chemical shifts derived from the heteronuclear dipolar correlated signals in Figure 2.2.A-D. This assigns the signals with the larger ^{1}H-^{15}N dipolar couplings to Phe 63 and those

with the smaller couplings to Phe 47. Based on the PISA wheel observed in the SLF spectrum of uniformly ^{15}N labeled MerE (data not shown), the resonance assigned to Phe 63 is in a tilted trans membrane helix, while that for Phe47 is outside the wheel region, as expected for a residue in an irregular inter-helical loop structure. Therefore, the experimental assignments are consistent with the topological prediction of the two residues based on hydrophathy plots and a large body of both solution NMR and solid-state NMR data (not shown).

2.5 Resonance Assignment of Uniformly ^{15}N-labeled Pf1 Coat Protein in Aligned Bicelle

The assignment method was demonstrated above with a membrane protein whose OS solid-state NMR spectra contain only two resonances for clarity. However, the method is intended for applications to uniformly ^{15}N labeled proteins with many resonances, where there is the greatest need for more powerful assignment methods. While some aspects of the procedure can be carried out using two-dimensional spectra, especially for smaller proteins, the goal is to develop a general method that is applicable to uniformly labeled samples of larger membrane proteins, which requires three-dimensional spectra. The application of this method to uniformly labeled proteins is demonstrated here with the well-characterized example of the membrane bound form of the 46-residue Pf1 coat protein. The spectra of Pf1 coat protein in magnetically aligned bilayers have been assigned using the previous generation of OS

solid-state NMR methods, which relied on the use of multiple selectively labeled samples and the shotgun method (Marassi and Opella, 2003; Opella et al., 2008).

The first step is to perform a "q titration" experiment in solution NMR (Figure 2.3) where "q" is systematically increased by adding long chain lipid to the sample. The q-titration experiment takes the protein from fast-tumbling micelles to slower-tumbling isotropic bicelles with a larger fraction of long chain lipids thought to make the environment more like a bilayer. The q-titration experiment serves two purposes. First, resonances from residues in the trans-membrane helices and other structured regions of the protein can be readily recognizes, since their signals have dramatically reduced intensities (due to broader line widths) in the samples with higher q values. This is because the protein has a slower overall correlation time when the q is increased, and it selectively affects the relaxation of resonances from regions with structures, whose effective correlation time slows along with that of the isotropic bicelles as the q is raised. Mobile residues are also affected by increasing the q, but to a much smaller extent, because the local backbone motions reduce the impact of the slower overall correlation times of the protein-containing bicelles. In the membrane-bound form of Pf1 coat protein, the signals from residues 23 through 43 are weak in q = 0.6 bicelles and completely disappear in q = 0.8 bicelles. This is typical behavior for residues in trans-membrane helices in monotopic and polytopic membrane proteins. The second purpose of performing a q-titration experiment is to monitor changes in chemical shifts as the lipid environment of the protein goes from that of a micelle (q = 0) to that of magnetically alignable bilayers (q > 2.5). This is critical because the

isotropic chemical shifts calculated from solid-state NMR spectra correspond to those of q = 3.2 DMPC:DHPC bilayers, whereas those observed in solution NMR spectra correspond to micelles (q = 0) or isotropic bicelles (q < 1). In order to minimize any errors in correlating the isotropic chemical shifts from these two similar but not identical samples, it is essential to optimize the lipid compositions and monitor the changes as a function of q. For Pf1 coat protein in 14-O-PC/6-O-PC bilayers, only small chemical shift changes were observed in the samples between q = 0.3 to q = 0.8, which allows us to utilize the chemical shift values measured in q = 0.3 bicelles for the assignment process.

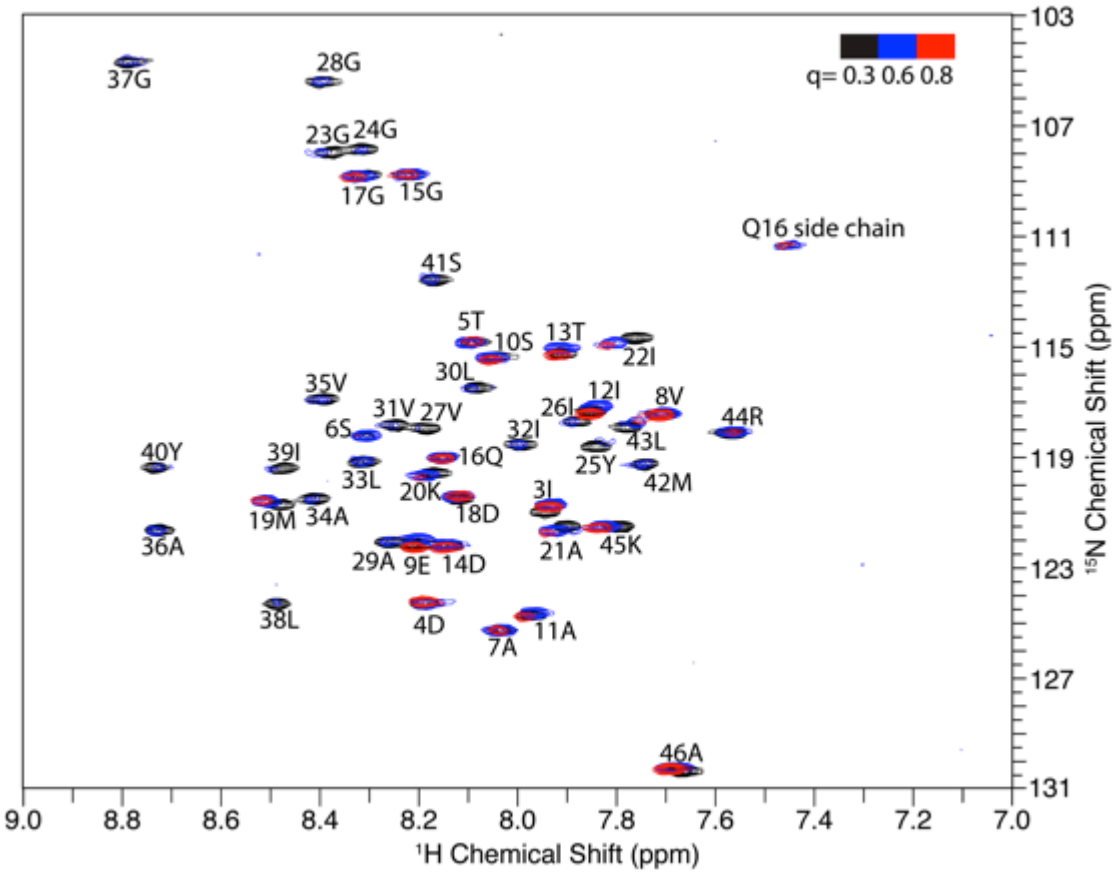

Figure 2.3. The bicelle q titration experiment of the membrane-bound form of Pf1 coat protein. The three superimposed HSQC solution NMR spectra (red, blue and black) were obtained from samples of Pf1 coat protein in isotropic bicelles with different q values, as colored coded in the upper right hand corner. The resonance assignments are marked for each resonance. The signal intensity of residues 23 to 43 drops below detection levels towards q=0.8 bicelles, and serve to define the residues in the trans-membrane helix.

Two-dimensional SLF spectra and three-dimensional HETCOR/SLF spectra acquired from samples aligned both perpendicular and parallel to the field are arranged for ease of comparisons in Figure 2.4. A strip plot representation of the three-dimensional spectra in Figure 2.4 is presented in Figure 2.5. In the initial trial, 20 signals were identified that had dipolar coupling frequencies > 2 kHz, which generally differentiates resonances associated with residues in trans-membrane helices (larger

couplings) from those in irregular non-helical regions (smaller couplings). There is one less resonance than expected, since the q-titration experiment showed that residues 23 – 43 are in a stable helical conformation. With further analysis, the signal labeled 21 (Figure 2.4.C) was selected from several additional candidates near the helical region of the spectrum and assigned to residue 25. The assignment procedure is described in details below.

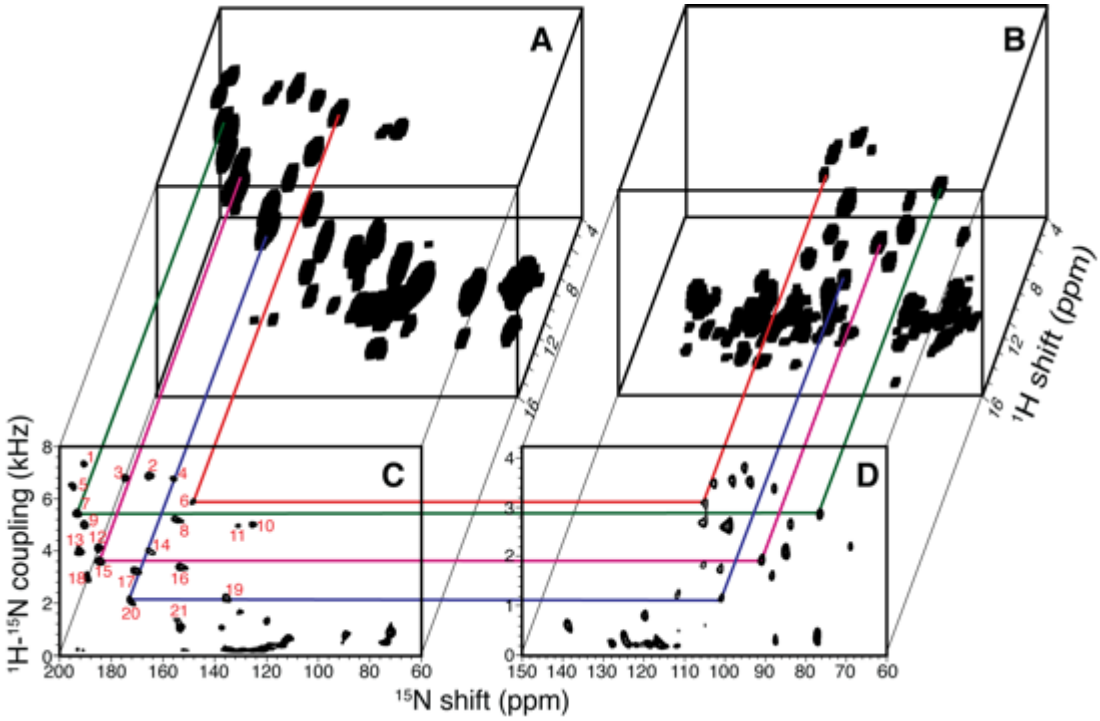

Figure 2.4. Solid-state NMR spectra of uniformly ^{15}N-labeled Pf1 coat protein in magnetically aligned bilayers. A. and C. The bilayer normals are parallel to the magnetic field. B. and D. The bilayer normals are perpendicular to the magnetic field. A. and B. Three-dimensional HETCOR/SLF spectra. C. and D. Two-dimensional SLF spectra. The 21 resonances in the helical wheel region are numbered in the order of the magnitude of their dipolar coupling frequencies (red number in panel C). Four representative correlations are shown in colored lines.

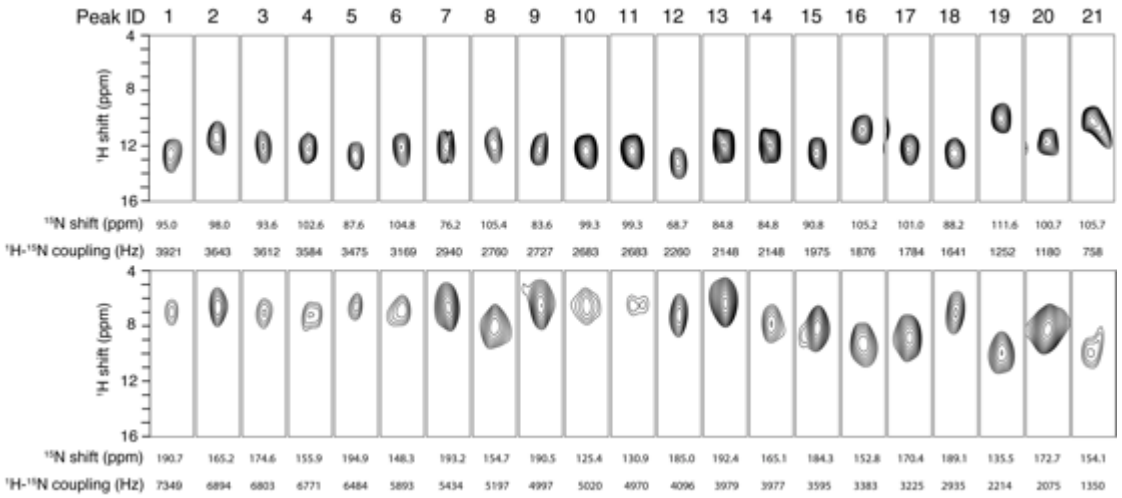

Figure 2.5. Strip plots extracted from the three-dimensional HETCOR/SLF spectra (Figure 2.4.A and 2.4.B) obtained for uniformly ^{15}N-labeled Pf1 coat protein in two differently aligned bicelles. Top: The bilayer normals are perpendicular to the magnetic field. Bottom: The bilayer normals are parallel to the magnetic field.

The assignment process starts with the correlation of the 20 resonances in each of the SLF spectra through their heteronuclear dipolar couplings (Figures 2.4.C and 2.4.D). All the signals in the trans-membrane helical region of the spectrum can be readily correlated, although peaks 9, 10 and 11 (Figure 2.4.C) are not resolved in the dipolar coupling dimension. The correlation of these three peaks was accomplished by noting that peak 9 is well separated from peaks 10 and 11 in the ^{15}N chemical shift frequency dimension. Due to the limited range of isotropic ^{15}N chemical shift frequencies, peak 9 can be correlated with some confidence to the peak at 84 ppm in the perpendicular sample (Figure 2.4.D). Consequently, peaks 10 and 11 can both be correlated to the peak at 102 ppm (Figure 2.4.D). The signal at 102 ppm has about twice the intensity of the others, suggesting that it represents two overlapped resonances. After the dipolar correlation, the isotropic chemical shifts can be derived from these data for comparison with the isotropic chemical shifts present in the

solution NMR heteronuclear chemical shift correlation spectrum (Figure 2.6 and Table 2.1).

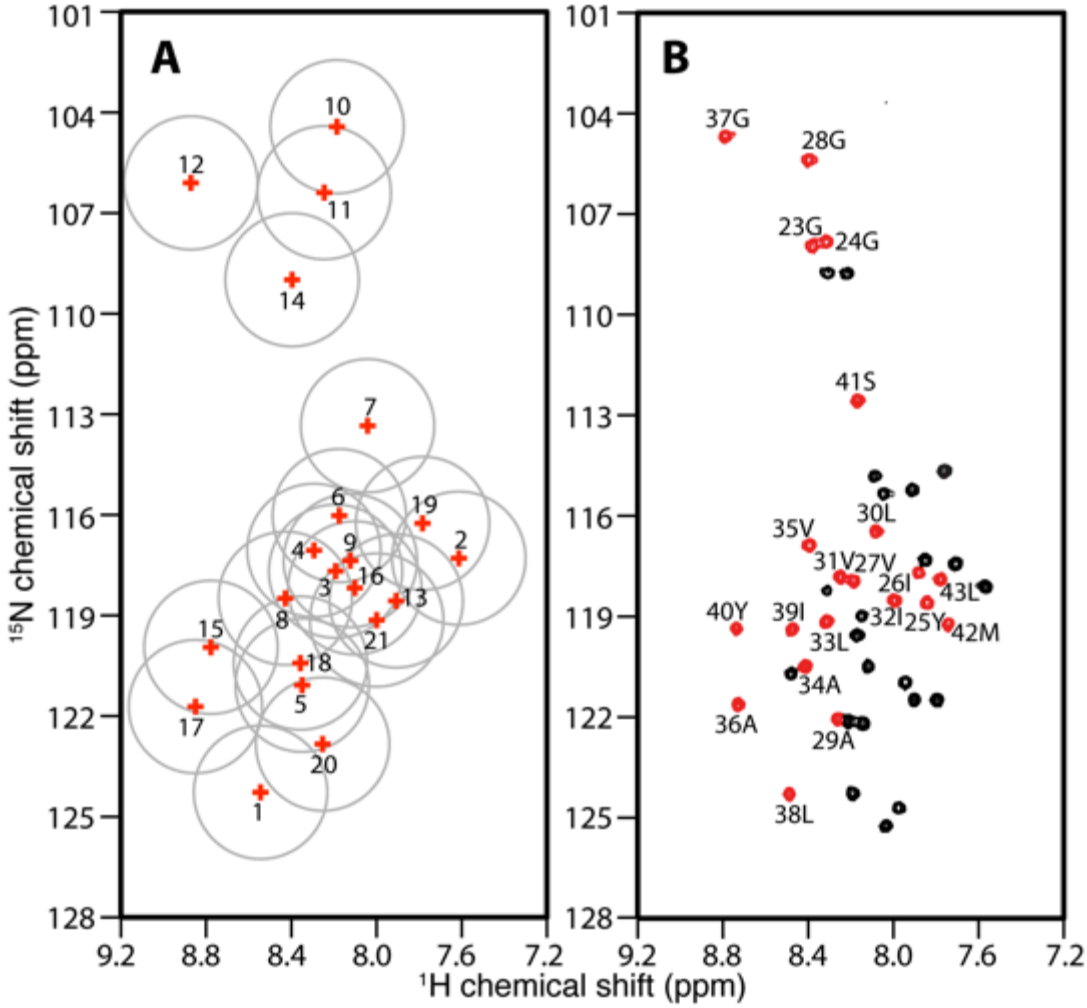

Figure 2.6. Spectral representations of the correlation of isotropic ^{15}N and ^{1}H chemical shifts. A. Solid-state NMR data obtained from samples of Pf1 coat protein in magnetically aligned bilayers. B. Solution NMR data obtained from samples of Pf1 coat protein in isotropic bicelles (q=0.3). A. The isotropic chemical shifts of all 21 peaks in the helical wheel region are calculated and labeled with their peak numbers based on the magnitudes of their heteronuclear dipolar couplings. The grey circles indicate the estimated uncertainty in their positions. B. An experimental two-dimensional HSQC spectrum. The peaks colored in red are from residues in the trans-membrane helical region of the protein. The resonances assignments are marked.

Table 2.1. Summary of data for the assignment and isotropic chemical shift calculations of uniformly ^{15}N-labeled Pf1 coat protein. The solution NMR data are aligned with the solid-state NMR data according to the final assignments described in the text.

Solid-state NMR										Solution NMR		
	Parallel Bicelle			Perpendicular Bicelle				Isotropic value			Isotropic value	
Peak ID	DC	^{15}N	^{1}H	DC	^{15}N	^{1}H	S_{rel}	^{15}N	^{1}H	Residue number	^{15}N	^{1}H
1	7349	190.65	6.99	3921	94.95	12.64	0.937	124.27	8.54	38	124.28	8.49
2	6894	165.23	6.65	3643	98.03	11.38	0.946	117.29	7.61	42	119.22	7.74
3	6803	174.58	7.07	3612	93.55	12.05	0.942	117.68	8.19	27	117.94	8.19
4	6771	155.86	7.20	3584	102.59	12.13	0.945	117.06	8.29	31	117.80	8.25
5	6484	194.92	6.60	3475	87.61	12.56	0.933	121.08	8.35	34	120.48	8.41
6	5893	148.33	7.06	3169	104.76	12.05	0.930	116.02	8.17	35	116.86	8.39
7	5434	193.23	6.70	2940	76.24	12.05	0.924	113.34	8.04	41	112.55	8.17
8	5197	154.66	8.01	2760	105.36	11.91	0.941	118.49	8.43	39	119.36	8.47
9	4997	190.52	6.52	2727	83.58	12.29	0.916	117.36	8.12	30	116.45	8.08
10	5020	125.43	6.52	2683	99.29	12.35	0.936	104.43	8.19	28	105.38	8.40
11	4970	130.87	6.73	2683	99.29	12.35	0.926	106.39	8.25	24	107.80	8.31
12	4096	185.04	7.23	2260	68.71	13.09	0.906	106.10	8.87	37	104.69	8.79
13	3979	192.39	6.36	2148	84.83	12.02	0.926	118.57	7.91	26	117.68	7.88
14	3977	165.05	7.86	2148	84.83	11.97	0.926	108.99	8.40	23	107.93	8.38
15	3595	184.29	8.14	1975	90.75	12.43	0.910	119.95	8.78	40	119.34	8.73
16	3383	152.76	9.30	1876	105.17	10.75	0.902	118.18	8.10	32	118.51	8.00
17	3225	170.34	8.85	1784	100.99	12.16	0.904	121.72	8.85	36	121.61	8.73
18	2935	189.10	7.07	1641	88.21	12.40	0.894	120.42	8.36	33	119.13	8.31
19	2214	135.50	9.98	1252	111.59	9.88	0.884	116.25	7.78	43	117.88	7.78
20	2075	172.71	8.30	1180	100.70	11.57	0.879	122.83	8.25	29	122.05	8.26
21	1350	154.06	9.95	758	105.73	10.23	0.891	119.14	8.00	25	118.57	7.84

Next, the isotropic chemical shifts calculated from the parallel and perpendicular solid-state NMR spectra are compared to those measured in the experimental solution NMR spectrum. This enables some signals that are well separated from others to be assigned by inspection. Seven signals labeled 10, 12, 7, 15, 17, 20 and 1 are assigned to residues 28, 37, 41, 40, 36, 29 and 38, respectively. These assignments are valuable in their own right, but they also serve as anchor points to determine the phase of the dipolar wave associated with the regular helical secondary structure (Mesleh et al., 2003; Mesleh and Opella, 2003; Mesleh et al., 2002). Meanwhile, the amplitude of the wave can be determined with some confidence from the largest and smallest values of the heteronuclear dipolar couplings that are observed in the helical region of the spectrum (Figure 2.7).

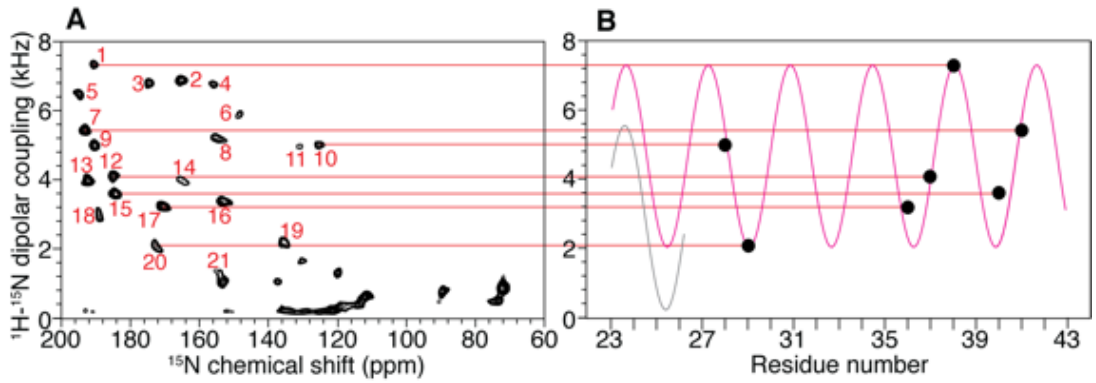

Figure 2.7. Dipolar wave analysis of the dipolar coupling frequencies measured for the residues in the transmembrane helix region of Pf1 coat protein. A. SLF spectrum of magnetically aligned bilayers with their normals parallel to the magnetic field. The peaks are labeled in the order of increasing magnitude of their dipolar coupling. B. The seven unambiguously assigned residues are used to fit a dipolar wave (magenta color) following the procedure described previously(Mesleh et al., 2003; Mesleh and Opella, 2003; Mesleh et al., 2002). The black dots represent the magnitudes of the dipolar couplings of the seven residues, and they are correlated through red lines to their respective peaks in the SLF spectrum. The separate dipolar wave in light grey is fitted to residues 23 to 25 to indicate a plausible distortion at the N-terminal end of the helix.

The rest of the resonance assignments follow readily from these two sources of information: the direct comparison of isotropic chemical shifts (Figure 2.6) and the dipolar wave analysis (Figure 2.7). By sequentially assigning the other fourteen resonances, any perturbation from the dipolar wave can be detected, which by itself provides strong evidence of any incorrect assignments. Based on the resonances assigned to residues 40 and 41, there are two possible candidates (resonances 2 and 13) for the signal from residue 42; however, only the dipolar coupling observed for signal 2 is consistent with the dipolar wave analysis. For residue 43, both peaks 19 and 13 are candidates. In the parallel SLF spectrum, the PISA wheel (Marassi and Opella, 2000; Wang et al., 2000) goes in the clockwise direction; in reading the dipolar wave from left to right (Figure 7B), the peaks on the rising part of the sine wave are located on the left side of the SLF spectrum (Figure 2.7.A) in the ^{15}N chemical shift region between 170 ppm and 200 ppm. Therefore, signal 13 can be ruled out, and signal 19 is assigned to residue 43. Three resonances, 5, 8 and 18, are candidates for residue 39 on the basis of their isotropic chemical shifts. However, 5 and 18 are on the "wrong side" of the PISA wheel, leaving resonance 8 as the only viable choice. For residue 35, the resonances labeled 3, 4, 6, 8 and 9 are all potential candidates. Resonances 3 and 9 can be ruled out by the PISA wheel analysis, and resonance 8 is already assigned; resonances 4 and 6 are too close to be distinguished by the dipolar wave analysis. This ambiguity is addressed later. For residue 34, the only possibilities are resonances 5 and 18. They are far apart in the dipolar wave analysis, and clearly residue 34 should be assigned to resonance 5. For residue 33, resonance 18 is the closest one in isotropic

chemical shift. In addition, in the vicinity of resonance 18, all the other signals are already assigned. Therefore, we assign resonance 18 to residue 33. Next, we searched for a resonance to assign to residue 32. There are several unassigned candidates, including resonances 3, 9, 13 and 16. Signal 21, which would be possible otherwise, is excluded for residue 33 as discussed later. Among the four plausible candidates, resonance 3 and 9 are ruled out by the dipolar wave analysis, and resonance 13 is on the wrong side of PISA wheel. Therefore, resonance 16 is assigned to residue 32. The resonances labeled 3, 4, 6 and 9 are candidates for assignment to residue 31. Except for resonance 9, the three other signals cannot be ruled out by dipolar wave analysis. The ambiguity remains until we proceed to residue 30. Resonance 9 is readily assigned to residue 30, since the only other candidate, resonance 6, is located on the "wrong side" of the PISA wheel. The ambiguity is now narrowed to resonances 4 and 6 for residues 31 and 35. By careful comparison of their positions in the dipolar wave, resonance 4 is more likely to be from residue 31 and resonance 6 from residue 35. This is also consistent with the isotropic chemical shift comparison, where residue 31 is clearly closer to resonance 4 than to 6. The validity of the dipolar wave fitting is further confirmed by recognizing that, in the middle of the helix, residues 26 to 39 nearly perfectly match the expected positions on the dipolar wave. The signals for residues 29 and 28 are already assigned, and residue 27 can be readily assigned to resonance 3 and residue 26 to resonance 13. However, this leaves no signal available for the next residue in the helix, residue 25. In attempting to proceed with this analysis through residues 23 and 24, we find that neither of the candidate resonances, 11 or 14,

fit to dipolar wave. This has structural implications, since it indicates that the dipolar wave describing the initial 7 anchoring residues is does not fit to this region of the protein. This is not entirely unexpected, since residues 23, 24, and 25 are near the end of the helix where structural distortions are most likely to be found.

Assigning residues 23, 24, and 25 requires a careful analysis of the dipolar wave fitting and a search for an additional signal in the vicinity of the helical region of the SLF spectra. This leads to the identification of resonance 21 (Figure 2.4.C), whose calculated isotropic chemical shift is close to that of residue 25. The assignment of resonance 21 to residue 25 is confirmed by an experimental SLF spectrum on a selectively ^{15}N-Tyr labeled sample (Figure 2.8). This assignment differs from our previously reported assignment for this residue (Opella et al., 2008; Park et al., 2010c). Note that resonance 21 could be assigned to other residues if only isotropic chemical shifts are considered. For example, residue 32 would be a good alternative candidate since it is the closest one in isotropic chemical shift. Indeed, residues 32 and 25 were previously noted to have overlapping resonances in earlier spectra (Opella et al., 2008). However, it is now established that in the vicinity of residue 32, the dipolar wave fitting has minimal errors, and therefore, assigning residue 32 to peak 21 would result in an erroneous distortion of the dipolar wave. In contrast, we already know that residues 23 and 24 (assigned to resonances 11 and 14, respectively) are significantly lower in frequency than predicted from the initial dipolar wave fitting; thus, there is a distinct possibility that the resonance from residue 25 is shifted down relative to the dipolar wave. A second dipolar wave can be generated for this region of the helix that

has approximately the same amplitude and phase, but is systematically shifted down on the frequency scale (Figure 2.7.B). This leads to the assignment of residue 23 to resonance 14, and of residue 24 to resonance 11. These two assignments cannot be confirmed by isotropic chemical shift analysis due to the close proximity of their resonances in the two-dimensional solution NMR spectrum. Neither can the assignments be confirmed by preparing selectively labeled samples since both are glycines. Therefore, the assignment of residue 23 and 24 presented here is based on the most likely result from the dipolar wave analysis, and it agrees with our previous assignment (Opella et al., 2008).

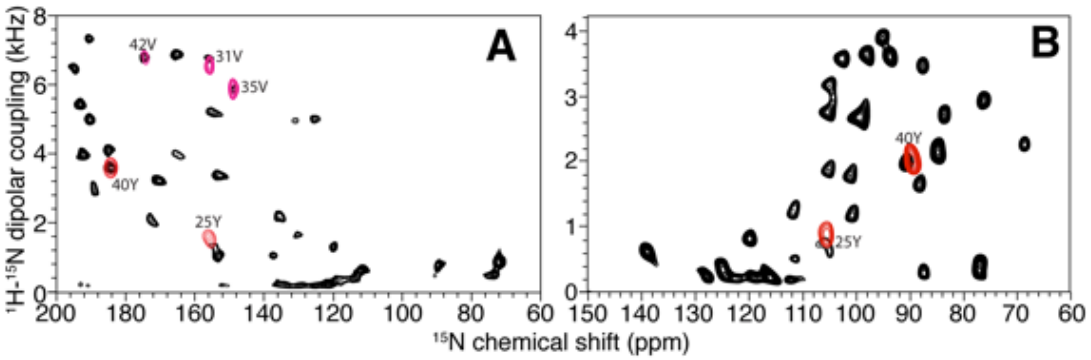

Figure 2.8. The resonance assignment of Tyr 25 confirmed using spectra from a ^{15}N-Tyr labeled sample of Pf1 coat protein. A. and B. SLF spectra. A. Bilayers with their normals parallel to the magnetic field. B. Bilayers with their normals perpendicular to the magnetic field. The SLF spectra of selectively ^{15}N-Tyr labeled Pf1 (red signals) are superimposed on the corresponding spectra of uniformly ^{15}N-labeled Pf1 (black signals). The assignments of the two Tyr resonances are marked.

2.6 Discussion

Using only a single uniformly ^{15}N labeled sample and a previously assigned isotropic spectrum, the vast majority of resonances in the OS solid-state NMR spectrum of the membrane-bound form of Pf1 coat protein could be assigned to

specific residues. While isotropic chemical shift assignments can be obtained readily in solution NMR and MAS solid-state NMR using only uniformly ^{13}C and ^{15}N labeled samples, in the method demonstrated here, they are calculated indirectly for OS solid-state NMR spectra based largely on matching the magnitudes of heteronuclear dipolar couplings in parallel and perpendicular aligned samples. The few examples of uncertainties and ambiguities that altered one earlier resonance assignment and may affect a few more are not surprising in the first applications of new methods. Most importantly, the experimental data from two different membrane proteins enabled us to demonstrate the practical application of a general assignment scheme that has the potential to enable the study of larger membrane proteins and to accelerate the entire process of structure determination in membrane bilayers.

There are many opportunities for the further development of this assignment method and extension to larger membrane proteins. First, as multidimensional $^{1}H/^{13}C/^{15}N$ triple-resonance OS solid-state NMR experiments are improved (Filipp et al., 2009; Sinha et al., 2007a; Sinha et al., 2007b), the method can be extended to include many additional chemical shifts and dipolar couplings, such as $^{13}C_{\alpha}$ and $^{13}C_{\beta}$ chemical shifts and ^{15}N-$^{13}C_{\alpha}$ and ^{1}H-^{13}C dipolar couplings. The incorporation of additional chemical shift frequencies will increase the accuracy of the correlations among the various NMR spectra (solution NMR, OS solid-state NMR, and MAS solid-state NMR), and the additional heteronuclear dipolar coupling dimensions will enable confident correlation of peaks in more crowded regions of the spectra from larger proteins. Secondly, for larger membrane proteins, such as G-protein coupled

receptors with seven trans-membrane helices, the line widths of signals prohibit their resolution and assignment in isotropic bicelle samples by existing solution NMR methods. Thus, an attractive alternative is to utilize MAS solid-state NMR methods, which have the potential to provide full or partial assignments of the isotropic spectra, and enable the structure determination to proceed on the basis of the angular constraints measured for the assigned resonances is the OS solid-state NMR spectra.

The demonstration of this assignment method that combines isotropic and anisotropic frequencies of resonances is not only a useful advance for protein structure determination by OS solid-state NMR, but also provides an example of one of the many potential ways to integrate all types of NMR data on membrane proteins, including solution NMR of micelles and isotropic bicelles, OS solid-state NMR of aligned bilayers, and MAS solid-state NMR of unoriented bilayers. Another example is the determination of angular constraints in the conventional applications of MAS solid-state NMR. The constraints are usually determined by analyzing powder patterns from unoriented samples (Wu et al., 2010), which become complicated when more than one resonance contribute to the signal, and therefore in dealing with uniformly labeled large proteins, the resolution often needs to be provided by other dimensions, leading to a significant increase in experimental time. In contrast, in OS solid-state NMR, each resonance's signal appears as a single peak, and both chemical shift and dipolar coupling dimensions provide simultaneously angular constraints and resolution. In this case, the method described in the article can bring the angular

constraints from OS solid-state NMR to complement the other structural information obtained in MAS solid-state NMR.

2.7 Material and Methods

Uniformly ^{15}N-labeled Pf1 coat protein samples were prepared as previously described (Thiriot et al., 2004). Purified bacteriophage particles were dissolved in a mixed organic solution (50% trifluoroethanol, 0.1% trifluoroacetic acid and 49.9% water). The resulting DNA precipitate was pelleted by centrifugation. The solvent was partially removed by flowing nitrogen gas over the clear supernatant, and then the sample was lyophilized. In order to completely remove any residual trifluoroacetic acid, water was repeatedly added to the protein powder and the sample lyophilized again. NMR samples were reconstituted from the protein powder.

We have previously described the preparation of magnetically aligned protein-containing bilayers for OS solid-state NMR spectroscopy (De Angelis et al., 2005; De Angelis et al., 2004; De Angelis and Opella, 2007). The phospholipids, 1,2-di-O-hexyl-*sn*-glycero-3-phosphocholine (6-O-PC) and 1,2-di-O-tetradecyl-*sn*-glycero-3-phosphocholine (14-O-PC), which are the non-hydrolyzable ether-linked analogues of 1,2-Dihexanoyl-*sn*-Glycero-3-Phosphocholine (DHPC) and 1,2-Dimyristoyl-*sn*-Glycero-3-Phosphocholin (DMPC), were used to enhance long-term stability. The lipids were obtained from Avanti Polar Lipids (www.avantilipids.com). Samples of Pf1 coat protein in q = 3.2 perpendicular bilayers were prepared by solubilizing the protein in an aqueous solution containing 100 μl water and 80 ul stock of 100 mg/ml

short-chain lipid (6-O-PC). After adjusting the pH to approximately 6.7, the solution was then added to 40 mg long-chain lipid (14-O-PC) in powder form, followed by extensive vortexing and temperature cycling (0°C/45°C). The opaque initial mixture becomes transparent upon mixing, indicating the formation of an orientable bilayer phase. The pH is then adjusted to exactly 6.7 when the sample is fluid at 0°C. 160 µl of the protein-containing bilayer solution is then transferred into a 5 mm flat-bottomed tube (New Era Enterprises (www.newera- spectro.com)), which was then sealed with a rubber cap and wrapped in a layer of plastic film. After the acquisition of spectra on the perpendicular sample, the same sample was "flipped" into a parallel alignment in order to minimize any batch-to-batch differences in sample preparation. To "flip" the bilayers, the sample tube was cooled on ice and the fluid solution was transferred to a microcentrifuge tube. 5 µl of 100 mM $YbCl_3 \bullet 6H_2O$ in water was added to the sample, followed by several temperature cycles and pH adjustment to 6.7. The sample was then returned to the 5 mm tube used for the NMR experiments.

The sample of Pf1 coat protein used for the solution NMR experiments was prepared by solubilizing 0.5 mg of the protein in 50 mM 6-O-PC, 10mM MES at pH 6.7. The bicelle q titration experiments were performed on the same sample by successively adding 14-O-PC to the sample tube to achieve the desired molar ratios of long-chain and short-chain lipids.

The MerE expression, purification and sample preparation is similar to the procedure of MerFt protein described previously (De Angelis et al., 2006b). The 78-residue MerE(Kiyono et al., 2009) gene was synthesized and cloned into pET-31b(+)

vector (Novagen, USA), which was incorporated into *E.coli* strain C41(λDE3) (Avidis, www.avidis.fr) through transformation. In case of preparation of the ^{15}N-Phe-labeled sample, ^{15}N-Phe and the other 19 unlabeled amino acids were added to 1 liter of M9 medium. Expression of the fusion protein was induced by adding 1 mM IPTG to the culture when the OD_{600} reached 0.6, and the culture was then incubated for another 8 hours at 37°C. The collected cells were disrupted using a probe sonicator, and the inclusion body was isolated by centrifugation. The MerE fusion protein was solubilized in 6M guanidine hydrochloride (GuHCl) and purified using Ni-NTA affinity chromatography. The fusion protein was then cleaved by cyanogen bromide (CNBr) at the Met sites and purified by size exclusion chromatography in the presence of SDS. The final protein powder was obtained after exhaustive dialysis and lyophilization.

The solution NMR experiments were performed on a Varian VNMR 500 MHz spectrometer equipped with a standard HCN triple-resonance probe. All experiments were performed at 60°C. The HSQC spectra were acquired using the pulse sequence gNhsqc(Kay et al., 1992) from BioPack (Varian Inc.) with 1024 complex t1 points and 128 complex t2 points. Data were processed using NMRPipe (Delaglio et al., 1995), and the spectra were referenced to the water peak whose chemical shift value at the given temperature was determined by NMRPipe. The assignments of the Pf1 coat protein resonances were adapted from those previously obtained for the protein in DHPC micelles (Opella et al., 2008), and the assignment of MerE was accomplished

through standard triple-resonance experiments on uniformly ^{13}C and ^{15}N labeled protein in DHPC micelles (unpublished data).

The solid-state NMR experiments were performed on a 700 MHz spectrometer with Bruker Avance console equipped with a home-built strip-shield double-resonance probe (Wu et al., 2009) and a set of "thin" room temperature shim coils with a limited number of gradients. Magnet drift was compensated by a linear ramp of current to the Z_0 coil. Field drift was less than 0.1 ppm per day during the experiments. All of the solid-state NMR experiments were performed at 42°C. All two-dimensional SLF spectra were obtained using the SAMPI4 pulse sequence (Nevzorov and Opella, 2003a, 2007) with 1 ms CP-MOIST (Levitt et al., 1986) for ^{1}H-^{15}N cross-polarization and SPINAL-16 (Fung et al., 2000; Sinha et al., 2005) for heteronuclear decoupling during data acquisition.

For the MerE protein, the two-dimensional HETCOR experiments (Nevzorov and Opella, 2007) utilized 4 SAMPI4 periods to perform semi-selective coherence transfer in samples aligned perpendicular to the field and 2 periods for samples aligned parallel to the field. For both SLF and HETCOR experiment, the B_1 field strength was between 47 kHz and 50 kHz on the ^{15}N and ^{1}H channels under matched conditions, and between 75 kHz and 79 kHz on the ^{1}H channel during ^{1}H chemical shift evolution. Typically, 40 real t1 points were signal averaged for 400 – 1000 scans for the SLF spectra; and 64 – 128 complex points were signal averaged for 100 - 200 scans for the HETCOR spectra.

For Pf1 coat protein, in both two-dimensional SLF experiments and three-dimensional HETCOR/SLF experiments (Nevzorov et al., 2007), the B_1 field strength was 50 kHz on the ^{15}N and ^{1}H channels under matched conditions, and between 70 kHz and 72 kHz on the ^{1}H channel during ^{1}H chemical shift evolution. 32 complex t1 points, 40 real t2 points and 512 complex t3 points were acquired for the three-dimensional HETCOR/SLF spectra. 80 real t1 points and 512 complex t2 points were acquired for the two-dimensional SLF spectra. 128 transients were signal averaged for the two-dimensional experiments and 16 – 32 scans were signal averaged for the three-dimensional experiments. The recycle delays were typically 6 sec for the three-dimensional experiments and 4 sec for the two-dimensional experiments. The ^{15}N and ^{1}H chemical shifts were referenced externally to ^{15}N-labeled solid ammonium sulfate defined as 26.8 ppm and internally to H_2O defined as 4.7 ppm at 42°C. The NMR data were processed and displayed using the programs NMRPipe (Delaglio et al., 1995), NMRView (Johnson and Blevins, 1994) and Sparky (Goddard and Kneller, 2008). The theoretical scaling factor for both the HETCOR (Nevzorov et al., 2007; Ramamoorthy et al., 1995) and SAMPI4 (Nevzorov and Opella, 2007) experiments were utilized in the data processing and plotting.

The PISA wheels shown in Figure 1 were simulated using in-house MATLAB (The MathWorks) script following a previously described procedure (Nevzorov and Opella, 2003b). The torsion angles of α-helix were $\Phi = -64°$ and $\Psi = -43°$. The order parameter used in the calculations was 0.8, which is typical for magnetically aligned protein-containing bilayers. The principal values of the consensus chemical shift

tensors for the ^{15}N amide sites were $\sigma_{11} = 64$, $\sigma_{22} = 77$ and $\sigma_{33} = 217$ ppm, and were $\sigma_{11} = 3$, $\sigma_{22} = 8$ and $\sigma_{33} = 17$ ppm for the corresponding ^{1}H amide sites.. To simulate the SLF and HETCOR spectra for proteins, the chemical shift tensors were varied randomly from site to site. For each residue along the helix, all six of the principal values listed above were varied using a normal distribution around the value with standard deviation of 6 ppm for the ^{15}N amide chemical shift and 0.6 ppm for the ^{1}H chemical shift. The newly generated values were then used as input for the same MATLAB script used to simulate the SLF and HETCOR spectra. The isotropic chemical shift frequencies were calculated using Equation 2.1 with $S_{rel} = 1$.

The data shown in Table 2.1 were calculated as follows: S_{rel} was defined as the ratio of the heteronuclear dipolar coupling between parallel and perpendicular alignments, divided by two. It was calculated separately for each pair of correlated peaks, and the average value was found to be 0.92 using Equation 2.3. Each S_{rel} value was used for the isotropic chemical shift calculation of the corresponding residue; alternatively, the averaged S_{rel} of 0.92 were also used, giving a similar result (data not shown). Differences between the results were well below the experimental errors. For the Pf1 coat protein, the isotropic chemical shifts of all the residues were averaged, and we found that the values from solid-state NMR experiments were 3.97 ppm larger for ^{15}N and 2.13 ppm larger for ^{1}H than those observed in the solution NMR spectra. These two values were applied as the universal correction factor to all the resonances, and the resulting predicted isotropic chemical shifts are listed in Table 2.1. Similar discrepancies may occur for other sets of experiments and protein samples, and a

systematic frequency correction is required to assure the accuracy of isotropic chemical shift correlations and measurements. The correlation between OS solid-state NMR and solution NMR is shown Figure 6, and the estimated values for the maximal discrepancy between the chemical shifts calculated from solid-state NMR and observed in solution NMR are 1.5 ppm for ^{15}N and 0.3 ppm for ^{1}H. More rigorous estimates of the errors will be possible in the future as more datasets become available. For the ^{15}N-Phe selectively labeled MerE sample, a similar calculation procedure was utilized. Universal correction factors of 1.4 ppm in ^{15}N and 3.3 ppm in ^{1}H were applied to the solution NMR data.

Chapter 2, in full, is a reprint of the material "A general assignment method for oriented sample (OS) solid-state NMR of proteins based on the correlation of resonances through heteronuclear dipolar couplings in samples aligned parallel and perpendicular to the magnetic field" as it appears in J. Magn. Reson. 209(2):195-206 by Lu GJ, Son WS, Opella SJ. The thesis author was the primary author of the paper.

Chapter 3. Pulse Sequence to Improve ^{1}H Amide Resonance Line Narrowing

3.1 Abstract

We demonstrate ^{1}H amide resonance line widths <300 Hz in ^{1}H/^{15}N heteronuclear correlation spectra of membrane proteins in aligned phospholipid bilayers. This is a substantial improvement over typically observed line widths of ~1 kHz. Furthermore, in a proton detected local field version of the experiment that measures heteronuclear dipolar couplings, line widths <130 Hz are observed. This dramatic line narrowing of ^{1}H amide resonances enables many more individual signals to be resolved and assigned from uniformly ^{15}N labeled membrane proteins in phospholipid bilayers under physiological conditions of temperature and pH. Finding that the decrease in line widths occurs only for membrane proteins that undergo fast rotational diffusion around the bilayer normal, but not immobile molecules, such as peptide single crystals, identifies a potential new direction for pulse sequence development that incorporates molecular dynamics into the design.

3.2 Introduction

It is essential to study membrane proteins in phospholipid bilayers under physiological conditions of temperature and pH, since their correct folding and function are closely linked to the chemical and physical properties of their environment. Convenient mimics, such as detergent micelles and isotropic bicelles are frequently used for solution NMR experiments; however, the high concentrations of

detergents in the samples have the potential to perturb the structures of these delicate and malleable proteins. Magnetically alignable bicelles with higher q values (molar ratio of long chain to short chain lipids) (Sanders et al., 1994b) may resemble the native environment more closely, but generally give very broad ^{1}H amide line widths for the embedded proteins that compromise the resolution and sensitivity of the spectra. Moreover, since crystal packing effects, sequence mutations and modification, and low temperatures associated with X-ray diffraction also have the potential to distort membrane protein structures, the only method currently capable of accurately determining the structures of unmodified membrane proteins in phospholipid bilayers under physiological conditions is solid-state NMR. Further development is necessary to improve the quality of the data, and the accuracy, precision, and speed of structure determination. This is the case for stationary, aligned samples in oriented sample (OS) solid-state NMR (Cross and Opella, 1983), magic angle spinning (MAS) solid-state NMR (Opella et al., 1979), and the recently developed rotational alignment (RA) NMR, which merges the two methods (Marassi et al., 2011; Park et al., 2010a).

In practice, NMR spectral resolution is determined by the ratio of the line widths of individual resonances to the total frequency span covered by the relevant signals in the spectrum. For example, in solution NMR of helical membrane proteins, the ^{1}H amide resonances are generally poorly resolved because their line widths are broadened by the relatively slow global reorientation of the protein and detergent/lipid assemblies (Son et al., 2012), and the frequency dispersion is limited since each residue in an α-helix has a similar chemical and structural environment. In contrast,

the frequency span of signals in solid-state NMR spectra of stationary aligned samples of the same proteins are often quite large, since the frequencies are dispersed by the angular-dependence of the anisotropic nuclear spin interactions, which include chemical shift anisotropy (CSA) and heteronuclear dipolar coupling (DC), in multi-dimensional solid-state NMR experiments.

It is challenging to obtain narrow ^{1}H amide line widths in solid-state NMR due to the dense network of homonuclear dipolar couplings resulting from the high abundance and high gyromagnetic ratio of hydrogens in organic molecules (Waugh et al., 1968), including polypeptides. Even with ultrafast MAS, ^{1}H resonance line widths of 150 Hz have only recently been achieved (Salager et al., 2010). Thus, the design and implementation of methods that can line narrow ^{1}H amide resonances from ^{15}N labeled membrane proteins in phospholipid bilayers, which preserve anisotropic information and large frequency spans, is an important goal for OS solid-state NMR.

In this article, we demonstrate that a pulse sequence, which provides no additional narrowing in a stationary peptide crystal, is highly effective at narrowing ^{1}H amide line widths of membrane proteins in aligned phospholipid bilayers. It improves the resolution in the ^{1}H chemical shift dimension of heteronuclear correlation (HETCOR) spectra, as well as in the ^{1}H-^{15}N dipolar coupling dimension of proton-detected local field (PDLF) (Schmidt-Rohr et al., 1994a) class experiments. Notably, the line widths observed for small membrane proteins, such as the membrane-bound form of the 46-residue Pf1 coat protein (Park et al., 2010b; Zeri et al., 2003b), are the same as those observed for larger proteins, such as the 81-residue mercury transporter

MerFm (De Angelis et al., 2006a) and the 350-residue G-protein coupled receptors CXCR1 (Park et al., 2011a), and examples of spectra from all three of these proteins are shown.

3.3 Narrowing of the ^{1}H Amide Resonances

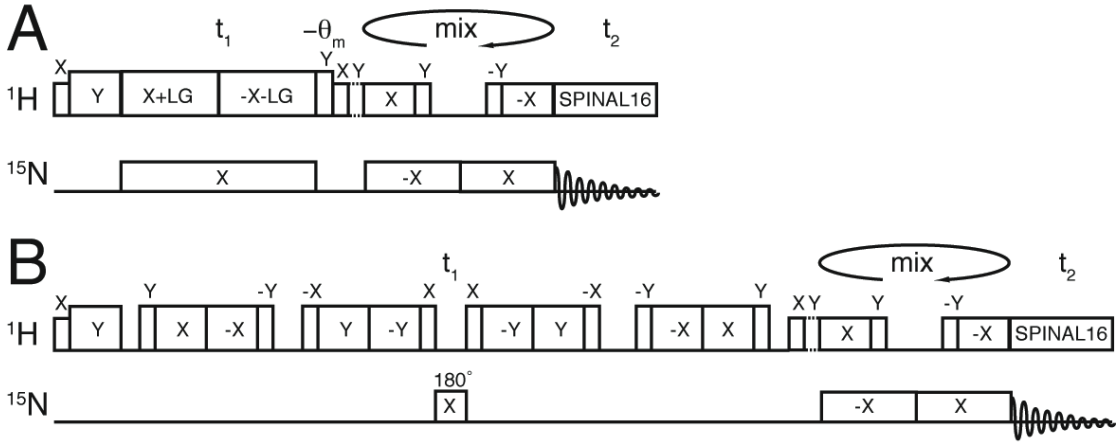

Figure 3.1. Timing diagrams for the pulse sequences. A. The conventional ^{1}H/^{15}N heteronuclear correlation HETCOR (Ramamoorthy et al., 1995) pulse sequence B. The high resolution variant of ^{1}H/^{15}N HETCOR for membrane proteins. It uses a modified magic sandwich pulse sequence (MSHOT-PI4) and a single refocusing π pulse during the ^{1}H chemical shift evolution period. Selective magnetization transfer occurs during the "mixing" period using SAMPI4 (Nevzorov and Opella, 2007).

The timing diagrams for two different two-dimensional ^{1}H/^{15}N HETCOR pulse sequences are compared in Figure 3.1, where the focus of attention is on the indirect ^{1}H chemical shift dimension. In a conventional HETCOR pulse sequence (Figure 3.1.A), frequency-switched Lee-Goldberg (FSLG) (Bielecki et al., 1989; Lee and Goldburg, 1965) irradiation is applied at the ^{1}H resonance frequency to achieve ^{1}H/^{1}H homonuclear decoupling, while continuous wave irradiation is applied at the ^{15}N (and/or ^{13}C frequencies) for heteronuclear decoupling. Results from a single crystal

sample of N-acetyl leucine (NAL) (Figure 3.2.C) and the membrane-bound form of Pf1 coat protein in phospholipid bilayers (Figure 3.2.A) demonstrate that the conventional pulse sequence gives ^{1}H amide line widths of ~700 Hz, even after extensive experimental optimization. To our knowledge, the narrowest previously reported ^{1}H line widths in solid-state NMR HETCOR spectra are ~ 1 kHz (Fu et al., 2009; Nevzorov et al., 2007). Thus, a new generation of probes, high power irradiation, and careful optimization of conditions yields a modest improvement in ^{1}H line widths. Notably, the line widths are slightly narrower in the protein sample than in the NAL crystal sample, which can be attributed to the slightly reduced order parameter observed in magnetically aligned bicelles.

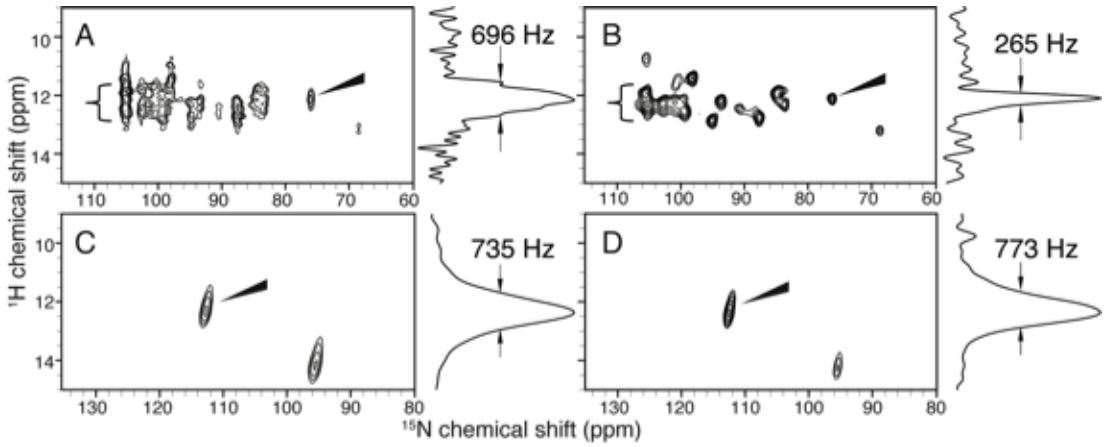

Figure 3.2. Comparison of the ^{1}H/^{15}N HETCOR pulse sequences performance on the membrane-bound form of Pf1 coat protein in magnetically aligned bicelles (top panels) and a NAL single crystal (bottom panels). A. and C. The experimental spectra were obtained from the conventional (Figure 1A) HETCOR pulse sequence. B. and D. The experimental spectra were obtained using the new version (Figure 1B) of the HETCOR pulse sequence. A one-dimensional spectral slice from the t1 dimension is shown on the right side of each two-dimensional spectrum, and the signal selected for each slice is labeled with an arrow on the respective two-dimensional spectra. The half brace labels the resonance peaks of I39 and V35 .No apodization functions were applied in processing the t1 dimension in any of the spectra, and Figure 3 shows the time domain evolution of signals that contribute to spectra A and B. The resonance assignments for all peaks in spectrum B are shown in Figure 3.6.

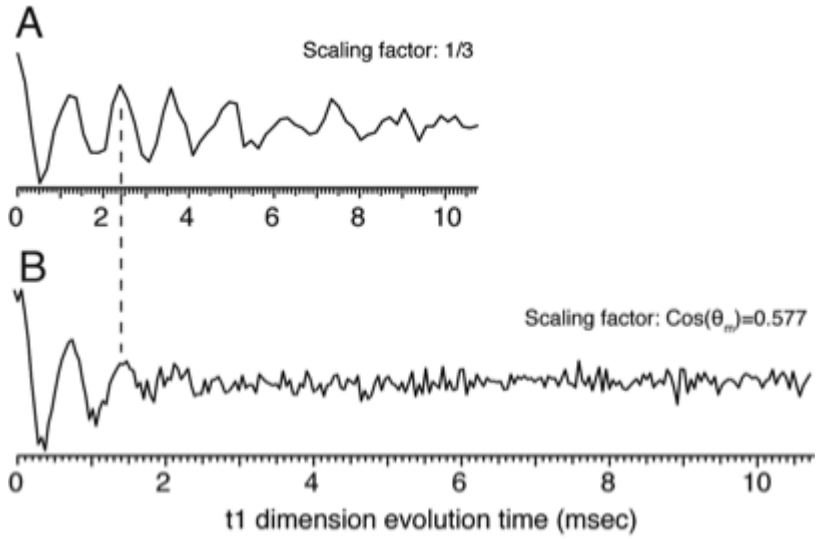

Figure 3.3. t1 time domain evolution of the Pf1 coat protein spectra in Figure 3.2 using the new (A) and conventional (B) HETCOR pulse sequence. The total t1 evolution time is approximately the same for the two spectra, however, due to their different scaling factors, the two oscillations are scaled accordingly in order to match the same frequency (shown by the dashed line).

Significantly narrower line widths (< 300 Hz) are observed in the ^{1}H chemical shift dimension (Figures 3.2.B and 3.3) when the pulse sequence diagrammed in Figure 3.1.B is applied to the same sample of a membrane protein in phospholipid bilayers. The time domain oscillation for the selected signal is shown in Figure 3.3. Notably, the effect of line narrowing can be observed throughout the spectrum; for example, the resonances of I39 and V35 overlap in Figure 2A, but are resolved in Figure 3.2.B. In contrast, the pulse sequence in Figure 3.1.B provides no additional narrowing of the signals from the stationary NAL crystal (Figure 3.2.D).

3.4 Description of Individual Components of MSHOT-PI4 / Pi

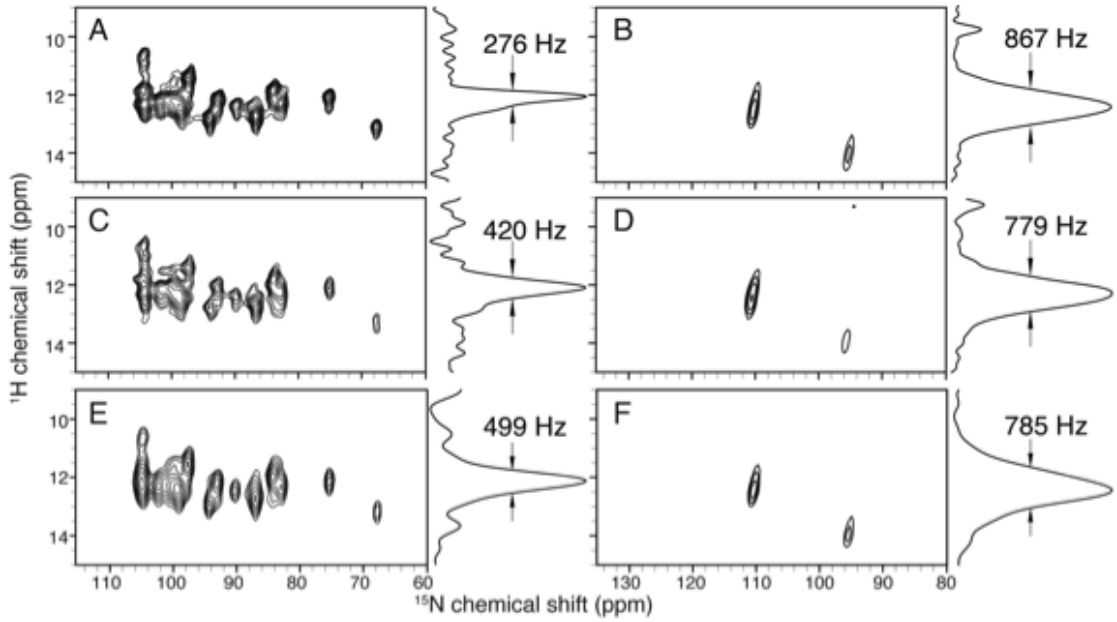

Figure 3.4. Separate evaluation of homonuclear and heternuclear decoupling schemes. Spectra from membrane-bound Pf1 coat protein (A, C and E) and NAL crystal (B, D and F). A and B. MSHOT with refocusing π pulse, which is the same pulse sequence as in Figure 1B. C and D. MSHOT with continuous wave decoupling in entire t1 dimension. E and F. FSLG with a single refocusing π pulse.

Since both the homonuclear and heteronuclear decoupling schemes are changed in the new pulse sequence, we investigated their effects separately. In a set of back-to-back experiments, we compared pulse sequences incorporating MSHOT-PI4 with a refocusing π pulse (first row in Figure 3.4), MSHOT-PI4 with CW irradiation (second row in Figure 3.4), and FSLG with a refocusing π pulse (third row in Figure 3.4). The spectra in Figure 3.4.A and 3.4.B reproduce the line widths observed in Figure 3.2, although the experiments were performed with a slightly different B_1 field and crystal orientation. While the line widths are similar in the NAL crystal spectra, the line widths for the membrane-bound form of the Pf1 coat protein shows that the replacement of FSLG by MSHOT provides ~200 Hz of line narrowing, and the replacement of CW irradiation by a single refocusing π pulse provides ~150 Hz of line

narrowing. Therefore, the changes in both the homonuclear and heteronuclear decoupling schemes contribute to the line narrowing provided by the pulse sequence on membrane protein undergoing rotational diffusion in phospholipid bilayers.

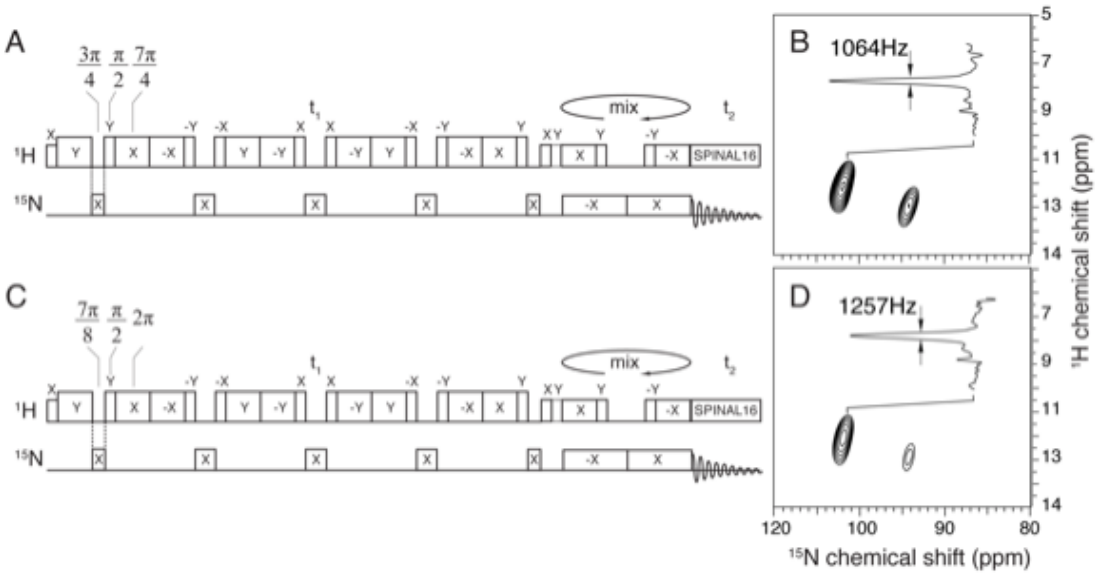

Figure 3.5. The comparison of finite pulse compensation scheme for HETCOR pulse sequence. The homonuclear decoupling during t1 is executed by MSHOT4 pulses with finite pulse compensation scheme described by either (A) Nevzorov and Opella (Nevzorov and Opella, 2007) or (C) Hohwy and Nielsen (Hohwy and Nielsen, 1997). The corresponding spectra acquired in NAL crystal sample are shown on the right side (B and D). One-dimensional slices for the left-most peak were extracted for line width comparison. Compared to the NAL crystal spectra in Figures 2 and 4, the slightly larger line widths observed in these spectra is most likely due to the lower ^{1}H B_1 field used in the experiments.

The homonuclear decoupling in the ^{1}H chemical shift dimension results from a magic sandwich pulse sequence (Rhim et al., 1971). In an ideal case, the magic sandwich has the general pattern of τ-π/2-2π-2π-π/2-τ, where the π/2 pulse is a δ pulse, and τ has the duration of a π pulse. In the actual NMR experiment, since the π/2 pulse cannot be a δ pulse, compensation for the finite pulse lengths has to be made. In the originally proposed MSHOT pulse sequence(Hohwy and Nielsen, 1997), Hohwy and

Nielsen set the length of τ to be 7π/8 and kept the 2π pulse at 2π; and in a recent elaboration of the SAMPI4 pulse sequence(Nevzorov and Opella, 2007), τ was set to be 3π/4 and the 2π pulse was shortened to 7π/4. Since in the first order approximation, the π/2 pulses retain a quarter of the homonuclear coupling evolution, both schemes average the first-order homonuclear coupling to zero. We compared the performance of these two finite pulse compensation schemes on an NAL single crystal sample (Figure 5), and found that the 3π/4 and 7π/4 combination (Figure 5A) yieldedsomewhat narrower linewidths. Consequently, this "PI4" finite pulse compensation scheme was incorporated into the general Z-rotational decoupling of the MSHOT pulse sequence, resulting in the pulse sequence we refer to as MSHOT-PI4. Note that the ^{15}N CW decoupling is applied only during periods without irradiation in the MSHOT pulse scheme (Fu et al., 2009; Fu et al., 2007). On membrane protein samples, we found that application of CW decoupling during the entire t1 dimension provided superior line narrowing, though it made little difference for the NAL sample.

3.5 Application to Larger Membrane Proteins

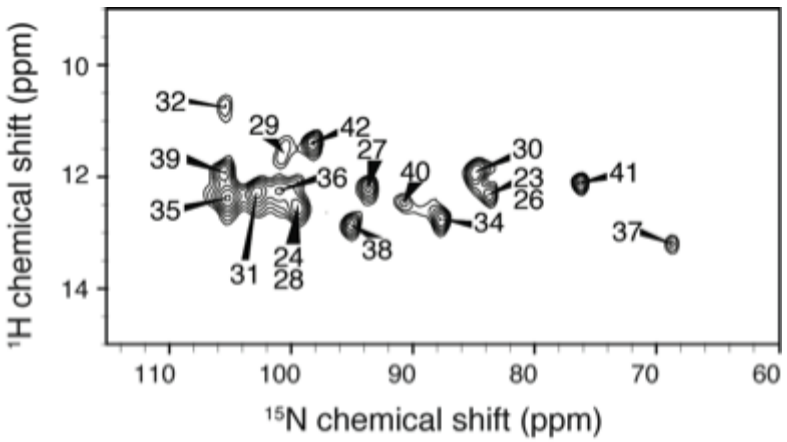

Figure 3.6. Resonance assignments of two-dimensional ^{1}H/^{15}N HETCOR spectrum of the Pf1 coat protein. Peaks are labeled with the residue number. Assignments are made from a previously recorded three-dimensional HETCOR-SLF spectrum (Lu et al., 2011).

All the signals from the membrane-bound form of the Pf1 coat protein in magnetically aligned bilayers can be readily assigned based on previous results (Lu et al., 2011) (Figure 6), and significantly, we find its MSHOT-PI4/Pi HETCOR spectrum has resolution equivalent to that observed in the most recent examples of separated local field (SLF) spectra of the same sample (Opella et al., 2008; Park et al., 2010c), where except for the same two pairs of resonances that are partially overlapped in both spectra, all other peaks exhibit single-site resolution. Note that the two-dimensional SLF spectrum (^{1}H-^{15}N heteronuclear dipolar coupling correlated with ^{15}N chemical shift) is the benchmark in OS solid-state NMR, in a large part due to the high resolution in ^{1}H-^{15}N heteronuclear dipolar coupling dimension. The ability of the MSHOT-PI4/Pi pulse sequence to obtain an additional third dimension with comparable resolution gives a boost in the size of membrane proteins amenable to OS solid-state NMR without any additional magnetization transfer steps, which can

reduce sensitivity. The only drawback is that polarization inversion is not practical in the three-dimensional experiment.

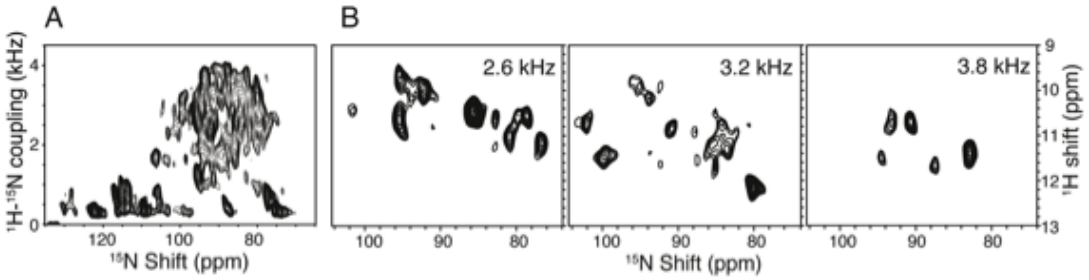

Figure 3.7. Two-dimensional SLF spectrum (A) and selective planes from three-dimensional HETCOR/SLF spectrum (B) on the mercury transport protein MerFm. More than 50 residues are heavily overlapped in the helical region (^{1}H-^{15}N dipolar coupling above 1 kHz), making it a challenging target for structure determination by solid-state NMR. The selected HETCOR planes display a resolution similar to that observed in membrane-bound form of Pf1 coat protein in Figure 3.6.

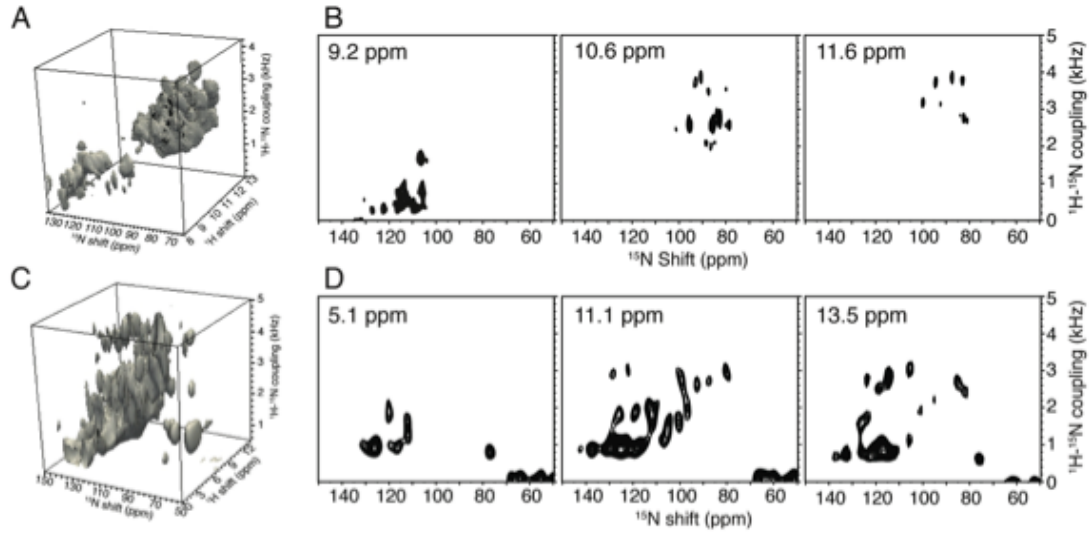

Figure 3.8. Three-dimensional HETCOR/SLF spectra of uniformly ^{15}N labeled membrane proteins in aligned phospholipid bilayers. A and C. Cubes displaying the three-dimensional spectra. A. 81-residue MerFm. C. 350-residue CXCR1. B. SLF planes at selected ^{1}H frequencies from the three-dimensional spectrum of MerFm. D. SLF planes at selected ^{1}H frequencies from the three-dimensional spectrum of CXCR1. The two-dimensional HETCOR pulse sequence shown in Figure 1B was used to acquire three-dimensional HETCOR/SLF spectra with the addition of systematic incrementation of the duration of the "mixing" interval of the SAMPI4 pulse (Nevzorov et al., 2007; Nevzorov and Opella, 2007).

Three-dimensional HETCOR/SLF spectra were acquired from samples of larger membrane proteins in phospholipid bilayers. Figure 3.7 shows spectra acquired from a sample of uniformly ^{15}N labeled MerFm, an 81-residue mercury transport protein with two transmembrane helices. More than 50 resonances are heavily overlapped in the helical region of a conventional two-dimensional SLF spectrum (Figure 3.7.A), however, almost all signals are resolved in the three-dimensional HETCOR/SLF spectrum. A cube representation of the three-dimensional spectrum is shown in Figure 3.8.A, and examples of HETCOR (Figure 3.7.B) and SLF planes (Figure 3.8.B) are shown. Figure 3.8.C and 3.8.D contain data from a three-dimensional spectrum obtained from a sample of the 350-residue G-protein coupled receptor CXCR1 with seven transmembrane helices in phospholipid bilayers. Comparisons with the spectra of the smaller membrane proteins demonstrates that the pulse sequence in Figure 1B is equally effective at narrowing the ^{1}H amide resonances of both small and large membrane proteins in phospholipid bilayers.

3.6 Line-narrowing in the Heteronuclear Dipolar Coupling Frequency Dimension

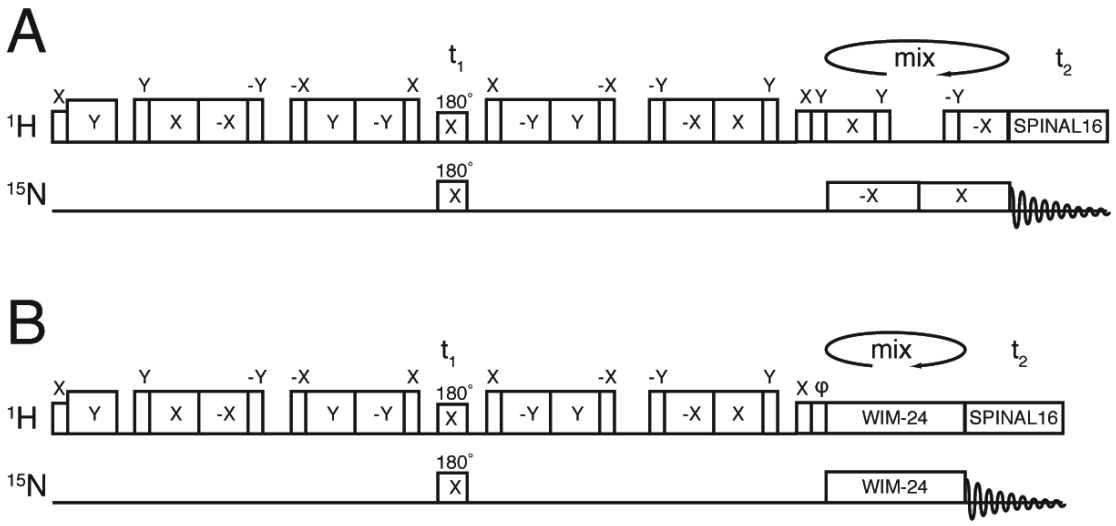

Figure 3.9. Two-dimensional PDLF pulse sequences. The pulse sequences in Figure 3.1.B are modified to perform PDLF class experiments by the addition of a π pulse in the ^{1}H channel at the same position as the ^{15}N channel refocusing π pulse. A. Selective magnetization transfer is performed by SAMPI4 (Nevzorov et al., 2007; Nevzorov and Opella, 2007). B. The transfer is performed by WIM. WIM-24 follows the same phase cycle as previously described (Caravatti et al., 1983), and the φ pulse is cycled between Y and -Y, and in combination with the preceding Y pulse, it cancels the spin-locked component (Caravatti et al., 1983). In our experience, WIM provides higher sensitivity for magnetization transfer, while SAMPI4 provides better dipolar coupling during evolution in three-dimensional experiments.

Another application of this experimental approach is to enhance the resolution in the heteronuclear dipolar coupling dimension in the PDLF class of experiments. Due to their generally broader line widths, laboratory-frame PDLF class experiments are used less frequently than the rotating-frame PISEMA class experiments (Gan, 2000; Wu et al., 2010). However, PDLF experiments have the advantage that they do not truncate the values of small dipolar couplings; therefore, they yield more accurate and better resolved signals from residues in loop, terminal or surface helices, which typically have relatively small heteronuclear dipolar couplings in aligned samples of membrane proteins. The pulse sequences in Figure 3.9 yield line widths that are

similar to the ~200 Hz line widths achieved by either PISEMA (Wu et al., 1994) or SAMPI4 (Nevzorov and Opella, 2007) pulse sequences, as demonstrated by the spectrum of the membrane-bound form of Pf1 coat protein in Figure 3.10.A. Notably, the spectrum is free from dipolar coupling truncation artifacts, such as the clustering of peaks at the low dipolar coupling frequencies that are observed in many PISEMA spectra of membrane proteins. A two-dimensional PDLF spectrum was also acquired on MerFm in phospholipid bilayers, and yielded a spectrum with single-site resolution for signals in the non-helical region (Figure 3.10.B).

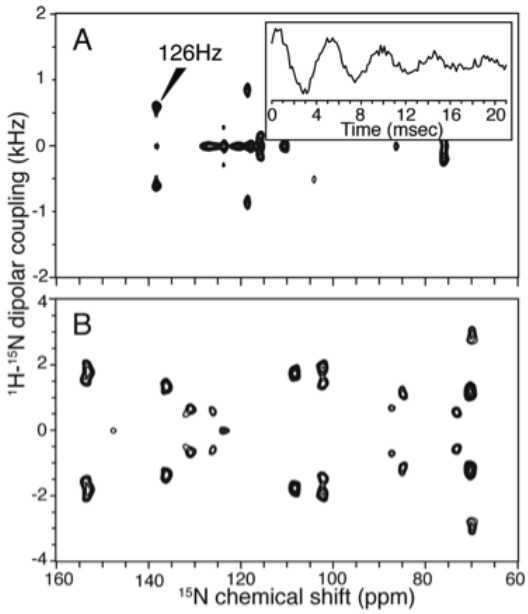

Figure 3.10. The application of two-dimensional PDLF spectroscopy to resolve resonances in the non-helical residues of membrane proteins in phospholipid bilayers. A. The spectrum was acquired on the membrane-bound form of Pf1 coat protein in phospholipid bilayers. The inset shows the indirect dimension time evolution of the signal from residue A46, which has a ^{15}N chemical shift of 138 ppm and is marked in the spectrum. Its line width is noted near the resonance. B. The spectrum was acquired on MerFm sample in parallel bicelle that are "flipped" from the regular perpendicular bicelle by the additional of lanthanide ion as described previously(De Angelis et al., 2005; De Angelis et al., 2004; De Angelis and Opella, 2007). The non-helical region of MerFm displays single-site resolution in the PDLF spectrum.

For some ^{1}H amide signals in the PDLF spectrum, such as that from alanine 46 of the membrane-bound form of Pf1 coat protein (Figure 3.10.A), the time domain oscillation can extend beyond 20 msec (Figure 3.10.A inset), which is comparable to the most extended ^{15}N oscillations (Park and Opella, 2010). The line widths of the ^{1}H signals would be ~40 Hz without the drawback of an unfavorable scaling factor of 0.33, which would be equivalent to the narrowest ^{15}N amide resonance line width observed to date (Park and Opella, 2010). Considering that ^{15}N is a dilute spin by virtue of its low gyromagnetic ratio and spatial separation in proteins, this result indicates the potential to achieve highly effective homonuclear and heteronuclear decoupling of amide ^{1}H sites in proteins despite their dense network of couplings and high gyromagnetic ratio.

3.7. Discussion

A likely reason for the enhanced line narrowing with the new pulse sequences is their ability to successfully avoid interference from protein motions, since the line narrowing is only found in membrane proteins in liquid crystalline phospholipid bilayers where they undergo rapid rotational diffusion about the bilayer normal (Park et al., 2011b). Notably, several early studies demonstrated that motions of organic compounds on a time scale similar to that of the pulse nutation frequency reduces the efficiency of pulse decoupling (Long et al., 1994; McMillan et al., 2003; Reichert, 2005; Rothwell and Waugh, 1981). Currently, the pulse nutation frequency in most OS solid-state NMR experiments is similar to the rotational diffusion frequency of

membrane proteins at approximately 10^5 Hz (Park et al., 2006b), and therefore interference effects may be present.. These interference effects have been well characterized for continuous wave (CW) decoupling but not for magic sandwich decoupling sequence, and the effect has not been revealed in NMR spectra of proteins.. It is straightforward to understand how the replacement of continuous wave decoupling by a single π pulse could enhance the resolution by removing the interference effect; however, it will require further theoretical and experimental studies to confirm the source of the line narrowing from MSHOT-PI4 sequence.

In conclusion, the finding that a pulse sequence specifically enhances the resolution of membrane protein sample by more than a factor of two illustrates the significant role of protein motions in determining the efficacy of pulse sequence performance. These effects may be generalizable to other pulse sequences that would be applicable to both OS solid-state NMR on aligned bilayer samples and RA MAS solid-state NMR on unoriented proteoliposome samples. The pulse sequences discussed in this article narrow ^{1}H resonances, and advance the application and potentially the design of solid-state NMR spectroscopy to membrane proteins in phospholipid bilayers.

3.8 Material and Methods

A full-length construct of the mercury transport protein MerF, which has its Cys residues replaced by Ser residues, is named MerFm (for modified) and its sequence, expression and purification have been described previously (De Angelis et

al., 2006b; Howell et al., 2005). The expression and purification of Pf1 coat protein (Park et al., 2010c) and CXCR1 (Park and Opella, 2010) have also been described previously. In the case of Pf1 coat protein and MerFm, magnetically aligned bicelle samples were prepared with 6-O-PC (1,2-di-O-hexyl-*sn*-glycero-3-phosphocholine) and 14-O-PC (1,2-di-O-tetradecyl-*sn*-glycero-3-phosphocholine) as previously described (De Angelis et al., 2006b; De Angelis and Opella, 2007; Park et al., 2010c); and in the case of CXCR1, the bicelle sample was prepared with DMPC (1,2-Dimyristoyl-*sn*-Glycero-3-Phosphocholin) and Triton X-100 with q=5 and with 20% (w/v) of DMPC. In addition, 2.5 mM NaN_3 and 20 mM HEPES (pH 7.3) is included in the CXCR1 sample.

The ^{15}N detected solid-state NMR spectra were obtained on 700 MHz Bruker Avance spectrometers. A homebuilt $^{1}H/^{15}N$ double-resonance probe with a strip-shield was used for all experiments (Wu et al., 2009) except for those on the CXCR1 sample, where a MAGC probe was used (Grant et al., 2009). These probes suppress the sample heating resulting from high frequency, high power radiofrequency irradiations.

The two spectra of Pf1 coat protein in Figure 3.2 were obtained back to back on the same sample. For both of them, the B_1 field for ^{1}H irradiation during t1 evolution was 71.4kHz, and 50kHz elsewhere in the sequence. 40 scans were collected for each t1 increment; 64 complex t1 point were recorded for the spectrum in Figure 3.2.B, and consequently, 64 MSHOT-PI4 cycles gave a t1 evolution time of 10.75 msec. To match the t1 length, 235 complex t1 points were collected for the spectrum in Figure 3.2.A with 4 FSLG pulses per increment. For both spectra, 3 cycles of

SAMPI4 was used to selectively transfer magnetization for peaks with high dipolar couplings. For the NAL spectrum in Figure 2C, 62.5kHz of ^{1}H power was used during t1 evolution and 80 complex points were collected with 4 FSLG pulses per increment. The spectrum in Figure 3.2.D used 72.9kHz ^{1}H power during t1 evolution and 64 complex points were collected. In both cases, excess increments were present after the signals had decayed into the noise level. 3 cycles of SAMPI4 was used in the mixing period, which selectively transferred magnetization for resonances with $^{1}H/^{15}N$ dipolar couplings > 1kHz. In all the experiments, after the first 90° pulse, a short spin-lock pulse (typically 100 μs) was incorporated in order for any transient effects to dissipate..

With the same samples, the spectra in Figure 3.4 were recorded back to back. During t1 evolution for the membrane-bound form of Pf1 coat protein sample, the B_1 field was at 72.9kHz for MSHOT-PI4 pulses, 62.5kHz for FSLG pulses, and 47.2kHz for CW decoupling in ^{15}N channel. 64 complex t1 points were recorded for all the spectra in Figure 3.5. Consequently, 64 MSHOT-PI4 cycles gave a t1 evolution time of 10.54 msec, 64 FSLG cycles with 4 pulses each gave 3.34 msec, where in both cases signals were allowed to decay to the noise level. A B_1 field of 47.2kHz was applied in the rest of the pulse sequence, and 3 cycles of SAMPI4 were used for magnetization transfer. The experimental conditions for the NAL crystal spectra were the same as those for the membrane-bound form of the Pf1 coat protein. The line widths were measured in NMRDraw (Delaglio et al., 1995) or Sparky (Goddard and Kneller, 2008).

For the spectra in Figure 3.5, the B_1 field was 62.5kHz for ^1H irradiation during t1 evolution, and 50kHz elsewhere in the sequence. 64 complex t1 points were collected for both spectra, giving an evolution time of 3.07 msec and 3.46 msec.

The conventional two-dimensional SLF spectrum was acquired with the SAMPI4 pulse sequence (Nevzorov and Opella, 2007), and 80 real t1 points and 512 complex t2 points were co-added. For the three-dimensional HETCOR/SLF spectrum on the sample of the MerFm protein, 30 complex t1 points, 48 real t2 point, 512 complex t3 points and 40 scans were collected. The three-dimensional data set of CXCR1 consisted of 20 complex t1 points, 20 real t2 points and 256 complex t3 points.

For the PDLF spectrum on the membrane-bound form of Pf1 coat protein, 128 real t1 points and 40 scans were collected. 72.9kHz ^1H radiofrequency pulses were used during t1 evolution. 9 cycles of SAMPI4 pulses at 47.2kHz matching B_1 field were used to ensure the transfer of magnetization for residues with small dipolar couplings. For the PDLF spectrum on the MerFm sample that was 'flipped' so that the bilayer normal was perpendicular to the magnetic field, 76 real t1 points and 80 scans were collected. 71.4kHz ^1H radiofrequency pulses were used during t1 evolution and 3 cycles of WIM pulses at 50kHz matching B_1 field were used to ensure the transfer of magnetization for residues with small dipolar couplings.

Chapter 3, in full, is a reprint of the material "Improved ^1H amide resonance line narrowing in oriented sample solid-state NMR of membrane proteins in

phospholipid bilayers" as it appears in J. Magn. Reson. 220:54-61 by Lu GJ, Park SH, Opella SJ. The thesis author was the primary author of the paper.

Chapter 4. Complete Resonance Assignment of MerF by Combining Multiple Strategies of Oriented Sample Solid-state NMR

4.1 Abstract

Oriented Sample (OS) solid-state NMR spectroscopy can be used to determine the three-dimensional structures of membrane proteins in magnetically or mechanically aligned lipid bilayers. The bottleneck for applying this technique to larger and more challenging proteins is making resonance assignments, which is conventionally accomplished through the preparation of multiple selectively isotopically labeled samples and performing an analysis of residues in regular secondary structure based on Polarity Index Slant Angle (PISA) Wheels and Dipolar Waves. Here we report the complete resonance assignment of the full-length mercury transporter, MerF, an 81-residue protein, which is challenging because of overlapping PISA Wheel patterns from its two trans-membrane helices, by using a combination of solid-state NMR techniques that improve the spectral resolution and provide correlations between residues and resonances. These techniques include experiments that take advantage of the improved resolution of the MSHOT4-Pi4/Pi pulse sequence; the transfer of resonance assignments through frequency alignment of heteronuclear dipolar couplings, or through dipolar coupling correlated isotropic chemical shift analysis; $^{15}N/^{15}N$ dilute spin exchange experiments; and the use of the proton-evolved local field (PELF) experiment with isotropic shift analysis to assign the irregular

terminal and loop regions of the protein, which is the major “blind spot” of the PISA Wheel/Dipolar Wave method.

4.2 Introduction

Oriented Sample (OS) solid-state NMR spectroscopy of stationary samples is an approach to determining the atomic resolution structures of biological macromolecules that can be aligned by their environment, such as proteins in virus particles or phospholipid bilayers (Murray et al., 2013; Opella, 2013; Opella et al., 2008). When the macromolecules are aligned relative to the magnetic field the angle-dependent NMR observables, such as anisotropic chemical shifts and heteronuclear dipole-dipole couplings, converge to single line resonances (or doublets) (Opella and Waugh, 1977). Signals are resolved since individual sites have different orientations relative to the direction of the field, and hence different resonance frequencies. Notably, resolution results from differences in orientation relative to the axis of alignment rather than differences in local environment.

The angles of N-H and C-H bonds, and chemical shift anisotropy vectors for each site of a membrane protein in liquid crystalline phospholipid bilayers can be measured relative to the axis of alignment with high accuracy and precision, and the three-dimensional structure of the protein can be determined using these angular restraints. However, the application of OS solid-state NMR to membrane proteins has been hindered by limitations in the methods for the assignment of resonances. Unlike solution NMR or magic angle spinning (MAS) solid-state NMR, systematic

assignment methods that rely on a sequential "walk" along the backbone atoms are lacking in OS solid-state NMR because of the difficulty in dealing with the network of ^{13}C-^{13}C homonuclear dipolar couplings in uniformly ^{13}C labeled samples. For a period of time, the main and only resonance assignment method was the analysis of Polarity Index Slant Angle (PISA) Wheels (Marassi and Opella, 2000; Wang et al., 2000) and Dipolar Waves (Mesleh et al., 2002) that required multiple amino-acid-type selectively labeled/unlabeled spectra. This method was used in the several structures (De Angelis et al., 2006b; Ketchem et al., 1993; Marassi and Opella, 2003; Opella et al., 1999; Park et al., 2010c; Park et al., 2003; Sharma et al., 2010) recently determined by OS solid-state NMR of aligned, stationary samples. For the full-length mercury transporter MerF used as an example in this article, the two long transmembrane helices, which include between them more than 50 residues, are tilted at similar angles, and as a result, the spectra contain overlapped PISA Wheels, rendering the protein a challenging target for OS solid-state NMR structure determination. Without severe spectral overlap, the PISA wheel/Dipolar Wave method (Marassi and Opella, 2003) works well for assigning resonances from residues in regular secondary structures but not with irregular regions of tertiary structures, such as those encountered in loops and structured terminal regions of membrane proteins. This is also an issue with MerF.

The methods that we combine for a more effective and comprehensive assignment strategy include: (1) The MSHOT4-Pi4/Pi pulse sequence (Lu and Opella, 2013; Lu et al., 2012), which provides three-dimensional heteronuclear correlation

(HETCOR)/separated local field (SLF) spectra of uniformly and selectively labeled samples. (2) The resonance assignment method of dipolar coupling correlated isotropic chemical shift (DCCICS) analysis (Lu et al., 2011), which was previously demonstrated on a smaller membrane protein. With selectively labeled samples, it complements the information obtained from PISA Wheel assignments. (3) Signals from the non-helical terminal and loop regions of the proteins have been difficult or impossible to assign with the PISA Wheel/Dipolar Wave approach. The proton-evolved local field (PELF) experiment (Schmidt-Rohr et al., 1994b) improved by the MSHOT4-Pi4/Pi pulse sequence, efficiently resolves signals from these regions, and in combination with DCCICS analysis it provides a general method to assign signals from regions with irregular tertiary structure. (4) Resonances can be assigned with MAS solid-state NMR methods, and subsequently their recoupled ^{1}H-^{15}N heteronuclear dipolar couplings can be measured under rotational alignment (RA) condition (Das et al., 2012; Park et al., 2010a). These dipolar couplings and their assignments are scaled and transferred to SLF spectra acquired from selectively labeled and aligned, stationary samples, and enabling assignment of the latter spectra. (5) $^{15}N/^{15}N$ dilute spin exchange can be applied to selectively labeled samples to single out the adjacent pairs of same type of amino acid residues (Cross et al., 1983; Marassi et al., 1999b).

4.3 Materials and Methods

The expression and purification of uniformly ^{15}N-labeled full-length MerF has been described in detail (Lu et al., 2013a). For the expression of amino acid type selectively ^{15}N labeled MerF, a ^{15}N-labeled amino acid (Cambridge Isotope Laboratories, www.isotope.com) was added to the growth media at a concentration of 0.1 g/l, while all the other 19 unlabeled amino acids were added at higher concentrations including 0.5 g/l Asp and Glu. The bacterial growth was generally shortened to < 3 hours after induction to minimize isotopic scrambling. In the last step of purification, size-exclusion chromatography on a Sephacryl S-200 column was followed by exhaustive dialysis to remove the sodium dodecyl sulfate (SDS) detergent. Alternatively, reverse-phase high-performance liquid chromatography (HPLC) (DeltaPak C4 Column, Waters, www.waters.com) was used (Lu et al., 2013a). In both cases, the resulting pure polypeptides were lyophilized for long-term storage prior to preparing the NMR samples.

Magnetically aligned bicelle samples for OS solid-state NMR were prepared from a mixture of long-chain 1,2-dimyristoyl-*sn*-glycero-3-phosphocholine (DMPC) and short-chain 1,2-dihexanoyl-*sn*-glycero-3-phosphocholine (DHPC) lipids at q=3.2 (Sanders et al., 1994a). In some samples, including the uniformly ^{15}N-labeled sample used for the three-dimensional experiments, DMPC and DHPC were substituted by the non-hydrolysable ether-linked lipids 1,2-di-O-tetradecyl-sn-glycero-3-phosphocholine (14-O-PC) and 1,2-di-O-hexyl-sn-glycero-3-phosphocholine (6-O-PC) for long-term stability. All lipids were from Avanti Polar Lipids (www.avantilipids.com). The protocols for preparing the magnetically aligned bicelle samples for OS solid-state

NMR have been described (De Angelis and Opella, 2007; Sanders et al., 1994a). Briefly, lyophilized MerF protein (in the range of 2 to 7 mg) was first solubilized in a 160μL solution containing 7mg DHPC, and then ~35mg lyophilized DMPC was mixed into the solution. The resulting solution was repeatedly cycled between 42°C and 0°C with vortexing at both temperatures to improve sample mixing and facilitate the formation of bicelles. The pH was then adjusted to 6.0. 170μL of the solution was transferred to a 5 mm outside diameter flat-bottomed thin-wall glass tube (NE-RG5-T-15-FB, New Era, http://www.newera-spectro.com), which was sealed with a rubber plug. "Flipped" bicelle samples with the bilayer normals parallel to the field were prepared by the addition of ~1.5mM $YbCl_3$ to the already formed bicelles. Isotropic bicelle samples (q=0.1) for solution NMR were prepared by mixing ~1mg MerF protein in 500μL solution containing 10% v/v D_2O, 100mM 6-O-PC, 10mM 14-O-PC, 20mM MES and 1mM NaN_3 at pH=6.0.

The solid-state NMR experiments were performed on a Bruker Avance 700 MHz spectrometer using a home-built $^{1}H/^{15}N$ double-resonance "low-E" probe with a strip shield (Wu et al., 2009). Sample temperature was maintained at 42°C and the recycle delay was 4-6 seconds. ^{15}N chemical shift frequencies were referenced to the signal from solid ammonium sulfate, which was set to 26.8 ppm (De Angelis et al., 2006b) and ^{1}H chemical shift frequencies were referenced to the internal $^{1}H_2O$ resonance set to 4.7 ppm. The ^{1}H carrier was set at 9 ppm for "unflipped" perpendicularly aligned bicelle samples and at 5 ppm for "flipped" parallel aligned bicelle samples. All two-dimensional SLF experiments performed on "unflipped"

bicelle samples utilized the SAMPI4 pulse sequence (Nevzorov and Opella, 2007). For "flipped" bicelle samples, both SAMPI4 and PISEMA (Wu et al., 1994) pulse sequences were used in order to cope with the larger dipolar couplings present in the samples. The three-dimensional HETCOR/SLF experiments and two-dimensional PELF experiments (Schmidt-Rohr et al., 1994b) used the MSHOT-Pi4/Pi sequence (Lu and Opella, 2013; Lu et al., 2012). All the experiments were performed with a radiofrequency field strength of ~ 50 kHz in both channels, except that the ^{1}H field strength was ~70 kHz during ^{1}H chemical shift evolution in two-dimensional HETCOR and three-dimensional HETCOR/SLF experiments and during the ^{1}H-^{15}N dipolar coupling dimension in PELF experiments. Spectra from the selectively ^{15}N labeled samples were acquired with between 20 and 48 real points in the t_1 dimension of PISEMA and SAMPI4 experiments, and the settings for the HETCOR/SLF and PELF experiments were similar to those previously described (Lu et al., 2012). For solution NMR experiments, the two-dimensional HSQC spectra were acquired at 50 °C on a 800 MHz spectrometer using a triple-resonance cryoprobe, and the chemical shifts are referenced to the $^{1}H_2O$ resonance defined as 4.534 ppm at 50 °C (Cavanagh et al., 1996). All the NMR data were processed using the program NMRPipe (Delaglio et al., 1995) and the spectra were assigned using the program Sparky (Goddard and Kneller).

4.4 Oriented Sample Solid-State NMR of Stationary Aligned Samples.

Alignment of the nuclear spin interactions present at all protein sites relative to a fixed external axis is the essential physical principle of oriented sample solid-state NMR spectroscopy. The basic approach is best illustrated by aligned, stationary samples, which can be prepared in several ways. The most common ones are mechanical alignment on glass plates and magnetic alignment in bicelles with $q > 2.5$ (De Angelis and Opella, 2007). It is also possible to align samples as drawn fibers (Opella and Waugh, 1977), in narrow tubes (Chekmenev et al., 2006), and potentially other methods. Although mechanically aligned samples of protein-containing phospholipids on glass plates are the simplest to prepare, and provide the greatest flexibility in terms of choice of lipids, temperature, etc., magnetic alignment has the strong advantages of providing spectra with narrower line widths and having no uncertainty about the precise direction of alignment. Both mechanically and magnetically aligned samples can be 'flipped' between alignments with the bilayer normals parallel and perpendicular to the direction of the applied magnetic field. Bilayers aligned on glass plates have the additional advantage that they can be oriented at any angle with respect to the field by tilting the plates and/or the coil, which is useful in some specialized experiments (Park et al., 2006b).

MerF in 14-O-PC/6-O-PC q=3.2 bicelles aligns spontaneously with the bilayer normals perpendicular to the direction of the field. Full-length MerF in bicelles forms particularly well-aligned samples, as judged by the line widths of individual resonances, and the overall resolution of the one-dimensional ^{15}N NMR spectrum of a uniformly ^{15}N labeled sample shown in Figure 4.1. Two features in particular

demonstrate that the sample is well aligned. The spectral region above 150 ppm is free of signal intensity, indicating the absence of residual powder pattern from unaligned or aggregated proteins and that the proteins are all undergoing fast uniaxial rotational diffusion. And the line widths of selected peaks are very narrow, approaching those of the best reported spectra, which required the use of Triton X-100 instead of DHPC as the "short chain" lipid and a small protein (Park and Opella, 2010). The ability to prepare well-aligned samples lays the foundation for the subsequent steps of spectroscopy and resonance assignments of signals associated with individual residues. The frequencies of these resolved signals carry angular information that is the principal source of restraints for structure calculations. The frequencies are also the source of resolution in the spectra.

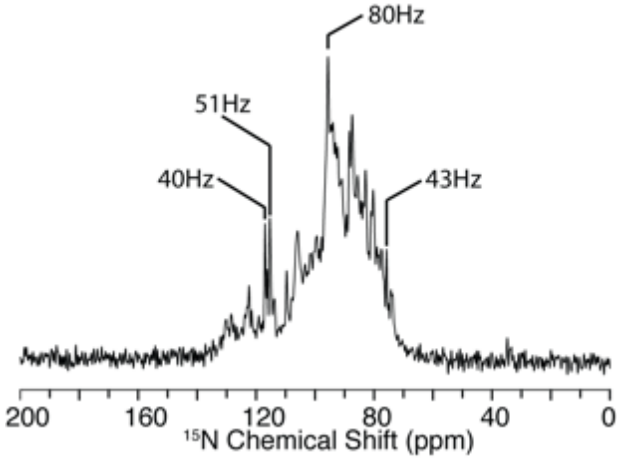

Figure 4.1. ^{15}N solid-state NMR spectrum of uniformly ^{15}N labeled full-length MerF in q=3.2 14-O-PC/6-O-PC bicelles aligned with their normals perpendicular to the direction of the magnetic field. Line widths of selected resonances are marked in the figure.

The next task is to resolve and assign individual resonance signals in the spectrum. In previous examples of single trans-membrane or small two trans-

membrane helical membrane proteins, this could be successfully accomplished with the combination of high-resolution two-dimensional SLF spectroscopy and the use of selective isotopic labeling. Since selectively labeled samples could be prepared for the majority of amino acids, signals from the rest could be identified by subtracting the spectra of selectively labeled samples from that of a uniformly labeled sample. With individual signals resolved and the confident assignment of their amino acid type, the resonance assignment could then be accomplished through the qualitative, geometric PISA Wheel (Marassi and Opella, 2000; Wang et al., 2000) and Dipolar Wave analysis (Mesleh et al., 2002). This assignment method has been described in detail in earlier publications for those regions of proteins with large amounts of regular alpha helix (Marassi and Opella, 2003) or beta sheet secondary structure (Marassi, 2001), and has been recently optimized and automated in the AssignFit program (Tian et al., 2012). The method relies on the periodic geometry of α-helical residues that can be displayed as a helical wheel and therefore present themselves as the PISA Wheel in SLF spectra.

However, in the structure determination of larger and more challenging proteins, such as MerF, these methods alone are not sufficient to resolve and unambiguously assign signals from all residues. The first challenge is that two-dimensional SLF spectra do not fully resolve signals from uniformly labeled samples (Figure 4.2.A), or even in some selectively labeled samples when multiple copies of the same amino acid are present, such as the 14 leucines in MerF (Figure 4.2.D). The second challenge is the difficulty in unambiguously assigning signals with PISA

Wheel analysis. Signals from residues in the two long trans-membrane helices produce overlapped PISA wheels in the crowded spectral region with ^{1}H-^{15}N dipolar couplings > 1.5 kHz. More critically, the third challenge is the assignment of the residues in the non-helical regions of the protein. Even for small membrane proteins, few irregularly structured residues could be readily assigned from the other signals in the selectively labeled samples. Since multiple sites are now present in this region and PISA Wheels and Dipolar Wave approaches are effective only for residues in regular secondary structures, an alternative assignment method needs to be developed.

Here we show that the first challenge can be addressed by application of the MSHOT-Pi4/Pi pulse sequence, which improves the resolution in the ^{1}H chemical shift dimension (Lu and Opella, 2013). This enables three-dimensional HETCOR/SLF spectroscopy to be used effectively with superior resolving power to that observed in two-dimensional SLF spectroscopy without much loss of sensitivity. In the uniformly ^{15}N labeled sample, except for 5 overlapped signals out of the total 64 observed amide signals, all are recognizable as distinct resonances in the three-dimensional HETCOR/SLF spectrum (Figure 4.2.B and 4.2.C). This enables the few residues that cannot be selectively labeled during bacterial expression to be readily identified among the unassigned peaks after accounting for all of the successfully labeled amino acids. Additionally, all resonances assigned by relying on multiple spectra and experiments are now mapped onto a single spectrum, which provides the practical advantage of minimizing the effects of minor sample-to-sample variations.

Using stationary, aligned samples in the form of magnetically aligned bilayers (q=3.2 bicelles), spectra from multiple selectively ^{15}N labeled samples are compared to that from a uniformly ^{15}N labeled sample (Figure 4.2). Although it is labor-intensive and time consuming to prepare multiple samples, these data provide a substantial amount of unambiguous information about the positions and assignments of resonances. Selectively ^{15}N-labeled samples were prepared for Ala, Arg, Gln, Ile, Leu, Lys, Phe, Thr, Tyr and Val. As noted, several of the other amino acids, i.e., Asp, Gly and Ser, could not be labeled with high incorporation and selectivity. Nine of the ten samples provide well-resolved two-dimensional SLF spectra (Figure 4.2.G-O). The leucine labeled sample is the exception; the 14 leucine resonances are not well resolved in two-dimensional spectra (Figure 4.2.D) but are fully resolved in a three-dimensional HETCOR/SLF spectrum as seen in the two examples of spectral planes (Figure 4.2.E and 4.2.F).

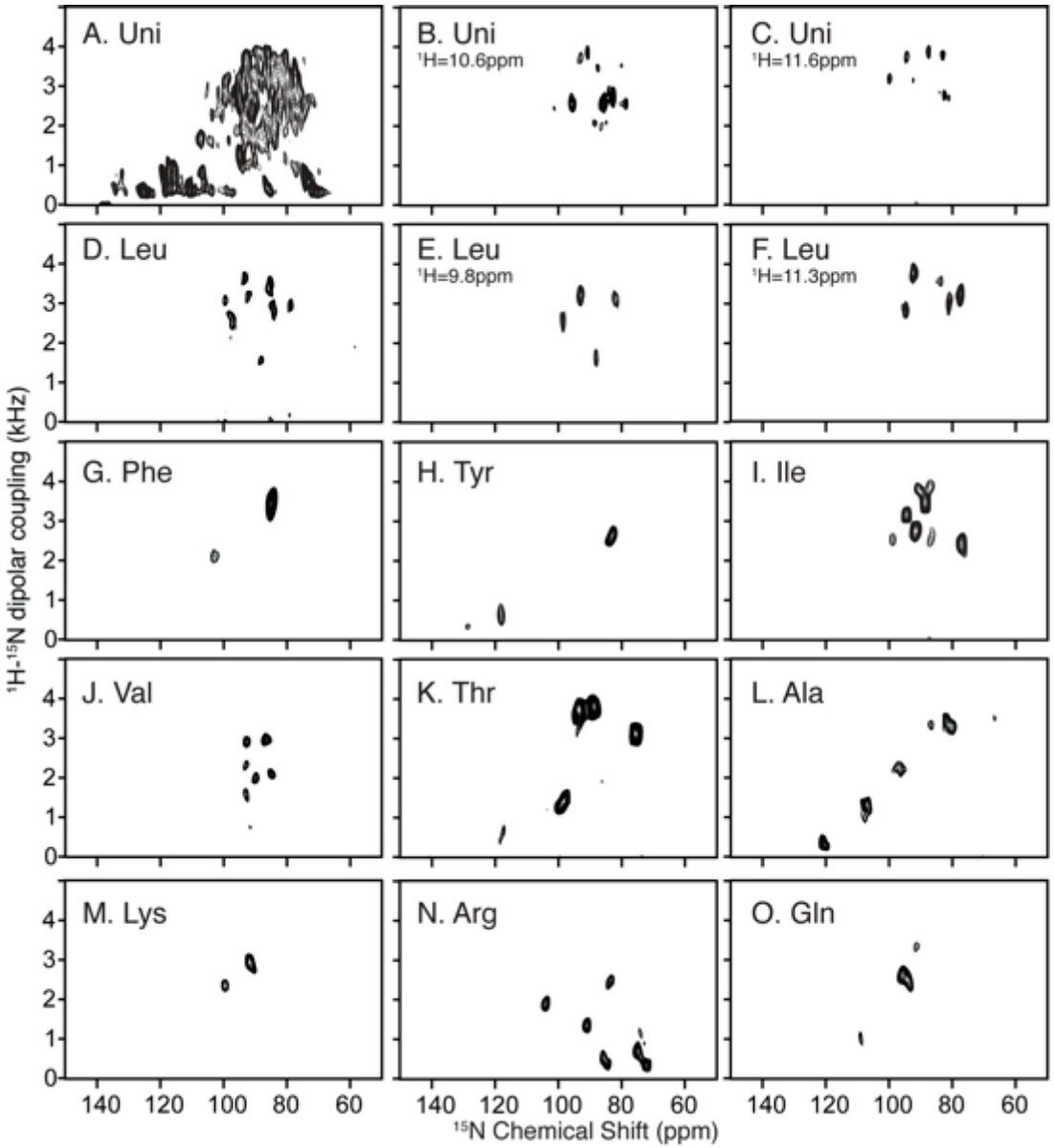

Figure 4.2. Two-dimensional SLF and three-dimensional HECTOR/SLF NMR spectra of uniformly and selectively ^{15}N labeled samples of MerF in q=3.2 14-O-PC/6-O-PC magnetically aligned bilayers (q=3.2 bicelles). A. Two-dimensional SLF spectrum of uniformly 15N labeled MerF. B. and C. Two-dimensional planes at the designated ^{1}H chemical shift frequencies from a three-dimensional HECTOR/SLF spectrum. D. Two-dimensional SLF spectrum of selectively ^{15}N leucine labeled MerF. E. and F. Two-dimensional planes at the designated ^{1}H chemical shift frequencies from a three-dimensional HECTOR/SLF spectrum. G-O. Two-dimensional SLF spectrum of other selectively labeled MerF samples. A-C are reprinted from (Lu et al., 2012). D and G-O are from (Howell, 2007).

4.5 Dipolar Coupling Correlated Isotropic Chemical Shift Analysis

For solution NMR and MAS solid-state NMR, both homonuclear and heteronuclear dipolar couplings are attenuated by motion, yielding isotropic chemical shift spectra and enabling the development of many magnetization transfer and sequential backbone assignment procedures. However, the ability to obtain angular information was lost until the introduction of methods to measure residual dipolar couplings (RDCs) in solution NMR of weakly aligned samples (Tolman et al., 1995) and dipolar recoupling in solid-state NMR (Griffin, 1998). OS solid-state NMR spectra of aligned, stationary samples, on the other hand, retain all the anisotropic information from the beginning. However, it has a major drawback, which is the difficulty of sequential backbone assignments due to the presence of unaveraged ^{1}H-^{1}H and ^{13}C-^{13}C dipolar couplings. These limitations can be largely overcome by a strategy of making resonance assignment using established methods on isotropic NMR spectra first and subsequently transferring the information to OS solid-state NMR spectra.

In dipolar coupling correlated isotropic chemical shift (DCCICS) analysis (Lu et al., 2011), the ^{1}H and ^{15}N isotropic chemical shifts are transferred from solution NMR spectra on low q isotropic bicelles (Son et al., 2012), as demonstrated using the selectively ^{15}N-Ile labeled sample of MerF shown in Figure 4.3 and Table 4.1. The underlying principle of the method is that the ^{1}H-^{15}N dipolar coupling for the same pair of nuclei differs by exactly a factor of two between parallel (flipped) and perpendicular (unflipped) aligned protein-containing bicelles. As a result, a one-to-one

correlation can be established between signals in SLF spectra of flipped and unflipped bicelles by aligning the appropriately scaled spectra. This enables two sets of anisotropic ^{15}N and ^{1}H chemical shifts to be measured for each residue, which are used to calculate the isotropic chemical shifts. These derived isotropic shifts can be compared with those observed in solution NMR spectra for regions of the protein that are not distorted by the presence of detergents or MAS solid-state NMR spectra to obtain their assignments. Notably, due to the broader line widths generally encountered in solid-state NMR, the isotropic chemical shift calculated in this manner have an error range, which was ~1.5 ppm for the ^{15}N chemical shift and ~0.3 ppm for the ^{1}H chemical shift in the previous well optimized case (Lu et al., 2011). The existence of this range, which can be improved through further spectroscopic development to improve resolution, currently relegates the DCCICS method to the role of assisting or confirming assignments rather than being able to make unique assignments on its own.

The assignment of the isoleucine resonances is shown here as an example of the DCCICS method (Figure 4.3 and Table 4.1). The assignment starts at residue I55, which is well separated in the DCCICS analysis. I55 also further confirms the PISA Wheel predicted for the second trans-membrane helix of MerF (L48 to R64), which is anchored by the assigned F54 and Y60 signals. From the PISA Wheel fitting, the assignments of residues I53, I59 and I62, which are all in the second helix, can be obtained, and agree with the DCCICS analysis. Next, I13 can be assigned: from DCCICS the signal could be either I12 or I13, but the subsequent PISA wheel fitting

shows that it can only be I13 in order to have I12 fit to one of the two isoleucine peaks left. I12 and I29 are then assigned to the last two isoleucine peaks. This assignment is further confirmed with the dipolar coupling frequency alignment method shown in the subsequent section “transfer of resonance assignments from rotational alignment solid-state NMR spectra”. The relatively large differences of residue I12 and I13 in DCCICS matching (Table 4.1) is likely due to the different membrane environments between low “q” isotropic bicelles and high “q” magnetically aligned bicelles. Because I12 and I13 are exposed to aqueous environment, they are susceptible to the variation in free detergent concentrations between the two samples. In contrast, the other isoleucine residues are likely to be in similar environments in both samples, because they are buried inside the membrane environment and are presumably in contact with long-chain 14-O-PC lipid in both samples (Lee et al., 2008).

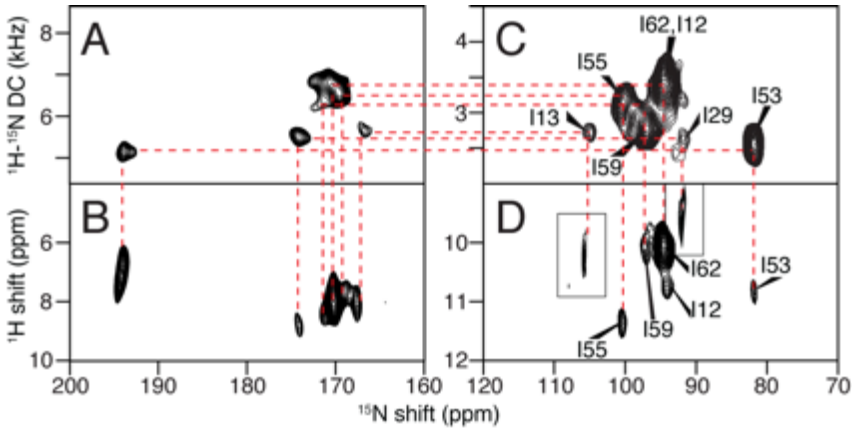

Figure 4.3. Example of the assignment of the isoleucine resonances of MerF by the method of heteronuclear dipolar coupling correlated isotropic chemical shift analysis. A., B., C., and D. are two-dimensional spectra of MerF in q=3.2 14-O-PC/6-O-PC bicelles. A. and B. are "flipped" with the bilayer normal parallel to the field; and C. and D. are "unflipped" with the bilayer normal perpendicular to the field. A. and C. are SLF spectra. B. and D. are HETCOR spectra. The assignment derived from combined DCCICS and PISA wheel analysis are labeled in spectra C and D. Insets in D are extracted from three-dimensional HETCOR/SLF spectrum of the same sample to occupy the missing peaks in two-dimensional spectrum due to selective magnetization transfer.

Table 4.1. Summary of data for the assignment and isotropic chemical shift calculations of MerF isoleucine residues for DCCICS analysis.

Residue assignment	Calculation from OS solid-state NMR		Measurement in solution NMR		The difference $\Delta\delta = \sqrt{(\Delta\delta_H)^2 + (\Delta\delta_N/5)^2}$
	^{15}N shift	^{1}H shift	^{15}N shift	^{1}H shift	
55	121.47	8.72	120.80	8.88	0.21
62	118.24	7.98	117.97	8.22	0.24
59	120.35	8.21	120.25	8.25	0.04
53	119.05	8.10	116.81	8.15	0.45
29	117.40	8.07	118.19	7.63	0.47
13	124.21	8.05	121.80	8.22	0.51
12	118.01	8.46	122.91	8.26	1.00

4.6 Resonance Assignment of Loop and Terminal Region

It is possible to use DCCICS to assign the non-helical regions of solid-state NMR spectra from aligned samples. This is especially valuable for those residues that

cannot be selectively labeled. The method relies on the MSHOT-Pi4 pulse sequence to improve the resolution of the PELF experiment. Previous DCCICS trials with SLF spectra resulted in incomplete assignments (data not shown) because the dipolar truncation effect (Gan, 2000) of rotating-frame SLF experiments often render those signals with small ^{1}H-^{15}N dipolar couplings at the similar dipolar couplings of ~0.3 kHz. As a result, one-to-one correlations cannot be easily established for signals from the same residues in spectra from flipped and unflipped bicelle samples. It also makes it difficult to resolve single signals with small heteronuclear dipolar couplings. Application of the improved PELF experiment addresses these issues, as shown in Figure 4.4.A and 4.4.B.

An important advantage of the application of DCCICS is that side chain amide groups can be readily distinguished (Figure 4.4.C and 4.4.D). These side chain signals, especially the GlnNε and the ArgNε with > 1 kHz dipolar couplings, can be easily misidentified as backbone amide signals. For example, after acquiring the SLF spectrum on selectively ^{15}N-Arg labeled MerF sample (Figure 4.2.N), an ArgNε peak at 1.5 kHz dipolar coupling (labeled in magenta in Figure 4.4) could be easily grouped together with the other two back bone amide peaks with large dipolar couplings (> 1 kHz). In this case, DCCICS analysis offers an unambiguous method of distinguishing backbone and side chain signals.

As shown in the preceding section, the currently existing error range of the DCCICS method makes it necessary to incorporate other information during resonance assignment. Here selective labeling with Ala, Leu, Tyr and Val was

necessary to identify most of the signals and assignments (labeled in cyan in Figure 4.4) in the terminal and loop regions of MerF, and their assignments were further verified in DCCICS analysis. After completing their assignment, DCCICS successfully provided additional assignments for the signals from D44, D69 and G41 (labeled yellow in Figure 4.4), which could not be selectively labeled. The combination of DCCICS, selective labeling and the improved PELF pulse sequence is able to provide complete assignments for all residues in the terminal and loop regions of MerF that are visible in solid-state NMR.

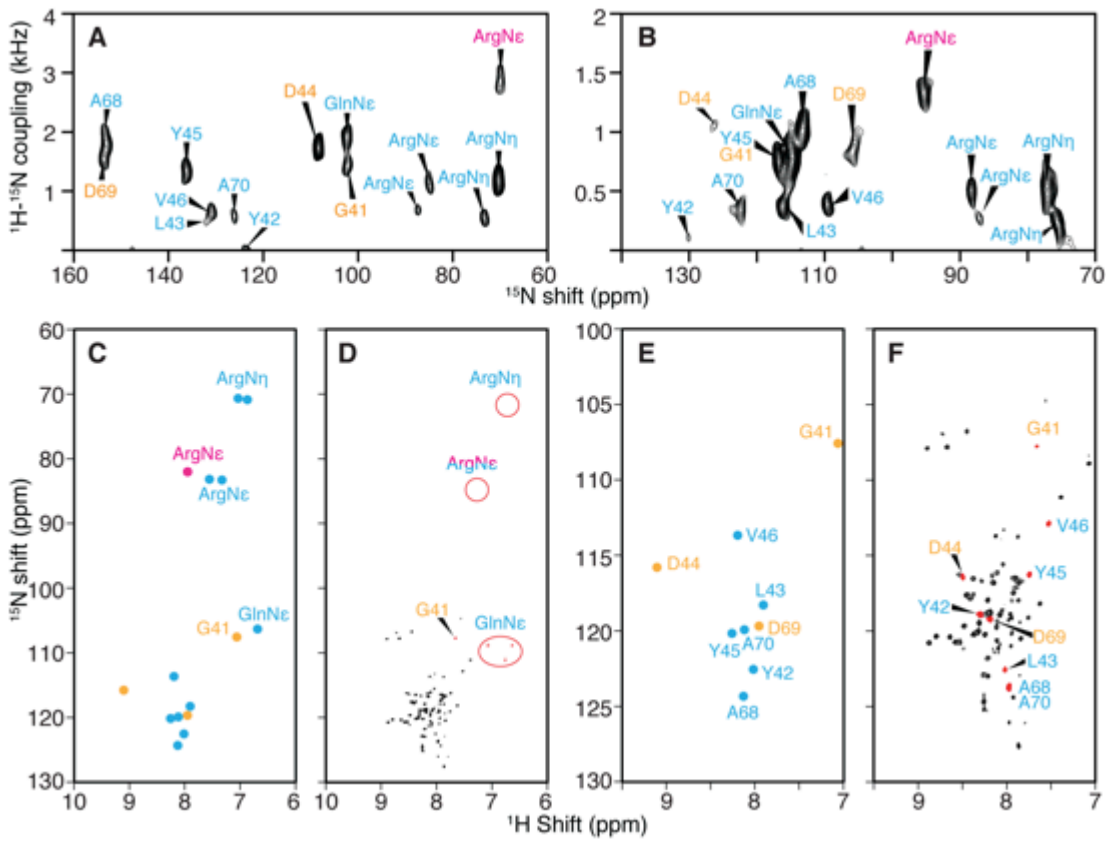

Figure 4.4. Resonance assignments of the terminal and loop regions of membrane proteins with irregular tertiary structure. PELF spectra of uniformly ^{15}N labeled MerF in flipped (A.) and unflipped (B.) bicelles. C. ^{1}H and ^{15}N isotropic chemical shifts calculated from the spectra in panels A. and B. and three-dimensional HETCOR/SLF spectra. D. Solution HSQC NMR spectrum and the chemical shift of side chains. E. and F. Expansion of the backbone amide resonance region of the spectra in panels C. and D. Those resonances whose assignments can be determined from selectively labeled spectra are labeled in cyan color. In this group, one of the ArgNε peak (magenta color) is an example that DCCICS analysis is crucial for avoiding its mis-assignment as a backbone amide resonance. The remaining resonances that could not be selectively labeled (yellow color) are successfully assigned by DCCICS analysis. A is reprinted from (Lu et al., 2012) after adding resonance assignments.

4.7 Transfer of Resonance Assignments from Rotational Alignment Solid-state NMR Spectra

Besides the DCCICS method, a straightforward way to transfer assignments from isotropic NMR spectra to anisotropic OS solid-state NMR spectra is through the frequency alignment of ^{1}H-^{15}N dipolar couplings to MAS solid-state NMR spectra, and it is enabled by the recent finding that dipolar couplings measured by MAS solid-state NMR under rotationally alignment condition have the same frequencies as those observed in spectra of aligned, stationary samples in OS solid-state NMR after being scaled by a known factor (Park et al., 2010a). Fig. 5 shows three examples where the individual assignment of residues in OS solid-state NMR spectra on selectively labeled samples can be made by aligning their dipolar coupling frequencies to those measured in the previously assigned RA solid-state NMR spectra of MerF (Lu et al., 2013a). The ^{1}H-^{15}N dipolar couplings measured from RA solid-state NMR spectra are equal to those measured from '"unflipped" bicelle samples by taking into account the established bicelle order parameter of ~0.8 (Sanders et al., 1994a) and the scaling factor of 0.5 due to the perpendicular alignment of the bilayer normals in the magnetic field.

T24, T40, V28 and V10 shown in Fig. 5 are all located near the end of a transmembrane helix, where PISA Wheel assignments often encounter difficulties because of ambiguity in determining the exact ending of the helix and possible deviations from an ideal helix in these regions. Here the assignment of these few key residues through dipolar coupling alignment in spectra of selectively labeled samples often provides a breakthrough in resolving the rest of the assignment of the specific amino acid type. The last example of I12 and I29 assignment further verifies the

isoleucine assignment made with combined DCCICS and PISA wheel method (Figure 4.3 and Table 4.1).

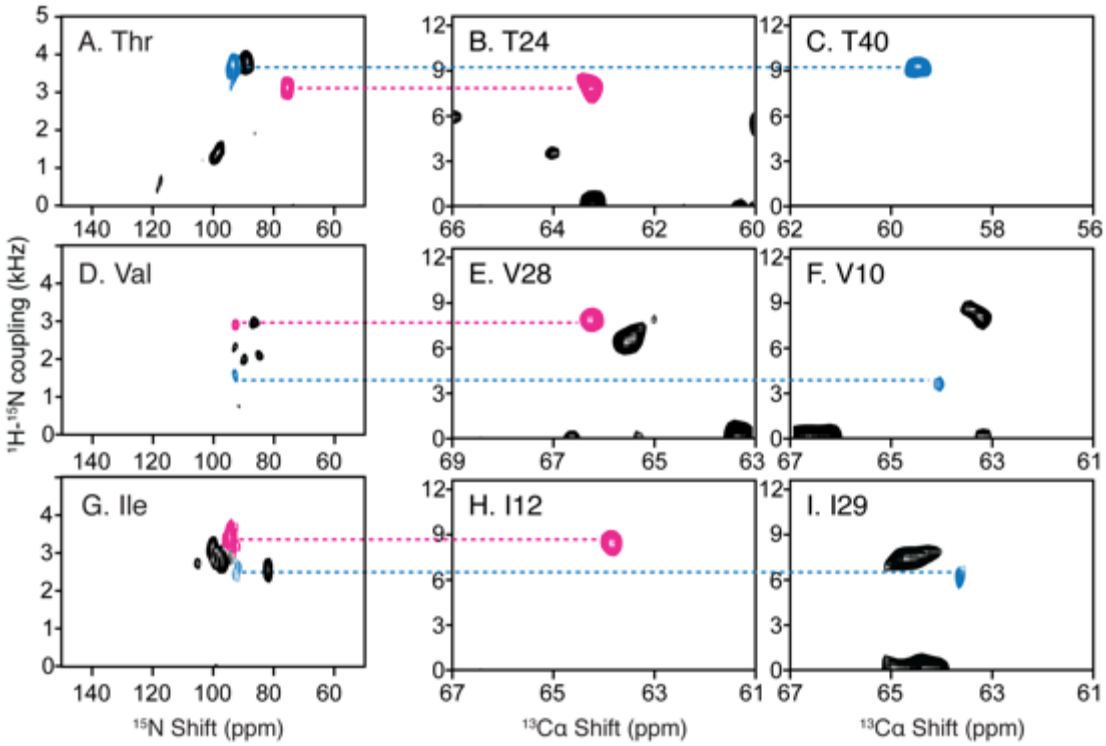

Figure 4.5. Resonance assignments of residues in OS solid-state NMR spectra utilizing the ^{1}H-^{15}N dipolar couplings measured in RA MAS solid-state NMR experiments. A. D. and G. Two-dimensional SLF spectrum of amino-acid-type selectively ^{15}N labeled MerF in 'unflipped' DMPC/DHPC bicelles. B. C. E. F. H. and I. Two-dimensional SLF spectral planes extracted from a three-dimensional HnNCa experiment, of which the third dimension is ^{15}N chemical shift (Lu et al., 2013a). The scales during aligning the ^{1}H-^{15}N dipolar couplings are adjusted for the scaling factors of the bicelles vs. liposomes (0.8) and of the alignment perpendicular to the magnetic field vs. rotational alignment parallel to the bilayer normal (0.5).

The dipolar coupling alignment method demonstrated above can be applied in a broader context before the full set of RA solid-state NMR spectra has been acquired and assigned. At least three three-dimensional spectra, HnNCa, HnNCo and HcCxCx, which require large amounts of signal averaging (Lu et al., 2013a). In one scenario, resonance assignments may have already been obtained for a protein under MAS

solid-state NMR experiments using conventional NCACX / NCOCX experiments (Pauli et al., 2001). In this case, only one additional experiment to recouple the dipolar coupling such as an HnNCa experiment (Lu et al., 2013a), is needed to enable a direct transfer of resonance assignment to OS solid-state NMR spectra. In another scenario, partial resonance assignments of MAS spectra may be available from a combination of selective labeling / unlabeling procedures (Banigan et al., 2013); and in this case, a dipolar recoupling dimension can be integrated into one experiment to bring the assignment information to OS solid-state NMR.

Notably, the frequency alignment can also be used to transfer resonance assignment in the reverse direction from OS solid-state NMR spectra to MAS solid-state NMR spectra in the same manner. This is an attractive option because of the economical use of ^{15}N-labeled amino acids and the high sensitivity of two-dimensional SLF experiments. Thus the amino-acid-type selective assignment information can be obtained efficiently in OS solid-state NMR, and subsequently to help resolve ambiguities encountered in assigning MAS solid-state NMR spectra.

4.8 Resonance assignment with ^{15}N/^{15}N Dilute Spin Exchange

It is difficult to transfer magnetization along the protein backbone atoms in OS solid-state NMR in the absence of uniform ^{13}C labeling. However, dilute spin exchange between proximate ^{15}N sites of sequential residues has been shown to be effective assignment method in some cases, (Cross et al., 1983; Marassi et al., 1999a), and more recently, through several alternative pulse sequences (Nevzorov, 2008; Tang

et al., 2012; Traaseth et al., 2010; Xu et al., 2008). The application of dilute spin diffusion methodology to membrane proteins has been limited by the low sensitivity of the experiments (Knox et al., 2010).

To apply dilute spin diffusion experiments to larger membrane protein, it is essential to simplify the spectrum using methods such as amino acid type selective labeling. Figure 4.6 demonstrates the application of two-dimensional dilute spin exchange ($^{15}N/^{15}N$) to selectively ^{15}N-Leu labeled MerF. There are three pairs of vicinal leucine residues in the sequence, residues 7 and 8, residues 30 and 31, and residues 47 and 48. Both Mismatched Hartmann-Hahn (MMHH) spin diffusion (Nevzorov, 2008) and proton-driven spin diffusion (Cross et al., 1983) have been used, and due to their different mechanisms, the intensities of cross peaks vary between the two types of spectra as expected. Two of the pairs, L7/8 and L47/48, are observed, while L30/31 cross peak cannot be observed because they have similar ^{15}N chemical shifts and the cross peak is buried under the axial peaks. Notably, the intensity of cross peaks scales down according to the square of the labeling efficiency. This aggravates the contrast between high-intensity diagonal peaks and low-intensity cross peaks in the spectra.

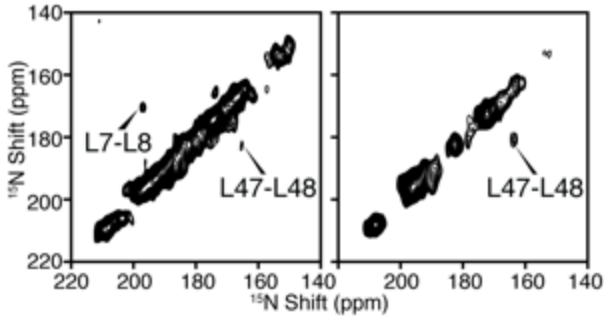

Figure 4.6. Two-dimensional $^{15}N/^{15}N$ dilute spin exchange spectra of selectively ^{15}N-Leu labeled MerF in DMPC/DHPC bicelles aligned with their bilayer normal parallel to the magnetic field. A. Spectrum obtained using Mismatched Hartmann-Hahn (MMHH) spin diffusion (Nevzorov, 2008). B. Spectrum obtained using Proton-driven Spin Diffusion (PDSD) (Cross et al., 1983).

4.9 Resonance Frequencies of MerF Protein

All the signals from the MerF residues that are immobile in the NMR time scale were assigned by this combinatorial set of resonance assignment methods described above. Signals from three N-terminal residues and 12 C-terminal residues are missing in OS solid-state NMR spectra of both uniformly and selectively 15N labeled samples, indicating that these residues are mobile. The resonance assignments and the anisotropic frequencies of the observed 64 residues are listed in Table 4.2.

Table 4.2. The resonance assignment of ^{1}H-^{15}N dipolar coupling, anisotropic ^{1}H chemical shift and anisotropic ^{15}N chemical shift frequencies of MerF in perpendicularly magnetically aligned bicelles. The ^{1}H-^{15}N dipolar coupling of residues G41-V46 and A68-A70 are from PELF spectrum, and all other data are from three-dimensional HETCOR/SLF spectrum.

Residue	^{1}H-^{15}N DC (kHz)	^{1}H CS (ppm)	^{15}N CS (ppm)
K5	2502	10.23	100.05
T6	3729	11.38	93.01
L7	2633	10.53	99.27
L8	3024	11.26	83.89
R9	1650	9.11	106.85

Table 4.2. The resonance assignment of ^{1}H-^{15}N dipolar coupling, anisotropic ^{1}H chemical shift and anisotropic ^{15}N chemical shift frequencies of MerF in perpendicularly magnetically aligned bicelles. The ^{1}H-^{15}N dipolar coupling of residues G41-V46 and A68-A70 are from PELF spectrum, and all other data are from three-dimensional HETCOR/SLF spectrum. (continued)

Residue	^{1}H-^{15}N DC (kHz)	^{1}H CS (ppm)	^{15}N CS (ppm)
V10	1833	10.20	93.94
S11	2673	11.29	81.12
I12	3672	10.31	93.62
I13	2934	10.21	105.44
G14	2106	11.55	78.28
T15	3910	11.00	93.15
T16	1548	8.88	102.88
L17	1575	10.09	90.50
V18	2124	10.53	84.83
A19	3413	11.35	87.94
L20	2442	10.25	101.01
S21	2110	10.14	88.62
S22	3615	11.33	85.81
F23	2476	10.42	101.41
T24	2574	10.59	78.74
V26	2088	10.64	88.61
L27	3081	10.78	84.16
V28	2865	10.61	91.48
I29	2560	9.69	92.23
L30	2757	11.65	82.60
L31	3514	10.91	87.44
G32	3313	11.20	85.03
V33	2454	9.99	92.43
V34	3076	11.46	86.38
G35	3868	11.69	87.50
L36	3033	11.59	96.26
S37	2382	10.46	92.49
A38	3738	11.35	82.87
L39	3732	11.49	94.61
T40	3766	10.67	92.96
G41	769	6.82	117.15
Y42	272	8.54	129.97
L43	160	8.56	121.56
D44	1066	10.33	127.70
Y45	769	9.34	116.45

Table 4.2. The resonance assignment of ^{1}H-^{15}N dipolar coupling, anisotropic ^{1}H chemical shift and anisotropic ^{15}N chemical shift frequencies of MerF in perpendicularly magnetically aligned bicelles. The ^{1}H-^{15}N dipolar coupling of residues G41-V46 and A68-A70 are from PELF spectrum, and all other data are from three-dimensional HETCOR/SLF spectrum. (continued)

Residue	^{1}H-^{15}N DC (kHz)	^{1}H CS (ppm)	^{15}N CS (ppm)
V46	385	9.18	109.74
L47	3181	10.08	95.36
L48	3117	10.74	101.90
A50	3519	10.88	80.27
L51	3732	11.49	94.61
A52	2559	10.63	95.68
I53	2638	11.06	81.12
F54	3468	11.19	87.31
I55	3196	11.45	99.57
G56	2515	11.18	76.88
L57	3144	12.12	80.17
T58	3904	10.73	90.82
I59	2759	9.85	95.95
Y60	2775	10.76	82.92
A61	3519	10.88	80.27
I62	3462	10.20	94.17
Q63	2559	10.63	95.68
R64	2575	10.46	85.74
K65	2759	9.85	95.95
R66	1650	9.11	106.85
Q67	3247	10.79	90.66
A68	1005	9.33	113.80
D69	862	9.23	106.19
A70	350	8.89	122.41

4.10 Discussion

A roadmap can be drawn to illustrate how these resonance assignment methods are closely connected and complementary to each other (Figure 4.7). Five complementary resonance assignment methods are shown. PISA wheel, Dipolar Wave or AssignFit analysis is the conventional choice, and remains as the main resonance

assignment method. Two other “information transfer” type of assignment methods, one introduced recently (Lu et al., 2011) and one in this article, bring in assignment information from isotropic NMR methods, including MAS solid-state NMR and solution NMR. The underlying motivation is to borrow the well-established assignment protocol in isotropic NMR methods and combine it with the advantage of OS solid-state NMR of preserving angular information of NMR observables. Two more categories of assignment method are listed, the spectroscopic method and sample preparation method. The former is an important focus of methodology development since the past few years. The latter is a category of many possible biochemical methods with site-directed mutagenesis and solid-phase peptide synthesis as two examples. The method is not demonstrated in this article but has been used in study of other membrane proteins (Gayen et al., 2013; Kochendoerfer et al., 2004). The strength of both methods are the low ambiguity, since a single known residue can be labeled or mutated. The disadvantages include the possibility of altering protein structure during mutagenesis, and the difficulties in synthesizing large hydrophobic polypeptides.

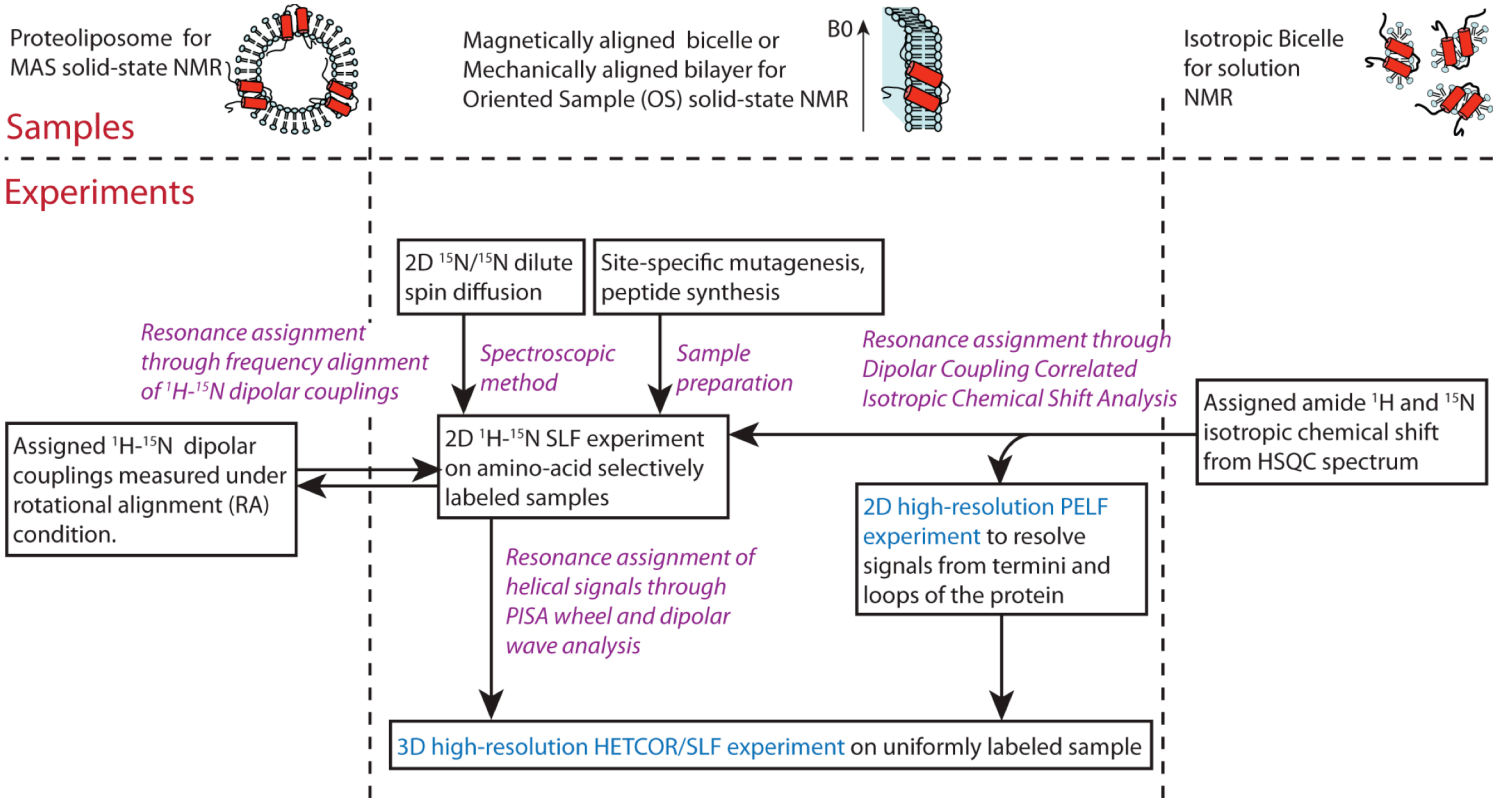

Figure 4.7. A roadmap for resonance assignments of membrane protein samples in OS solid-state NMR. Purple highlights the five complementary resonance assignment methods. Cyan highlights the experiments with significantly improved resolution by new pulse sequences.

It should be noted that the two "information transfer" methods (Figure 4.7) bring assignments from the samples where membrane proteins are in slightly different lipid mimetic environments than the one used in OS solid-state NMR. Recently, examples from several membrane proteins have shown that the different detergent/lipid environment could alter the structures of the proteins (Cross et al., 2013; Raschle et al., 2010; Zheng and Jia, 2013; Zhou and Cross, 2013; Zoonens et al., 2013). Here the two sources of information, the proteoliposome and the isotropic bicelles, need to be treated separately. Firstly, the transfer can be performed relatively safely between samples of proteoliposome and magnetically aligned bicelle. Aligned bicelle has been established as a lipid bilayer environment similar to that of proteoliposome (Warschawski et al., 2011). Additionally, the high ratio of long-chain lipid to short-chain detergent in aligned bicelle samples reduces the free detergent concentration, making them similar to proteoliposome. An example is that the structures of the truncated form of MerF (MerFt) determined in liposome and aligned bicelle have also shown high degree of agreement (Das et al., 2012). On the other hand, the resonance assignment transfer between isotropic bicelle or detergent micelle and the high-q magnetically aligned bicelles deserves more carefulness. In favorable cases, the protein structure may stay the same (Franzin et al., 2007); but in some other cases such as MerFt in aligned bicelle versus in sodium dodecyl sulfate (SDS) micelle (Howell et al., 2005; Lu et al., 2013a), the structure and dynamics can be largely different. In general, using the same set of lipid/detergent for aligned bicelle and isotropic bicelle can minimize the difference encountered in assignment transfer.

Previously, DCCICS has been successfully applied to Pf1 coat protein between q=0 DHPC micelle and q=3.2 DMPC/DHPC bicelle (Lu et al., 2011). Here, we have transferred assignments between q=0.1 and q=3.2 14-O-PC/6-O-PC bicelle, and as discussed in previous section, residues I12 and I13 have experienced larger differences in chemical shifts, presumably due to the different environments.

In conclusion, the combination of a set of resonance assignment methods demonstrated in this article will likely find its greatest utility in assigning the spectra of larger membrane proteins by OS solid-state NMR. The assigned NMR observables contain angular restraints that can be directly used to calculate the three-dimensional structure of membrane proteins.

Chapter 4, in full, is a reprint of the material “Resonance assignments of a membrane protein in phospholipid bilayers by combining multiple strategies of oriented sample solid-state NMR” as it appears in J. Biomol. NMR 58(1): 69-81 by Lu GJ, Opella SJ. The thesis author was the primary author of the paper.

Chapter 5. Motion-Adapted Pulse Sequences for Oriented Sample (OS) Solid-state NMR of Biopolymers

5.1 Abstract

One of the main applications of solid-state NMR is to study the structure and dynamics of biopolymers, such as membrane proteins, under physiological conditions where the polypeptides undergo global motions as they do in biological membranes. The effects of NMR radiofrequency irradiations on nuclear spins are strongly influenced by these motions. For example, we previously showed that the MSHOT-Pi4 pulse sequence yields spectra with resonance line widths about half of those observed using the conventional pulse sequence when applied to membrane proteins undergoing rapid uniaxial rotational diffusion in phospholipid bilayers. In contrast, the line widths were not changed in microcrystalline samples where the molecules did not undergo global motions. Here we demonstrate experimentally and describe analytically how some Hamiltonian terms are susceptible to sample motions, and it is their removal through the critical $\pi/2$ Z-rotational symmetry that confers the "motion adapted" property to the MSHOT-Pi4 pulse sequence. This leads to the design of separated local field pulse sequence "Motion-adapted SAMPI4" and is generalized to a approach for the design of decoupling sequences whose performance is superior in the presence of molecular motions. It works by cancelling the spin interaction by explicitly averaging the reduced Wigner matrix to zero, rather than utilizing the 2π

nutation to average spin interactions. This approach is applicable to both stationary and magic angle spinning solid-state NMR experiments.

5.2 Introduction

Compared to other methods of protein structure determination, such as X-ray crystallography and solution NMR spectroscopy, solid-state NMR spectroscopy offers several advantages for applications to membrane proteins; in particular, solid-state NMR enables them to be studied in their native environment of liquid crystalline phospholipid bilayers under physiological conditions (Opella, 2013; Park et al., 2012b; Zhou and Cross, 2013). This can be accomplished with protein-containing bilayer samples that are either magnetically or mechanically aligned relative to the magnetic field using Oriented Sample (OS) solid-state NMR or unoriented proteoliposomes samples using Rotationally Aligned (RA) solid-state NMR (Das et al., 2012). In the samples for both types of solid-state NMR experiments, the proteins undergo rapid rotational diffusion about the lipid bilayer normal (Cone, 1972). The motional averaging of powder patterns from dipole-dipole and chemical shift interactions were observed in some of the earliest high-resolution solid-state NMR experiments on polycrystalline samples (Mehring et al., 1971), in the ^{31}P NMR spectra of phospholipids (McLaughlin et al., 1975), and in the ^{13}C' NMR spectra of bacteriorhodopsin in bilayers (Lewis et al., 1985).

There are additional effects of motions on solid-state NMR spectra and radiofrequency pulses. Griffin and co-workers observed considerable line broadening

of resonances in Magic Angle Spinning (MAS) solid-state NMR spectra of bacteriorhodopsin undergoing rotational diffusion(Lewis et al., 1985), and further exploited the motion effects in multiple pulse sequence (Long et al., 1994). Similar effects have been observed in organic molecules, lipids, and membrane proteins (Bain, 2003; Fares et al., 2005; McMillan et al., 2003; Palmer et al., 1996; Reichert, 2005; Schmidt et al., 1986; Spiess, 1983; Suwelack et al., 1980). Meanwhile, interferences between rotor rotation and pulse sequence have been utilized in many recoupling methods in MAS solid-state NMR (Gullion and Schaefer, 1989; Oas et al., 1988; Raleigh et al., 1988).

Although the line broadening effects of molecular motions in solid-state NMR spectra been well characterized, there have been relatively few studies focused on reduction of such line broadening under similar circumstances. For example, we have demonstrated a pulse sequence for static OS solid-state NMR (Lu et al., 2012) that reduced ^{1}H line widths by more than a factor of two compared to previous versions of the pulse sequence in samples where the proteins undergo fast rotational diffusion. The narrow ^{1}H line widths enabled more accurate measurements of ^{1}H chemical shift frequencies in solid-state NMR heteronuclear correlation (HETCOR) spectra and ^{1}H-^{15}N dipolar couplings in proton-detected local field (PDLF) spectra. Furthermore, the relatively narrow ^{1}H resonance line widths enhanced the resolution in multidimensional spectra where the ^{1}H chemical shift was one of the frequency dimensions. Interestingly, substantial line narrowing was only observed for membrane proteins undergoing rapid rotational diffusion, but not for a static crystal sample of N-

acetylated leucine. The pulse sequence incorporated two modifications that combined to improve its performance. The first modification was to replace the continuous-wave heteronuclear decoupling with a single refocusing π pulse. While it had been shown by Waugh and co-workers that continuous wave decoupling is susceptible to interference from molecular motion (Rothwell and Waugh, 1981), by contrast a single π pulse is largely independent of any interference effects from protein motion, and the situation does not require further analysis. The second modification was the replacement of the frequency-switched Lee-Goldberg (FSLG) sequence by a Z-rotational magic sandwich sequence MSHOT-Pi4 for ^{1}H-^{1}H homonuclear decoupling.

In this article, the superior performance of MSHOT-Pi4 pulse sequence for membrane protein samples is explained and generalized, including (i) an analytical derivation that identifies the Hamiltonian terms susceptible to interference from sample motion and explains how they are eliminated in the MSHOT-Pi4 sequence; (ii) the critical role of the π/2 Z-rotational symmetry in MSHOT-Pi4 sequence and the experimentally verified prediction that MSHOT4 has better performance than either MSHOT2 sequence with π symmetry or MSHOT6 with π/3 symmetry; and (iii) the design and experimental spectra of a rotating-frame separated local field pulse sequence Motion-adapted SAMPI4 developed from MSHOT-Pi4 with reduced interference from sample motions.

5.3 Materials and Methods

The expression and purification of Pf1 coat protein has been described previously (Opella et al., 2008). Magnetically aligned bicelle samples of Pf1 coat protein were prepared with 6-O-PC (1,2-di-O-hexyl-*sn*-glycero-3-phosphocholine) and 14-O-PC (1,2-di-O-tetradecyl-*sn*-glycero-3-phosphocholine) as previously described (Lu et al., 2011; Opella et al., 2008; Park et al., 2010c).

^{15}N-detected solid-state NMR spectra were obtained on a 700 MHz Bruker Avance spectrometer equipped with a homebuilt ^{1}H/^{15}N double-resonance probe with a strip-shield to minimize heating of the lossy samples from high frequency, high power radiofrequency irradiations (Wu et al., 2009).

For the heternuclear correlation (HETCOR) spectra of the membrane-bound form of Pf1 coat protein (Figure 5.3), all experiments were performed with 71.4 kHz ^{1}H irradiation during t1 evolution and 50 kHz ^{1}H and ^{15}N irradiation elsewhere in the sequence. 3 cycles of SAMPI4 was used in the mixing period of the pulse sequence (Lu et al., 2012), which selectively transferred magnetization for resonances with ^{1}H/^{15}N dipolar couplings > 1 kHz. All three experiments had the same total t1 evolution time of 10.584 msec. Specifically, the spectra acquired with 2- and 4-phase cycled magic sandwich sequences (Figure 5.3.A and 5.3.B) had 64 complex t1 points with 168 μsec dwell times; and the one with a 6-phase cycled magic sandwich (Figure 5.3.C) had 43 complex t1 points with a 252 μsec dwell time. The number of scans was increased from 40 to 60 in the 6-phase cycled magic sandwich spectrum to approximately match the total acquisition time in order to obtain comparative signal to noise levels. All experiments were processed identically without apodization applied

in the indirect dimension where the ^{1}H line width was measured. The ^{1}H carrier frequency was 10.8 ppm with the water signal set at 4.7 ppm, and the ^{15}N carrier frequency was 117 ppm by referencing to solid ammonium sulfate.

The Motion-adapted SAMPI4 spectra were obtained on the membrane-bound form of Pf1 coat protein (Figure 5.4.A) using 49.0 kHz radiofrequency pulses on both ^{1}H and ^{15}N channels. 39 real t1 points were acquired in the indirect dimension giving a total evolution time of 4.65 msec for ^{1}H-^{15}N dipolar coupling. As the control experiment (Figure 5.4.B), the original SAMPI4 pulse sequence (Nevzorov and Opella, 2007) was used with two dwells in each increment. 50 kHz radiofrequency pulse, 40 real t1 points and the total t1 evolution time of 4.68 msec were used. The scaling factors for the two sequences are slightly different, as described in the Results and Discussion section. The ^{1}H carrier was at ~9 ppm and ^{15}N carrier at ~120 ppm. The data processing and line width measurements were performed with NMRDraw (Delaglio et al., 1995) and Sparky (Goddard and Kneller, 2008).

The simulations were carried out with SIMPSON 2.0 (Bak et al., 2000). The four-spin system used in the simulations included three ^{1}H and one ^{15}N nuclei. The three ^{1}H nuclei had 10 kHz dipolar couplings between each pair, but only one of them had a 5 kHz dipolar coupling to the ^{15}N atom. This same ^{1}H atom had 1 kHz chemical shift offset with respect to the ^{1}H carrier, while the other two were on resonance. The ^{1}H chemical shift was monitored in the indirect dimension and the magnetization was "transferred" for ^{15}N detection through three SAMPI4 periods with 50 kHz irradiation, as in the HETCOR experiments. The ^{1}H irradiation in the indirect dimension was set

to 100 kHz for the B_1 field of magic sandwich sequence and the B_{eff} field of the Lee-Goldberg sequence. The sample rotation was set at various frequencies indicated on Figure 3, and the angle between the rotational axis and the magnetic field was chosen to be 80°. The time step over which the Hamiltonian was considered time independent was set at 0.5 μsec.

5.4. Theory of Magic Sandwich and Lee-Goldberg Decoupling for Static Sample

We start by formulating the Lee-Goldberg and magic sandwich homonuclear decoupling sequences without molecular motion with spherical tensor operators. Two different mechanisms of averaging homonuclear dipolar coupling are identified; the setting of the reduced Wigner matrices to zero, and the 2π pulse nutation averaging of a spin interaction. We then consider pulse sequences in the presence of molecular motion, where the ineffectiveness of the second mechanism is demonstrated. Finally, the discussion is extended to rotating-frame separated local field experiments where both homonuclear and heteronuclear dipolar couplings are present.

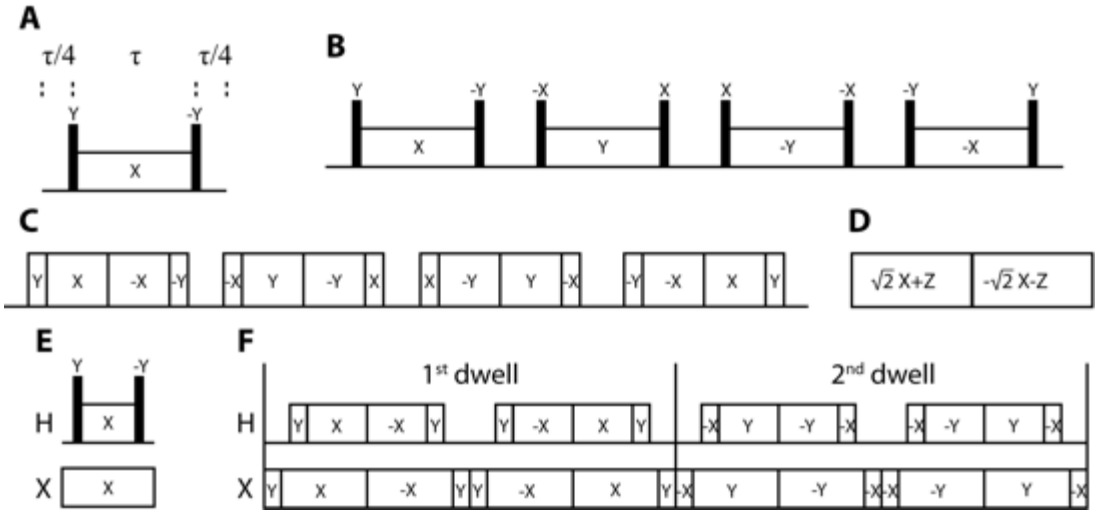

Figure 5.1. Pulse sequence elements discussed in the chapter. A. Basic magic sandwich sequence element. B. Basic element of MSHOT-4. C. Experimental implementation of MSHOT-4 (MSHOT-Pi4 sequence). D. Frequency-switched Lee-Goldberg sequence element. E. Separated local field sequence with basic magic sandwich elements. F. Motion-adapted SAMPI4 sequence, where the first and second dwells are shown, and the next two dwells have all pulse phases increase by 180° and so forth.

For the case of two dipolar-coupled like spins, such as two ^{1}H nuclei, in the usual rotating frame in a high magnetic field (Zeeman interaction representation), the Hamiltonian of the system under radiofrequency (rf) irradiation can be written as

$$H(t) = H_{rf}(t) + H_D(t). \qquad \text{Eq. 5.1}$$

Using spherical tensor operator notations, the homonuclear dipolar coupling under high magnetic field takes the form (Mehring and Weberruss, 2001)

$$H_D(t) = \sqrt{6}\omega_D T_{20}^{AB}, \qquad \text{Eq. 5.2}$$

where ω_D and T_{20}^{AB} are the spatial and spin part of the dipolar coupling Hamiltonian, respectively. The conversions between spherical tensor operators and the Cartesian spin operators are

$$T_{20}^{AB} = \frac{1}{\sqrt{6}}(3I_{Az}I_{Bz} - \vec{I}_A \cdot \vec{I}_B), \quad \text{Eq. 5.3a}$$

$$T_{2,\pm1}^{AB} = \mp\frac{1}{2}(I_{Az}I_B^{\pm} + I_A^{\pm}I_{Bz}), \quad \text{Eq. 5.3b}$$

$$T_{2,\pm2}^{AB} = \frac{1}{2}I_A^{\pm}I_B^{\pm}, \quad \text{Eq. 5.3c}$$

$$T_{10}^{A} = I_{Az}, \quad \text{Eq. 5.3c}$$

$$T_{1,\pm1}^{A} = \mp\frac{1}{\sqrt{2}}I_A^{\pm}. \quad \text{Eq. 5.3e}$$

In a basic magic sandwich period (Figure 5.1.A) (Rhim et al., 1971), the central spin-lock period is flanked by a pair of ideal delta 90° Y and –Y pulses. The overall effect of the radiofrequency pulses can be described as a rotation with the Euler angles

$$R(\omega_1 t, \frac{\pi}{2}, 0) = \exp\{-i\omega_1 t \hat{I}_z\}\exp\{-i\frac{\pi}{2}\hat{I}_y\}, \quad \text{Eq. 5.4}$$

where ω_1 is the irradiation frequency during the spin-lock period. The rotation transforms the spin part of the dipolar coupling Hamiltonian through the transformation equation:

$$R(\omega_1 t, \frac{\pi}{2}, 0)T_{20}^{AB}R^{-1}(\omega_1 t, \frac{\pi}{2}, 0) = \sum_{m=-2}^{+2} T_{2m}^{AB}\exp\{-im\omega_1 t\}d_{m0}^2(\frac{\pi}{2}), \quad \text{Eq. 5.5}$$

where $d_{m0}^2(\theta)$ is the reduced Wigner matrix element. The time propagator can then be approximated using Average Hamiltonian Theory with stroboscopic observation from time t_0 to $t_0 + \tau$,

$$U(t_0 + \tau) \cong U_{rf}(t_0, t_0 + \tau)\exp\{-i\overline{H}\tau\}, \quad \text{Eq. 5.6}$$

where $\overline{H}$ is the average Hamiltonian. With the central spin lock set to be $\tau = (2\pi / \omega_1)$, $U_{rf}(t_0, t_0 + \tau) = \exp\{-i\omega_1 \tau \hat{I}_z\} = 1$ and therefore the radiofrequency pulses do not cause a net rotation of the spins. The first order term of $\overline{H}$ under the Magnus expansion can be separated into five components according to the "m" values in the spherical tensors:

$$\overline{H}^{(1)} = \overline{H}^{(1)}_{m=0} + \overline{H}^{(1)}_{m=+1} + \overline{H}^{(1)}_{m=-1} + \overline{H}^{(1)}_{m=+2} + \overline{H}^{(1)}_{m=-2}, \qquad \text{Eq. 5.7}$$

$$\overline{H}^{(1)}_{m=0} = \frac{1}{\tau}\int_{t_0}^{t_0+\tau} dt\sqrt{6}\omega_D T^{AB}_{20} d^2_{00}(\frac{\pi}{2}), \qquad \text{Eq. 5.8a}$$

$$\overline{H}^{(1)}_{m=\pm1} = \frac{1}{\tau}\int_{t_0}^{t_0+\tau} dt\sqrt{6}\omega_D T^{AB}_{2,\pm1} d^2_{\pm10}(\frac{\pi}{2})\exp\{-i \pm \omega_1 t\}, \qquad \text{Eq. 5.8b}$$

$$\overline{H}^{(1)}_{m=\pm2} = \frac{1}{\tau}\int_{t_0}^{t_0+\tau} dt\sqrt{6}\omega_D T^{AB}_{2,\pm2} d^2_{\pm20}(\frac{\pi}{2})\exp\{-i \pm 2\omega_1 t\}. \qquad \text{Eq. 5.8c}$$

In the rigid lattice limit or the fast motion limit, where the frequency of the motion is much faster than $1/\tau$, the spatial part of the dipolar coupling Hamiltonian, ω_D, is time independent. In the next section (Section 5.5), the case when the frequency of motion is near the time scale of $1/\tau$ will be discussed. Here we treat ω_D as a constant, and evaluate the five components of the first order average Hamiltonian.

The m=±1 and m=±2 components both vanish to zero, but by two different mechanisms. The m=±1 components are zero due to the corresponding reduced Wigner matrix $d^2_{\pm1,0}(\frac{\pi}{2}) = \mp\sqrt{\frac{3}{2}}\sin\frac{\pi}{2}\cos\frac{\pi}{2} = 0$. The elimination of m=±2 components, however, is not because of the reduced Wigner matrix, which is $d^2_{\pm2,0}(\frac{\pi}{2}) = \sqrt{\frac{3}{8}}\sin^2\frac{\pi}{2} = \sqrt{\frac{3}{8}}$; instead, it is due to the term $\exp\{-i \pm 2\omega_1 t\}$ integrated to zero when $\tau = (2\pi/\omega_1)$. Notably, it is the difference between these two mechanisms of

averaging that will influence the pulse sequence performance when molecular motion is present, as discussed in Section B. Only the time-invariant m=0 component survives, and since $d^2_{00}(\frac{\pi}{2}) = \frac{1}{2}(3\cos^2\frac{\pi}{2} - 1) = -\frac{1}{2}$, it gives $\overline{H}^{(1)} = -\frac{1}{2}(\sqrt{6}\omega_D T^{AB}_{20}) = -\frac{1}{2}H_D$. The magic sandwich sequence removes the homonuclear dipolar coupling by setting the total radiofrequency-free time to be $\frac{1}{2}\tau$. In practice, the magic sandwich is often designed with reflection symmetry (Takegoshi and McDowell, 1985) and is capable of canceling higher order Hamiltonians. Here we limit our discussion to the first order average Hamiltonian.

Homonuclear decoupling under the Lee-Goldberg condition (Figure 5.1.D) (Goldburg and Lee, 1963; Lee and Goldburg, 1965) can be evaluated using the same sets of formulae. The spin-lock pulse at the magic angle θ_m can be described as a rotation with the Euler angles

$$R(\omega_{eff}t,\theta_m,0) = \exp\{-i\omega_{eff1}t\hat{I}_z\}\exp\{-i\theta_m\hat{I}_y\}, \qquad \text{Eq. 5.9}$$

where ω_{eff} is the frequency of the effective field resulting from both B_1 field and offset. The resulting first order average Hamiltonian of homonuclear dipolar coupling is

$$\overline{H}^{(1)} = \frac{1}{\tau}\int_{t_0}^{t_0+\tau} dt\sqrt{6}\omega_D \sum_{m=-2}^{+2} T^{AB}_{2m}\exp\{-im\omega_{eff}t\}d^2_{m0}(\theta_m), \qquad \text{Eq. 5.10}$$

$$\overline{H}^{(1)}_{m=0} = \frac{1}{\tau}\int_{t_0}^{t_0+\tau} dt\sqrt{6}\omega_D T^{AB}_{20} d^2_{00}(\theta_m), \qquad \text{Eq. 5.11a}$$

$$\overline{H}^{(1)}_{m=\pm1} = \frac{1}{\tau}\int_{t_0}^{t_0+\tau} dt\sqrt{6}\omega_D T^{AB}_{2,\pm1} d^2_{\pm10}(\theta_m)\exp\{-i\pm\omega_{eff}t\}, \qquad \text{Eq. 5.11b}$$

$$\overline{H}^{(1)}_{m=\pm2} = \frac{1}{\tau}\int_{t_0}^{t_0+\tau} dt\sqrt{6}\omega_D T^{AB}_{2,\pm2} d^2_{\pm20}(\theta_m)\exp\{-i\pm2\omega_{eff}t\}. \qquad \text{Eq. 5.11c}$$

Out of the five reduced Wigner matrices, only $d^2_{00}(\theta_m) = \frac{1}{2}(3\cos^2\theta_m - 1) = 0$. Consequently, only the m=0 component is averaged to zero through the first mechanism, and the other four components m=±1 and m=±2 are averaged through the second mechanism.

In summary, two different mechanisms of eliminating homonuclear dipolar coupling are distinguished, one by explicitly setting the reduced Wigner matrixes to zero, and the other by performing a 2π nutation on the spin interaction. The magic sandwich and Lee-Goldberg decoupling sequences eliminate the homonuclear dipolar coupling by both mechanisms for different "m" components. As shown below, the second mechanism becomes ineffective in the presence of molecular motion, and this distinguishes the pulse sequence performance when applied to membrane proteins undergoing fast rotational diffusion about the bilayer normal.

5.5 Theory of Pulse Sequence Performance under Molecular Motion and the MSHOT-Pi4 Sequence

In a molecule undergoing rotational motion at a frequency ω_r, the spatial part of the dipolar coupling Hamiltonian $\omega_D(t)$ becomes time dependent. Since $\omega_D(t)$ is a

second-rank tensor operator, it can be written as a linear combination of the dipolar couplings tensors (A_{2p}) in the molecular frame:

$$\omega_D(t) = \sum_{p=-2}^{+2} A_{2p} \exp\{-ip\omega_r t\} d^2_{p0}(\beta). \qquad \text{Eq. 5.12}$$

Consequently, the time-dependent component $\exp\{-ip\omega_r t\}$ interferes with the pulse nutation in the calculation of an average Hamiltonian (Equation 5.8 and 5.11). In the fast motion regime ($\omega_r >> \omega_1$), the interference is negligible. However, when $\omega_r \approx \omega_1$ and/or $\omega_r \approx 2\omega_1$, the second mechanism of averaging homonuclear dipolar coupling becomes ineffective, since the integration of $\int_{t_0}^{t_0+\tau} dt \exp\{-im\omega_1 t\}\exp\{-ip\omega_r t\}$ is non-zero when $m\omega_1 + p\omega_r \approx 0$. As a result, the $m = \pm 2$ terms in magic sandwich decoupling (Equation 5.8c) and both $m = \pm 1$ and $m = \pm 2$ terms in Lee-Goldberg decoupling (Equation 5.11b and 5.11c) become non-zero over time τ, leaving residual homonuclear dipolar coupling in the first-order average Hamiltonian. Table 5.1 summarizes these possible non-zero terms. These two conditions are analogous to the single-quantum rotary resonance (Oas et al., 1988) and the double-quantum HORROR condition (Nielsen et al., 1994), with the difference being that (i) the angle β is not at magic angle, and (ii) ω_r represent a random molecular motion rather than a specifically set rotor speed.

Table 5.1. The list of undesirable first-order average Hamiltonian terms generated from the interference between sample rotational motion and radiofrequency (rf) pulse sequence. [a] ω_r is the simplified rotational diffusion frequency of the membrane protein sample, and ω_1 is the frequency of the rf pulses. [b]m is the spin-part of the Hamiltonian and is related to the rf pulse frequency. p is the space-part of the Hamiltonian and is related to the rotational frequency. [c]These terms would disappear for ideal perpendicularly aligned bicelles, i.e. the rotational axis is perpendicular to the magnetic field and there is no "wobbling" motion of the bicelle.

		$\omega_r = 2\omega_1$ [a]	$\omega_r = \frac{1}{2}\omega_1$	$\omega_r = \frac{1}{2}\omega_1$
Lee-Goldberg decoupling		{m=±2, p=±1} [b,c]	{m=±1, p=±1} [c], {m=±2, p=±2}	{m=±1, p=±2}
Magic sandwich decoupling		{m=±2, p=±1} [c]	{m=±2, p=±2}	None
MSHOT-Pi4		None	None	None
SAMPi4	Homodipole	{m=±2, p=±1} [c]	{m=±2, p=±2}	None
	Heterodipole	{m=±2, p=±1} [c]	{m=±2, p=±2}	None
Motion-adapted SAMPi4	Homodipole	None	None	None
	Heterodipole	None	None	None

Figure 5.1.B shows one of the magic sandwich variants with Z-rotational symmetry (MSHOT) sequences, MSHOT-4, which has 4 steps of Z-rotation and consequently a phase difference of $\pi/2$ among them. The MSHOT-Pi4 sequence (Lu et al., 2012) is the practical implementation of MSHOT-4. The MSHOT pulse sequence, which stands for magic sandwich with high order truncation, was initially introduced as a way to eliminate higher order average Hamiltonians (Hohwy and Nielsen, 1997). Due to the special property of tensor operators, Z-rotation of the pulse phase was shown to modify the average Hamiltonian by adding only a phase factor $e^{-im\phi}$ to the Hamiltonian. For example, the second block in MSHOT-4 has a phase shift of $\phi = +\pi/2$ along the Z axis, and it results in $e^{-im\phi} = -1$ for $m = \pm 2$

components. The $m = \pm 2$ components in the second block thus become the inverse of the $m = \pm 2$ components in the first block:

$$\overline{H}^{(1)}_{m=\pm 2,\phi=\pi/2} = -\frac{1}{\tau}\int_{t_0}^{t_0+\tau} dt\sqrt{6}\omega_D T^{AB}_{2,\pm 2} d^2_{\pm 20}(\frac{\pi}{2})\exp\{-i \pm 2\omega_1 t\}, \qquad \text{Eq. 5.13}$$

If $\omega_D(t)$ takes the form shown in Equation 12 and is assumed to have the same constant ω_r frequency as the first block, then these two blocks cancel, averaging the $m = \pm 2$ components to zero. Thus, all first-order homonuclear dipolar coupling terms are fully averaged in a full MSHOT cycle. Notably, in an experimental situation $\omega_D(t)$ is more complicated than that expressed in Equation 5.12, since the molecular motion is random rather than at a constant frequency, ω_r. Therefore, $m = \pm 2$ components cannot be fully averaged to zero, and the interference between rf pulses and molecular motions can never be fully eliminated. A more rigorous quantum mechanical treatment of random molecular motion may involve the use of stochastic Liouville equation (Ghose, 2000; Kubo, 1969; Levitt and Di Bari, 1992), however, in this article we use the simpler average Hamiltonian theory aiming to differentiate pulse sequences' susceptibility to molecular motion.

Notably, those MSHOT sequences that do not possess $\pi/2$ Z-rotations would not be able to cancel the $m = \pm 2$ components, and therefore would still be subject to some interference by molecular motion. Examples include MSHOT-2 and MSHOT-6, and experimental spectra from these sequences are included in the Results and Discussion section. The results in MSHOT-6 are particularly interesting; from the original derivation of Z-rotational sequence, it is capable of canceling residual

homonuclear dipolar coupling to the same order as MSHOT-4 (Hohwy and Nielsen, 1997) and should perform equally well. However, we predict that MSHOT-4 is superior to MSHOT-6 in the presence of molecular motions.

In the case of Lee-Goldberg decoupling, both m=±1 and m=±2 components become non-zero in the presence of molecular motion. The situation is not alleviated with the reflection symmetry that is usually imposed in frequency-switched Lee-Goldberg (FSLG) (Bielecki et al., 1989) (Figure 5.1.D) or phase-modulated Lee-Goldberg (PMLG) (Vinogradov et al., 1999) methods. The two symmetrical parts of the sequence correspond to the rotation of $R(\omega_{eff}t,\theta_m,0)$ and $R(-\omega_{eff}t,\theta_m,0)$, and they lead to the same reduced Wigner matrices that cannot cancel each other. As a consequence, both FSLG and PMLG remain susceptible to interferences from molecular motion.

5.6 Theory of Rotating-frame Separated Local Field Experiment under Molecular Motion

Polarization Inversion Spin Exchange at the Magic Angle (PISEMA) (Wu et al., 1994) is distinguished from the original laboratory-frame separated local field experiments, because the magnetization is locked in the rotating frame by the radio-frequency irradiation, and the heteronuclear dipolar coupling is encoded in the flip-flop Hamiltonian $I^+S^- + I^-S^+$ rather than the laboratory-frame term I_zS_z. The rotating-frame separated local field experiments are generally found to give higher resolution, because of $T_{1\rho}$ being longer than T_2 and the dipolar truncation effect (Gan, 2000); as a

result, they are widely used and many variants have been designed since the original version of PISEMA was introduced, for example, SAMPI4 (Nevzorov and Opella, 2007) and HIMSELF (Dvinskikh et al., 2006).

The basic magic sandwich element in SAMMY (Nevzorov and Opella, 2003a) or SAMPI4 (Nevzorov and Opella, 2007) with two unlike spins A and B is shown in Figure 5.1.E. The heteronuclear dipolar coupling $H_{IS}(t)$ is $2\omega_{IS}(t)T_{10}^{A}T_{10}^{B}$ with T_{10}^{A} and T_{10}^{B} being the first rank spherical tensor operator of spins A and B, respectively. During the central spin-lock period, $H_{IS}(t)$ evolves at the exact Hartmann-Hahn match condition and results in the following first order average Hamiltonian

$$\overline{H}^{(1)} = \frac{1}{\tau}\int_{t_0}^{t_0+\tau} dt \;\; 2\omega_D \;\; \{R(\omega_1 t,\frac{\pi}{2},0)T_{10}^{A}R^{-1}(\omega_1 t,\frac{\pi}{2},0)\} \;\; \{R(\omega_1 t,\frac{\pi}{2},0)T_{10}^{A}R^{-1}(\omega_1 t,\frac{\pi}{2},0)\}$$
$$= \frac{1}{\tau}\int_{t_0}^{t_0+\tau} dt \;\; 2\omega_D \;\; \sum_{m=-1}^{+1}\sum_{n=-1}^{+1} T_{1m}^{A}\exp\{-im\omega_1 t\}d_{m0}^{2}(\frac{\pi}{2})T_{1m}^{B}\exp\{-in\omega_1 t\}d_{m0}^{2}(\frac{\pi}{2}) \qquad \text{Eq. 5.14}$$

where reduced Wigner matrix elements are $d_{00}^{1}(\frac{\pi}{2}) = \cos\frac{\pi}{2} = 0$ and $d_{\pm1,0}^{1}(\frac{\pi}{2}) = \mp\frac{1}{\sqrt{2}}\sin\frac{\pi}{2} = \mp\frac{1}{\sqrt{2}}$. Different from the single spin situation, the sum of 'm' and 'n' values is used here to categorize the average Hamiltonian:

$$\overline{H}_{m+n=0}^{(1)} = -\frac{1}{\tau}\int_{t_0}^{t_0+\tau} dt \;\; \omega_D\{T_{1,+1}^{A}T_{1,-1}^{B} + T_{1,-1}^{A}T_{1,+1}^{B}\}, \qquad (15a)$$

$$\overline{H}_{m+n=+2}^{(1)} = \frac{1}{\tau}\int_{t_0}^{t_0+\tau} dt \;\; \omega_D T_{1,+1}^{A}T_{1,+1}^{B}\exp\{-i2\omega_1 t\}, \qquad (15b)$$

$$\overline{H}_{m+n=-2}^{(1)} = \frac{1}{\tau}\int_{t_0}^{t_0+\tau} dt \;\; \omega_D T_{1,-1}^{A}T_{1,-1}^{B}\exp\{i2\omega_1 t\}. \qquad (15c)$$

$$\overline{H}_{m+n=\pm1}^{(1)} = 0 \qquad (15d)$$

With $\tau = 2\pi/\omega_1$ the double-quantum m+n=±2 terms vanish through the first mechanism, i.e. $\exp\{-i \pm 2\omega_1 t\}$ integrates to zero. Only the zero-quantum m+n=0 component survives and gives rise to the familiar flip-flop Hamiltonian $\overline{H}^{(1)} = \frac{\omega_D(t)}{2}(I^+S^- + I^-S^+)$. In the presence of molecular motion, however, m+n=±2 would not vanish since $\exp\{-ip\omega_r t\}$ interferes with the averaging of the $\exp\{-i \pm 2\omega_1 t\}$ term.

Similarly, a motion-adapted version of SAMPI4 sequence can be designed by rotating the pulse sequence phase of both nuclei by $\pi/2$ across the four quadrants. Figure 5.1.F shows a practical example of this Motion-adapted SAMPI4 pulse sequence. It can be readily shown that $e^{-im\phi}e^{-in\phi} = -1$ for all the m+n=±2 terms after $\phi = \pi/2$ rotation, while the m+n=0 term remains the same. Since the nucleus I (^{1}H) now experiences the exact same sequence as MSHOT-PI4, the cancellation of ^{1}H-^{1}H homonuclear dipolar coupling should be also motion adapted. However, in our initial testing, the performance of the sequence is similar to the original SAMPI4 sequence.

5.7 Relevance to the Rotational Diffusion of Membrane Proteins in Aligned Bicelle

The principle of motion interference is highly relevant to acquiring high-resolution NMR spectra of membrane proteins and other biopolymers, many of which undergo global reorientation about a single axis. First, the rotational diffusion of the protein about the bilayer normal has been measured to occur at ~ 10^6 Hz by NMR and other techniques (Fooksman et al., 2007; Guigas and Weiss, 2006; Lewis et al., 1985;

Park et al., 2006b), which is close to the relevant frequencies generated by the radiofrequency irradiations in the pulse sequences (40kHz~200kHz). Secondly, any types of motions that produce a spatial rotational factor $\exp\{-im\omega_r t\}$ have the potential to interfere with the pulse sequence. Therefore, many other types of motion, especially local segmental motions, can be translated into rotational motion of membrane proteins and analyzed with the same method.

In the specific case of a membrane protein, the rotational diffusion always occurs about the axis defined by the bilayer normal. For magnetically aligned bicelles, the rotational axis would exactly align either parallel or perpendicular to the direction of the magnetic field. This results in $\beta = 0$ for the parallel bicelle and $\beta = \pi/2$ for the perpendicular bicelle under ideal situations. In Equation 5.12, $\omega_D(t) = \sum_{p=-2}^{+2} A_{2p} \exp\{-ip\omega_r t\} d^2_{p0}(\beta)$, where $d^2_{\pm 1,0}(\beta) = \mp\sqrt{\frac{3}{2}} \sin\beta\cos\beta$ and $d^2_{\pm 2,0}(\beta) = \sqrt{\frac{3}{8}} \sin^2\beta$. Consequently, all the time-dependent parts of $\omega_D(t)$ ($p = \pm 1$ and $p = \pm 2$ components) vanish for a parallel bicelle, and $p = \pm 1$ but not $p = \pm 2$ components vanish for a perpendicular bicelle. Therefore, motion in an ideal parallel bicelle does not interfere with the pulse sequence performance; and in an ideal perpendicular bicelle, motion only interferes through $p = \pm 2$ components. In practical situations, however, "wobbling" motions of the bicelle often exist and could cause the fluctuation of the rotational diffusion axis. Consequently, the deviation of β angle away from 0 and $\pi/2$ re-introduces the time-dependent components as well as the motion interference to pulse sequence performance. For magnetically aligned bicelles,

the existence of the "wobbling" motion can be quantified by the order parameter, which is usually less than unity (~ 0.85) (Prosser et al., 1998; Sanders et al., 1994a). By contrast, in mechanically aligned bilayers, the order parameter is usually equal to 1.0. It could suggest that the "wobbling" of the rotational diffusion axis is minimal in mechanically aligned bilayers, which therefore is potentially less susceptible to motion interference.

5.8 Numerical Simulation of ^{1}H Line Width at Various Sample Rotation Rates

Three pulse sequences are compared, including (i) the conventional HETCOR sequence FSLG-CW (Nevzorov and Opella, 2007; Ramamoorthy et al., 1995), which uses FSLG for ^{1}H-^{1}H homonuclear decoupling and continuous wave (CW) irradiation for ^{1}H-^{15}N heteronuclear decoupling, and (ii) the recently described MSHOT-Pi4/Pi (Lu et al., 2012). The MSHOT-Pi4 sequence (Figure 5.1.C) was the practical implementation of the basic MSHOT-4 sequence with the added inverse spin-lock components for reducing the effect of radiofrequency field inhomogeneity and the finite pulse compensation scheme adapted from the SAMPI4 sequence. The MSHOT-Pi4 sequence on the ^{1}H channel was combined with the single π pulse on the ^{15}N channel, and thus the total sequence was named MSHOT-Pi4/Pi. In addition, the third sequence, a two-phase Z-rotational MSHOT (MSHOT-2), is simulated as well; the only difference between it and the MSHOT-Pi4 sequence is that pulse phases are only X and –X, rather than being cycle through all four quadrants. The two phase cycled magic sandwich sequence was first described in the TREV-8 sequence (Takegoshi and

McDowell, 1985) and the current version MSHOT-2 sequence uses the same finite pulse compensation scheme as SAMPI4 (Nevzorov and Opella, 2007) and MSHOT-Pi4 (Lu et al., 2012).

Numerical simulations of the effects of motion on the radiofrequency irradiations were performed with the *SIMPSON* package (Bak et al., 2000) by setting the sample to rotate at various constant speeds (Figure 5.2). Two-dimensional ^{1}H-^{15}N HETCOR spectra were simulated for three dipolar coupled ^{1}H and one ^{15}N spins, and the indirect dimension was used to analyze the performance of the sequences, which is similar to the strategy previously used to develop the MSHOT-Pi4/Pi pulse sequence (Lu et al., 2012).

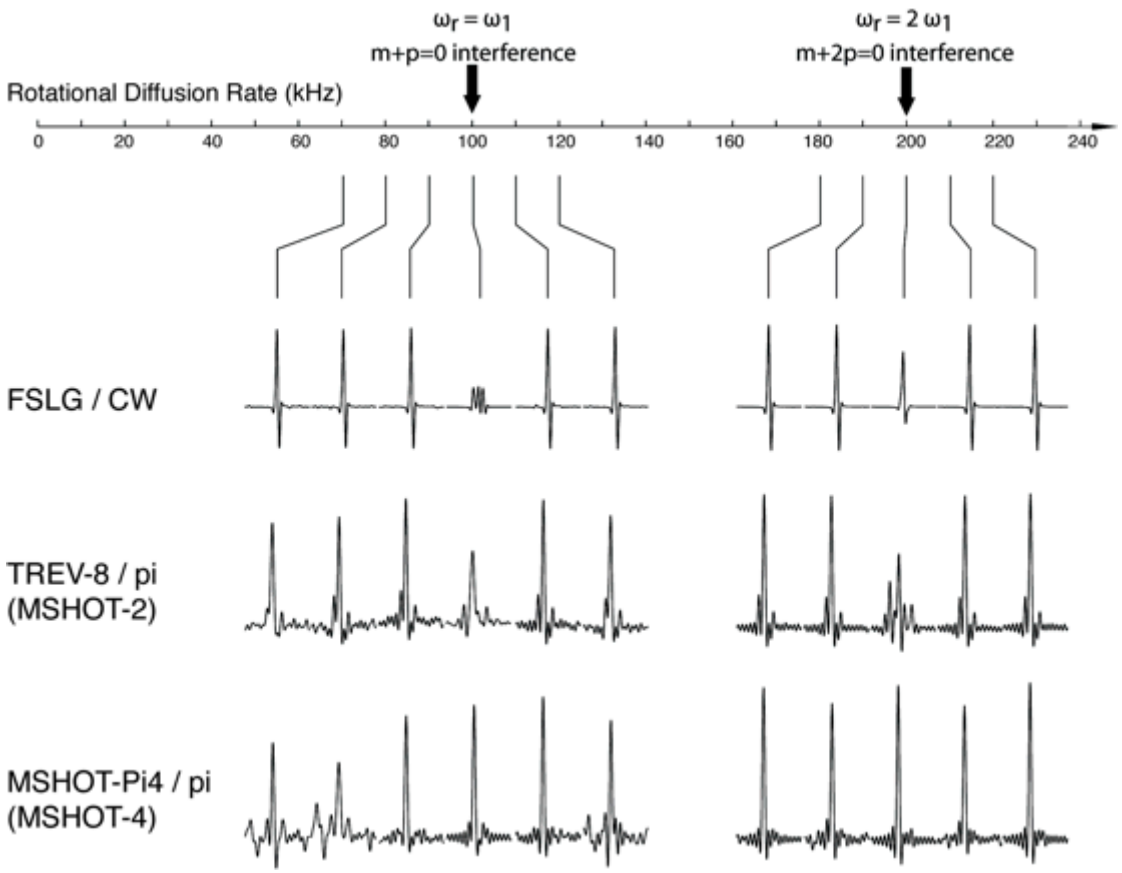

Figure 5.2. Numerical simulation of ^{1}H chemical shift line width at various sample rotation rates with SIMPSON software. A. FSLG and continuous wave (CW) for homonuclear and heternuclear decoupling. B. MSHOT-2 (magic sandwich with two phase cycling, TREV-8) and a single π refocusing pulse for homonuclear and heternuclear decoupling. C. MSHOT-4 (magic sandwich with four phase cycling, MSHOT-Pi4) and a single π refocusing for homonculear and heternuclear decoupling. Effective field of all three homonuclear decoupling sequences are set at 100 kHz, and therefore the m=±1 and m=±2 components of the average Hamiltonian falls at 100kHz and 200kHz. Line broadening occurs when the rotational frequency of the nuclei coincides with these two frequencies. From theoretical analysis, interference with FSLG decoupling occur at both frequencies, TREV-8 has reduced interference at 100 kHz frequency, and MSHOT-Pi4 is resistant to interference at both frequencies.

The purpose of comparing the three sequences is that, from the theoretical analysis, the motion interference with FSLG decoupling occurs for both m=±1 and m=±2 components, MSHOT-2 is interfered only by the m=±1 component, and

MSHOT-4 is resistant to both sources of interference. Therefore, MSHOT-2 should have less interference at 100kHz and MSHOT-4 should be free from interference at both frequencies. From the result, the two interference points can be clearly visible, and for MSHOT-Pi4, the two interference points are largely removed as predicted.

Here we simulate the rotational motion analogous to the case of off-magic-angle spinning of the sample. The angle between the magnetic field and the axis of rotation is arbitrarily chosen to be 80° in order to mimic the case of perpendicular bicelle with wobbling motion, and the sample motion is simulated as a constant rotation. While the rotational diffusion of the protein sample can be simulated more rigorously as a random-walk motion, the common numerical simulation software for solid-state NMR, for example, SIMPSON (Bak et al., 2000) and Spinevolution (Veshtort and Griffin, 2006), are not equipped with this option. In our simulation, the interference of m=±1 and m=±2 components occurs only in a very narrow window at 100 kHz and 200 kHz. With more randomized motion, the spectral interference is likely to occur at a broader range of frequencies and with a less pronounced decrease of intensity. In addition, the ability of these pulse sequences to remove interference from motion would be compromised by the randomness of dipolar fluctuations.

5.9 Experimental Comparison of MSHOT-2, MSHOT-4 and MSHOT-6

One prediction described in the Theory section is the critical role of Z-rotation symmetry at $\pi/2$ phase for removing the motion interference, and Z-rotation at other phases would not suffice. Here MSHOT-2, MSHOT-4 and MSHOT-6 sequences are

evaluated experimentally for homonuclear decoupling with membrane-bound form of Pf1 coat protein in magnetically aligned bicelles (Figure 5.3). Two-dimensional HETCOR spectra were acquired back-to-back on the same sample, and from the measured line width, MSHOT-4 shows better resolution than both MSHOT-2 and MSHOT-6. This provides an important validation for the analytically derived principle of motion interference.

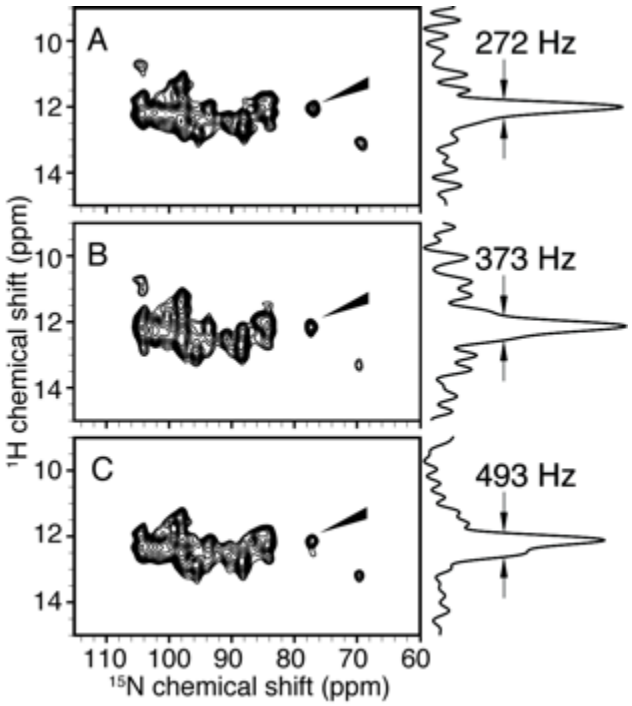

Figure 5.3. Experimental spectra acquired on membrane-bound form of Pf1 coat protein in magnetically aligned bilayers with (A) MSHOT-4 (i.e. MSHOT-Pi4), (B) MSHOT-2 and (C) MSHOT-6 decoupling. All three sequences are magic sandwich sequences with the only difference being that MSHOT-Pi4 has 4-phase cycling, MSHOT-2 has 2-phase cycling and MSHOT-6 has 6-phase cycling. From theoretical analysis, only the 4-phase cycling scheme possesses the critical $\pi/2$ Z-rotational symmetry and offers resistance to motion interference at both $\omega_r = 2\omega_1$ and $\omega_r = \omega_1$ frequencies. Agreeing with this prediction, experimental results show that MSHOT-Pi4 gives the narrowest line width.

5.10 Experimental Spectra of Motion-resistant Separated Local Field Experiments

The resolution and resonance line widths in the heteronuclear dipolar coupling dimensions are compared for spectra acquired with Motion-adapted SAMPI4 and the original SAMPI4 sequence on the membrane-bound form of Pf1 coat protein (Figure 5.4). However, only slight improvement is observed between the two pulse sequences.

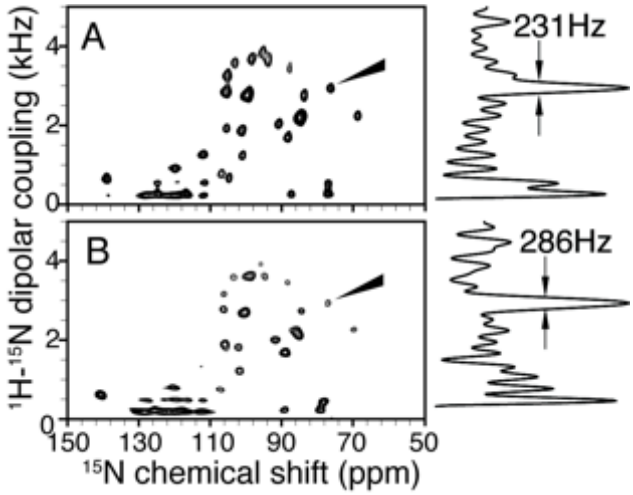

Figure 5.4. Experimental separated local field spectra acquired with (A) Motion-adapted SAMPI4 sequence or (B) regular SAMPI4 sequence for membrane-bound form of Pf1 coat protein in magnetically aligned bicelle. One-dimensional spectral slices from the t1 dimension of the selected peaks are shown on the right side of the two-dimensional spectra. The two sequences give rise to similar line width and spectra.

The first plausible reason for the similar performance between Motion-adapted SAMPI4 and the original SAMPI4 is that separated local field spectra are usually acquired with lower levels of radiofrequency power due to the limitations of the low-γ ^{15}N channel of the probe. With our 5mm static low-E probes, the B_1 field for the separated local field spectra is usually around 50 kHz, while in the HETCOR

experiments the ^{1}H B_1 field is typically ~ 80 kHz. Since the rotational diffusion rate is around 10^5 to 10^6 Hz, the separated local field experiments may fortuitously avoid most of the motion interference.

Another reason for the similar performance between the two sequences is that the Motion-adapted SAMPI4 sequence has 90° or 180° pulses on the ^{15}N channel in the window where ^{1}H are not irradiated. Compared to the simple inversion of ^{15}N spin-lock in the original SAMPI4 sequence, these 90° pulses are likely to produce undesired terms in the average Hamiltonian. In fact, the inversion of ^{15}N spin-lock in the middle of the original SAMPI4 sequence is beneficial in cancelling higher order or cross terms (Nevzorov and Opella, 2007). We have tested replacing these simple 90° and 180° by composite pulses. For example, a composite pulse of $90_{270}90_{180}90_{90}$ can produce a 90° rotation on Z axis (Freeman et al., 1981) and a pulse of $90_{-45}90_{45}90_{-45}$ can produce 180° rotation on X axis (Madhu et al., 2001). Both can fit into the short window of $3\pi/2$ duration between the ^{1}H spin lock periods. However, as these sequences lead to a variety of terms in the Hamiltonian, none of them have shown a significantly superior performance to the current version of Motion-adapted SAMPI4 or the original SAMPI4.

For a separated local field experiment with ideal magic sandwich sequences (assuming the $\pi/2$ pulses are infinitely short), the heteronuclear dipolar coupling evolves during the dual-channel spin-lock period, which constitutes 2/3 of the total dwell. Therefore, the scaling factor of the pulse sequence is 0.67. The scaling factor for SAMPI4 was derived analytically; because the heteronuclear dipolar coupling

evolves more than 2/3 of the dwell time (1.0927 times) (Nevzorov and Opella, 2007), and consequently, the scaling factor is 0.73. For the Motion-adapted SAMPI4, the scaling factor was measured experimentally with respect to the spectra acquired by the original SAMPI4 sequence, and it was found that the dipolar coupling evolves less than 2/3 of the dwell time (0.92 times), resulting in a measured scaling factor of 0.61.

5.11 Conclusion

An analytically derived expression accounts for the previous observations of superior line narrowing of the MSHOT-Pi4 sequence for membrane protein samples. The derivation leads to a generalized principle for the design the motion-adapted pulse sequences, which is to cancel the spin interaction explicitly by setting the reduced Wigner matrix to zero; and it also unveils the role of the critical $\pi/2$ phase in the Z-rotational symmetry of MSHOT-Pi4 sequence. This principle is further extended to the design of separated local field pulse sequence and the resulting Motion-adapted SAMPI4 is tested experimentally.

Chapter 5, in full, is a reprint of the material “Motion-adapted pulse sequences for oriented sample (OS) solid-state NMR of biopolymers” as it appears in J. Chem. Phys. 139(8):084203 by Lu GJ, Opella SJ. The thesis author was the primary author of the paper.

Chapter 6. Mechanism of Dilute-Spin-Exchange in Solid-State NMR

6.1 Abstract

In the stationary, aligned samples used in oriented sample (OS) solid-state NMR, ^{1}H-^{1}H homonuclear dipolar couplings are not attenuated as they are in magic angle spinning (MAS) solid-state NMR; consequently, they are available for participation in dipolar coupling-based spin-exchange processes. Here we describe analytically the pathways of ^{15}N-^{15}N spin-exchange mediated by ^{1}H-^{1}H homonuclear dipolar couplings. The mixed-order proton-relay mechanism can be differentiated from the third spin assisted recoupling (TSAR) mechanism by setting the ^{1}H off-resonance frequency so that it is at the “magic angle” during the spin-exchange interval in the experiment, since the “magic angle” irradiation nearly quenches the former but only slightly attenuates the latter. Experimental spectra from a single crystal of N-acetyl leucine (NAL) confirm that this proton-relay mechanism plays the dominant role in ^{15}N-^{15}N dilute-spin-exchange in OS solid-state NMR in crystalline samples. Remarkably, the "forbidden" spin-exchange condition under “magic angle” irradiation results in ^{15}N-^{15}N cross-peaks intensities that are comparable to those observed with on-resonance irradiation in applications to proteins. The mechanism of the proton relay in dilute-spin-exchange is crucial for the design of polarization transfer experiments.

6.2 Introduction

Experiments that result in the exchange of magnetization between two nuclei rank among the most valuable tools in solid-state NMR (Caravatti et al., 1982; Frey and Opella, 1984; Szeverenyi et al., 1982). They characterize molecular structure and dynamics, and have a particularly valuable role in the assignment of signals to specific sites in organic and biological molecules (Cross et al., 1983). Notably, the through-space coupling of two nuclear spins was the first spin-interaction to be elucidated in the earliest NMR experiments (Pake, 1948). When two nuclei with spin S=1/2 are in close spatial proximity, and isolated from other nuclei, then a doublet results in the spectrum due to their dipole-dipole coupling. Importantly, when the coupling is weak because of low-γ or large separation of the (dilute, e.g. ^{13}C or ^{15}N) nuclei, then a doublet may not be observed. However, the weak dipole-dipole couplings that are present are often sufficient for the exchange of magnetization between proximate sites. Multiple coupling pathways including homonuclear spin-diffusion (Macura and Ernst, 1980; Virlet and Ghesquieres, 1980) have been observed. In essentially all plausible mechanisms, the nuclei in closer proximity yield stronger exchange signals than those with greater separation.

The introduction of the second-order third spin assisted recoupling (TSAR) method of polarization transfer between two low-γ nuclei (^{13}C or ^{15}N) that are both coupled to a third high-γ (^{1}H) nucleus (Lewandowski et al., 2007) (Figure 6.1.A) has led to a renaissance in studies of dilute-spin-exchange spectroscopy (Agarwal et al., 2013; Bertini et al., 2010; Bertini et al., 2011; Das et al., 2012; De Paëpe, 2012; De Paepe et al., 2008; De Paepe et al., 2011; Giffard et al., 2012; Jehle et al., 2010;

Khitrin et al., 2011; Knox et al., 2010; Lamley and Lewandowski, 2012; Lewandowski et al., 2009; Lin and Opella, 2011; Loquet et al., 2012; Lu et al., 2013b; Nevzorov, 2008; Nevzorov, 2009; Nielsen et al., 2012a; Nielsen et al., 2012b; Tang et al., 2012; Traaseth et al., 2010; Van Melckebeke et al., 2010). Here we demonstrate theoretically and experimentally that the dominant mechanism of spin-exchange between dilute nuclei in a stationary crystalline sample is "mixed-order proton-relay", which relies on transfers between proximate ^{1}H nuclei (Figure 6.1.B).

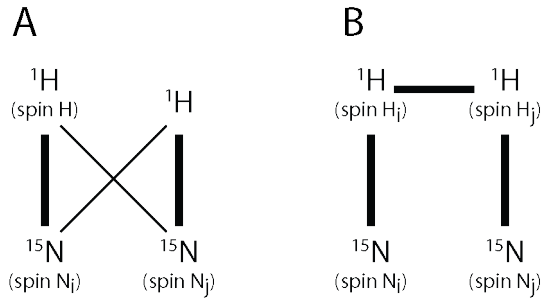

Figure 6.1. Schematic drawings of the dipolar coupling networks relevant to ^{15}N-^{15}N dilute-spin-exchange. A. The second-order TSAR mechanism. B. The "mixed-order proton-relay" mechanism. The numbering of spins from A to D is used in the analytical derivations on these mechanisms.

Spin-exchange between ^{15}N nuclei is frequently utilized in protein NMR studies for resonance assignment and structure determination because of the importance of the amide sites located in the polypeptide backbone. TSAR was adapted for stationary, aligned samples in oriented sample (OS) solid-state NMR as the mismatched Hartmann-Hahn (MMHH) condition (Nevzorov, 2008). TSAR and several other second-order recoupling experiments (Lange et al., 2003; Scholz et al., 2008; Weingarth et al., 2009), including proton driven spin diffusion (PDSD) (Dumez et al., 2012; Grommek et al., 2006), rely on the presence of nearby ^{1}H nuclei to

transfer magnetization between ^{15}N sites. The ^{1}H nucleus participation in the magnetization transfer is proposed to be through simultaneous coupling to both ^{15}N nuclei. Here we demonstrate that an alternative mechanism is operative, namely polarization transfer through ^{1}H-^{1}H coupling. Notably, this mechanism does not require that each ^{1}H nucleus be coupled to both ^{15}N nuclei. Moreover, it more closely reflects the distribution of nuclei in polypeptides where ^{15}N nuclei are usually located on different residues; only rarely does a ^{1}H nucleus have sizable dipolar couplings to two or more ^{15}N nuclei. By comparing the effects of on-resonance versus "magic-angle" off-resonance ^{1}H spin-lock irradiation (Goldburg and Lee, 1963) it is possible to separate the two transfer mechanisms for dilute-spin-exchange.

6.3 Materials and Methods

The expression, purification, and sample preparation of intact fd bacteriophage have been described previously (Zeri et al., 2003a). ^{15}N-detected solid-state NMR spectra were obtained on a 700 MHz Bruker Avance spectrometer equipped with a homebuilt $^{1}H/^{15}N$ double-resonance probe with a strip-shield to minimize heating of the lossy samples due to the high frequency, high power radiofrequency irradiations (Wu et al., 2009).

^{15}N-^{15}N spin exchange experiments on a N-acetyl leucine (NAL) single crystal were performed with 45.45 kHz radiofrequency irradiation, 1 msec cross-polarization, 0.1 sec Z-filter and 5 msec mixing time. During mixing, ^{1}H irradiation was elevated to 50 kHz (+10% mismatched condition) for on-resonance spin lock or was dropped to

40.82 kHz with 28.87 kHz offset (+10% mismatched for effective B_1 field). Similarly, the spin exchange experiments on the fd bacteriophage sample used 45.45 kHz irradiation, 1 msec cross-polarization, 0.1 sec Z-filter and various mixing times. The control experiment used a 0.1 sec Z-filter but no spin-lock spin exchange period. Several mismatched conditions were described above, and notably, the 22% mismatch corresponds to ^{1}H irradiation frequency of 55.6 kHz on resonance or 45.45 kHz with 32 kHz offset. 20 complex t1 points, 384 complex t2 points and 400 scans were collected in each experiment. Spectral widths of 10 kHz and 50 kHz were used in the t1 and t2 dimensions, respectively. With a 4 sec relaxation delay between each scan, the total time for each experiment was ~ 18 hours. For the spectra of 4 sec PDSD mixing, the number of scan was reduced to 208, giving approximately the same total experimental time. The spectra for fd bacteriophage were processed with an exponential window function corresponding to 200 Hz line broadening. The data processing and visualization used NMRDraw (Delaglio et al., 1995) and Sparky (Goddard and Kneller, 2008).

Numerical simulations were carried out with SIMPSON 2.0 (Bak et al., 2000). Numerical simulations of OS solid-state NMR spectra used the same setup as that of the experimental spectra of the NAL single crystal, namely, 45.45 kHz radiofrequency irradiations, 0.1 sec Z-filter time and 5 msec mixing time. Cross-polarization was replaced by putting initial magnetization directly on the two ^{15}N nuclei. The crystal file of “alpha0beta0” was used. The spin networks are shown in the figures. In the simulations of the buildup curves, initial magnetization was put only at one of the ^{15}N

nuclei, and the other ^{15}N nucleus was monitored during detection. Only the spin-lock mixing period was simulated with variable length.

6.4 Overview of Mixed-order Proton-relay Mechanism

Using average Hamiltonian theory, ^{15}N-^{15}N spin exchange can be analyzed in both types of dipolar coupling networks (Figure 6.1), and we focus the discussion on the terms responsible for the transfer between ^{15}N nuclei in stationary samples. In the case of TSAR, these are the trilinear terms $T_{10}^{H}(T_{1,+1}^{Ni}T_{1,-1}^{Nj}+T_{1,-1}^{Ni}T_{1,+1}^{Nj})$, where spins N_i and N_j are the two ^{15}N and spin H is the ^{1}H (De Paepe et al., 2011). It can be shown that in a simplified scenario of a three-spin system, the change of ^{1}H spin lock irradiation from the on-resonance frequency to the "magic-angle" offset frequency attenuates the amplitude of the polarization transfer according to $\overline{H}_{TSAR}(on\ resonance)\rightarrow\frac{2}{3}\overline{H}_{TSAR}(magic\ angle)$.

In contrast, for the spin network shown in Figure 6.1.B, three mechanisms can be identified. The first is referred to as the "third-order mechanism". The flip-flop terms between the two ^{15}N nuclei, mediated by a variety of terms derived from the ^{1}H spins, appears in the third-order average Hamiltonian and drives the polarization transfer between the ^{15}N nuclei. The second and third mechanisms are referred to as "multiple-step mechanisms". They involve the first-order and second-order average Hamiltonians and transfer the polarization in more than one step. Collectively they constitute a "mixed-order proton-relay mechanism". It can be shown that most of the

terms responsible for ^{15}N polarization transfer are averaged to zero when the ^{1}H spin-lock irradiation is set to the "magic angle"; and the few terms that remain are attenuated by at least an order of magnitude. Thus, a "magic-angle" ^{1}H spin-lock nearly quenches the spin exchange, which can be expressed as $\overline{H}_{proton-relay}(on\ resonance) \rightarrow \sim 0\ (magic\ angle)$. The analytical derivations of these mechanisms are described below.

6.5 Theory of Second-order TSAR Mechanism

The second-order TSAR mechanism can be described with a minimum of three spins. Here we consider one ^{1}H spin (spin H) coupled to two ^{15}N spins (spins N_i and N_j) (Figure 6.1.A), and for simplicity we omit other internal Hamiltonian terms such as chemical shifts. Using spherical tensor operator notations, the Hamiltonian of the system in the usual rotating frame under a high magnetic field can be written as (Mehring and Weberruss, 2001)

$$\mathrm{H(t)} = \mathrm{H_{rf}(t)} + \mathrm{H_D(t)}, \qquad \text{Eq. 6.1}$$

$$\mathrm{H_D(t)} = 2\omega_{AB}\mathrm{T}^{A}_{10}\mathrm{T}^{B}_{10} + 2\omega_{AC}\mathrm{T}^{A}_{10}\mathrm{T}^{C}_{10}. \qquad \text{Eq. 6.2}$$

In the absence of MAS, the dipolar couplings are not attenuated, and the spatial part of the dipolar coupling Hamiltonian $\omega_{H,Ni}$ and $\omega_{H,Nj}$ are time independent. Note the conversions between spherical tensor operators and the Cartesian spin operators are:

$$T^{AB}_{20} = \frac{1}{\sqrt{6}}(3I_{Az}I_{Bz} - \vec{I}_A \cdot \vec{I}_B), \qquad \text{Eq. 6.3a}$$

$$T^{AB}_{2,\pm1} = \mp\frac{1}{2}(I_{Az}I^{\pm}_{B} + I^{\pm}_{A}I_{Bz}), \qquad \text{Eq. 6.3b}$$

$$T_{2,\pm 2}^{AB} = \frac{1}{2} I_A^{\pm} I_B^{\pm}, \qquad \text{Eq. 6.3c}$$

$$T_{10}^{A} = I_{Az}, \qquad \text{Eq. 6.3d}$$

$$T_{1,\pm 1}^{A} = \mp \frac{1}{\sqrt{2}} I_A^{\pm}. \qquad \text{Eq. 6.3e}$$

For stationary, aligned samples used in OS solid-state NMR, the pulse sequence of polarization transfer by TSAR usually involves spin-lock pulses on both channels under mismatched Hartmann-Hahn conditions (Nevzorov, 2008). Therefore, we define the irradiation frequencies of the two channels to be

$$\omega_H = \omega_1 + \Delta\omega, \qquad \text{Eq. 6.4a}$$

$$\omega_N = \omega_1, \qquad \text{Eq. 6.4b}$$

where $\Delta\omega$ accounts for the mismatched amplitude. The overall effect of the on-resonance spin-lock pulses on ^{15}N can be described as a rotation with the Euler angles

$$R_N(\omega_1 t, \frac{\pi}{2}, 0) = \exp\{-i\omega_1 t S_z\} \exp\{-i\frac{\pi}{2} S_y\}. \qquad \text{Eq. 6.5a}$$

The spin-lock irradiations on the ^{1}H channel are usually on resonance but here it is generalized to be at any angle θ, for the convenience of subsequent discussions of spin-locking at the "magic angle":

$$R_H(\omega_1 t, \theta, 0) = \exp\{-i(\omega_1 + \Delta\omega) t\ I_z\} \exp\{-i\theta\ I_y\}. \qquad \text{Eq. 6.5b}$$

Note the rotation transforms the spin part of the internal Hamiltonian (in this case $H_D(t)$) through the following general transformation equation:

$$R(\alpha,\beta,\gamma) T_{k,q} R^{-1}(\alpha,\beta,\gamma) = \sum_{p=-k}^{+k} T_{k,p} \exp\{-i\alpha p\} d_{p,q}^{k}(\beta) \exp\{-i\gamma q\}. \qquad \text{Eq. 6.6}$$

This provides a convenient way of analyzing pulse sequences, such as deriving the following interaction frame Hamiltonian:

$$\tilde{H}_{\text{int}} = U_{rf}^{-1}(t_0, t_0+\tau) H_{\text{int}} U_{rf}(t_0, t_0+\tau)\,. \qquad \text{Eq. 6.7}$$

In the current case, H_{int} includes only the H_D described in Eq. 6.2. The relative ease of performing spin rotation calculations is the main reason for using spherical tensors instead of Cartesian tensors.

The time propagator can then be approximated using Average Hamiltonian Theory with stroboscopic observation from time t_0 to $t_0 + \tau$,

$$U(t_0+\tau) \cong U_{rf}(t_0, t_0+\tau)\exp\{-i\overline{H}\tau\}\,, \qquad \text{Eq. 6.8}$$

where $\overline{H}$ is the average Hamiltonian. Using a Magnus expansion, the first few terms in $\overline{H}$ are represented using the general formulae of Bialynicki–Birula *et al.* (Bialynicki-Birula et al., 1969):

$$\overline{H}^{(1)} = \frac{1}{\tau}\int_{t_0}^{t_0+\tau} \tilde{H}_{\text{int}}\, dt\,, \qquad \text{Eq. 6.9a}$$

$$\overline{H}^{(2)} = -\frac{i}{2\tau}\int_{t_0}^{t_0+\tau} dt_1 \int_{t_0}^{t_0+t_1} dt_2 [\tilde{H}_{\text{int}}(t_1), \tilde{H}_{\text{int}}(t_2)]\,, \qquad \text{Eq. 6.9b}$$

$$\overline{H}^{(3)} = -\frac{1}{6\tau}\int_{t_0}^{t_0+\tau} dt_1 \int_{t_0}^{t_0+t_1} dt_2 \int_{t_0}^{t_0+t_2} dt_3 ([\tilde{H}_{\text{int}}(t_1),[\tilde{H}_{\text{int}}(t_2), \tilde{H}_{\text{int}}(t_3)] + [\tilde{H}_{\text{int}}(t_3),[\tilde{H}_{\text{int}}(t_2), \tilde{H}_{\text{int}}(t_1)])$$

Eq. 6.9c

Notably, the order numbers in the second-order TSAR mechanism and mixed-order proton-relay mechanisms refer to the number described here during the Magnus expansion. Since spin lock irradiations in this class of experiments usually last for

several milliseconds, we can assume that both $\omega_1\tau$ and $\Delta\omega\tau$ satisfy the integers of 2π. Explicitly, this can be written as

$$\tau = \frac{2\varepsilon_1\pi}{\omega_1} = \frac{2\varepsilon_2\pi}{\Delta\omega}, \qquad \text{Eq. 6.10}$$

where ε_1 and ε_2 are both integers.

For the minimal three-spin system and the simplified internal Hamiltonian, we can explicitly evaluate the first two orders in the Magnus expansion using Mathematica with the assistance of scripts from MathNMR (Jerschow, 2005) and SpinDynamica (Levitt):

$$\overline{H}^{(1)} = 0, \qquad \text{Eq. 6.11a}$$

$$\overline{H}_I^{(2)} = -\frac{2\omega_{H,Ni}\omega_{H,Nj}(\omega_1+\Delta\omega)sin^2(\theta)}{\Delta\omega(2\omega_1+\Delta\omega)} T_{10}^H (T_{1,+1}^{Ni}T_{1,-1}^{Nj} + T_{1,-1}^{Ni}T_{1,+1}^{Nj}), \qquad \text{Eq. 6.11b}$$

$$\overline{H}_{II}^{(2)} = \frac{1}{2\omega_1\Delta\omega(2\omega_1+\Delta\omega)}(\omega_1(\omega_1+\Delta\omega)(\omega_{H,Ni}^2+\omega_{H,Nj}^2)sin^2(\theta)T_{10}^H + (\Delta\omega(2\omega_1+\Delta\omega)cos^2(\theta) - \omega_1^2 sin^2(\theta))(\omega_{H,Ni}^2 T_{10}^{Ni} + \omega_{H,Nj}^2 T_{10}^{Nj})). \qquad \text{Eq. 6.11c}$$

The most relevant Hamiltonian is $\overline{H}_I^{(2)}$ in Eq. 6.11b, which contains the three-spin trilinear terms for polarization transfer between spins N_i and N_j; the magnitude of this term has a $sin^2(\theta)$ relationship with the ^{1}H channel spin-lock angle θ. Therefore; the term is only attenuated when the ^{1}H spin-lock pulse is changed from the on-resonance condition ($\theta = \pi/2$) to the "magic-angle" condition:

$$\overline{H}_I^{(2)}(on\ resonance) \rightarrow \frac{2}{3}\overline{H}_I^{(2)}(magic\ angle). \qquad \text{Eq. 6.12}$$

6.6 Theory of Third-order Proton-relay Mechanism

For the proton-relay mechanism diagrammed in Figure 6.1.B, the minimal system contains four spins, rather than the three spins of the TSAR mechanism. It is straightforward to envision that the key flip-flop terms between the two ^{15}N atoms would appear in the third-order average Hamiltonian terms. We can use the same set of formulae described in the last section to derive this mechanism. We denote the two ^{1}H spins to be H_i and H_j and the two ^{15}N spins to be N_i and N_j (Figure 6.1.B), and the internal Hamiltonian now contains:

$$H_D(t) = \sqrt{6}\omega_{Hi,Hj}T_{20}^{Hi,Hj} + 2\omega_{Hi,Ni}T_{10}^{Hi}T_{10}^{Ni} + 2\omega_{Hj,Nj}T_{10}^{Hj}T_{10}^{Nj}. \qquad \text{Eq. 6.13}$$

The third order average Hamiltonian evaluated from Equation 9c contains many terms; for simplicity, we only evaluate those terms containing zero-quantum flip-flop terms between spin N_i and N_j $T_{1,+1}^{Ni}T_{1,-1}^{Nj} + T_{1,-1}^{Ni}T_{1,+1}^{Nj}$. It is noted that double-quantum terms also exist in addition to the zero-quantum terms that we quantify here, as those analyzed for TSAR mechanism (De Paepe et al., 2008; De Paepe et al., 2011). The zero-quantum terms include:

$$\overline{H}_I^{(3)} = T_{10}^{Hi}T_{10}^{Hj}(T_{1,+1}^{Ni}T_{1,-1}^{Nj} + T_{1,-1}^{Ni}T_{1,+1}^{Nj})\omega_{Hi,Hj}\omega_{Hi,Ni}\omega_{Hj,Nj}sin^2(\theta)\times \frac{4\omega_1^2 - 2\omega_1\Delta\omega - \Delta\omega^2 + 3(4\omega_1^2 - 6\omega_1\Delta\omega - 3\Delta\omega^2)cos(2\theta)}{2\Delta\omega^2(2\omega_1 + \Delta\omega)^2}, \qquad \text{Eq. 6.14a}$$

$$\overline{H}_{II}^{(3)} = (T_{1,+1}^{Hi}T_{1-1}^{Hj} + T_{1,-1}^{Hi}T_{1,+1}^{Hj})(T_{1,+1}^{Ni}T_{1,-1}^{Nj} + T_{1,-1}^{Ni}T_{1,+1}^{Nj})\omega_{Hi,Hj}\omega_{Hi,Ni}\omega_{Hj,Nj} \times$$
$$(\frac{-2\omega_1^4 + 4\omega_1^3\Delta\omega - 18\omega_1^2\Delta\omega^2 - 20\omega_1\Delta\omega^3 - 5\Delta\omega^4}{4\omega_1^2\Delta\omega_1^2(2\omega_1 + \Delta\omega)^2} +$$
$$\frac{(8\omega_1^4 + 8\omega_1^3\Delta\omega - 28\omega_1^2\Delta\omega^2 - 32\omega_1\Delta\omega^3 - 8\Delta\omega^4)cos(2\theta)}{4\omega_1^2\Delta\omega_1^2(2\omega_1 + \Delta\omega)^2} + \quad , \qquad \text{Eq. 6.14b}$$
$$\frac{3(-2\omega_1^4 - 4\omega_1^3\Delta\omega - 6\omega_1^2\Delta\omega^2 - 4\omega_1\Delta\omega^3 - \Delta\omega^4)cos(4\theta)}{4\omega_1^2\Delta\omega_1^2(2\omega_1 + \Delta\omega)^2})$$

$$\overline{H}_{III}^{(3)} = (T_{2,+1}^{Hi,Hj} + T_{2,-1}^{Hi,Hj})(T_{1,+1}^{Ni}T_{1,-1}^{Nj} + T_{1,-1}^{Ni}T_{1,+1}^{Nj})\omega_{Hi,Hj}\omega_{Hi,Ni}\omega_{Hj,Nj}\frac{-sin(2\theta)(3cos^2(\theta)-1)}{\sqrt{2}\Delta\omega(2\omega_1 + \Delta\omega)}$$

Eq. 6.14c

$$\overline{H}_{IV}^{(3)} = (T_{2,+2}^{Hi,Hj} + T_{2,-2}^{Hi,Hj})(T_{1,+1}^{Ni}T_{1,-1}^{Nj} + T_{1,-1}^{Ni}T_{1,+1}^{Nj})\omega_{Hi,Hj}\omega_{Hi,Ni}\omega_{Hj,Nj}\frac{-2sin^2(\theta)(3cos^2(\theta)-1)}{\Delta\omega(2\omega_1 + \Delta\omega)}.$$

Eq. 6.14d

We note that $\overline{H}_{I}^{(3)}$ and $\overline{H}_{II}^{(3)}$ contain a mixture of the term $T_{20}^{Hi,Hj}(T_{1,+1}^{Ni}T_{1,-1}^{Nj} + T_{1,-1}^{Ni}T_{1,+1}^{Nj})$ and other terms that originate from commutation between homonuclear and heteronuclear dipolar couplings.

In the next step, we evaluate the dependence of these flip-flop terms in the third-order average Hamiltonian on the ^{1}H channel with spin-lock angle θ. We can readily see both $\overline{H}_{III}^{(3)}$ and $\overline{H}_{IV}^{(3)}$ vanish when θ is the magic angle. $\overline{H}_{I}^{(3)}$ and $\overline{H}_{II}^{(3)}$ do not vanish at the magic angle, but are reduced by factors of around 18 and 16, respectively, if one assumes the ratio $\omega_1/\Delta\omega = 10$, *i.e.,* the 10% mismatched condition previously shown to be optimal for ^{15}N-^{15}N spin exchange in a NAL crystal (Nevzorov, 2008). This is summarized below for a comparison with Equation 6.12:

$$\overline{H}_{I}^{(3)}(on\ resonance, \frac{\omega_1}{\Delta\omega}=10) \rightarrow\sim \frac{1}{18}\overline{H}_{I}^{(3)}(magic\ angle, \frac{\omega_1}{\Delta\omega}=10), \quad \text{Eq. 6.15a}$$

$$\overline{H}_{II}^{(3)}(on\ resonance, \frac{\omega_1}{\Delta\omega}=10) \rightarrow\sim \frac{1}{16}\overline{H}_{II}^{(3)}(magic\ angle, \frac{\omega_1}{\Delta\omega}=10), \quad \text{Eq. 6.15b}$$

$$\overline{H}_{III}^{(3)}(on\ resonance) \rightarrow 0\ (magic\ angle), \quad \text{Eq. 6.15c}$$

$$\overline{H}_{IV}^{(3)}(on\ resonance) \rightarrow 0\ (magic\ angle), \quad \text{Eq. 6.15d}$$

Interestingly, $\overline{H}_{I}^{(3)}$ and $\overline{H}_{II}^{(3)}$ reaches zero when the ^{1}H channel spin-lock angle θ is 52.92° and 56.53°, respectively. Both of the angles are very close to the magic angle of 54.7°.

6.7 Theory of Multiple-step Proton-relay Mechanism and Repolarization of ^{1}H

Other pathways for polarization transfer from one ^{15}N atom to the other in the same four-spin system (Figure 6.1.B) are through multiple-step polarization transfer via ^{1}H. They can also be viewed as proton-relay mechanisms, and their difference from the one described in the last section is that the Hamiltonian terms in the above section can convert polarization in the first ^{15}N (expressed as I_z^{Ni}) directly to the polarization in the second one (I_z^{Nj}), while the mechanisms described here convert polarization I_z^{Ni} to I_z^{Hi} (the first ^{1}H) or I_z^{Hj} (the second ^{1}H) and then, in the subsequent step, to I_z^{Nj}. These pathways are summarized in Figure 6.2.

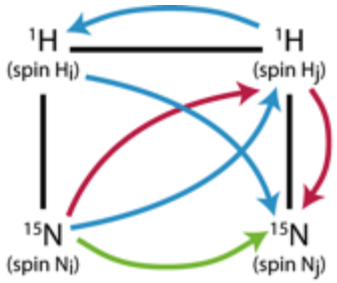

Figure 6.2. Schematic drawing of the pathways for spin exchange from one ^{15}N atom to the other. (Green) Third-order proton-relay mechanism. (Magenta) Second-order two-step mechanism. (Cyan) Mixed-order three-step mechanism.

We start by deriving the second-order average Hamiltonian terms for the four-spin system. Similar to the case of the TSAR mechanism, trilinear terms involving three spins appear as $T_{10}^{Hi}(T_{1,+1}^{Ni}T_{1,-1}^{Hj}+T_{1,-1}^{Ni}T_{1,+1}^{Hj})$ and $T_{10}^{Hj}(T_{1,+1}^{Hi}T_{1,-1}^{Nj}+T_{1,-1}^{Hi}T_{1,+1}^{Nj})$. The term $T_{10}^{Hi}(T_{1,+1}^{Ni}T_{1,-1}^{Hj}+T_{1,-1}^{Ni}T_{1,+1}^{Hj})$ can transfer polarization from spin N_i (a ^{15}N nucleus) to spin H_j (a ^{1}H nucleus). In contrast to the TSAR mechanism, which involves only heteronuclear couplings, spins H_i and H_j are coupled through homonuclear dipolar couplings, and therefore additional trilinear terms in the form of $T_{10}^{Hj}(T_{1,+1}^{Hi}T_{1,-1}^{Ni}+T_{1,-1}^{Hi}T_{1,+1}^{Ni})$ and $T_{10}^{Hi}(T_{1,+1}^{Hj}T_{1,-1}^{Nj}+T_{1,-1}^{Hj}T_{1,+1}^{Nj})$ also appear. The term $T_{10}^{Hi}(T_{1,+1}^{Hj}T_{1,-1}^{Nj}+T_{1,-1}^{Hj}T_{1,+1}^{Nj})$ can thus transfer magnetization from spin H_j to spin N_j. The relevant second-order Hamiltonian terms for these two steps are extracted out:

$$\overline{H}_I^{(2)} = T_{10}^{Hi}(T_{1,+1}^{Ni}T_{1,-1}^{Hj}+T_{1,-1}^{Ni}T_{1,+1}^{Hj})\omega_{Hi,Hj}\omega_{Hi,Ni}sin(\theta)\frac{1-3cos^2(\theta)}{2\Delta\omega}, \qquad \text{Eq. 6.16a}$$

$$\overline{H}_{II}^{(2)} = T_{10}^{Hi}(T_{1,+1}^{Hj}T_{1,-1}^{Nj}+T_{1,-1}^{Hj}T_{1,+1}^{Nj})\omega_{Hi,Hj}\omega_{Hj,Nj}sin(\theta)\frac{1-3cos^2(\theta)}{\Delta\omega}. \qquad \text{Eq. 6.16b}$$

Then the evolution of density matrix can be followed through the formulae

$$\rho(t) = \exp(-iHt)\rho(t_0)\exp(iHt). \qquad \text{Eq. 6.17}$$

When $\rho(t_0) = I_z^{Ni}$, we can obtain non-zero I_z^{Hj} and I_z^{Nj} in $\rho(t)$.

Similarly, polarization transfer from spin N_i to spin N_j can occur in three steps (cyan color, Figure 6.2). In the first step, the same second-order Hamiltonian terms (Equation 6.16a) transfers polarization to spin H_j. In the second step, the first-order Hamiltonian term will drive the polarization to spin H_i. The first-order Hamiltonian contains only the homonuclear dipolar coupling

$$\overline{H}^{(1)} = \sqrt{6}\omega_{Hi,Hj} T_{20}^{Hi,Hj} \frac{3cos^2(\theta)-1}{2}. \qquad \text{Eq. 6.18}$$

Lastly, the trilinear term will transfer magnetization from spin H_i to spin N_j:

$$\overline{H}_{III}^{(2)} = T_{10}^{Hj}(T_{1,+1}^{Hi}T_{1,-1}^{Nj} + T_{1,-1}^{Hi}T_{1,+1}^{Nj})\omega_{Hi,Hj}\omega_{Hj,Nj} sin(\theta)\frac{1-3cos^2(\theta)}{2\Delta\omega}. \qquad \text{Eq. 6.19}$$

The important realization is again that all relevant terms in Equation 6.16, 6.18 and 6.19 have a $1-3cos^2(\theta)$ dependence on the ^{1}H channel spin-lock angle θ. Therefore, these mechanisms of polarization transfer will also be quenched by setting the ^{1}H channel spin-lock irradiation at the magic angle.

Another difference of these two mechanisms from the one shown in the last section is that they lead to repolarization of ^{1}H. Due to their large differences in gyromagnetic ratios, the cross- polarization from low-γ nuclei back to high-γ nuclei usually causes substantial depolarization of the former. Since ^{1}H usually experiences shorter $T_{1\rho}$ and faster decay, their repolarization during spin exchange may become a pathway to drain the magnetization. This is related to one of the speculated reasons for the performance of these pulse sequences in biological sample, which will be discussed in later sections.

6.8 Numerical Simulations and Experimental Results

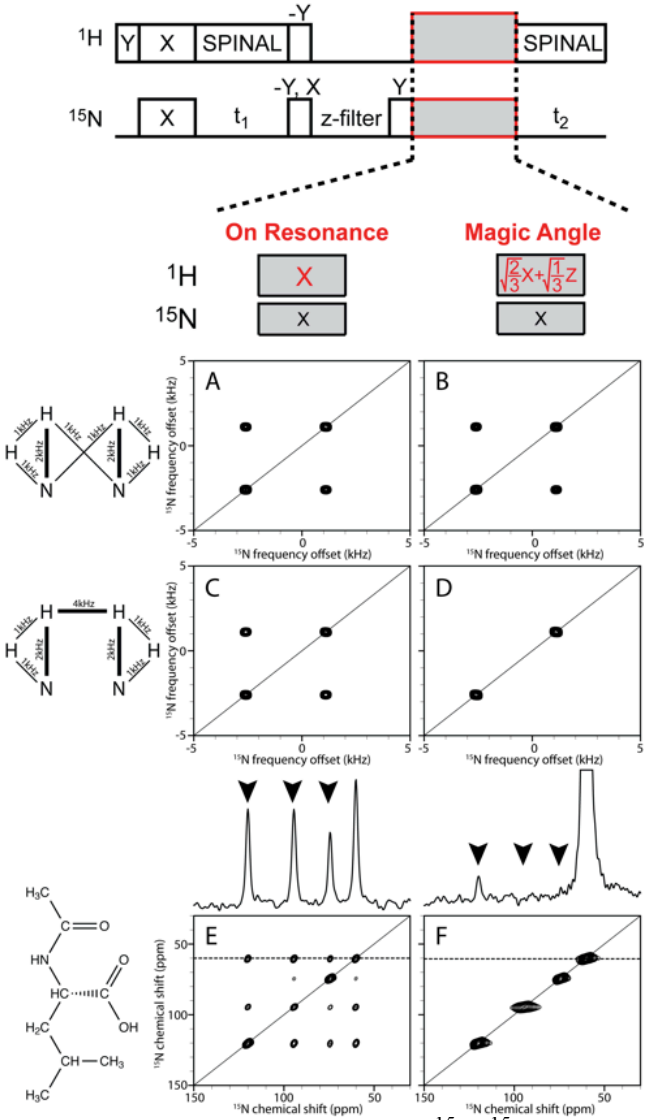

Figure 6.3. Numerical simulation and experimental ^{15}N-^{15}N spin exchange spectra that differentiate TSAR and proton-relay mechanisms by ^{1}H spin-lock pulses on-resonance or off-resonance at the magic angle. The pulse sequences are drawn on the top. A., B., C., and D. are simulated spectra. E. and F. are experimental spectra. A., C., and E. are with on-resonance ^{1}H spin-lock irradiation. B., D., and F. are with "magic-angle" ^{1}H spin-lock irradiation. A. and B. Numerical simulation on the spin network for the TSAR mechanism, where "magic-angle" irradiation only slightly attenuates the spin exchange. C. and D. Numerical simulation on the spin network for proton-relay mechanisms, where "magic-angle" irradiation nearly quenches the spin exchange. E. and F. Experimental results obtained from the NAL single crystal sample. The arrows indicate the cross-peaks resulting from spin-exchange. Notably, the four resonances arise from the four uniquely oriented amide sites in each unit cell of an NAL crystal.

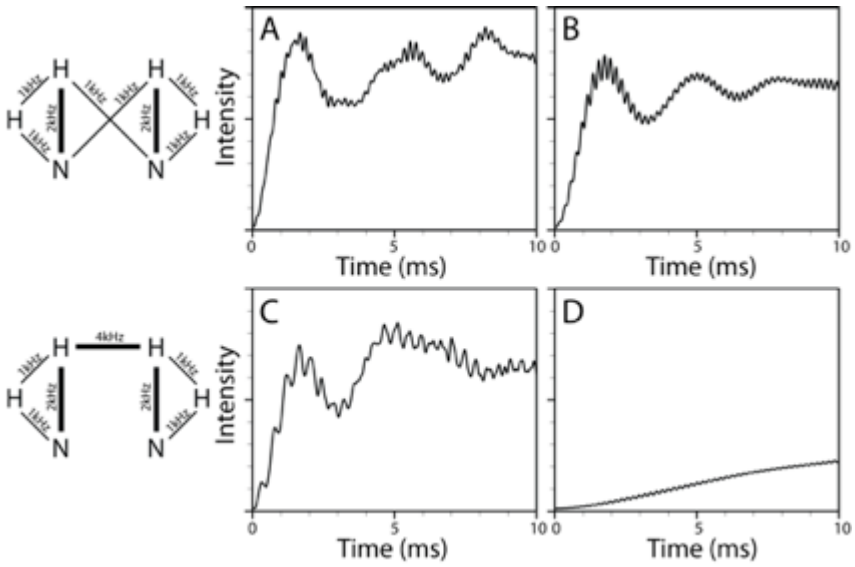

Figure 6.4. Numerical simulation of the polarization buildup curve resulting from ^{15}N-^{15}N spin-exchange. A. and C. On-resonance ^{1}H spin-lock pulse. B. and D. Magic-angle ^{1}H spin-lock pulse. Drawn on the left are the spin networks proposed for TSAR mechanism (top row) and for mixed-order proton-relay mechanism (bottom row).

The analytical results described in the previous section have shown that by switching the ^{1}H irradiation frequency from on-resonance to off-resonance at the magic angle, the "mixed-order proton-relay" mechanism will be nearly quenched, while the TSAR mechanism will only be slightly attenuated. This suggest an experimental method to differentiate the two mechanisms by comparing the polarization transfer efficiency in the presence of on-resonance and off-resonance "magic-angle" ^{1}H irradiation. The numerical simulations of the two-dimensional ^{15}N-^{15}N spin exchange spectra (Figure 6.3.A-D) and the magnetization buildup curve (Figure 6.4) validate the conclusions. The dipolar coupling networks used for simulation of the different mechanisms are drawn on the left of Figure 6.3.A-D. The

TSAR mechanism (Figure 6.3.A-B) relies on the same ^{1}H being coupled to two ^{15}N atoms, but the proton-relay mechanisms (Figure 6.3.C-D) do not. Instead, proton-relay mechanisms transfer polarization via ^{1}H-^{1}H homonuclear dipolar couplings. In the simulated spectra, all expected cross-peaks are visible, except for those in Figure 6.3.D, which supports the theoretical result of "magic-angle" irradiation suppressing polarization transfers via proton-relay mechanisms.

The comparison of the two experimental spectra obtained from a single crystal of NAL (Figure 6.3.E-F) shows nearly completely quenched spin exchange in the presence of the "magic-angle" spin-lock irradiation, which demonstrates that the proton-relay mechanism is the main contributor to the ^{15}N-^{15}N spin exchange. The spin-lock contact time is 5 msec for both simulations and experiments, and during this interval the cross-peaks in Figure 6.2.E approach saturation, since their intensities are nearly the same as the diagonal peaks. For the spectrum in Figure 6.2.F, however, we observed continuing but slow buildup beyond 9 msec, the longest duration tested. This agrees with the simulation of the polarization buildup (Figure 6.4.D). MMHH contact times around 5 msec are most relevant with the consideration of applying these pulse sequences to protein samples in OS solid-state NMR, because their shorter $T_{1\rho}$ values usually results in loss of signal intensity at longer mixing times (Goldburg and Lee, 1963; Knox et al., 2010; Tang et al., 2012; Zeri et al., 2003a).

Under MAS conditions, the proton-relay mechanism is suppressed because of the averaging of homonuclear dipolar couplings. The extent of suppression is directly related to the spinning speed. This might provide a partial explanation for the contrast

between the mixing times used in MAS solid-state NMR and OS solid-state NMR. In ^{15}N-^{15}N correlation experiments under MAS condition (Lewandowski et al., 2009), the mixing time is typically 20 msec but most of the observed cross-peaks are sequential in helix (~ 3 Å) or β-sheet (< 5 Å) structures. By contrast, in OS solid-state NMR, most reports show that 5 msec mixing provides all cross-peaks among ^{15}N spins in a NAL single crystal, which has inter-molecular ^{15}N-^{15}N distances greater than 6.5 Å. Under slow spinning, the incomplete averaging of homonuclear couplings makes the situation resemble that encountered in OS solid-state NMR, but this requires an analysis beyond that in this article.

6.9 Dilute Spin Exchange in Protein Sample: Selectively ^{15}N-Val Labeled Fd Bacteriophage

To optimize the spin exchange conditions and to test the different effects of on-resonance and "magic-angle" ^{1}H spin-lock pulses to protein samples, multiple spectra need to be collected, and in each spectrum, the signals must have reasonably large signal-to-noise ratios. Additionally, for quantification a signal would ideally be from an isolated cross-peak involving only one pair of assigned ^{15}N nuclei rather than a cluster of cross-peaks.

Considering all these criteria, we have chosen to perform experiments on a magnetically aligned sample of selectively ^{15}N-Val labeled fd bacteriophage. The high-resolution structure of the major coat protein in intact fd bacteriophage has been solved by OS solid-state NMR (Zeri et al., 2003a). Interestingly, the sequence of the

fd coat protein contains four nearby valines, V29, V30, V31 and V33. The first three valines are sequential and can be tested for sequential resonance assignments, while the spin exchange with V33 can be potentially used for longer-range i/i+3 and i/i+4 spin exchange experiments. The four valine signals are reasonably well separated in one-dimensional OS solid-state NMR spectrum (Zeri et al., 2003a). These properties allow us to perform multiple 18-hour experiments to test each spin exchange condition and monitor the cross-peak intensity for a single pair of ^{15}N nuclei with a signal-to-noise ratio greater than 6:1, which can be difficult to obtain with other protein samples (Knox et al., 2010).

In the example spectra (Figure 6.5.A), cross-peaks from the V29/V30 and V30/V31 pairs are of sizable intensity. Since the cross-peaks of V30/V31 are close to the diagonal, we focus on the two cross-peaks of V29/V30 for the quantification and systematic comparison of intensities. Cross-peaks involving V33 are near or below the noise level in the current experiments. Therefore, the characterization of long-range spin exchange may require longer signal averaging or the development of stronger samples, and it is beyond the scope of the present study. The pulse length and mismatch percentage between ^{1}H and ^{15}N channels are the first parameters to optimize (Figure 6.5.B), and on-resonance ^{1}H spin-lock pulses are used in this case. While in all spectra a 5 ms pulse length yields the highest intensity, a 22% mismatch has provided slightly higher intensity than other conditions. This optimal mismatch percentage agrees with the previously found optimal condition for the similar filamentous Pf1 bacteriophage (Knox et al., 2010). Therefore, we chose 5 ms length and 22%

mismatch for the comparison between on-resonance and "magic-angle" ^{1}H spin-lock pulses (Figure 6.5.C). Remarkably, the results are quite different from those obtained from the NAL single crystal. While the "magic-angle" ^{1}H spin-lock irradiation nearly quenches the spin exchange in the NAL single crystal, it provides better conditions than the on-resonance pulse in the aligned sample of fd bacteriophage. It should be noted that the highest cross-peak intensity using "magic-angle" irradiation appears in the spectrum with 7 msec mixing time, rather than 5 msec mixing time in those spectra using on-resonance irradiation, possibly because the "magic-angle" spin-lock lengthens $T_{1\rho}$. We have also tested "magic-angle" ^{1}H spin-lock pulse on a sample of the membrane-bound form of uniformly ^{15}N-labeled Pf1 coat protein in magnetically aligned bicelles. The data showed strong cross-peaks from ^{15}N-^{15}N spin exchange, which are about the same intensity as those from on-resonance irradiations.

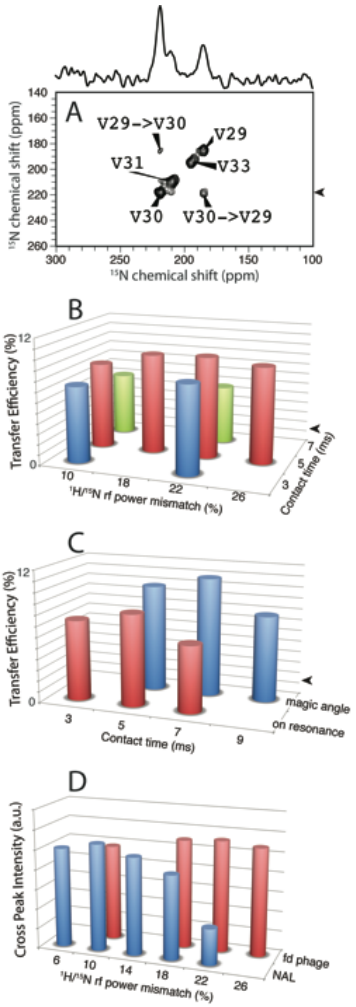

Figure 6.5. Experimental optimization of ^{15}N-^{15}N spin exchange condition in the sample of ^{15}N-Val labeled intact fd bacteriophage. A. An example spectrum and the resonance assignments. The arrow indicates where the one-dimensional slice is extracted. The average intensity of the two well-separated cross-peaks between V29 and V30 are used to quantify the spin exchange efficiency. B. Optimization of the mismatch percentage and contact time with on-resonance ^{1}H channel spin-lock pulse. C. Comparison of cross-peak intensity between the on-resonance and magic-angle ^{1}H spin-lock pulses, with the mismatch percentage maintained at 22%. Transfer efficiency is calculated by dividing the cross-peak intensity in the experiments by the main peak intensity in the control experiment, which uses a 0.1 sec Z-filter and no spin-lock pulses (Tang et al., 2012). Notably, the mismatch percentage for magic-angle pulses is calculated from the ratio of B_{eff} of ^{1}H channel and B_1 of ^{15}N channel; by contrast, the ratio of the two B_1 fields is used in the calculation for on-resonance pulses. D. The sensitivity to the mismatch percentage is different between NAL single crystal and fd phage sample. Cross-peak intensities are plotted in an arbitrary scale (a.u.).

In conclusion, the experimental results from protein samples undergoing global motions, such as filamentous bacteriophage particles and membrane proteins rotating about the bilayer normal, are in contrast to the analytical derivations and experimental results from the NAL single crystal. While the "magic-angle" ^{1}H spin-lock irradiation nearly quenches the spin exchange in a single crystal, in proteins it provides strong cross-peaks that are of similar intensities as the on-resonance case. This phenomenon may result from the combined effect of several underlying mechanisms, which are discussed in the following section.

6.10. Discussion of Motion Interference and Spin Exchange Distance

We recently generalized the "motion-adapted" properties of a homonuclear decoupling sequence MSHOT-Pi4/Pi, whose performance is especially efficient for membrane protein samples but not for single crystals (Lu and Opella, 2013; Lu et al., 2012). The underlying mechanism of the "motion-adapted" property was characterized theoretically and experimentally as the interference between the protein's rotational exchange motion and the radiofrequency pulses. Importantly, in recent work to apply multiple contact cross-polarization to enhance signals, Nevzorov and co-workers observed much more pronounced signal enhancement for membrane protein sample than for NAL single crystal (Nevzorov, 2011b; Tang and Nevzorov, 2011), and this technique was later adapted to enhance signals in MAS solid-state NMR on membrane proteins undergoing rotational diffusion (Lu et al., 2013a). Another study analyzed the effect of the static disorder and uniaxial rotational diffusion of the protein samples on

the appearance of separated local field spectra, and showed evidence of inhomogeneously broadened line widths (Nevzorov, 2011a). Here the discovery that a "magic-angle" ^{1}H spin-lock pulse is a "forbidden" condition in a single crystal, but provides better ^{15}N-^{15}N spin exchange in a bacteriophage sample, is to a certain extent, another case of a "motion-adapted" sequence, and may have its roots in a similar underlying mechanism.

This speculation is supported theoretically, since we previously showed that a "magic-angle" ^{1}H spin-lock pulse (*i.e.,* Lee-Goldberg condition) has the highest susceptibility to motional interference, compared to other homonuclear decoupling sequences such as SAMPI4 and MSHOT-Pi4 (Lu and Opella, 2013). The reason is because in the first-order average Hamiltonian,

$$\overline{H}^{(1)} = \frac{1}{\tau}\int_{t_0}^{t_0+\tau} dt\sqrt{6}\omega_D \sum_{m=-2}^{+2} T_{2m}^{AB} \exp\{-im\omega_{eff}t\} d_{m0}^{2}(\theta_{magic}), \qquad \text{Eq. 6.20}$$

the spatial component, ω_D, of the homonuclear dipolar coupling, which becomes time-dependent as a result of sample rotational motion, interferes with the averaging of $\exp\{-im\omega_{eff}t\}$ and causes the Hamiltonian term to become non-zero. The same effect occurs for most of the Hamiltonians discussed in this article. Note that all the Hamiltonian terms shown in Equations 6.11, 6.14, 6.16, 6.18 and 6.19 are calculated by integration over the τ period under the assumption that dipolar couplings $\omega_{Hi,Hj}$, $\omega_{Hi,Ni}$ and $\omega_{Hj,Nj}$ are time-independent. These terms will have more complicated dependence on the ^{1}H spin lock angle θ, and many additional terms would appear if the spatial part of the dipolar couplings interferes with their averaging by the term

$\exp\{-im\omega t\}$. Therefore, we could qualitatively conclude that, when motion interference effects exist for a protein undergoing global reorientation, the "magic-angle" ^{1}H spin-lock pulse becomes much less efficient in stopping the polarization transfer through ^{1}H-^{1}H homonuclear dipolar couplings, and this condition is no longer "forbidden."

Similarly, sample motions can also cause the Hartmann-Hahn match or mismatch condition to be more promiscuous in protein samples. For example, rotational motions at the mismatched frequency can partially recreate the matching condition between the two channels. This may be one of the reasons that in the NAL single crystal the mismatch percentage strongly influences the cross-peak intensity, but in the fd bacteriophage sample the effect is much less pronounced (Figure 6.5.D). The less specific matching conditions in protein samples further increase the potential spin-exchange pathways, but also may result in the adverse effect that the polarization on the ^{15}N spins can be drained through transferring to the ^{1}H spins.

We have described how the sample motions may partially reverse the inhibition of polarization transfer from "magic-angle" irradiations; however, this still leaves the open question of how the "magic-angle" pulse can produce cross-peak intensities similar to, or even in some case larger than, the on-resonance pulse. One of the reasons may be that "magic-angle" irradiation provides tighter restrictions on polarization transfers than on-resonance irradiation does. Therefore, pathways between a pair of ^{15}N spins may become more local in nature and involve a smaller group of ^{1}H spins. More specifically, magic-angle irradiation strongly suppresses the

multiple-step mechanisms, and thus reduces the repolarization of ^{1}H spins. Since ^{1}H spins in protein samples usually experience fast decay and short $T_{1\rho}$ relaxation times, the reduction in ^{1}H repolarization may conserve the energy during spin-exchange. The slowdown of decay and conservation of energy is reflected by the polarization reaching maxima at longer contact time when magic-angle irradiation is applied (Figure 5C). Another view of spin exchange was recently provided by Khitrin *et al.* based on spin temperature theory (Khitrin et al., 2011), where the authors drew analogy between the on-resonance MMHH pulse sequence and the cross-relaxation driven spin diffusion (CRDSD) (Xu et al., 2008). The article has only analyzed the on-resonance MMHH pulses, and we have noted the "magic-angle" spin-lock irradiations described here would add additional complication to the situation by slowing down the equilibration in the proton bath. Potentially, the analysis from spin temperature theories on magic-angle irradiation may also contribute important views to the question.

It should also be noted that ^{15}N spins in fd bacteriophage sample are closer in space than those in NAL single crystals, which provides better opportunities for second-order TSAR mechanism to function; however, the ^{1}H-^{15}N dipolar coupling between non-bonded ^{1}H and ^{15}N spins are still very small. We have calculated the orientation-dependent ^{1}H-^{15}N dipolar couplings between the amide groups of residues V29 and V30 based on the structure of the coat protein in intact fd bacteriophage particles (Zeri et al., 2003a). While the directly-bonded ^{1}H and ^{15}N have dipolar couplings > 6 kHz, the inter-residual dipolar couplings relevant to the TSAR

mechanism are only 208 Hz and 167 Hz. Other possible ^{1}H simultaneously coupled to both ^{15}N have dipolar couplings of 410 Hz and 24 Hz, or 167 Hz and 56 Hz. The lack of ^{1}H that can strongly couple to both ^{15}N undermines the efficient spin-exchange through the TSAR mechanism. Nevertheless, we note that a dipeptide single crystal N-acetyl-L-^{15}N-valyl-L-^{15}N-leucine (NAVL) was previously used to monitor spin-exchange for the intramolecular cross-peak between valine and leucine (Khitrin et al., 2011; Traaseth et al., 2010), and the comparison of this rigid crystal sample with biological protein sample undergoing rotational motions may be useful for further understanding spin-exchange. The increase of spin-exchange through the TSAR mechanism is likely to work synergistically with the reduction in ^{1}H repolarization and the motion-induced ^{1}H coupling pathways to make magic-angle pulse an efficient condition.

In terms of the practical applications, the angle of the ^{1}H spin-lock irradiation, which can be varied from on-resonance to the "magic-angle," offers a potential way to adjust the range of spin-exchange and provides another degree of freedom to optimize dilute-spin-exchange experiments. Notably, it has also been shown that varying the mismatch percentage can also be used to adjust the range of spin-exchange through the dipolar truncation effect in MMHH experiments (Tang et al., 2012). Due to the complexity of spin-exchange mechanisms, optimal conditions may need to be identified empirically for each sample, especially proteins undergoing global reorientation.

6.11. Comparison of PDSD and MMHH

For ^{15}N-^{15}N spin-exchange in OS solid-state NMR, the comparisons of proton-driven spin diffusion (PDSD) and the recently developed pulse sequences, MMHH or CRDSD, have been made in single crystals (Khitrin et al., 2011; Traaseth et al., 2010) and membrane proteins in aligned bicelles (Lu and Opella, 2014; Tang et al., 2012). Depending on the orientation of the single crystal, PDSD was reported to give much higher cross-peak intensity or nearly no cross-peak intensity with up to 4 seconds mixing. Similarly, with membrane-bound Pf1 coat protein it was shown that the PDSD spectrum had high-intensity cross-peaks for many sequential connections, but also missed several connections that were otherwise shown in MMHH spectra (Tang et al., 2012). In our recent application to a mercury transporter protein (Lu and Opella, 2014), similar trends showed that the PDSD spectrum provided a strong cross-peak for one pair of neighboring leucines while it was completely missing for the other pair. The MMHH spectrum showed cross-peaks for both pairs of residues, albeit with intensities that were much lower than the single cross-peak observed in the PDSD spectrum.

In the fd bacteriophage sample we systematically optimized the spin exchange conditions. For PDSD experiments, we varied the mixing time between 3 and 6 seconds. A 4 sec mixing time was found to give the largest V29-V30 cross-peak intensity, agreeing with the results obtained from a NAVL single crystal (Traaseth et al., 2010). One of the cross-peaks is compared to the MMHH spectrum and the control experiment in Figure 6.6. The cross-peak in the PDSD spectrum shows significantly higher intensity than that in the MMHH spectrum, agreeing with previous reports.

Notably, we have already taken into account that the amount of time needed to collect each scan is different between MMHH and PDSD experiments, for the fd bacteriophage sample, even with far fewer scans, the cross-peak intensity of the PDSD spectrum is still higher than that of the MMHH spectrum. By contrast, we have found that in the NAL single crystal sample the performance of MMHH mixing exceeds that of PDSD, after taking into account the different amount of time for each experiment. Qualitatively, the higher intensity in the PDSD spectrum compared to the MMHH spectrum is likely due to the differences in T_1 and $T_{1\rho}$ relaxation times. For intact bacteriophage or membrane proteins in aligned bicelles, $T_{1\rho}$ is even shorter than that in a single crystal, leading to a rapid decay of the MMHH cross-peaks.

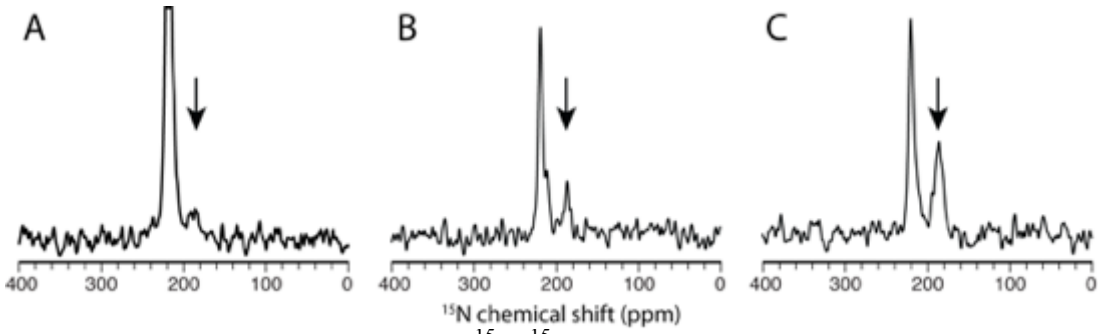

Figure 6.6. One-dimensional slice of ^{15}N-^{15}N spin-exchange spectrum in the sample of ^{15}N-Val labeled intact fd bacteriophage. Arrows denote the V30-V29 cross-peak. A. Control spectrum with 0.1 sec Z-filter and no MMHH pulse. B. Magic-angle MMHH spin-exchange spectrum with 7 msec contact time and 22% mismatched amplitude. C. 4 sec PDSD spin-exchange spectrum. All the spectra are acquired with approximately the same amount of time for reliable comparison of signal to noise, and the plots are scaled to match the same noise level.

6.12. Conclusion

Awareness of the proton-relay mechanism for spin-exchange is important for designing polarization transfer experiments. Switching of the ^{1}H irradiation frequency

between on-resonance and off-resonance up to the “magic angle” offers another degree of freedom to optimize the exchange of magnetization, especially for biological samples where substantial motions may be present.

Chapter 6 is, in full, a reprint of the material “Mechanism of dilute-spin-exchange in solid-state NMR” as it appears in J. Chem. Phys. 140(12):124201 by Lu GJ, Opella SJ. The thesis author was the primary author of the paper.

Chapter 7. The Structure of the Mercury Transporter MerF in Phospholipid Bilayers: a Large Conformational Rearrangement Results from N-terminal Truncation

7.1 Abstract

The three-dimensional structure of the 81-residue mercury transporter MerF determined in liquid crystalline phospholipid bilayers under physiological conditions by Rotationally Aligned (RA) solid-state NMR has two long helices, which extend well beyond the bilayer, with a well-defined inter-helical loop. Truncation of the N-terminal 12 residues, which are mobile and unstructured when the protein is solubilized in micelles, results in a large structural rearrangement of the protein in bilayers. In the full-length protein, the N-terminal helix is aligned nearly parallel to the membrane normal and forms an extension of the first transmembrane helix. By contrast this helix adopts a perpendicular orientation in the truncated protein. The close spatial proximity of the two Cys-containing metal binding sites in the three-dimensional structure of full-length MerF provides insights into possible transport mechanisms. These results demonstrate that major changes in protein structure can result from differences in amino acid sequence (e.g. full-length vs. truncated proteins) as well as the use of a non-native membrane mimetic environment (e.g. micelles) vs. liquid crystalline phospholipid bilayers. They provide further evidence of the importance of studying unmodified membrane proteins in near-native bilayer

environments in order to obtain accurate structures that can be related to their functions.

7.2 Introduction

The three-dimensional structure of a protein is determined by two principal factors: its sequence of amino acids and its environment (Anfinsen, 1973). For globular proteins that are soluble in aqueous solution the focus of the 'folding problem' has been on the sequence of amino acids, while the environmental contribution has been largely ignored because various solvent conditions and even crystallization generally result in minimal perturbation of their structures, as demonstrated by many examples where essentially the same structures have been determined by X-ray crystallography and solution NMR. For membrane proteins, in contrast, drastic modifications have been made to both the amino acid sequences and the choice of membrane mimicking environments to facilitate structure determination. For example, to enhance crystallization, amino acid sequences have been subject to multiple mutations, truncations of termini and loops, and insertions of globular proteins, such as T4 lysozyme, in the middle of the protein (Rosenbaum et al., 2007). A wide range of membrane mimetic environments has been used in studies of membrane proteins by both X-ray crystallography and solution NMR (Warschawski et al., 2011), including mixed organic solvents, detergent micelles, isotropic bicelles, nanodiscs, and lipid cubic phases of monoolein and cholesterol (Landau and Rosenbusch, 1996). Relatively little is known about the effects of these environments

on membrane protein structures because so few structures have been determined in liquid crystalline phospholipid bilayers for comparisons.

Rotationally aligned (RA) solid-state NMR (Das et al., 2012; Park et al., 2010a) merges elements of Oriented Sample (OS) solid-state NMR[5], as performed on stationary, aligned samples, with those of Magic Angle Spinning (MAS) solid-state NMR of unoriented 'powder' samples (Schaefer and Stejskal, 1976). The robustness of RA solid-state NMR has been demonstrated by the structure determination of a 350-residue G-protein coupled receptor (GPCR) in phospholipid bilayers (Park et al., 2012b). The most distinctive feature of the method is its reliance on a universal property of membrane proteins, which is that they undergo rapid rotational diffusion about the bilayer normal in liquid crystalline phospholipid bilayers (Cone, 1972). In early high resolution solid-state NMR experiments it was shown that motion about a single axis yields an axially symmetric powder pattern with its frequency breadth scaled by the angle between the principal axis of the nuclear spin interaction, e.g., the bond axis in a two-spin dipolar couplings (DC) (Gutowsky and Pake, 1950). The same spectroscopic principles applied to chemical shift anisotropy (CSA) in ^{31}P NMR spectra of phospholipids (McLaughlin et al., 1975) and ^{13}C' NMR spectra of bacteriorhodopsin (Lewis et al., 1985) demonstrated that both lipid and protein components undergo rapid rotational diffusion in liquid crystalline bilayers. The frequency of the parallel edge of the motionally scaled powder patterns is exactly the same as that measured from the single-line resonance signals observed from stationary, aligned samples in OS solid-state NMR spectra. Thus, it is possible to

obtain the same angular restraints for the calculation of the three-dimensional structures of the membrane proteins from stationary mechanically or magnetically aligned, or unoriented proteoliposome samples (Park et al., 2010a). The spectral resolution for the unoriented samples results from the application of MAS solid-state NMR to the uniformly ^{13}C and ^{15}N labeled proteins, which is followed by recoupling of the motionally averaged powder patterns (Chan and Tycko, 2003; Griffin, 1998).

```
                                10         20         30         40         50         60         70         80
Full-length MerF        KDPKTLLRV SIIGTTLVAL SSFTPVLVIL LGVVGLSALT GYLDYVLLPA LAIFIGLTIY AIQRKRQADA SSTPKFNGVK KS*
Truncated MerF (MerFt)             IGTTLVAL SSFTPVLVIL LGVVGLSALT GYLDYVLLPA LAIFIGLTIY AIQRKRQADA SS*
```

Figure 7.1. Amino acid sequences of full-length 81-residue MerF and truncated 60-residue MerFt.

Mercury transport membrane proteins play a crucial role in the bacterial mercury detoxification system (Barkay et al., 2003; Melnick and Parkin, 2007; Parks et al., 2013). They transport ionic mercury from the periplasmic protein MerP (Qian et al., 1998; Serre et al., 2004; Steele and Opella, 1997) across the bilayer to MerA (Johs et al., 2011; Schiering et al., 1991), the enzyme that reduces Hg(II) to Hg(0). The 81-residue MerF (Wilson et al., 2000) has two trans-membrane helices and two mercury-binding sites, both of which contain a pair of cysteine residues. We have expressed MerF without the N-terminal methionine and with the cysteines mutated to serines (Figure 7.1). In principle, this is the same as studying an unmodified MerF protein because the spectra of polypeptides with and without Ser substituted for Cys are identical. However, the absence of cysteines increases the stability of the samples; future studies will compare these and other mutations of MerF to understand structure-function relationships. Since the initial solution NMR spectra of MerF in micelles (Howell et al., 2005) were dominated by intense, narrow resonances from mobile residues near the N- and C- termini, a total of 12-residues from the N-terminus and 9-residues from the C-terminus were removed, eliminating all of the mobile residues to form a 60-residue truncated protein, which retained the helix-loop-helix core of the native protein. This was the first example of a membrane protein with more than a single trans-membrane helix used in the development of many NMR methods. We have determined the three-dimensional structure of MerFt (truncated) in micelles by solution NMR (Howell et al., 2005), in magnetically aligned bilayers by OS solid-state

NMR (De Angelis et al., 2006b), and in proteoliposomes by RA solid-state NMR (Das et al., 2012).

Here we describe the structure determination of the full-length MerF protein by RA solid-state NMR in its native phospholipid bilayer environment. This structure provides some of the first insights into its mechanism of transporting metal ions across into the cell. It also enables direct comparisons of the structures of the full-length and truncated forms of the protein under identical experimental conditions. Remarkably, we find drastic structural perturbations caused by removal of the N-terminal residues. These residues are mobile and unstructured in micelles, but are differently structured in the full-length and truncated forms of the protein in bilayers.

7.3 NMR Experiments and Structural Calculation

MerF was isolated and purified from bacteria, and reconstituted into 1,2-di-O-tetradecyl-*sn*-glycero-3-phosphocholine (14-o-PC) proteoliposomes. The significant reduction of the ^{13}C' powder pattern due to motional averaging verifies that the protein is undergoing rotational diffusion fast enough (>10^6 Hz) to fully average the powder patterns of the ^{13}C and ^{15}N nuclear spin interactions at 25°C, a temperature above the gel to liquid crystalline phase transition of protein-containing 14-o-PC bilayers.

Next, two-dimensional ^{13}C-^{13}C and ^{13}C-^{15}N correlation spectra (Figure 7.2) provides the initial characterization of the protein. ^{13}C-^{15}N correlation spectrum locates each pair of the backbone amide ^{15}N and ^{13}Cα. Similar to HSQC spectrum in solution NMR, it serves as the basis for later resonance assignments. On the other

hand, ^{13}C-^{13}C correlation spectrum allows the visualization of all the side chain ^{13}C resonances and preliminary resonance assignments. Short ^{13}C-^{13}C mixing time using 50 ms PDSD or 20 ms DARR usually allows only intra-residual correlation; in contrast, long mixing time of 200 ms DARR allows the identification of many correlation between sequential residues. However, the resolution in the two-dimensional ^{13}C-^{13}C limits the accomplishment of the complete resonance assignments.

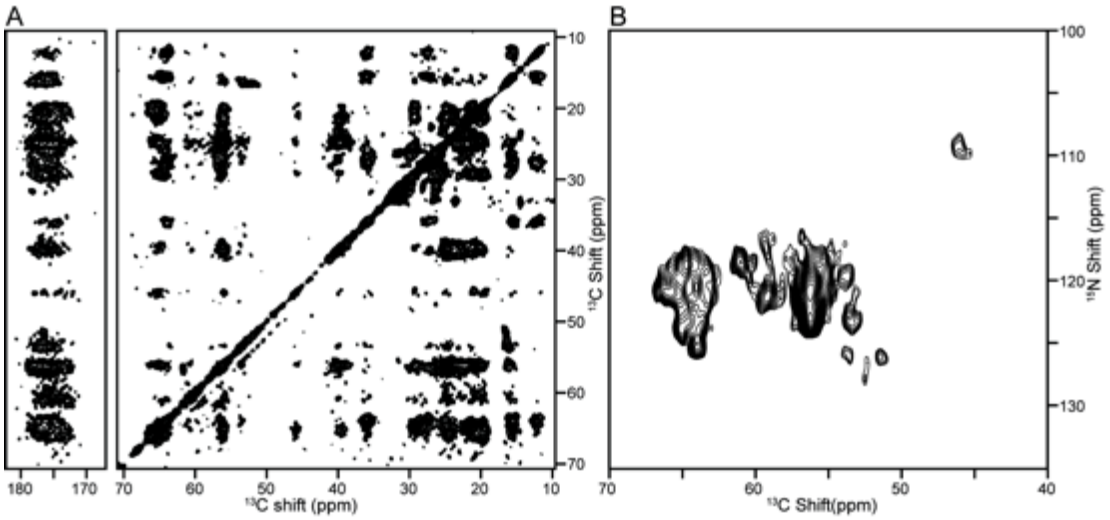

Figure 7.2. Two-dimensional MAS spectra of uniformly $^{13}C/^{15}N$ labeled MerF in 14-o-PC proteoliposomes at 25°C: A. Homonuclear $^{13}C/^{13}C$ spin-exchange correlation spectrum with 200ms DARR mixing. B. Heteronuclear $^{13}C/^{15}N$ correlation spectrum.

The analysis of three-dimensional HnNCo, HnNCa and HcCxCx MAS solid-state NMR spectra provided simultaneous resonance assignments and measurements of structural restraints in the form of DCs. Figure 7.3 shows the pulse sequence and correlation scheme. Figure 7.4 shows representative resonance assignment through sequential backbone "walk", and Figure 7.5 shows an example of the observance of angular restraints in the form of ^{1}H-^{15}N and ^{1}H-$^{13}C\alpha$ heteronuclear dipolar coupling.

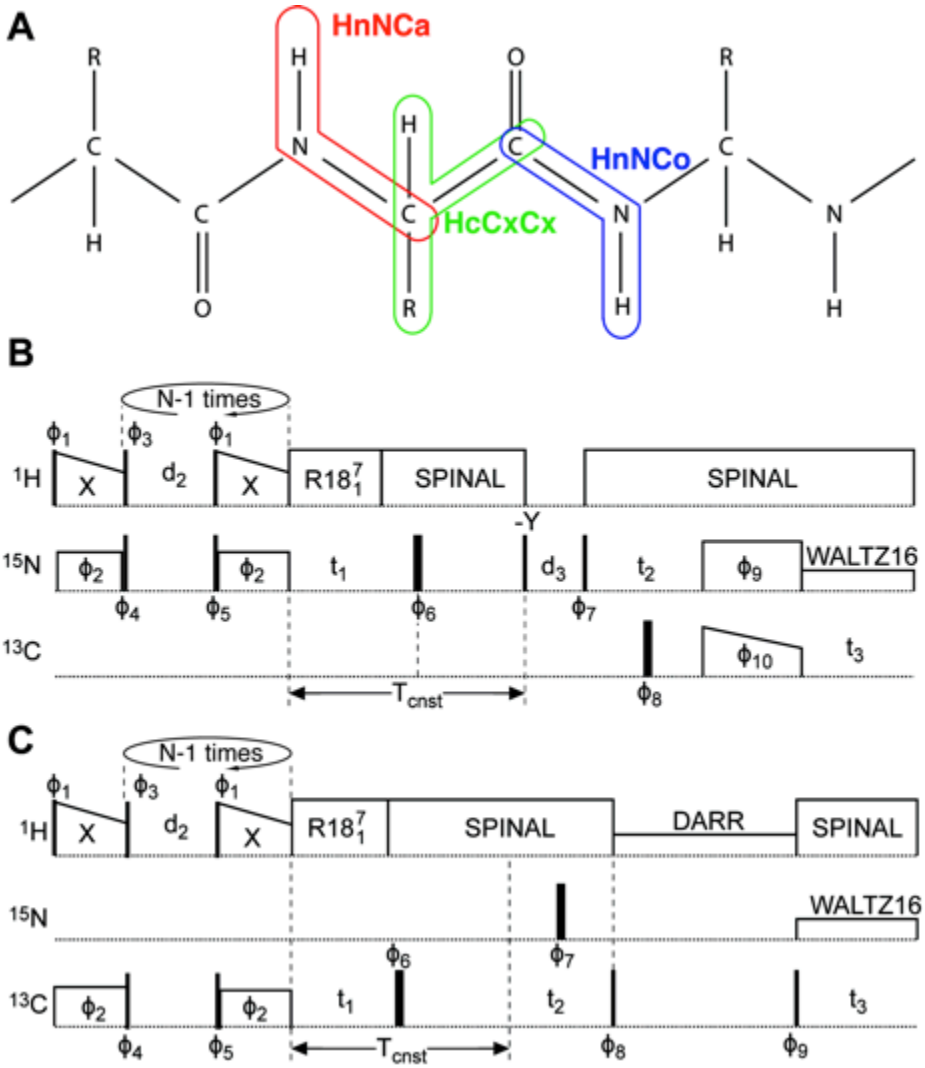

Figure 7.3. Schematic drawing and timing diagrams for the three three-dimensional experiments. A. Schematic drawing of a polypeptide outlines the atoms in the coupling pathways utilized in the NMR experiments. B. and C. The timing diagrams for the three three-dimensional experiments used to make resonance assignments and measure the frequencies that provided the angular restraints for structure determination. The inclusion of one dipolar coupling dimension in each of the experiments increases the resolution of the spectra, and it is especially important for discerning the assignments among the same types of amino acids, since their ^{13}Cα, ^{13}C' and amide ^{15}N atoms typically have similar chemical shift frequencies. The use of these experiments combines the resonance assignments and dipolar coupling measurements in a single step, reducing the total number of three-dimensional experiments that are required. B. The pulse sequence for HnNCa and HnNCo experiments with ^{1}H-^{15}N multiple-contact cross polarization. C. The pulse sequence for the HcCxCx experiment with ^{1}H-^{13}C multiple-contact cross polarization.

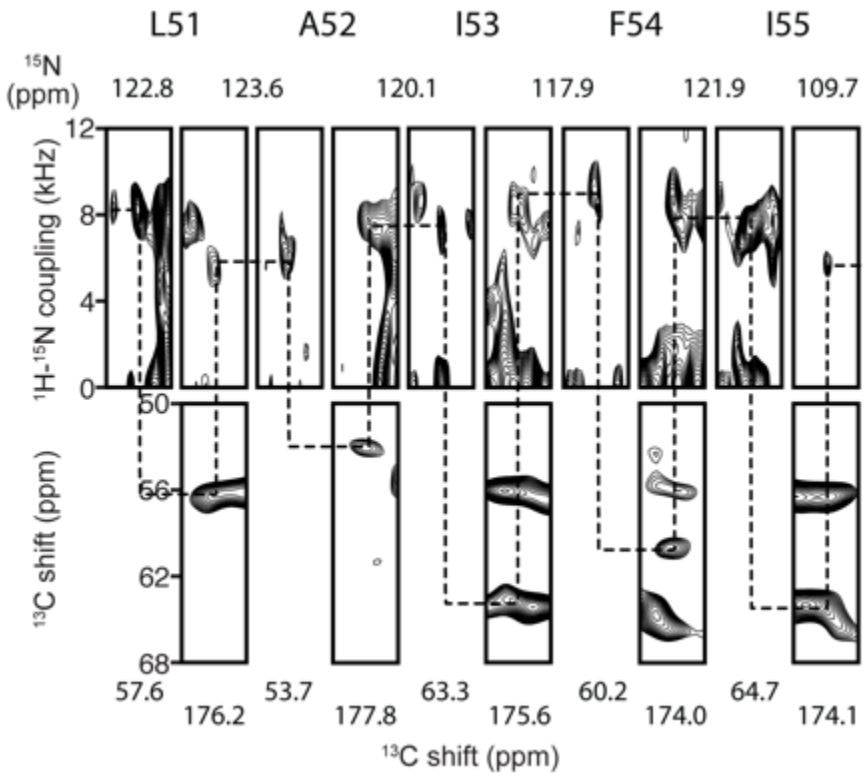

Figure 7.4. Representative strip plots for residues L51-I55 of uniformly $^{13}C/^{15}N$ labeled MerF in 14-o-PC proteoliposomes at 25 °C. Dashed lines are provided as guides through the backbone resonance walk. For each residue, the connectivities proceed through the sequence of HnNCa, HcCxCx and HnNCo experiments.

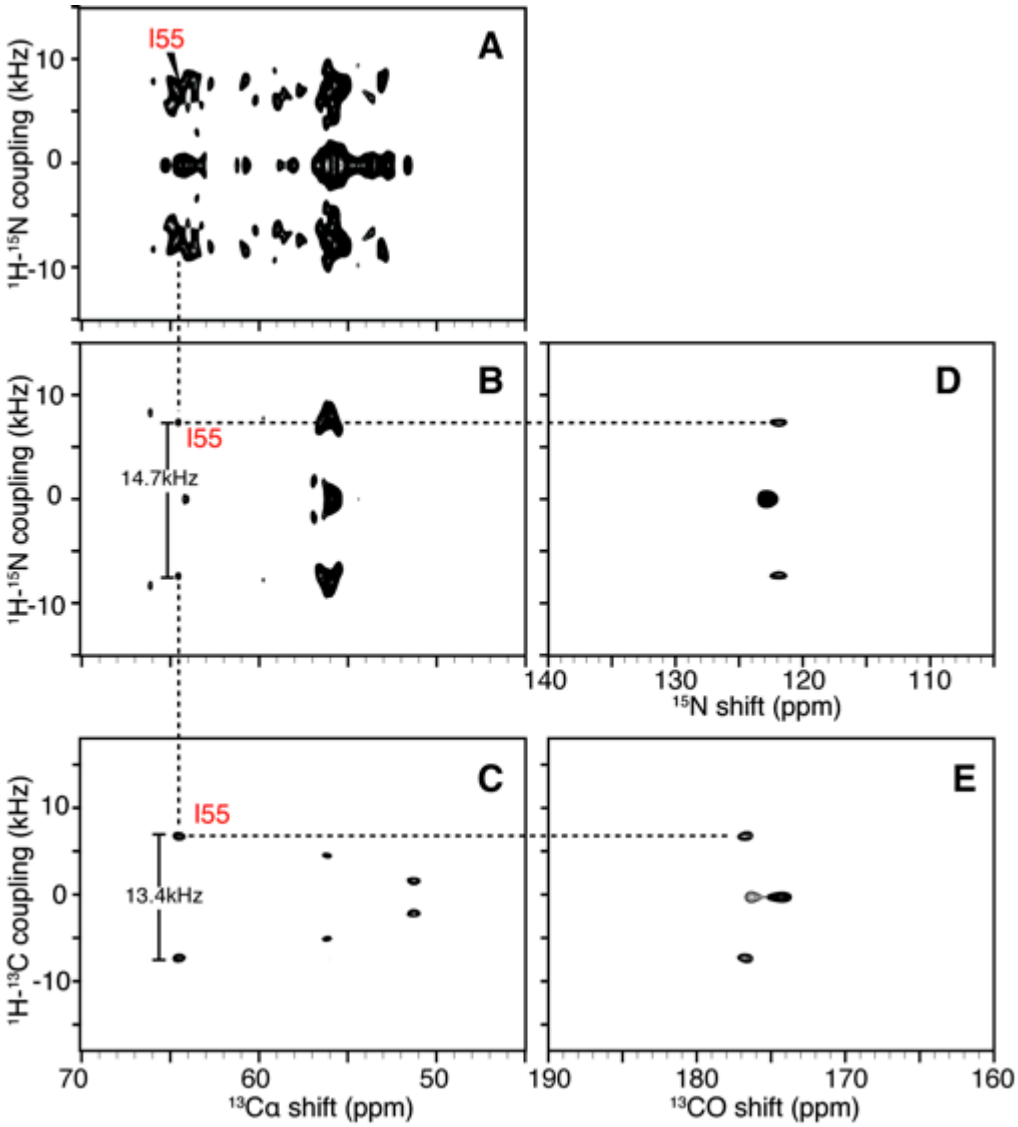

Figure 7.5. Examples of spectroscopic data for residue I55 obtained from MAS solid-state NMR spectra of uniformly $^{13}C/^{15}N$ labeled MerF in 14-o-PC proteoliposomes at 25°C: A. Two-dimensional ^{1}H-^{15}N DC/^{13}C shift separated local field (SLF) spectrum. B. and D. Two-dimensional ^{1}H-^{15}N DC/$^{13}C\alpha$ shift and ^{1}H-^{15}N DC/^{15}N shift SLF planes selected from a three-dimensional HnNCa spectrum at the ^{15}N shift frequency of 120.7 ppm and the $^{13}C\alpha$ shift frequency of 64.6 ppm. C. and E. Two-dimensional ^{1}H-$^{13}C\alpha$ DC/$^{13}C\alpha$ shift and ^{1}H–$^{13}C\alpha$ DC/^{13}C' shift SLF planes selected from a three-dimensional HcCxCx spectrum at the 13C' shift frequency of 176.8 ppm and the $^{13}C\alpha$ shift frequency of 64.1 ppm. All spectral planes are associated with residue I55. The dashed line traces the correlations among the resonance frequencies. The DC frequencies in the spectra correspond to the rotary resonance recoupling at n=2 of the motionally averaged powder pattern (Zhao et al., 2001).

The first benefit of the approach is the improvement of the spectral resolution through the inclusion of a DC frequency dimension in each experiment. The site-to-site variation of the motionally averaged DC frequencies is able to resolve signals from the same types of amino acids even in situations where their $^{13}C\alpha$, $^{13}C'$ and amide ^{15}N shifts have similar frequencies (Table 7.1 for an example statistics). The second benefit is that only two magnetization transfer steps are required, compared to the three or more transfer steps in resonance assignment methods based on the observation of isotropic chemical shifts (Franks et al., 2007; Pauli et al., 2001). Not only is the sensitivity significantly improved, but also the total number of three-dimensional experiments is reduced. Multiple-contact cross polarization (Pines et al., 1973) was incorporated into MAS pulse sequences capable of efficient dipolar recoupling using $R18^7_1$ (Levitt, 2007). Notably, the approach is applicable only to membrane proteins undergoing rotational diffusion, and not polycrystalline or other immobile proteins.

Table 7.1. The ranges of the chemical shift and dipolar couplings of leucine residues with respect to all residues in MerF. The limited ranges of isotropic chemical shifts illustrate the advantage of using dipolar coupling to resolve signals from the same types of amino acids.

	Leucine residues	All residues excluding Glycines	Leucine span percentage
^{15}N chemical shift (ppm)	118.06 to 124.02	104.52-125.73	28%
^{13}Cα chemical shift (ppm)	55.15 to 57.80	51.18 to 66.37	17%
^{13}C' chemical shift (ppm)	174.67 to 177.52	171.37 to 178.13	42%
^{1}H-^{15}N dipolar coupling (kHz)	1.23 to 19.01	1.23 to 19.01	100%
^{1}H-^{13}Cα dipolar coupling (kHz)	0.6 to 15.1	0.2 to 17.7	83%

A long-range inter-helical distance restraint between F23 and Q63 or Q67 unambiguously assigned from ^{13}C-^{13}C correlation spectra due to the distinctive chemical shifts of carbons in aromatic rings and Cγ of Gln (Figure 7.6) was incorporated along with the DC frequencies in the calculation of the protein structure. Table 7.2 summarizes all the completely assigned NMR observables of MerF. Table 7.3 and Figure 7.7 summarizes the structural restraints and the quality of structural calculation, which follows a protocol similar to that described previously (Das et al., 2012). The structure of MerF in phospholipid bilayers is shown in Figure 7.8.

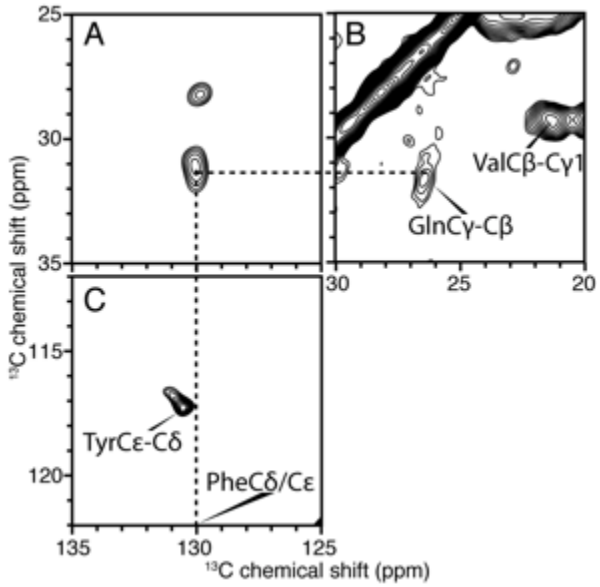

Figure 7.6. Interhelical long-range distance restraints for MerF structure determination. A. Two-dimensional ^{13}C-^{13}C correlation spectrum obtained with 200ms DARR mixing for through-space correlation of atoms separated by < 5.5 Å (Zech et al., 2005). A distinct cross-peak between Phe Cδ or Cε and Gln Cγ is marked. B. and C. Two-dimensional ^{13}C-^{13}C spectrum obtained with 50ms PDSD mixing for intra-residual correlation. B. Gln Cγ has a unique chemical shift frequency that can be distinguished from Val, Pro and Lys signals. C. The chemical shift of Phe Cδ is well separated from that of Tyr Cδ, which rules out the assignment of the cross-peak in Panel A. to be between Y60 and Gln. Therefore, the crosspeak in Panel A. can only be between Gln Cγ and Phe Cδ or Cε. Since both Q63 and Q67 are in the same helix as F54 and are separated by nine or more residues, they are more than 10 Å apart in space. Consequently, a cross-peak is only feasible between F23 and Q63 or Q67. Many other inter-helical cross-peaks are possibly observed in the spectrum of 200ms DARR mixing; however, only this peak can be unambiguously assigned due to the unique chemical shifts of both Gln Cγ and Phe aromatic ring atoms.

Table 7.2. Values of the isotropic chemical shifts and dipolar couplings measured for individual residues in MerF in 14-o-PC liposomes.

Residue	^{15}N chemical shift (ppm)	^{13}Cα chemical shift (ppm)	^{13}C' chemical shift (ppm)	^{1}H-^{15}N dipolar coupling (kHz)	^{1}H-^{13}Cα dipolar coupling (kHz)
K5	120.90	58.78	176.70	10.82	15.6
T6	121.66	65.62	173.63	-3.87	3.2
L7	124.02	56.09	176.32	16.66	10.8
L8	122.08	56.18	175.82	16.90	0.6
R9	120.75	56.59	176.26	9.07	17.7
V10	119.30	64.09	175.99	7.13	11.9
S11	120.48	61.55	174.79	15.09	10.7
I12	125.38	63.85	176.98	16.75	2.0
I13	122.45	63.91	175.22	13.77	14.9
T15	120.57	66.15	174.67	17.73	8.4
T16	120.30	65.95	173.33	6.34	15.9
L17	123.25	56.29	175.94	8.71	13.3
V18	120.68	64.84	176.24	15.38	15.2
A19	120.35	53.88	177.01	15.42	13.1
L20	119.22	55.89	177.09	13.57	12.9
S21	116.93	57.96	172.15	11.85	12.3
S22	121.91	59.27	172.44	18.52	7.6
F23	120.76	56.22	175.11	7.25	6.5
T24	119.53	63.38	174.14	15.34	13.8
V26	120.73	65.46	175.44	12.96	10.9
L27	120.38	56.18	177.36	18.71	7.1
V28	120.42	66.37	174.36	14.89	12.7
I29	121.96	63.70	176.32	11.96	12.9
L30	122.40	56.79	175.82	15.62	1.6
L31	118.64	56.70	177.53	17.29	0.9
V33	123.00	65.95	174.23	16.51	15.3
V34	123.38	65.16	176.16	15.38	1.7
L36	121.01	55.89	177.20	12.20	15.1
S37	119.22	59.90	174.23	10.82	13.7
A38	125.19	53.06	178.02	18.25	8.9
L39	118.06	55.15	174.84	19.01	5.4
T40	104.52	59.98	171.37	18.27	14.4
Y42	120.78	57.31	172.92	1.65	2.6
L43	123.03	56.50	174.78	1.23	13.8
D44	121.32	56.50	174.78	3.46	14.8
Y45	120.64	59.78	174.01	-1.57	14.6
V46	120.49	60.05	173.03	-1.18	1.6

Table 7.2. Values of the isotropic chemical shifts and dipolar couplings measured for individual residues in MerF in 14-o-PC liposomes. (continued)

Residue	^{15}N chemical shift (ppm)	^{13}Cα chemical shift (ppm)	^{13}C' chemical shift (ppm)	^{1}H-^{15}N dipolar coupling (kHz)	^{1}H-^{13}Cα dipolar coupling (kHz)
L47	120.99	56.70	176.32	16.31	9.0
L48	122.02	57.80	174.67	14.91	11.8
A50	119.13	54.68	177.69	12.89	9.8
L51	122.78	57.57	176.65	17.24	6.0
A52	123.87	53.73	178.02	12.29	16.2
I53	120.07	63.30	176.10	13.67	0.5
F54	117.59	60.21	175.96	17.94	14.6
I55	121.88	64.70	176.87	14.69	13.4
L57	121.97	56.25	176.05	15.24	1.6
T58	121.37	66.34	173.46	16.95	0.2
I59	122.49	63.40	175.99	15.33	11.1
Y60	120.95	60.00	174.89	15.29	15.2
A61	119.91	54.64	178.13	12.20	10.9
I62	122.48	64.20	176.21	15.97	2.8
Q63	118.55	55.74	176.98	13.77	13.7
R64	120.75	56.66	176.37	12.49	5.6
K65	120.97	57.10	176.76	14.26	17.0
R66	121.03	56.30	175.88	8.04	3.3
Q67	122.08	54.94	174.56	14.60	10.7
A68	125.73	51.18	176.50	7.06	3.1
D69	119.35	53.15	174.90	-4.20	2.3

Table 7.3. NMR and refinement statistics for MerF. [a]Evaluated for 10 lowest energy structures out of a total 200 calculated structures for residues 5-69 of MerF. [b]Evaluated with the program PROCHECK (Laskowski et al., 1996).

Experimental NMR restraints	
Total dihedral angle restraints	
phi	79
psi	78
Total dipolar coupling (DC) restraints	
^{1}H-^{15}N DC	59
^{1}H-^{13}C DC	58
Total distance restraints	
inter-helical long-range	1
short-range	48

Structure statistics[a]	
Violations (mean and s.d.)	
Dihedral angle restraints (°)	0.000 ± 0.000
^{1}H-^{15}N DC restraints (kHz)	0.000 ± 0.000
^{1}H-^{13}CA DC restraints (kHz)	3.600 ± 0.966
Deviations from idealized geometry	
Bond lengths (Å)	0.004 ± 0.000
Bond angles (°)	0.546 ± 0.024
Impropers (°)	0.449 ± 0.030
Average pairwise r.m.s.d. (Å)	
Heavy	2.58 ± 0.31
Backbone	1.48 ± 0.27

Ramachandran plot statistics[b]	
residues in most favoured regions (%)	87.990 ± 2.162
residues in additional allowed regions (%)	11.590 ± 2.260
residues in generously allowed regions (%)	0.420 ± 0.676
residues in disallowed regions (%)	0.000 ± 0.000

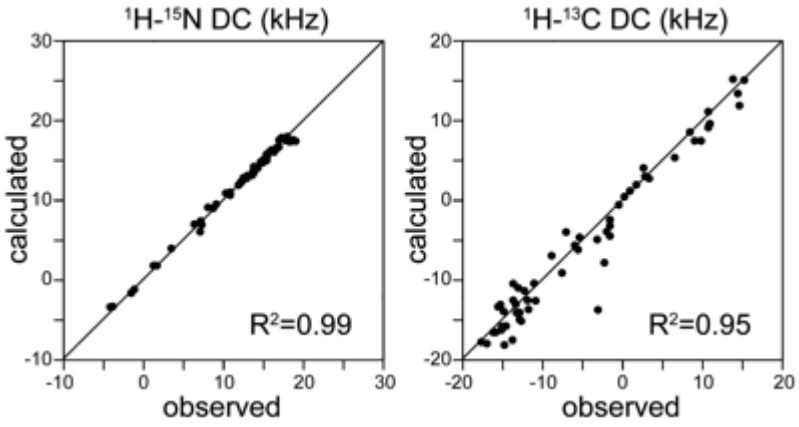

Figure 7.7. Plots of the correlations between observed and back-calculated values of ^{1}H-^{15}N and ^{1}H-^{13}C dipolar coupling used to calculate the structure of MerF in phospholipid bilayers. The R^2 correlation coefficients are shown for each type of restraint.

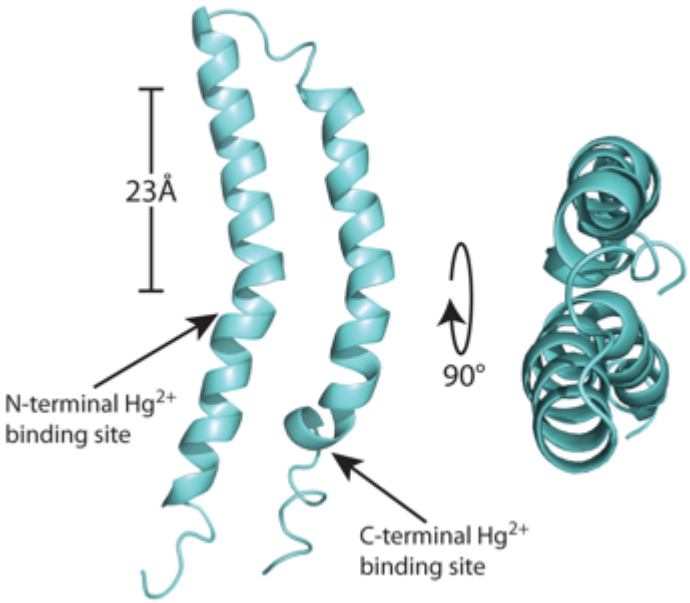

Figure 7.8. The three-dimensional structure of MerF is shown as a ribbon diagram in aqua with the two mercury-binding sites labeled with arrows. The average backbone pairwise rmsd is 1.5 Å. The scale bar corresponds to the 23Å thickness of the hydrocarbons in 14-o-PC lipid bilayer. Both termini of the protein are in the cytosol. The coordinates are deposited in the PDB as 2m67 and the associated data in the BMRB as 19115.

7.4 Significances of the MerF Structure

The motionally averaged DC values provide a direct measurement of the orientations of individual bonds in the polypeptide relative to a common axis, the bilayer normal. Comparing the DCs of the full-length protein to those of the truncated protein (Das et al., 2012), it is clear that the N-terminal portion of the protein, residue I13 through Pro25, has a significantly different structure as a consequence of the truncation performed 12 residues away from Pro25. In contrast, the core of the protein, including the two transmembrane helices and the inter-helical loop, is nearly identical in the full-length and truncated proteins. As examples, the DCs for residues Ala52 (unchanged) and Ala19 (dramatically changed) are compared in Figure 7.9.

The superposition of the structures of the full-length (aqua) and truncated (magenta) proteins in Figure 3 is highly informative. The truncation of the N-terminal residues, which are mobile and unstructured in micelles, results in a dramatic rearrangement of the amphipathic helix (I13-Pro25). These residues change from an orientation parallel to the bilayer surface to one that is nearly perpendicular to bilayer surface and appears to be a continuation of the first trans-membrane helix that extends out of the bilayer. Both structures were determined under identical sample conditions and methods; therefore, the observed structural rearrangement must result solely from the alteration of the amino acid sequence of the protein. In contrast to the N-terminal truncation, the C-terminal truncation does not result in significant structural changes. Clearly, this strengthens the requirement of caution in the use of truncations and other protein modifications of membrane proteins.

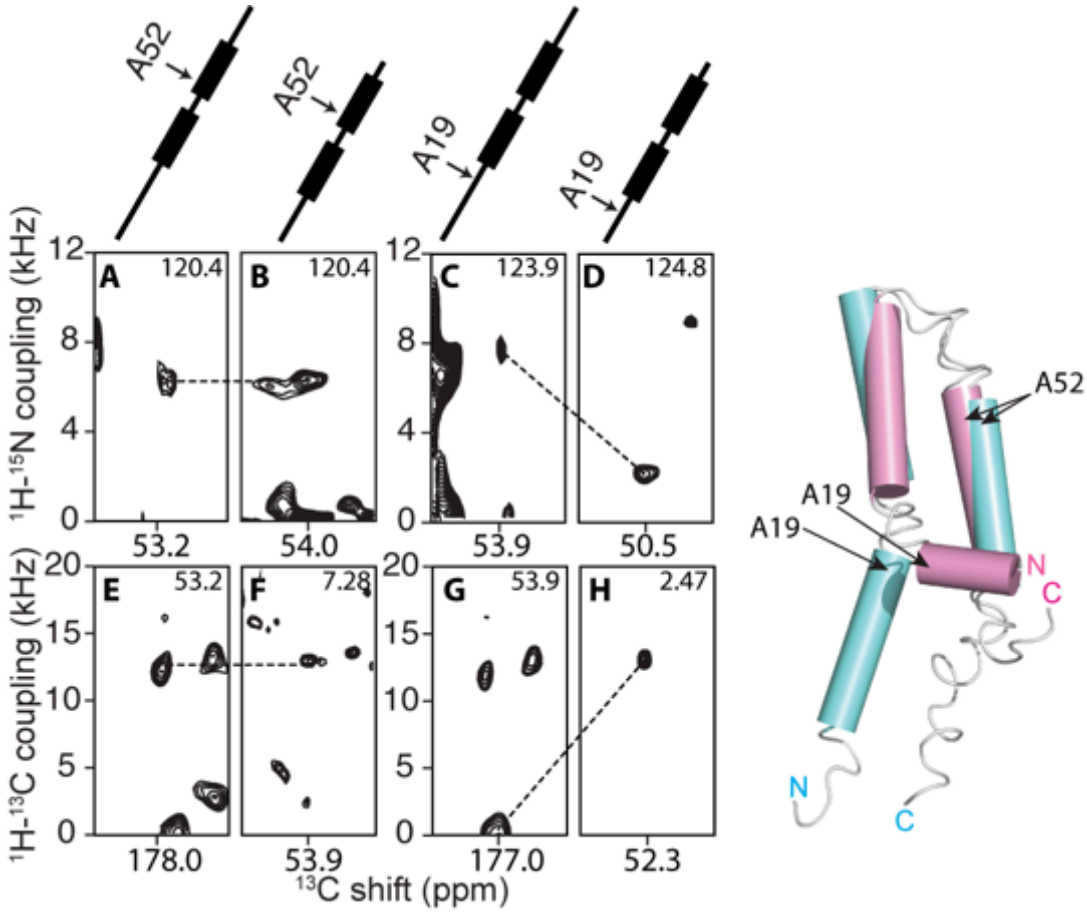

Figure 7.9. Left: Observed changes in orientationally dependent frequencies demonstrate drastic changes in the structure of MerF caused by truncation of residues at the N-terminus. At the top are schematic drawings of the MerF secondary structure (thicker lines are trans-membrane helices) marked with the positions of the residues contributing to the signals. A, C, E and G are slices from spectra of MerF. B, D, F and H are slices from spectra of MerFt. The left panels (A, B, E and F) are from Ala52 located in the second trans-membrane helix. Both the ^{1}H-^{15}N and ^{1}H-^{13}C DCs of Ala52 are very similar for the full-length and truncated proteins. The right panels (C, D, G and H) are from Ala19, located in the N-terminal region, where the conformational change occurs and consequently large changes in DC values are observed. All slices are extracted from three-dimensional spectra at the noted values of the third dimension. Right: The structure of the truncated 60-residue protein (magenta) is superimposed on the structure of the full-length 81-residue protein (aqua).

A key question in the study of the mercury transport mechanism is the location of the N-terminal Hg(II) binding site, which is shown in Figure 7.8 to be in close

proximity to the second Hg(II) binding site, both of which are located at the bilayer's hydrophobic to hydrophilic interface. Previous biochemical studies and predictions on various mercury transporter proteins are inconsistent in identifying the location of this binding site, ranging from the interface on the cytosolic side (Sahlman et al., 1997) to the middle of the first transmembrane helix (Wilson et al., 2000). The structure in Figure 7.8 supports the existence of the former topology. The second important observation is the proximity of the two metal binding sites on MerF, which supports the possibility of direct intramolecular Hg(II) transfers. Notably, the existence of direct contact has been hypothesized from various studies on mercury ligand exchange (Johs et al., 2011) and mercury coordination chemistry (Melnick and Parkin, 2007; Rulı´šek and Vondrášek, 1998). In any transport mechanism tight control of Hg(II) is essential because of its high reactivity in solution, and the only way to transfer Hg(II) while maintaining tight control is through direct contact and ligand exchange between Hg(II) binding sites.

The determination of the structure of the full-length MerF protein enables comparisons with the previously determined structure of the truncated MerFt protein. Drastic structural rearrangements are induced by truncation of terminal residues, and residues 5 – 12, which are mobile in micelles, are structured in phospholipid bilayers. Moreover, the structure of the full-length protein under near-native conditions provides insights into the mechanism of transport of mercury across from a mercury-binding protein in the periplasm to an enzyme in the cytoplasm.

7.5 Materials and Methods

The expression and purification of MerF followed previously described protocols used for similar proteins(De Angelis et al., 2006b; Howell et al., 2005; Lu et al., 2012; Lu et al., 2011; Son et al., 2012). The gene encoding the full-length construct of MerF was cloned into an *E. coli* pET31b+ vector (Novagen, www.emdmillipore.com) for expression of a KSI-MerF-His_6 fusion protein with the three polypeptide segments separated by methionine residues. The fusion protein was expressed in *E. coli* C41(DE3) cells (Lucigen, www.lucigen.com) in M9 minimal medium containing 1 g/L ^{15}N labeled ammonium sulfate (Cambridge Isotope Laboratories (CIL), www.isotope.com) as the sole nitrogen source, 2-3 g/L of $^{13}C_6$-glucose (CIL) as the sole carbon source, 50 mg/L of carbenicillin as the antibiotic. The cell cultures were grown by shaking (250 rpm) at 37°C until the OD_{600} reached 0.6. Expression of the fusion protein was induced by adding 1 mM IPTG and growing for an additional 3-5 hr. Cells were harvested by centrifugation, resuspended in 60 ml lysis buffer (20 mM Tris-HCl, 500 mM NaCl, 15% glycerol, pH 8.0) per liter of cell culture, and lysed by a probe sonicator (Fisher Scientific Sonic Dismembrator 550, www.fishersci.com) on ice. The inclusion bodies containing the fusion protein were separated by centrifugation at 13,000 rpm (JA-20 rotor, Beckman Coulter, www.beckmancentrifuge.com), and then solubilized in the binding buffer (20 mM Tris-HCl, 500 mM NaCl, 6 M guanidine hydrochloride, 5 mM imidazole, pH 8.0). Following a 30-minute centrifugation at 17,000 rpm, the supernatant was separated and allowed to bind Ni-NTA agarose (Qiagen, www.qiagen.com) beads in a column

pre-equilibrated with binding buffer. The column was then washed with washing buffer (20 mM Tris-HCl, 500 mM NaCl, 6 M guanidine hydrochloride, 50 mM imidazole, pH 8.0), and the fusion proteins were eluted with elution buffer (20 mM Tris-HCl, 500 mM NaCl, 6 M guanidine hydrochloride, 500 mM imidazole, pH 8.0). The polypeptides were then dialyzed extensively in water and lyophilized. The polypeptides were re-solubilized in 70% formic acid, and then cleaved for 5 hours in the presence of excess of cyanogen bromide and the absence of light. The reaction was terminated by adding two volumes of 1 M NaOH; the polypeptides were then dialyzed and lyophilized. Isotopically labeled MerF was further purified by reverse-phase HPLC (DeltaPak C4 Column, Waters, www.waters.com).

20 mg of 1,2-di-O-tetradecyl-*sn*-glycero-3-phosphocholine (14-o-PC) powder (Avanti Polar Lipids, www.avantilipids.com) and 4 mg of MerF were separately dissolved in solutions containing 1% SDS and 20 mM MES, pH 6.1. The two solutions were mixed with gentle shaking for 1 hour. The removal of SDS follows the protocol previously described(Park et al., 2012a; Park et al., 2012b). The bulk of the SDS was removed by dialyzing the solution for 24 hours against >100 fold excess volume of 20 mM MES buffer, pH 6.1. The solution was dialyzed again for 8-12 hours against a >100 fold excess volume of 20 mM MES buffer, pH 6.1 with 10 mM KCl. A third dialysis repeated using the conditions of the first one to remove residual KCl and SDS.

MerF-containing proteoliposomes were concentrated by ultracentrifugation (390,000 g, Beckman Ti 70.1 rotor, overnight, 15°C, www.beckmancentrifuge.com)

and the pellet was packed into the 3.2mm MAS rotor for NMR studies.

The NMR experiments and associated parameters are described in Table 7.4. The experimental NMR data were processed and analyzed using NMRPipe (Delaglio et al., 1995) and Sparky(Goddard and Kneller, 2008). ^{1}H decoupling was achieved with SPINAL-64(Fung et al., 2000). ^{13}C-^{13}C correlation was achieved with proton-driven spin diffusion (PDSD) (Bloembergen, 1949; Frey and Opella, 1984) or dipolar assisted rotational resonance (DARR) (Takegoshi et al., 2001). Multiple-contact cross polarization(Pines et al., 1973; Tang and Nevzorov, 2011) was implemented for magnetization transfer between ^{1}H and ^{15}N/^{13}C. The magnetization transfer between ^{15}N and ^{13}Cα or ^{13}C' was performed using SPECIFIC-CP (Baldus et al., 1998). Heteronuclear dipolar recoupling was performed using the $R18^{7}_{1}$ sequence(Carravetta et al., 2000; Levitt, 2007; Zhao et al., 2001).

Table 7.4. NMR experiments and parameters. DC: dipolar coupling; CS: chemical shift; CP: cross polarization; MAS: magic angle spinning; DARR: dipolar assisted rotational resonance; PDSD: proton driven spin diffusion; rf: radio frequency; SPECIFIC-CP: spectrally induced filtering in combination with CP; SPINAL: small phase incremental alternation.

Two-dimensional ^{13}C-^{13}C Correlation	short-range	long-range
MAS spinning speed (Hz)	11111	11111
mixing time [ms]	50 (PDSD)	200 (DARR)
acquisition time (t2/t1) [ms]	10/6.56	12.9/6.56
carrier frequency (t2/t1) [ppm]	100/40	100/40
π/2 pulse (^{1}H/^{13}C) [μs]	2.7/4.7	2.7/4.7
CP contact time [μs]	200	200
CP pulse shape (^{1}H)	Linear (100-80%)	Linear (100-80%)
CP rf field strength (^{1}H/^{13}C) [kHz]	66/55	66/55
^{1}H decoupling field strength (sw-TPPM) [kHz]	100	100
recycle delay [s]/number of acquisitions	2/896	2/2240
spectral width (F2/F1) [kHz]	39.68/12.315	39.68/12.315

Two-dimensional ^{15}N-$^{13}C\alpha$ Correlation	
MAS spinning speed (Hz)	11111
acquisition time (t2/t1) [ms]	10.4/6.08
carrier frequency (t2/t1) [ppm]	55/120
CP total contact time [μs]	1000
CP number of contacts	4
CP delay between contacts [ms]	100
CP rf field strength (^{1}H/^{15}N) [kHz]	49.6/38.5
CP pulse shape (^{1}H)	Linear (100-80%)
SPECIFIC-CP contact time [ms]	2.5
SPECIFIC-CP rf field strength (^{15}N/$^{13}C\alpha$) [kHz]	27/16
SPECIFIC-CP pulse shape (^{13}C)	tan (100-90%)
^{1}H decoupling rf field strength (SPINAL64) [kHz]	100
recycle delay [s]/number of acquisitions	2/7168
spectral width (F2/F1) [kHz]	50/3.125

Three-dimensional HnNCa (^{1}H-^{15}N DC / ^{15}N CS / $^{13}C\alpha$ CS)	
MAS spinning speed (Hz)	11111
acquisition time (t3/t1/t2) [ms]	10.46/1.26/3.52
carrier frequency (^{1}H/^{13}C/^{15}N) [ppm]	7/55/120
CP total contact time [μs]	1000
CP number of contacts	4
CP delay between contacts [ms]	100
CP rf field strength (^{1}H/^{15}N) [kHz]	49.6/38.5
CP pulse shape (^{1}H)	Linear (100-80%)

Table 7.4. NMR experiments and parameters. DC: dipolar coupling; CS: chemical shift; CP: cross polarization; MAS: magic angle spinning; DARR: dipolar assisted rotational resonance; PDSD: proton driven spin diffusion; rf: radio frequency; SPECIFIC-CP: spectrally induced filtering in combination with CP; SPINAL: small phase incremental alternation. (continued)

Z-filter [ms]	5
SPECIFIC-CP contact time [ms]	2.5
SPECIFIC-CP rf field strength (^{15}N/^{13}Cα) [kHz]	27/16
SPECIFIC-CP pulse shape (^{13}C)	tan (100-90%)
$R18^7_1$ pulse lengh rf field strength [kHz]	100
$R18^7_1$ ^{1}H carrier frequency [ppm]	9
^{1}H decoupling rf field strength (SPINAL64) [kHz]	100
recycle delay [s]/number of acquisitions	2/1216
spectral width (F3/F1/F2) [kHz]	50/5.55/3.125

Three-dimensional HnNCo (^{1}H-^{15}N DC / ^{15}N CS / ^{13}C' CS)	
MAS spinning speed (Hz)	11111
acquisition period (t3/t1/t2) [ms]	10.46/1.26/3.52
carrier frequency (^{1}H/^{13}Cα/^{13}C'/^{15}N) [ppm]	7/55/174/120
CP total contact time [μs]	1000
CP number of contacts	4
CP delay between contacts [ms]	100
CP rf field strength (^{1}H/^{15}N) [kHz]	49.6/38.5
CP pulse shape (^{1}H)	linear (100-80%)
Z-filter [ms]	5
SPECIFIC-CP contact time [ms]	2.5
SPECIFIC-CP rf field strength (^{15}N/^{13}C') [kHz]	27/38
SPECIFIC-CP pulse shape (^{13}C)	tan (100-90%)
$R18^7_1$ pulse lengh rf field strength [kHz]	100
$R18^7_1$ ^{1}H carrier frequency [ppm]	9
^{1}H decoupling rf field strength (SPINAL64) [kHz]	100
recycle delay [s]/number of acquisitions	2/2144
spectral width (F3/F1/F2) [kHz]	50/5.55/3.125

Three-dimensional HcCxCx (^{1}H-^{13}C DC / ^{13}C CS / ^{13}C CS)	
MAS spinning speed (Hz)	13889
acquisition period (t3/t1/t2) [ms]	10/1.368/2.28
carrier frequency (^{1}H/^{13}Cα/^{13}CX/^{15}N) [ppm]	7/55/100/120
CP total contact time [μs]	320
CP number of contacts	4
CP delay between contacts [ms]	15
CP rf field strength (^{1}H/^{15}N) [kHz]	64/50
CP pulse shape (^{1}H)	linear (100-90%)

Table 7.4. NMR experiments and parameters. DC: dipolar coupling; CS: chemical shift; CP: cross polarization; MAS: magic angle spinning; DARR: dipolar assisted rotational resonance; PDSD: proton driven spin diffusion; rf: radio frequency; SPECIFIC-CP: spectrally induced filtering in combination with CP; SPINAL: small phase incremental alternation. (continued)

$R18^7_1$ pulse lengh rf field strength [kHz]	125
$R18^7_1$ ^1H carrier frequency [ppm]	7
DARR mixing time [ms]	20
^1H decoupling rf field strength (SPINAL64) [kHz]	100
recycle delay [s]/number of acquisitions	2/208
spectral width (F3/F1/F2) [kHz]	50/13.889/41.667

Chapter 7 is a reprint of the material "The structure of the mercury transporter MerF in phospholipid bilayers: a large conformational rearrangement results from N-terminal truncation" as it appears in J. Am. Chem. Soc. 135(25):9299-9302 by Lu GJ, Tian Y, Vora N, Marassi FM, Opella SJ. The thesis author was the primary author of the paper.

Chapter 8. Updated Structure of Mercury Transporter MerF with Additional Restraints and Dynamics Information

8.1 Abstract

Rotationally aligned (RA) and Oriented Sample (OS) solid-state NMR spectroscopy are two complementary techniques that can be used to determine the high-resolution structures of membrane proteins in lipid bilayers at physiological conditions. RA solid-state NMR can provide dihedral angle restraints, distance restraints and angular restraints in the form of heternuclear dipolar couplings. However, the pulse sequence provides less accurate measurement on the chemical shift anisotropies (CSA), another important form of angular restraints, because of the broad powder pattern resulting from recoupling un-oriented samples. On the other hand, OS solid-state NMR can accurately determine amide ^{1}H and ^{15}N CSAs of individual residues in the separated-local field (SLF) spectra. Therefore, the combination of restraints from the two techniques can provide a mean to improve the calculated membrane protein structure. Here, this principle is demonstrated by a mercury transporter protein MerF, whose structure has been recently determined by RA solid-state NMR to the backbone root-mean-square deviation (bbRMSD) of 1.48 Å. The inclusion of CSA measured by OS solid-state NMR into the same structural calculation protocol improves the bbRMSD to 1.03 Å. Secondly, the boundary between immobile residues and residues undergoing rotational motion is defined by two-dimensional INEPT (Insensitive Nuclei Enhanced Polarization Transfer)

experiment. The protein dynamics information and isotropic chemical shift of the mobile residues obtained from the experiment is used to determine the usage of dihedral angle restraints for the mobile residues of the protein. Thirdly, newly developed structure calculation protocol is employed. The combination of the three aspects results in the updated MerF structure of improved quality.

8.2 Isotropic dynamics of the terminal residues of MerF

INEPT pulse scheme selectively transfers polarization between ^{1}H and dilute spins (^{13}C or ^{15}N) using through-bond J coupling. Only residues undergoing rapid isotropic rotational diffusion, a condition similar to that required by solution NMR, can be observed with INEPT pulse sequences. For MerF protein in proteoliposome, only N- and C-terminal residues are visible in the spectra, and resonance assignment can be easily accomplished with the knowledge of the typical chemical shifts of each amino acids. Other than the 4 lysine residues, all others can be assigned to specific residues.

Notably, since we previously knew that only the N- and C- terminal residues, but not the inter-helical loop, are mobile (Lu et al., 2013a), here we can count the assignment and accurately draw the line between mobile and immobile residues. For example, residue P4 was previously unknown about its dynamics, because K5 is immobile, D3 is not, and proline cannot be assigned by sequential backbone “walk”. Here we only observe one proline peak, which can only be P74. Therefore, P4 is determined to be an immobile residue.

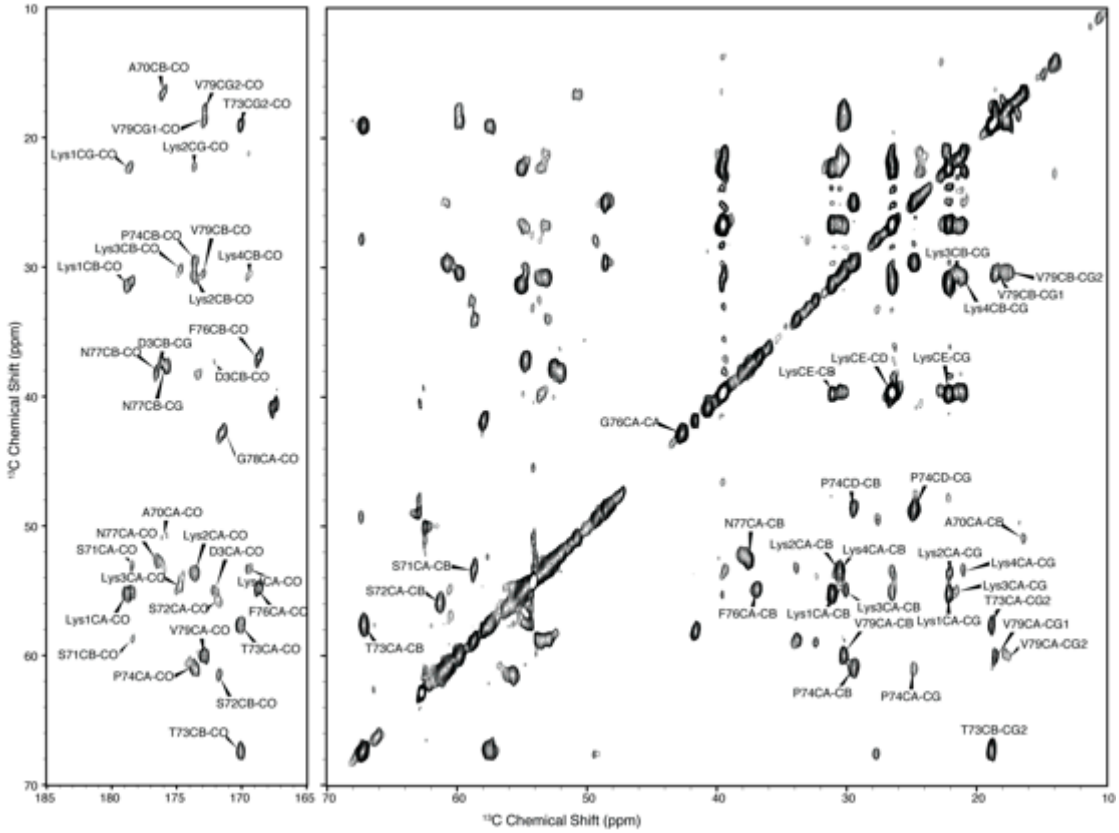

Figure 8.1. Two-dimensional ^{13}C-^{13}C correlation spectrum of MerF using INEPT transfer to selectively detect residues undergoing rapid isotropic rotational motion. Resonance signals are assigned to the N-terminal K2 and D3 residues, and the C-terminal A70 to S82 residues.

The solid-state NMR experiments were performed on an Agilent DD2 800 MHz spectrometer using a home-built $^{1}H/^{13}C/^{15}N$ triple-resonance MAS probe as previously described (Lu et al., 2013a). Sample spinning frequency was 11111 Hz and the temperature was maintained at 25°C. The recycle delay was 2 seconds. Two-dimensional through-bond correlation spectroscopy (TOBSY) was used to identify the mobile residues undergoing isotropic motion. INEPT pulse scheme selectively transfers polarization from ^{1}H to ^{13}C only for the mobile residues. In the pulse

sequence (Figure 8.2), ϕ_1 = x,x,x,x,x,x,x,x,-x,-x,-x,-x,-x,-x,-x,-x; ϕ_2 = x,-x,x,-x; ϕ_3 = y,y,-y,-y; ϕ_4 =x,x,x,x,y,y,y,y,-x,-x,-x,-x,-y,-y,-y,-y; ϕ_5 =x,-x,x,-x,y,-y,y,-y; ϕ_6 (real points) =-y,-y,-y,-y,-x,-x,-x,-x,y,y,y,y,x,x,x,x; ϕ_6 (imaginary points) =x,x,x,x,-y,-y,-y,-y,-x,-x,-x,-x,y,y,y,y; ϕ_7 =x,x,x,x,-y,-y,-y,-y,-x,-x,-x,-x,y,y,y,y; ϕ_{rec} =x,x,-x,-x,y,y,-y,-y. Thin black line indicates 90° pulse and thick black line indicates 180° pulse. The INEPT transfer time T_{inept} is set at 1 msec. ^{13}C-^{13}C through-bond mixing is achieved by the symmetry pulse scheme $P9^1_3$ (Hardy et al., 2001; Yang et al., 2011). $P9^1_3$ was applied without additional phase cycling (i.e. ϕ=x) for a total time of 12.15 msec. 100 kHz rf field was used in all ^1H pulses. 66.7 kHz rf field was used in all ^{13}C pulses, which meets the requirement of the $P9^1_3$ pulse scheme. The MerF TOBSY spectrum was acquired with 192 scans, 160 complex t_1 points and 2000 t_2 points. The spectrum width was 40 kHz and 100 kHz in the two dimensions, respectively. ^{13}C carrier frequency was set at 55 ppm, and ^1H carrier was at 5 ppm. All the NMR data were processed using the program NMRPipe (Delaglio et al., 1995) and the spectra were assigned using the program Sparky (Goddard and Kneller).

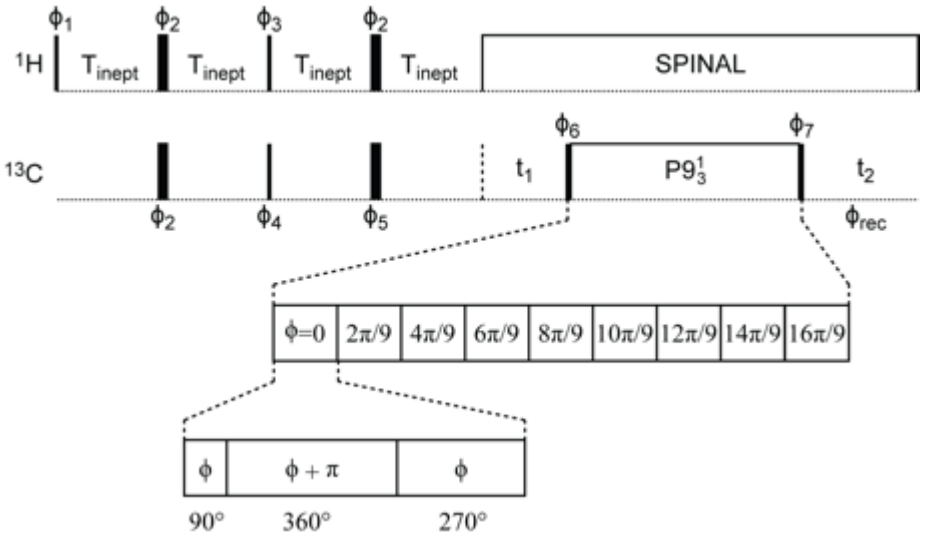

Figure 8.2. Pulse sequence scheme of the two-dimensional through-bond correlation spectroscopy (TOBSY) with INEPT transfer to selectively detect residues of rapid isotropically rotational motion.

8.3 Improvement of the RMSD of the Structure Additional Angular Restraints and Dynamics Information

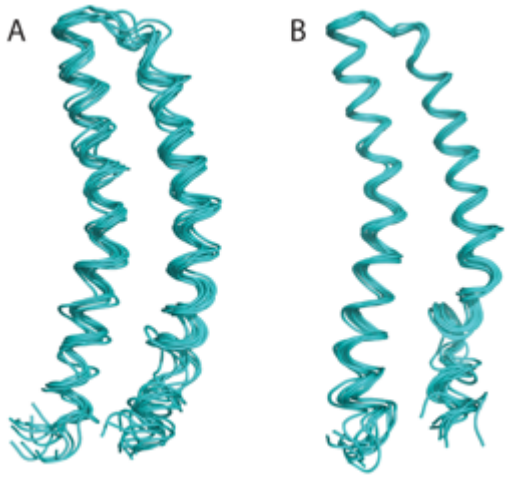

Figure 8.3. Improvement in the precision and R.M.S.D. of the calculated MerF structure. (A) MerF structure previously calculated with restraints only from RA MAS solid-state NMR (PDB ID: 2M67) (Lu et al., 2013a), and the average backbone pairwise rmsd previously reported is 1.48 Å for the immobile residues K5-D69. (B) MerF structure previously calculated with combined structural restraints from OS solid-state NMR and RA MAS solid-state NMR. The average backbone pairwise rmsd for the same residues is 1.03 Å.

8.4 Updated Structure of MerF

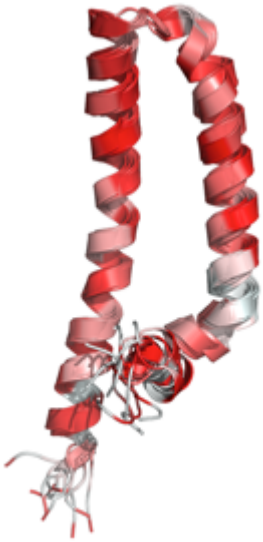

Figure 8.4. Updated structure of MerF (PDB ID: 2MOZ). Red color identifies the hydrophobic region and white identifies the hydrophilic region.

Two-stage calculation protocol (Lu et al., 2013a; Park et al., 2012b) is designed to achieve atomic resolution 3D structure of membrane proteins, with Rosetta and Xplor-nih (Schwieters and Clore, 2001). The initial coarse-grained models are generated in Rosetta. Molecular fragments are obtained from Robetta server (Kim et al., 2004) with primary sequence, 30k decoys are calculated using the membrane protocol (Rohl et al., 2004; Yarov-Yarovoy et al., 2006) in Rosetta package on a local workstation. All 30k decoys are refinement against 50 NH dipolar coupling restraints obtained from oriented sample ssNMR experiments, in the all-atom mode. After the all-atom refinement, clusters are calculated with cluster radius of 6Å for residue 5 through 73. That provides total of 45 clusters, and 11168 candidates formed the most populated cluster (37.2% population). Among the 11168 candidates, the 1000 lowest

energy structures are accepted for extracting dihedral restraints, and the lowest energy candidate is employed as the initial structure for further refinement in Xplor-nih.

The simulated annealing protocol is performed to calculate high-resolution structures against all available experimental restraints. That includes, 64 NH dipolar coupling restraints from oriented sample experiments (14 of them have ambiguous sign), and 64 ^{15}N CSA restraints; 59 NH dipolar coupling restraints from MAS experiments (14 of them have ambiguous sign), and 58 CaHa dipolar coupling restraints (all have ambiguous sign); also 49 NOE and 74 pairs of dihedral angle (f/y) restraints. The routinely used refinement protocol in Xplor-nih is processed in four stages: (1) torsion angle dynamics at high-temperature (3,000 K) for a time of 15 ps or 15,000 timesteps; (2) torsion angle dynamics with simulated annealing, where the temperature is reduced from the initial high temperature value to 50 K in steps of 12.5 K, for a time of 0.2 ps or 1000 timesteps per temperature step; (3) 500 steps of Powell torsion angle minimization; and (4) 500 steps of Powell Cartesian minimization.

Dihedral angle restraints and distance restraints were applied with respective force constants of k_{CDIH}=300 kcal•mol^{-1}•rad^{-2} and k_{NOE}=20 kcal•mol^{-1}•Å^{-2}. NH dipolar coupling potentials have force constants set to 1 kcal•mol^{-1}•rad^{-2} at high temperature stage, and ramped to 3 kcal•mol^{-1}•rad^{-2} and 5 kcal•mol^{-1}•rad^{-2} for unsigned and signed restraints respectively during annealing stage. CSA and CαHα dipolar coupling potentials have force constants 0.1 kcal•mol^{-1}•rad^{-2} at high temperature and ramped 0.5 kcal•mol^{-1}•rad^{-2} during annealing. The axial alignment

parameter (Da) is set to 10 kHz initially and allowing to vary during the calculation, where Rhombicity (Rh) is fixed at 0 to reflect the physics of the solid state condition (Tian et al., 2012). The torsionDB statistical torsion angle potential (Bermejo et al., 2012) was implemented with a force constant set to k_{tDB}=0.02 kcal•mol^{-1}•rad^{-2} in the high temperature stage and ramped geometrically from 0.02 to 2 kcal•mol^{-1}•rad^{-2} during simulated annealing. Atomic overlap was prevented by limiting allowed repulsions to those between atoms separated by four or more covalent bonds (nbxmod=4).

100 structures are calculated, and the 10 lowest experimental energy structures are accepted as the representative structure ensemble for MerF. The backbone RMSD of the 10 chosen structures is 1.12±0.51 Å and all-heavy atom RMSD is 2.07±0.53 Å for residue 5 through 69. The averaged Da value is 10.35 kHz for restraints from OS data, and 9.89 kHz for restraints from MAS data. When the NH bond length is 1.05 Å, the maximum of Da is 10.52 kHz, thus the Da values give the order parameter of 0.98 and 0.94 for the respective sample conditions.

8.5 Analysis and Comparison of the Structures

All the signals from the MerF residues that are immobile in the NMR time scale were assigned by the PISA wheel method with assistance from implementation of the resolution-improved pulse sequences and new resonance assignment methods described above. Signals from three N-terminal residues and 12 C-terminal residues

are missing in OS solid-state NMR spectra of both uniformly and selectively 15N labeled samples, indicating that these residues are mobile.

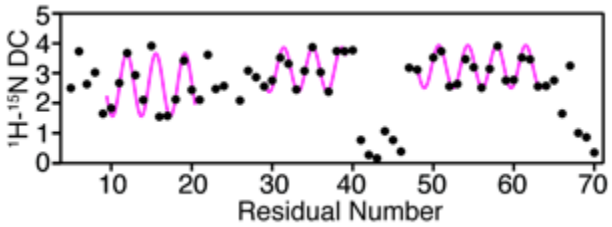

Figure 8.5. Plot of experimental ^{1}H-^{15}N dipolar coupling frequencies as a function of residue number with Dipolar Wave fits (Mesleh et al., 2002). Note that ^{1}H-^{15}N dipolar coupling values are from perpendicularly aligned bicelles where the values are scaled down to ~ 0.4 by the order parameter and alignment.

The recent full-length MerF structure determined by RA solid-state NMR showed a large rearrangement of N-terminal domain compared to the truncated MerF (MerFt) structures (Lu et al., 2013a), and this protein truncation effect is more readily appreciated in the SLF spectra from OS solid-state NMR (Figure 8.6). The peaks previously assigned to the N-terminal amphipathic helix in the MerFt protein (De Angelis et al., 2006b) mainly locates at ^{15}N chemical shift above 110 ppm; in contrast, the full-length MerF protein has much less peaks in this region and more peaks appear in the helical region with high tilt angle. It is clearly seen in the selectively labeled samples how these peaks move from the region above 110 ppm in MerFt spectra to helical region in MerF spectra, while those peak corresponding to transmembrane residues stay at the same place between the two constructs.

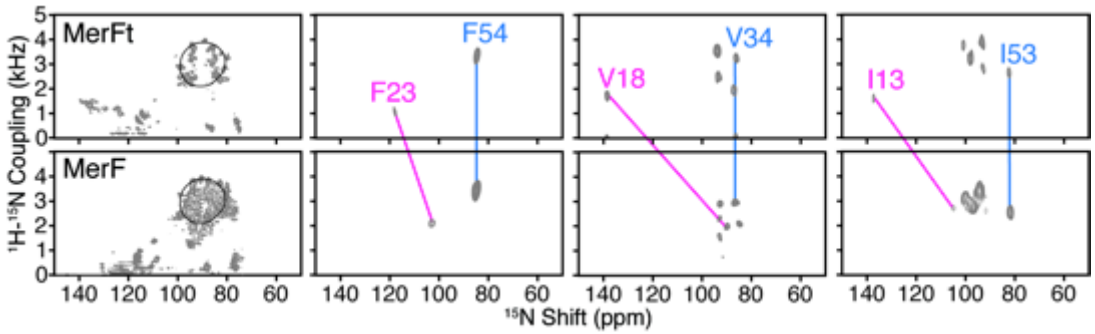

Figure 8.6. Two-dimensional SLF spectra spectrum of uniformly and selectively labeled samples of truncated MerF (MerFt) (top row) and full-length MerF (bottom row). Examples of residues from transmembrane core region of the protein are labeled by cyan line, and those of residues from N-terminal domain are labeled in magenta. SLF spectra of MerFt is reprinted from previous publication (De Angelis et al., 2006b).

Chapter 8 is currently being prepared for submission for publication of the material.

Chapter 9. Conclusion

It is important to study membrane protein structures in native-like lipid bilayer environment instead of detergent micelle, because of the potential structural distortions caused by the non-native curvature of the micelle (Zhou and Cross, 2013). Solid-state NMR is a method that can yield atomic-resolution structural restraints for membrane proteins in lipid bilayer at physiological pH and temperature. In this thesis, solid-state NMR methodologies are developed which revolve around the aim of determining the structure of the full-length mercury transporter protein MerF.

The structural study of full-length MerF has initially started in magnetically aligned bicelle using OS solid-state NMR, and here the two major technical challenges are the spectral resolution and resonance assignments. Several methods are developed to tackle the two challenges. (i) New pulse sequence, MSHOT-Pi4/Pi, has been developed and is based on the magic sandwich pulse with the additional quadratic $\pi/2$ Z-rotational symmetry. In comparison to the previous pulse sequence of FSLG/CW, the new sequence reduce the ^{1}H resonance line width by more than a factor of two, and can be used to observe either ^{1}H chemical shift or ^{1}H-^{15}N dipolar coupling. (ii) New resonance assignment method, Dipolar Coupling Correlated Isotropic Chemical Shift (DCCICS) Analysis, has been developed that is able to transfer resonance assignment from isotropic NMR methods. The method exploits the unique property of unflipped and flipped aligned bicelles. The ^{1}H-^{15}N dipolar couplings for specific resonance signal in the two types of bicelles always differ by exactly a factor of two,

while the chemical shifts are at the perpendicular and parallel edge of the power pattern, respectively. Therefore, dipolar coupling provides the correlation between spectra acquired from the two samples, enabling the calculation of the isotropic chemical shifts from OS solid-state NMR. Thus, resonance assignment from other isotropic NMR methods can be transferred to OS solid-state NMR through the isotropic chemical shift. (iii) ^{15}N-^{15}N correlation spectroscopy using either PDSD or MMHH pulse sequences provides a pure spectroscopic sequential assignment method. The MMHH developed by Nevzorov was first tested in membrane-bound Pf1 coat protein sample in the lab (Knox et al., 2010) and later applied to the study of MerF. (iv) Combined usage of all these resonance assignment strategies and previously established Shotgun approach (Marassi and Opella, 2003) has resulted in the complete assignment of all backbone immobile residues of the full-length MerF protein by OS solids-state NMR. Some resonance assignment tactics are also devised along the way. For example, the combination of DCCICS analysis with the new high-resolution PELF experiments are especially suitable for assigning the terminal and loop residues, which was previously inaccessible by the Shotgun approach. Another example is resonance assignment through aligning ^{1}H-^{15}N dipolar coupling between OS solid-state NMR spectra of amino-acid selectively ^{15}N labeled sample and the HnNCa experiment of RA solid-state NMR.

The structural study of full-length MerF has also been carried out in RA solid-state NMR. The method is developed in the lab as a new method that can study membrane protein structures in proteoliposome, another lipid bilayer environment.

The method combines the strength of magic-angle-spinning (MAS) solid-state NMR in obtaining resonance assignment and the concept of alignment from OS solid-state NMR in obtaining angular restraints. During the application of the method to MerF, two minor developments have been carried out. Firstly, multi-contact cross polarization has been incorporated into the pulse sequences to improve the sensitivity of the experiments. Secondly, three three-dimensional experiments, HnNCa / HnNCo / HcCxCx have been used to simultaneously carry out sequential backbone "walk" resonance assignment and the observation of angular structural restraints in the form of dipolar couplings, instead of the conventional experimental set of NCaCx/NCoCx/CaNCo. The usage of these three experiments is a strategy uniquely suitable for RA solid-state NMR because of the site-to-site variation of dipolar couplings. The strategy provides an opportunity to resolves resonances with overlapping isotropic chemical shifts, such as those from the same type of amino acids, and also improves the sensitivity of the experiments with only one-bond resonance transfer.

The first structure of full-length MerF is determined in proteoliposome with RA solid-state NMR. In comparison to the previously determined structure of the truncated MerF (MerFt), the full-length structure reveals that the protein truncation between residue I12 and I13 has cause large conformational rearrangement up to residue P25, more than ten residues away from the truncation site. In the full-length structure, the entire N-terminal domain from K2 to P25 has adopted a close-to-perpendicular orientation to the lipid bilayer surface, in contrast to the parallel

orientation in the structure of MerFt. This serves as an example to demonstrate the importance of studying full-length unmodified protein by structural biologists. Additionally, the full-length structure reveals again that both mercury-binding sites are located at the intracellular side of the membrane. Therefore, the structure is suggested to be a conformation that allows intramolecular Hg^{2+} transfer between the N-terminal and C-temrinal binding sites of MerF.

Subsequently, after the complete assignment of MerF in OS solid-state NMR, an updated MerF structure is calculated incorporating all angular restraints and additional dynamics information. INEPT experiment in RA solid-state NMR has been performed on MerF in proteoliposome and the experiment selectively detects signals from residues undergoing rapid isotropic rotational motion. In the case of MerF, the two-dimensional experiment has provided chemical shift assignments for both N-terminal residues K2-D3 and C-terminal residues A70-S82. The experiment provides a way to direct map out the mobile residues, and the isotropic chemical shift information can be used to calculate dihedral angle restraints and obtain the secondary structure of the protein in this region. The new dynamics information of MerF suggests the treatment of C-terminal residues as the random coil conformation without dihedral angle restraints during structural calculation. On the other hand, the ^{15}N CSA observed in OS solid-state NMR provides another set of angular restraints. With an improved protocol, a new MerF structure is calculated with improved RMSD and correct conformation at the terminal residues.

Lastly, as a side direction, the theory underlying the observation that the MSHOT-Pi4 pulse sequence selectively improves the resolution of membrane protein samples but not of standard single crystal samples has been analytically generalized as the principle of motion-adapted pulse sequence. The interference between sample spatial rotational motion and the radio-frequency pulse rotation in the quantum spin space is found to be the cause of the selectivity. As a related endeavor, the mechanisms of ^{15}N-^{15}N dilute spin exchange under MMHH condition and the effect magic-angle ^{1}H spin-lock pulses have been analyzed theoretically and demonstrated in standard and biological samples. Mixed-order proton-relay mechanism is proposed to be the main contributor to ^{15}N-^{15}N dilute spin exchange in stationary aligned sample, and once again, the difference of pulse performance between standard and biological samples is observed that may be a consequence of sample motion and other factors.

Bibliography

Agarwal, V., Sardo, M., Scholz, I., Böckmann, A., Ernst, M., and Meier, B. (2013). PAIN with and without PAR: variants for third-spin assisted heteronuclear polarization transfer. J Biomol NMR *56*, 365-377.

Anfinsen, C.B. (1973). Principles that govern the folding of protein chains. Science (New York, NY) *181*, 223-230.

Bain, A.D. (2003). Chemical exchange in NMR. Prog Nucl Magn Reson Spectrosc *43*, 63-103.

Bak, M., Rasmussen, J.T., and Nielsen, N.C. (2000). SIMPSON: a general simulation program for solid-state NMR spectroscopy. J Magn Reson *147*, 296-330.

Baldus, M., Petkova, A.T., Herzfeld, J., and Griffin, R.G. (1998). Cross polarization in the tilted frame: assignment and spectral simplification in heteronuclear spin systems. Mol Phys *95*, 1197 - 1207.

Banigan, J., Gayen, A., and Traaseth, N. (2013). Combination of 15N reverse labeling and afterglow spectroscopy for assigning membrane protein spectra by magic-angle-spinning solid-state NMR: application to the multidrug resistance protein EmrE. J Biomol NMR *55*, 391-399.

Barkay, T., Miller, S.M., and Summers, A.O. (2003). Bacterial mercury resistance from atoms to ecosystems. FEMS Microbiol Rev *27*, 355-384.

Barrineau, P., Gilbert, P., Jackson, W.J., Jones, C., Summers, A., and Wisdom, S. (1985). The Structure of the mer Operon. In Plasmids in Bacteria, D. Helinski, S. Cohen, D. Clewell, D. Jackson, and A. Hollaender, eds. (Springer US), pp. 707-718.

Bermejo, G.A., Clore, G.M., and Schwieters, C.D. (2012). Smooth statistical torsion angle potential derived from a large conformational database via adaptive kernel density estimation improves the quality of NMR protein structures. Protein Sci *21*, 1824-1836.

Bertini, I., Bhaumik, A., De PaeÃàpe, G., Griffin, R.G., Lelli, M., Lewandowski, J.R., and Luchinat, C. (2010). High-Resolution Solid-State NMR Structure of a 17.6 kDa Protein. J Am Chem Soc *132*, 1032-1040.

Bertini, I., Gonnelli, L., Luchinat, C., Mao, J., and Nesi, A. (2011). A New Structural Model of Aβ40 Fibrils. J Am Chem Soc *133*, 16013-16022.

Bialynicki-Birula, I., Mielnik, B., and Plebański, J. (1969). Explicit solution of the continuous Baker-Campbell-Hausdorff problem and a new expression for the phase operator. AnPhy *51*, 187-200.

Bielecki, A., Kolbert, A.C., and Levitt, M.H. (1989). Frequency-switched pulse sequences: Homonuclear decoupling and dilute spin NMR in solids. Chem Phys Lett *155*, 341-346.

Bloembergen, N. (1949). On the interaction of nuclear spins in a crystalline lattice. Physica *15*, 386-426.

Caravatti, P., Bodenhausen, G., and Ernst, R.R. (1982). Heteronuclear solid-state correlation spectroscopy. Chemical Physics Letters *89*, 363-367.

Caravatti, P., Braunschweiler, L., and Ernst, R.R. (1983). Heteronuclear correlation spectroscopy in rotating solids. Chem Phys Lett *100*, 305-310.

Carravetta, M., Edén, M., Zhao, X., Brinkmann, A., and Levitt, M.H. (2000). Symmetry principles for the design of radiofrequency pulse sequences in the nuclear magnetic resonance of rotating solids. Chem Phys Lett *321*, 205-215.

Castellani, F., van Rossum, B., Diehl, A., Schubert, M., Rehbein, K., and Oschkinat, H. (2002). Structure of a protein determined by solid-state magic-angle-spinning NMR spectroscopy. Nature *420*, 98-102.

Cavanagh, J., Fairbrother, W.J., Palmer III, A.G., and Skelton, N.J. (1996). Protein NMR spectroscopy : principles and practice (San Diego: Academic Press).

Cavanagh J, F.W., Palmer AG, Skelton NJ (1996). Protein NMR spectroscopy: principles & practice. *Academic Press, San Diego*.

Chan, J.C.C., and Tycko, R. (2003). Recoupling of chemical shift anisotropies in solid-state NMR under high-speed magic-angle spinning and in uniformly [sup 13]C-labeled systems. J Chem Phys *118*, 8378-8389.

Chekmenev, E.Y., Gor'kov, P.L., Cross, T.A., Alaouie, A.M., and Smirnov, A.I. (2006). Flow-Through Lipid Nanotube Arrays for Structure-Function Studies of Membrane Proteins by Solid-State NMR Spectroscopy. Biophys J *91*, 3076-3084.

Cone, R.A. (1972). Rotational diffusion of rhodopsin in the visual receptor membrane. Nature: New biology *236*, 39-43.

Cornilescu, G., Delaglio, F., and Bax, A. (1999). Protein backbone angle restraints from searching a database for chemical shift and sequence homology. J Biomol NMR *13*, 289-302.

Cross, T., Murray, D., and Watts, A. (2013). Helical membrane protein conformations and their environment. Eur Biophys J, 1-25.

Cross, T.A., Frey, M.H., and Opella, S.J. (1983). Nitrogen-15 spin exchange in a protein. J Am Chem Soc *105*, 7471-7473.

Cross, T.A., and Opella, S.J. (1983). Protein structure by solid state NMR. J Am Chem Soc *105*, 306-308.

Das, B.B., Nothnagel, H.J., Lu, G.J., Son, W.S., Tian, Y., Marassi, F.M., and Opella, S.J. (2012). Structure determination of a membrane protein in proteoliposomes. J Am Chem Soc *134*, 2047-2056.

De Angelis, A.A., Howell, S.C., Nevzorov, A.A., and Opella, S.J. (2006a). Structure determination of a membrane protein with two trans-membrane helices in aligned phospholipid bicelles by solid-state NMR spectroscopy. J Am Chem Soc *128*, 12256-12267

De Angelis, A.A., Howell, S.C., Nevzorov, A.A., and Opella, S.J. (2006b). Structure determination of a membrane protein with two trans-membrane helices in aligned phospholipid bicelles by solid-state NMR spectroscopy. J Am Chem Soc *128*, 12256-12267.

De Angelis, A.A., Howell, S.C., and Opella, S.J. (2006c). Assigning solid-state NMR spectra of aligned proteins using isotropic chemical shifts. J Magn Reson *183*, 329-332.

De Angelis, A.A., Jones, D.H., Grant, C.V., Park, S.H., Mesleh, M.F., and Opella, S.J. (2005). NMR experiments on aligned samples of membrane proteins. Methods Enzymol *394*, 350-382.

De Angelis, A.A., Nevzorov, A.A., Park, S.H., Howell, S.C., Mrse, A.A., and Opella, S.J. (2004). High-Resolution NMR Spectroscopy of Membrane Proteins in Aligned Bicelles. J Am Chem Soc *126*, 15340-15341.

De Angelis, A.A., and Opella, S.J. (2007). Bicelle samples for solid-state NMR of membrane proteins. Nature Protocols *2*, 2332-2338.

De Paëpe, G. (2012). Dipolar Recoupling in Magic Angle Spinning Solid-State Nuclear Magnetic Resonance. Annu Rev Phys Chem *63*, 661-684.

De Paepe, G., Lewandowski, J.R., Loquet, A., Bockmann, A., and Griffin, R.G. (2008). Proton assisted recoupling and protein structure determination. J Chem Phys *129*, 245101-245121.

De Paepe, G., Lewandowski, J.R., Loquet, A., Eddy, M., Megy, S., Bockmann, A., and Griffin, R.G. (2011). Heteronuclear proton assisted recoupling. J Chem Phys *134*, 095101-095118.

Delaglio, F., Grzesiek, S., Vuister, G.W., Zhu, G., Pfeifer, J., and Bax, A. (1995). NMRPipe: A multidimensional spectral processing system based on UNIX pipes. J Biomol NMR *6*, 277-293.

DeSilva, T.M., Veglia, G., Porcelli, F., Prantner, A.M., and Opella, S.J. (2002). Selectivity in heavy metal- binding to peptides and proteins. Biopolymers *64*, 189-197.

Di Lello, P., Benison, G.C., Valafar, H., Pitts, K.E., Summers, A.O., Legault, P., and Omichinski, J.G. (2004). NMR Structural Studies Reveal a Novel Protein Fold for

MerB, the Organomercurial Lyase Involved in the Bacterial Mercury Resistance System,Ä†,,Ä°. Biochemistry *43*, 8322-8332.

Dumez, J.-N., Halse, M.E., Butler, M.C., and Emsley, L. (2012). A first-principles description of proton-driven spin diffusion. Phys Chem Chem Phys *14*, 86-89.

Dvinskikh, S.V., Yamamoto, K., and Ramamoorthy, A. (2006). Heteronuclear isotropic mixing separated local field NMR spectroscopy. J Chem Phys *125*, 034507.

Fares, C., Qian, J., and Davis, J.H. (2005). Magic angle spinning and static oriented sample NMR studies of the relaxation in the rotating frame of membrane peptides. J Chem Phys *122*, 194908.

Filipp, F.V., Sinha, N., Jairam, L., Bradley, J., and Opella, S.J. (2009). Labeling strategies for 13C-detected aligned-sample solid-state NMR of proteins. J Magn Reson *201*, 121-130.

Fooksman, D.R., Edidin, M., and Barisas, B.G. (2007). Measuring rotational diffusion of MHC class I on live cells by polarized FPR. Biophys Chem *130*, 10-16.

Franks, W., Kloepper, K., Wylie, B., and Rienstra, C. (2007). Four-dimensional heteronuclear correlation experiments for chemical shift assignment of solid proteins. J Biomol NMR *39*, 107-131.

Franzin, C.M., Teriete, P., and Marassi, F.M. (2007). Structural similarity of a membrane protein in micelles and membranes. J Am Chem Soc *129*, 8078-8079.

Freeman, R., Frenkiel, T.A., and Levitt, M.H. (1981). Composite Z pulses. J Magn Reson *44*, 409-412.

Frey, M.H., and Opella, S.J. (1984). Carbon-13 spin exchange in amino acids and peptides. J Am Chem Soc *106*, 4942-4945.

Fu, R., Gordon, E.D., Hibbard, D.J., and Cotten, M. (2009). High Resolution Heteronuclear Correlation NMR Spectroscopy of an Antimicrobial Peptide in Aligned Lipid Bilayers: Peptide-Water Interactions at the Water-Bilayer Interface. J Am Chem Soc *131*, 10830-10831.

Fu, R., Truong, M., Saager, R.J., Cotten, M., and Cross, T.A. (2007). High-resolution heteronuclear correlation spectroscopy in solid state NMR of aligned samples. J Magn Reson *188*, 41-48.

Fung, B.M., Khitrin, A.K., and Ermolaev, K. (2000). An improved broadband decoupling sequence for liquid crystals and solids. J Magn Reson *142*, 97-101.

Gan, Z. (2000). Spin Dynamics of Polarization Inversion Spin Exchange at the Magic Angle in Multiple Spin Systems. J Magn Reson *143*, 136-143.

Gayen, A., Banigan, J.R., and Traaseth, N.J. (2013). Ligand-Induced Conformational Changes of the Multidrug Resistance Transporter EmrE Probed by Oriented Solid-State NMR Spectroscopy. Angew Chem Int Ed *52*, 10321-10324.

Ghose, R. (2000). Average Liouvillian theory in nuclear magnetic resonance - Principles, properties, and applications. Concepts in Magnetic Resonance *12*, 152-172.

Giffard, M., Hediger, S., Lewandowski, J.R., Bardet, M., Simorre, J.-P., Griffin, R.G., and De Paepe, G. (2012). Compensated second-order recoupling: application to third spin assisted recoupling. Phys Chem Chem Phys *14*, 7246-7255.

Goddard, T.D., and Kneller, D.G. (2008). SPARKY 3 (University of California, San Francisco.).

Goldburg, W.I., and Lee, M. (1963). Nuclear Magnetic Resonance Line Narrowing by a Rotating rf Field. Phys Rev Lett *11*, 255.

Grant, C.V., Yang, Y., Glibowicka, M., Wu, C.H., Park, S.H., Deber, C.M., and Opella, S.J. (2009). A Modified Alderman-Grant Coil makes possible an efficient cross-coil probe for high field solid-state NMR of lossy biological samples. J Magn Reson *201*, 87-92.

Griffin, R.G. (1998). Dipolar recoupling in MAS spectra of biological solids. Nat Struct Biol *5*, 508-512.

Grommek, A., Meier, B.H., and Ernst, M. (2006). Distance information from proton-driven spin diffusion under MAS. Chem Phys Lett *427*, 404-409.

Guigas, G., and Weiss, M. (2006). Size-Dependent Diffusion of Membrane Inclusions. Biophys J *91*, 2393-2398.

Gullion, T., and Schaefer, J. (1989). Rotational-echo double-resonance NMR. J Magn Reson *81*, 196-200.

Gutowsky, H.S., and Pake, G.E. (1950). Structural Investigations by Means of Nuclear Magnetism. II. Hindered Rotation in Solids. J Chem Phys *18*, 162-170.

Hardy, E.H., Verel, R., and Meier, B.H. (2001). Fast MAS Total Through-Bond Correlation Spectroscopy. J Magn Reson *148*, 459-464.

Hobman, J., Kholodii, G., Nikiforov, V., Ritchie, D.A., Strike, P., and Yurieva, O. (1994). The sequence of the mer operon of pMER327/419 and transposon ends of pMER327/419, 330 and 05. Gene *146*, 73-78.

Hohwy, M., and Nielsen, N. (1997). Elimination of high order terms in multiple pulse nuclear magnetic resonance spectroscopy: Application to homonuclear decoupling in solids. J Chem Phys *106*, 7571-7586.

Howell, S.C. (2007). Application of nuclear magnetic resonance spectroscopy to the structure determination of the integral membrane proteins of the Mer operon (Dissertation). In University of California, San Diego (University of California, San Diego, California, USA).

Howell, S.C., Mesleh, M.F., and Opella, S.J. (2005). NMR structure determination of a membrane protein with two transmembrane helices in micelles: MerF of the bacterial mercury detoxification system. Biochemistry *44*, 5196-5206.

Jan, A., Murtaza, I., Ali, A., and Rizwanul Haq, Q. (2009). Mercury pollution: an emerging problem and potential bacterial remediation strategies. World J Microbiol Biotechnol *25*, 1529-1537.

Jehle, S., Rajagopal, P., Bardiaux, B., Markovic, S., Kuhne, R., Stout, J.R., Higman, V.A., Klevit, R.E., van Rossum, B.-J., and Oschkinat, H. (2010). Solid-state NMR and SAXS studies provide a structural basis for the activation of [alpha]B-crystallin oligomers. Nat Struct Mol Biol *17*, 1037-1042.

Jerschow, A. (2005). MathNMR: Spin and spatial tensor manipulations in Mathematica. J Magn Reson *176*, 7-14.

Johnson, B.A., and Blevins, R.A. (1994). NMR View: A computer program for the visualization and analysis of NMR data. J Biomol NMR *4*, 603-614.

Johs, A., Harwood, I.M., Parks, J.M., Nauss, R.E., Smith, J.C., Liang, L., and Miller, S.M. (2011). Structural Characterization of Intramolecular Hg2+ Transfer between Flexibly Linked Domains of Mercuric Ion Reductase. J Mol Biol *413*, 639-656.

Kay, L., Keifer, P., and Saarinen, T. (1992). Pure absorption gradient enhanced heteronuclear single quantum correlation spectroscopy with improved sensitivity. J Am Chem Soc *114*, 10663-10665.

Ketchem, R., Hu, W., and Cross, T. (1993). High-resolution conformation of gramicidin A in a lipid bilayer by solid-state NMR. Science (New York, NY) *261*, 1457-1460.

Ketchem, R.R., Roux, B., and Cross, T.A. (1997). High-resolution polypeptide structure in a lamellar phase lipid environment from solid state NMR derived orientational constraints. Structure *5*, 1655-1669.

Khitrin, A.K., Xu, J., and Ramamoorthy, A. (2011). Cross-correlations between low-γ nuclei in solids via a common dipolar bath. J Magn Reson *212*, 95-101.

Kim, D.E., Chivian, D., and Baker, D. (2004). Protein structure prediction and analysis using the Robetta server. Nucleic Acids Res *32*, W526-W531.

Kiyono, M., Sone, Y., Nakamura, R., Pan-Hou, H., and Sakabe, K. (2009). The MerE protein encoded by transposon Tn21 is a broad mercury transporter in Escherichia coli. FEBS Lett *583*, 1127-1131.

Knox, R.W., Lu, G.J., Opella, S.J., and Nevzorov, A.A. (2010). A Resonance Assignment Method for Oriented-Sample Solid-State NMR of Proteins. J Am Chem Soc *132*, 8255-8257.

Kochendoerfer, G.G., Jones, D.H., Lee, S., Oblatt-Montal, M., Opella, S.J., and Montal, M. (2004). Functional characterization and NMR spectroscopy on full-length Vpu from HIV-1 prepared by total chemical synthesis. J Am Chem Soc *126*, 2439-2446.

Krämer, U., Talke, I.N., and Hanikenne, M. (2007). Transition metal transport. FEBS Lett *581*, 2263-2272.

Kubo, R. (1969). Stochastic Theories of Randomly Modulated Systems. J Phys Soc Jpn *S 26*, 1-&.

Kurita, J.-i., Shimahara, H., Utsunomiya-Tate, N., and Tate, S.-i. (2003). Measurement of 15N chemical shift anisotropy in a protein dissolved in a dilute liquid crystalline medium with the application of magic angle sample spinning. J Magn Reson *163*, 163-173.

Lafrance-Vanasse, J., Lefebvre, M., Di Lello, P., Sygusch, J., and Omichinski, J.G. (2009). Crystal Structures of the Organomercurial Lyase MerB in Its Free and Mercury-bound Forms: INSIGHTS INTO THE MECHANISM OF METHYLMERCURY DEGRADATION. J Biol Chem *284*, 938-944.

Lamley, J.M., and Lewandowski, J.R. (2012). Simultaneous acquisition of homonuclear and heteronuclear long-distance contacts with time-shared third spin assisted recoupling. J Magn Reson *218*, 30-34.

Landau, E.M., and Rosenbusch, J.P. (1996). Lipidic cubic phases: A novel concept for the crystallization of membrane proteins. Proc Natl Acad Sci *93*, 14532-14535.

Lange, A., Seidel, K., Verdier, L., Luca, S., and Baldus, M. (2003). Analysis of Proton−Proton Transfer Dynamics in Rotating Solids and Their Use for 3D Structure Determination. J Am Chem Soc *125*, 12640-12648.

Laskowski, R., Rullmann, J.A., MacArthur, M., Kaptein, R., and Thornton, J. (1996). AQUA and PROCHECK-NMR: Programs for checking the quality of protein structures solved by NMR. J Biomol NMR *8*, 477-486.

Ledwidge, R., Patel, B., Dong, A., Fiedler, D., Falkowski, M., Zelikova, J., Summers, A.O., Pai, E.F., and Miller, S.M. (2005). NmerA, the Metal Binding Domain of Mercuric Ion Reductase, Removes Hg2+ from Proteins, Delivers It to the Catalytic Core, and Protects Cells under Glutathione-Depleted Conditions,Ä†,,Ä°. Biochemistry *44*, 11402-11416.

Lee, D., Walter, K.F.A., Brückner, A.-K., Hilty, C., Becker, S., and Griesinger, C. (2008). Bilayer in Small Bicelles Revealed by Lipid-Protein Interactions Using NMR Spectroscopy. J Am Chem Soc *130*, 13822-13823.

Lee, M., and Goldburg, W.I. (1965). Nuclear-Magnetic-Resonance Line Narrowing by a Rotating rf Field. Phys Rev *140*, A1261.

Levitt, M.H. SpinDynamica, pp. www.SpinDynamica.soton.ac.uk.

Levitt, M.H. (2007). Symmetry-Based Pulse Sequences in Magic-Angle Spinning Solid-State NMR, Vol 9 (Chichester, UK: John Wiley & Sons, Ltd).

Levitt, M.H., and Di Bari, L. (1992). Steady state in magnetic resonance pulse experiments. Phys Rev Lett *69*, 3124-3127.

Levitt, M.H., Suter, D., and Ernst, R.R. (1986). Spin dynamics and thermodynamics in solid-state NMR cross polarization. J Chem Phys *84*, 4243-4255.

Lewandowski, J.R., De Paëpe, G., and Griffin, R.G. (2007). Proton Assisted Insensitive Nuclei Cross Polarization. Journal of the American Chemical Society *129*, 728-729.

Lewandowski, J.R., PaeÃàpe, G.D., Eddy, M.T., and Griffin, R.G. (2009). 15N-15N Proton Assisted Recoupling in Magic Angle Spinning NMR. J Am Chem Soc *131*, 5769-5776.

Lewis, B.A., Harbison, G.S., Herzfeld, J., and Griffin, R.G. (1985). NMR structural analysis of a membrane protein: bacteriorhodopsin peptide backbone orientation and motion. Biochemistry *24*, 4671-4679.

Lin, E.C., and Opella, S.J. (2011). 1H assisted 13C/15N heteronuclear correlation spectroscopy in oriented sample solid-state NMR of single crystal and magnetically aligned samples. J Magn Reson *211*, 37-44.

Long, J.R., Sun, B.Q., Bowen, A., and Griffin, R.G. (1994). Molecular Dynamics and Magic Angle Spinning NMR. J Am Chem Soc *116*, 11950-11956.

Loquet, A., Sgourakis, N.G., Gupta, R., Giller, K., Riedel, D., Goosmann, C., Griesinger, C., Kolbe, M., Baker, D., Becker, S., and Lange, A. (2012). Atomic model of the type III secretion system needle. Nature *486*, 276-279.

Lu, G.J., and Opella, S.J. (2013). Motion-adapted pulse sequences for oriented sample (OS) solid-state NMR of biopolymers. J Chem Phys *139*, 084203.

Lu, G.J., and Opella, S.J. (2014). Resonance assignments of a membrane protein in phospholipid bilayers by combining multiple strategies of oriented sample solid-state NMR. J Biomol NMR *58*, 69-81.

Lu, G.J., Park, S.H., and Opella, S.J. (2012). Improved 1H amide resonance line narrowing in oriented sample solid-state NMR of membrane proteins in phospholipid bilayers. J Magn Reson *220*, 54-61.

Lu, G.J., Son, W.S., and Opella, S.J. (2011). A general assignment method for oriented sample (OS) solid-state NMR of proteins based on the correlation of resonances through heteronuclear dipolar couplings in samples aligned parallel and perpendicular to the magnetic field. J Magn Reson *209*, 195-206.

Lu, G.J., Tian, Y., Vora, N., Marassi, F.M., and Opella, S.J. (2013a). The structure of the mercury transporter MerF in phospholipid bilayers: a large conformational rearrangement results from N-terminal truncation. J Am Chem Soc *135*, 9299-9302.

Lu, J.-X., Qiang, W., Yau, W.-M., Schwieters, Charles D., Meredith, Stephen C., and Tycko, R. (2013b). Molecular Structure of β-Amyloid Fibrils in Alzheimer's Disease Brain Tissue. Cell *154*, 1257-1268.

Lund, P.A., and Brown, N.L. (1987). Role of the merT and merP gene products of transposon Tn501 in the induction and expression of resistance to mercuric ions. Gene *52*, 207-214.

Macura, S., and Ernst, R.R. (1980). Elucidation of cross relaxation in liquids by two-dimensional N.M.R. spectroscopy. Molecular Physics *41*, 95-117.

Madhu, P.K., Zhao, X., and Levitt, M.H. (2001). High-resolution 1H NMR in the solid state using symmetry-based pulse sequences. Chem Phys Lett *346*, 142-148.

Marassi, F.M. (2001). A simple approach to membrane protein secondary structure and topology based on NMR spectroscopy. Biophys J *80*, 994-1003.

Marassi, F.M., Das, B.B., Lu, G.J., Nothnagel, H.J., Park, S.H., Son, W.S., Tian, Y., and Opella, S.J. (2011). Structure determination of membrane proteins in five easy pieces. Methods.

Marassi, F.M., Gesell, J.J., Valente, A.P., Kim, Y., Oblatt-Montal, M., Montal, M., and Opella, S.J. (1999a). Dilute spin-exchange assignment of solid-state NMR spectra of oriented proteins: acetylcholine M2 in bilayers. J Biomol NMR *14*, 141-148.

Marassi, F.M., Gesell, J.J., Valente, A.P., Kim, Y., Oblatt-Montal, M., Montal, M., and Opella, S.J. (1999b). Dilute spin-exchange assignment of solid-state NMR spectra of oriented proteins: acetylcholine M2 in bilayers. J Biomol NMR *14*, 141-148.

Marassi, F.M., and Opella, S.J. (2000). A solid-state NMR index of helical membrane protein structure and topology. J Magn Reson *144*, 150-155.

Marassi, F.M., and Opella, S.J. (2003). Simultaneous assignment and structure determination of a membrane protein from NMR orientational restraints. Protein Sci *12*, 403-411.

McDermott, A. (2009). Structure and Dynamics of Membrane Proteins by Magic Angle Spinning Solid-State NMR. Annu Rev Biophys *38*, 385-403.

McLaughlin, A.C., Cullis, P.R., Hemminga, M.A., Hoult, D.I., Radda, G.K., Ritchie, G.A., Seeley, P.J., and Richards, R.E. (1975). Application of 31P NMR to model and biological membrane systems. FEBS Lett *57*, 213-218.

McMillan, D.E., Hazendonk, P., and Hodgkinson, P. (2003). Interference of homonuclear decoupling and exchange in the solid-state NMR of perfluorocyclohexane. J Magn Reson *161*, 234-241.

Mehring, M., Griffin, R.G., and Waugh, J.S. (1971). 19F Shielding Tensors from Coherently Narrowed NMR Powder Spectra. J Chem Phys *55*, 746-755.

Mehring, M., and Weberruss, V.A. (2001). Object-Oriented Magnetic Resonance: Classes and Objects, Calculations and Computations (New York: Academic Press).

Melnick, J.G., and Parkin, G. (2007). Cleaving Mercury-Alkyl Bonds: A Functional Model for Mercury Detoxification by MerB. Science (New York, NY) *317*, 225-227.

Mesleh, M.F., Lee, S., Veglia, G., Thiriot, D.S., Marassi, F.M., and Opella, S.J. (2003). Dipolar waves map the structure and topology of helices in membrane proteins. J Am Chem Soc *125*, 8928-8935.

Mesleh, M.F., and Opella, S.J. (2003). Dipolar Waves as NMR maps of helices in proteins. J Magn Reson *163*, 288-299.

Mesleh, M.F., Veglia, G., DeSilva, T.M., Marassi, F.M., and Opella, S.J. (2002). Dipolar Waves as NMR Maps of Protein Structure. J Am Chem Soc *124*, 4206-4207.

Misra, T.K., Brown, N.L., Fritzinger, D.C., Pridmore, R.D., Barnes, W.M., Haberstroh, L., and Silver, S. (1984). Mercuric ion-resistance operons of plasmid R100 and transposon Tn501: the beginning of the operon including the regulatory region and the first two structural genes. Proc Natl Acad Sci *81*, 5975-5979.

Murray, D.T., Das, N., and Cross, T.A. (2013). Solid State NMR Strategy for Characterizing Native Membrane Protein Structures. Acc Chem Res *46*, 2172-2181.

Nakahara, H., Silver, S., Miki, T., and Rownd, R.H. (1979). Hypersensitivity to Hg2+ and hyperbinding activity associated with cloned fragments of the mercurial resistance operon of plasmid NR1. J Bacteriol *140*, 161-166.

Nevzorov, A. (2011a). Orientational and Motional Narrowing of Solid-State NMR Lineshapes of Uniaxially Aligned Membrane Proteins. J Phys Chem B *115*, 15406-15414.

Nevzorov, A., Park, S., and Opella, S. (2007). Three-dimensional experiment for solid-state NMR of aligned protein samples in high field magnets. J Biomol NMR *37*, 113-116.

Nevzorov, A.A. (2008). Mismatched Hartmann-Hahn conditions cause proton-mediated intermolecular magnetization transfer between dilute low-spin nuclei in NMR of static solids. J Am Chem Soc *130*, 11282-11283.

Nevzorov, A.A. (2009). High-resolution local field spectroscopy with internuclear correlations. J Magn Reson *201*, 111-114.

Nevzorov, A.A. (2011b). Ergodicity and efficiency of cross-polarization in NMR of static solids. J Magn Reson *209*, 161-166.

Nevzorov, A.A., and Opella, S.J. (2003a). A "magic sandwich" pulse sequence with reduced offset dependence for high-resolution separated local field spectroscopy. J Magn Reson *164*, 182-186.

Nevzorov, A.A., and Opella, S.J. (2003b). Structural fitting of PISEMA spectra of aligned proteins. J Magn Reson *160*, 33-39.

Nevzorov, A.A., and Opella, S.J. (2007). Selective averaging for high-resolution solid-state NMR spectroscopy of aligned samples. J Magn Reson *185*, 59-70.

Nielsen, A., Székely, K., Gath, J., Ernst, M., Nielsen, N., and Meier, B. (2012a). Simultaneous acquisition of PAR and PAIN spectra. J Biomol NMR *52*, 283-288.

Nielsen, N., Strassø, L., and Nielsen, A. (2012b). Dipolar Recoupling. In Solid State NMR, J.C.C. Chan, ed. (Springer Berlin Heidelberg), pp. 1-45.

Nielsen, N.C., Bildsoe, H., Jakobsen, H.J., and Levitt, M.H. (1994). Double-quantum homonuclear rotary resonance: Efficient dipolar recovery in magic-angle spinning nuclear magnetic resonance. J Chem Phys *101*, 1805-1812.

Nucifora, G., Silver, S., and Misra, T.K. (1989). Down regulation of the mercury resistance operon by the most promoter-distal gene <i>merD</i&gt. Molecular and General Genetics MGG *220*, 69-72.

Oas, T.G., Griffin, R.G., and Levitt, M.H. (1988). Rotary resonance recoupling of dipolar interactions in solid-state nuclear magnetic resonance spectroscopy. J Chem Phys *89*, 692-695.

Opella, S.J. (2013). Structure Determination of Membrane Proteins by Nuclear Magnetic Resonance Spectroscopy. Annu Rev Anal Chem *6*, 305-328.

Opella, S.J., Frey, M.H., and Cross, T.A. (1979). Detection of individual carbon resonances in solid proteins. J Am Chem Soc *101*, 5856-5857.

Opella, S.J., Ma, C., and Marassi, F.M. (2001). Nuclear magnetic resonance of membrane-associated peptides and proteins. Methods Enzymol *339*, 285-313.

Opella, S.J., Marassi, F.M., Gesell, J.J., Valente, A.P., Kim, Y., Oblatt-Montal, M., and Montal, M. (1999). Structures of the M2 channel-lining segments from nicotinic acetylcholine and NMDA receptors by NMR spectroscopy. Nat Struct Biol *6*, 374-379.

Opella, S.J., and Waugh, J.S. (1977). Two-dimensional 13C NMR of highly oriented polyethylene. J Chem Phys *66*, 4919-4924.

Opella, S.J., Zeri, A.C., and Park, S.H. (2008). Structure, dynamics, and assembly of filamentous bacteriophages by nuclear magnetic resonance spectroscopy. Annu Rev Phys Chem *59*, 635-657.

Pake, G.E. (1948). Nuclear Resonance Absorption in Hydrated Crystals: Fine Structure of the Proton Line. J Chem Phys *16*, 327-336.

Palmer, A.G., Williams, J., and McDermott, A. (1996). Nuclear Magnetic Resonance Studies of Biopolymer Dynamics. J Phys Chem *100*, 13293-13310.

Park, S., Loudet, C., Marassi, F., Dufourc, E., and Opella, S. (2008). Solid-state NMR spectroscopy of a membrane protein in biphenyl phospholipid bicelles with the bilayer normal parallel to the magnetic field. J Magn Reson.

Park, S.H., Casagrande, F., Chu, M., Maier, K., Kiefer, H., and Opella, S.J. (2011a). Optimization of Purification and Refolding of the Human Chemokine Receptor CXCR1 Improves the Stability of Proteoliposomes for Structure Determination. Biochim Biophys Acta, submitted for publication.

Park, S.H., Casagrande, F., Chu, M., Maier, K., Kiefer, H., and Opella, S.J. (2012a). Optimization of purification and refolding of the human chemokine receptor CXCR1 improves the stability of proteoliposomes for structure determination. Biochim Biophys Acta-Biomembr *1818*, 584-591.

Park, S.H., Casagrande, F., Das, B.B., Albrecht, L., Chu, M., and Opella, S.J. (2011b). Local and global dynamics of the G-protein-coupled receptor CXCR1. Biochemistry, 2371-2380.

Park, S.H., Das, B.B., Casagrande, F., Tian, Y., Nothnagel, H.J., Chu, M., Kiefer, H., Maier, K., De Angelis, A.A., Marassi, F.M., and Opella, S.J. (2012b). Structure of the chemokine receptor CXCR1 in phospholipid bilayers. Nature *491*, 779-783.

Park, S.H., Das, B.B., De Angelis, A.A., Scrima, M., and Opella, S.J. (2010a). Mechanically, Magnetically, and "Rotationally Aligned" Membrane Proteins in Phospholipid Bilayers Give Equivalent Angular Constraints for NMR Structure Determination. J Phys Chem B *114*, 13995-14003.

Park, S.H., De Angelis, A.A., Nevzorov, A.A., Wu, C.H., and Opella, S.J. (2006a). Three-dimensional structure of the transmembrane domain of Vpu from HIV-1 in aligned phospholipid bicelles. Biophys J *91*, 3032-3042.

Park, S.H., Marassi, F.M., Black, D., and Opella, S.J. (2010b). Structure and dynamics of the membrane-bound form of Pf1 coat protein: Implications of structural rearragnement for virus assembly. Biophysical Journal *99*, 1465-1474.

Park, S.H., Marassi, F.M., Black, D., and Opella, S.J. (2010c). Structure and Dynamics of the Membrane-Bound Form of Pf1 Coat Protein: Implications of Structural Rearrangement for Virus Assembly. Biophys J *99*, 1465-1474.

Park, S.H., Mrse, A.A., Nevzorov, A.A., De Angelis, A.A., and Opella, S.J. (2006b). Rotational diffusion of membrane proteins in aligned phospholipid bilayers by solid-state NMR spectroscopy. J Magn Reson *178*, 162-165.

Park, S.H., Mrse, A.A., Nevzorov, A.A., Mesleh, M.F., Oblatt-Montal, M., Montal, M., and Opella, S.J. (2003). Three-dimensional structure of the channel-forming trans-membrane domain of virus protein "u" (Vpu) from HIV-1. J Mol Biol *333*, 409-424.

Park, S.H., and Opella, S.J. (2010). Triton X-100 as the "Short-Chain Lipid" Improves the Magnetic Alignment and Stability of Membrane Proteins in Phosphatidylcholine Bilayers for Oriented-Sample Solid-State NMR Spectroscopy. J Am Chem Soc *132*, 12552-12553.

Parks, J.M., Johs, A., Podar, M., Bridou, R., Hurt, R.A., Smith, S.D., Tomanicek, S.J., Qian, Y., Brown, S.D., Brandt, C.C., Palumbo, A.V., Smith, J.C., Wall, J.D., Elias, D.A., and Liang, L. (2013). The Genetic Basis for Bacterial Mercury Methylation. Science (New York, NY) *339*, 1332-1335.

Pauli, J., Baldus, M., van Rossum, B., de Groot, H., and Oschkinat, H. (2001). Backbone and Side-Chain 13C and 15N Signal Assignments of the α-Spectrin SH3 Domain by Magic Angle Spinning Solid-State NMR at 17.6 Tesla. ChemBioChem *2*, 272-281.

Pines, A., Gibby, M.G., and Waugh, J.S. (1973). Proton-enhanced NMR of dilute spins in solids. J Chem Phys *59*, 569-590.

Prosser, R.S., Hwang, J.S., and Vold, R.R. (1998). Magnetically Aligned Phospholipid Bilayers with Positive Ordering: A New Model Membrane System. Biophys J *74*, 2405-2418.

Qian, H., Sahlman, L., Eriksson, P.-O., Hambraeus, C., Edlund, U., and Sethson, I. (1998). NMR Solution Structure of the Oxidized Form of MerP, a Mercuric Ion Binding Protein Involved in Bacterial Mercuric Ion Resistance,Ä†,,Ä°. Biochemistry *37*, 9316-9322.

Raleigh, D.P., Levitt, M.H., and Griffin, R.G. (1988). Rotational resonance in solid state NMR. Chem Phys Lett *146*, 71-76.

Ramamoorthy, A., Wu, C.H., and Opella, S.J. (1995). Three-dimensional solid-state NMR experiment that correlates the chemical shift and dipolar coupling frequencies of two heteronuclei. J Magn Reson, Ser B *107*, 88-90.

Raschle, T., Hiller, S., Etzkorn, M., and Wagner, G. (2010). Nonmicellar systems for solution NMR spectroscopy of membrane proteins. Curr Opin Struct Biol *20*, 471-479.

Reichert, D. (2005). NMR Studies of Dynamic Processes in Organic Solids. In Annual Reports on NMR Spectroscopy, G.A. Webb, ed. (Academic Press), pp. 159-203.

Rhim, W.K., Pines, A., and Waugh, J.S. (1971). Time-Reversal Experiments in Dipolar-Coupled Spin Systems. Phys Rev B *3*, 684.

Rohl, C.A., Strauss, C.E.M., Misura, K.M.S., and Baker, D. (2004). Protein Structure Prediction Using Rosetta. In Methods Enzymol, B. Ludwig, and L.J. Michael, eds. (Academic Press), pp. 66-93.

Rosenbaum, D., Cherezov, V., Hanson, M., Rasmussen, S., Thian, F., Kobilka, T., Choi, H.-J., Yao, X.-J., Weis, W., Stevens, R., and Kobilka, B. (2007). GPCR Engineering Yields High-Resolution Structural Insights into 2-Adrenergic Receptor Function. Science (New York, NY) *318*, 1266-1273.

Rothwell, W.P., and Waugh, J.S. (1981). Transverse relaxation of dipolar coupled spin systems under rf irradiation: Detecting motions in solids. J Chem Phys *74*, 2721-2732.

Ruiz, O.N., and Daniell, H. (2009). Genetic engineering to enhance mercury phytoremediation. Curr Opin Biotechnol *20*, 213-219.

Rúiek L., and Vondrášek, J. (1998). Coordination geometries of selected transition metal ions (Co2+, Ni2+, Cu2+, Zn2+, Cd2+, and Hg2+) in metalloproteins. J Inorg Biochem *71*, 115-127.

Sahlman, L., Wong, W., and Powlowski, J. (1997). A Mercuric Ion Uptake Role for the Integral Inner Membrane Protein, MerC, Involved in Bacterial Mercuric Ion Resistance. J Biol Chem *272*, 29518-29526.

Salager, E., Dumez, J.-N., Stein, R.S., Steuernagel, S., Lesage, A., Elena-Herrmann, B., and Emsley, L. (2010). Homonuclear dipolar decoupling with very large scaling factors for high-resolution ultrafast magic angle spinning 1H solid-state NMR spectroscopy. Chem Phys Lett *498*, 214-220.

Sanders, C.R., Hare, B.J., Howard, K.P., and Prestegard, J.H. (1994a). Magnetically-oriented phospholipid micelles as a tool for the study of membrane-associated molecules. Prog Nucl Magn Reson Spectrosc *26*, 421-444.

Sanders, C.R., Hare, B.J., Howard, K.P., and Prestegard, J.H. (1994b). Magnetically-oriented phospholipid micelles as a tool for the study of membrane-associated molecules. Progress in Nuclear Magnetic Resonance Spectroscopy *26*, 421-444.

Schaefer, J., and Stejskal, E.O. (1976). Carbon-13 nuclear magnetic resonance of polymers spinning at the magic angle. J Am Chem Soc *98*, 1031-1032.

Schiering, N., Kabsch, W., Moore, M.J., Distefano, M.D., Walsh, C.T., and Pai, E.F. (1991). Structure of the detoxification catalyst mercuric ion reductase from Bacillus sp. strain RC607. Nature *352*, 168-172.

Schmidt, A., Smith, S.O., Raleigh, D.P., Roberts, J.E., Griffin, R.G., and Vega, S. (1986). Chemical exchange effects in the NMR spectra of rotating solids. J Chem Phys *85*, 4248-4253.

Schmidt-Rohr, K., Nanz, D., Emsley, L., and Pines, A. (1994a). NMR measurement of resolved heteronuclear dipolar couplings in liquid crystals and lipids. J Phys Chem *98*, 6668-6670.

Schmidt-Rohr, K., Nanz, D., Emsley, L., and Pines, A. (1994b). NMR Measurement of Resolved Heteronuclear Dipole Couplings in Liquid Crystals and Lipids. J Phys Chem *98*, 6668-6670.

Scholz, I., Huber, M., Manolikas, T., Meier, B.H., and Ernst, M. (2008). MIRROR recoupling and its application to spin diffusion under fast magic-angle spinning. Chem Phys Lett *460*, 278-283.

Schwieters, C.D., and Clore, G.M. (2001). Internal Coordinates for Molecular Dynamics and Minimization in Structure Determination and Refinement. J Magn Reson *152*, 288-302.

Serre, L., Rossy, E., Pebay-Peyroula, E., Cohen-Addad, C., and Covès, J. (2004). Crystal Structure of the Oxidized Form of the Periplasmic Mercury-binding Protein MerP from Ralstonia metallidurans CH34. J Mol Biol *339*, 161-171.

Sharma, M., Yi, M., Dong, H., Qin, H., Peterson, E., Busath, D.D., Zhou, H.-X., and Cross, T.A. (2010). Insight into the Mechanism of the Influenza A Proton Channel from a Structure in a Lipid Bilayer. Science (New York, NY) *330*, 509-512.

Sinha, N., Filipp, F.V., Jairam, L., Park, S.H., Bradley, J., and Opella, S.J. (2007a). Tailoring 13C labeling for triple-resonance solid-state NMR experiments on aligned samples of proteins. Magnetic resonance in chemistry : MRC *45 Suppl 1*, S107-115.

Sinha, N., Grant, C.V., Park, S.H., Brown, J.M., and Opella, S.J. (2007b). Triple resonance experiments for aligned sample solid-state NMR of (13)C and (15)N labeled proteins. J Magn Reson *186*, 51-64.

Sinha, N., Grant, C.V., Wu, C.H., De Angelis, A.A., Howell, S.C., and Opella, S.J. (2005). SPINAL modulated decoupling in high field double- and triple-resonance solid-state NMR experiments on stationary samples. J Magn Reson *177*, 197-202.

Son, W.S., Park, S.H., Nothnagel, H.J., Lu, G.J., Wang, Y., Zhang, H., Cook, G.A., Howell, S.C., and Opella, S.J. (2012). 'q-Titration' of long-chain and short-chain lipids differentiates between structured and mobile residues of membrane proteins studied in bicelles by solution NMR spectroscopy. J Magn Reson *214*, 111-118.

Spiess, H.W. (1974). Molecular motion studied by NMR powder spectra. I. Lineshape calculation for axially symmetric sheilding tensors. Chem Phys *6*, 217-225.

Spiess, H.W. (1983). Molecular dynamics of solid polymers as revealed by deuteron NMR. Colloid Polym Sci *261*, 193-209.

Spiess, H.W., Grosescu, R., and Haeberlen, H. (1974). Molecular motion studied by NMR powder spectra. II. Experimental results for solid P4 and solid Fe(CO)5. Chem Phys *6*, 226-234.

Steele, R.A., and Opella, S.J. (1997). Structures of the reduced and mercury-bound forms of MerP, the periplasmic protein from the bacterial mercury detoxification system. Biochemistry *36*, 6885-6895.

Suwelack, D., Rothwell, W.P., and Waugh, J.S. (1980). Slow molecular motion detected in the NMR spectra of rotating solids. J Chem Phys *73*, 2559-2569.

Szeverenyi, N.M., Sullivan, M.J., and Maciel, G.E. (1982). Observation of spin exchange by two-dimensional fourier transform 13C cross polarization-magic-angle spinning. J Magn Reson *47*, 462-475.

Takegoshi, K., and McDowell, C.A. (1985). A "magic echo" pulse sequence for the high-resolution NMR spectra of abundant spins in solids. Chem Phys Lett *116*, 100-104.

Takegoshi, K., Nakamura, S., and Terao, T. (2001). 13C-1H dipolar-assisted rotational resonance in magic-angle spinning NMR. Chem Phys Lett *344*, 631-637.

Tang, W., Knox, R., and Nevzorov, A. (2012). A spectroscopic assignment technique for membrane proteins reconstituted in magnetically aligned bicelles. J Biomol NMR *54*, 307-316.

Tang, W., and Nevzorov, A.A. (2011). Repetitive cross-polarization contacts via equilibration-re-equilibration of the proton bath: Sensitivity enhancement for NMR of membrane proteins reconstituted in magnetically aligned bicelles. J Magn Reson *212*, 245-248.

Thiriot, D.S., Nevzorov, A.A., Zagyanskiy, L., Wu, C.H., and Opella, S.J. (2004). Structure of the coat protein in Pf1 bacteriophage determined by solid-state NMR spectroscopy. J Mol Biol *341*, 869-879.

Tian, Y., Schwieters, C.D., Opella, S.J., and Marassi, F.M. (2012). AssignFit: A program for simultaneous assignment and structure refinement from solid-state NMR spectra. J Magn Reson *214*, 42-50.

Tjandra, N., Omichinski, J.G., Gronenborn, A.M., Clore, G.M., and Bax, A. (1997). Use of dipolar 1H-15N and 1H-13C couplings in the structure determination of magnetically oriented macromolecules in solution. Nat Struct Mol Biol *4*, 732-738.

Tolman, J.R., Flanagan, J.M., Kennedy, M.A., and Prestegard, J.H. (1995). Nuclear magnetic dipole interactions in field-oriented proteins: information for structure determination in solution. Proc Natl Acad Sci *92*, 9279-9283.

Traaseth, N.J., Gopinath, T., and Veglia, G. (2010). On the Performance of Spin Diffusion NMR Techniques in Oriented Solids: Prospects for Resonance Assignments and Distance Measurements from Separated Local Field Experiments. J Phys Chem B *114*, 13872-13880.

Traaseth, N.J., Shi, L., Verardi, R., Mullen, D.G., Barany, G., and Veglia, G. (2009). Structure and topology of monomeric phospholamban in lipid membranes determined by a hybrid solution and solid-state NMR approach. Proc Natl Acad Sci *106*, 10165-10170.

Van Melckebeke, H., Wasmer, C., Lange, A., Ab, E., Loquet, A., Böckmann, A., and Meier, B.H. (2010). Atomic-Resolution Three-Dimensional Structure of HET-s(218−289) Amyloid Fibrils by Solid-State NMR Spectroscopy. J Am Chem Soc *132*, 13765-13775.

Veshtort, M., and Griffin, R.G. (2006). SPINEVOLUTION: A powerful tool for the simulation of solid and liquid state NMR experiments. J Magn Reson *178*, 248-282.

Vinogradov, E., Madhu, P.K., and Vega, S. (1999). High-resolution proton solid-state NMR spectroscopy by phase-modulated Lee-Goldburg experiment. Chem Phys Lett *314*, 443-450.

Virlet, J., and Ghesquieres, D. (1980). NMR Longitudinal cross relaxation induced by natural abundance 13C-13C dipolar interaction in organic solids. Hexamethylethane. Chemical Physics Letters *73*, 323-327.

Wang, J., Denny, J., Tian, C., Kim, S., Mo, Y., Kovacs, F., Song, Z., Nishimura, K., Gan, Z., Fu, R., Quine, J.R., and Cross, T.A. (2000). Imaging Membrane Protein Helical Wheels. J Magn Reson *144*, 162-167.

Wang, J., Kim, S., Kovacs, F., and Cross, T.A. (2001). Structure of the transmembrane region of the M2 protein H+ channel. Protein Science *10*, 2241-2250.

Warschawski, D.E., Arnold, A.A., Beaugrand, M., Gravel, A., Chartrand, E., and Marcotte, I. (2011). Choosing membrane mimetics for NMR structural studies of transmembrane proteins. Biochim Biophys Acta-Biomembr *1808*, 1957-1974.

Waugh, J.S., Huber, L.M., and Haeberlen, U. (1968). Approach to High-Resolution nmr in Solids. Phys Rev Lett *20*, 180-182.

Weingarth, M., Demco, D.E., Bodenhausen, G., and Tekely, P. (2009). Improved magnetization transfer in solid-state NMR with fast magic angle spinning. Chem Phys Lett *469*, 342-348.

Wilson, J.R., Leang, C., Morby, A.P., Hobman, J.L., and Brown, N.L. (2000). MerF is a mercury transport protein: different structures but a common mechanism for mercuric ion transporters? FEBS Lett *472*, 78-82.

Wu, C.H., Das, B.B., and Opella, S.J. (2010). 1H-13C hetero-nuclear dipole-dipole couplings of methyl groups in stationary and magic angle spinning solid-state NMR experiments of peptides and proteins. J Magn Reson *202*, 127-134.

Wu, C.H., Grant, C.V., Cook, G.A., Park, S.H., and Opella, S.J. (2009). A strip-shield improves the efficiency of a solenoid coil in probes for high-field solid-state NMR of lossy biological samples. J Magn Reson *200*, 74-80.

Wu, C.H., Ramamoorthy, A., and Opella, S.J. (1994). High-Resolution Heteronuclear Dipolar Solid-State NMR Spectroscopy. J Magn Reson, Ser A *109*, 270-272.

Xu, J., Struppe, J., and Ramamoorthy, A. (2008). Two-dimensional homonuclear chemical shift correlation established by the cross-relaxation driven spin diffusion in solids. J Chem Phys *128*, 052308.

Yang, J., Aslimovska, L., and Glaubitz, C. (2011). Molecular Dynamics of Proteorhodopsin in Lipid Bilayers by Solid-State NMR. J Am Chem Soc *133*, 4874-4881.

Yarov-Yarovoy, V., Schonbrun, J., and Baker, D. (2006). Multipass membrane protein structure prediction using Rosetta. Proteins *62*, 1010-1025.

Zech, S.G., Wand, A.J., and McDermott, A.E. (2005). Protein Structure Determination by High-Resolution Solid-State NMR Spectroscopy: Application to Microcrystalline Ubiquitin. J Am Chem Soc *127*, 8618-8626.

Zeri, A.C., Mesleh, M.F., Nevzorov, A.A., and Opella, S.J. (2003a). Structure of the coat protein in fd filamentous bacteriophage particles determined by solid-state NMR spectroscopy. Proc Natl Acad Sci USA *100*, 6458-6463.

Zeri, A.C., Mesleh, M.F., Nevzorov, A.A., and Opella, S.J. (2003b). Structure of the coat protein in fd filamentous bacteriophage particles determined by solid-state NMR spectroscopy. Proc Natl Acad Sci U S A *100*, 6458-6463.

Zhao, X., Edén, M., and Levitt, M.H. (2001). Recoupling of heteronuclear dipolar interactions in solid-state NMR using symmetry-based pulse sequences. Chem Phys Lett *342*, 353-361.

Zheng, J., and Jia, Z. (2013). Structural biology: Tiny enzyme uses context to succeed. Nature *497*, 445-446.

Zhou, H.-X., and Cross, T.A. (2013). Influences of Membrane Mimetic Environments on Membrane Protein Structures. Annu Rev Biophys *42*, 361-392.

Zoonens, M., Comer, J., Masscheleyn, S., Pebay-Peyroula, E., Chipot, C., Miroux, B., and Dehez, F. (2013). Dangerous Liaisons between Detergents and Membrane Proteins. The Case of Mitochondrial Uncoupling Protein 2. J Am Chem Soc *135*, 15174-15182.